Abstract

Title of Dissertation:	METABOLIC PROFILING OF BRAIN MICROVASCULAR ENDOTHELIAL CELLS: INVESTIGATING THE ROLE OF SEX, STRESS, APOE GENOTYPE, AND EXERCISE IN ALZHEIMER'S DISEASE RISK
	Callie Margaret Weber, Doctor of Philosophy, 2024
Dissertation directed by:	Professor Alisa Morss Clyne, Fischell Department of Bioengineering

Alzheimer's disease (AD) is the 7th leading cause of death in the United States, yet there are still no effective treatments to prevent or slow the progression of the disease. AD develops from a combination of genetic and lifestyle risk factors including female sex, elevated stress hormone exposure, the apolipoprotein (APOE) ε4 genotype, and a sedentary lifestyle. In order to better identify the manifestations of AD, it is vital to understand how each of these risk factors impact brain health and lead to neurological dysfunction associated with AD.

Brain microvascular endothelial cells (BMEC) line the blood vessels of the brain and have specialized tight junctions designed to strictly regulate nutrient and waste transfer between the blood and the brain. Two of the early indicators of AD development are breakdown of the tight junctions and whole brain glucose hypometabolism. Since BMEC form the first line of defense for the brain against neurotoxic compounds in

the blood and are responsible for glucose transport to the rest of the brain, the overarching goal of this thesis is to understand how female sex, elevates stress hormone exposure, the APOE ε4 genotype, and a sedentary lifestyle induce breakdown of tight junction proteins and glucose hypometabolism in BMEC.

I first demonstrate that female sex exacerbates endothelial dysfunction in response to high levels of a stress hormone, Angiotensin II (AngII). Specifically, I show that in response to AngII, female endothelial cells increase oxidative stress and inflammatory responses while male endothelial cells do not. Next, I used CRISPR/Cas9 to generate a set of induced pluripotent stem cells (iPSC) homozygous for the APOE ε3 and ε4 genotype and differentiated them into BMEC (hiBMEC). Using the hiBMEC I showed the APOE ε4 genotype induces barrier deficiencies that are partially mediated through reduced levels of protein deacetylase Sirtuin 1 (SIRT1), and that the APOE ε4 genotype causes glucose hypometabolism through decreased insulin signaling. Finally, by adding serum from sedentary and exercise trained individuals to genotype-matched hiBMEC, I show that APOE ε3 and ε4 hiBMEC have divergent responses to treatment with serum from sedentary and exercise trained individuals. Treatment with exercise trained serum increases SIRT1 and glycolytic enzymes compared to sedentary serum, while exercise trained serum decreases SIRT1 and glycolytic enzymes in APOE ε4 hiBMEC compared to sedentary serum.

The work described in this thesis gives a fundamental, mechanistic understanding to the roles of female sex, stress hormone exposure, the APOE ε4 genotype, and a sedentary lifestyle in BMEC dysfunction and hypometabolism, giving insight into how these factors contribute to AD development and progression.

METABOLIC PROFILING OF BRAIN MICROVASCULAR ENDOTHELIAL CELLS: INVESTIGATING THE ROLE OF SEX, STRESS, APOE GENOTYPE, AND EXERCISE IN ALZHEIMER'S DISEASE RISK

by

Callie Margaret Weber

Dissertation submitted to the Faculty of the Graduate School of the
University of Maryland, College Park, in partial fulfillment
of the requirements for the degree of
Doctor of Philosophy
2024

Advisory Committee:
Professor Alisa Morss Clyne, Chair
Professor Jerome Carson Smith
Associate Professor Helim Aranda-Espinoza
Associate Professor Kimberly Stroka
Associate Professor Ganesh Sriram

© Copyright by

Callie Margaret Weber

2024

Acknowledgements

The completion of this thesis would not have been possible without the hard work, love, and support of many people along the way. First, I would like to express my deepest gratitude to my thesis advisor, Dr. Alisa Morss Clyne, for her support, guidance, and patience as we developed and completed this project. You have taught me so much about navigating the academic world, mentorship, and finding balance in this job, and I could not have done any of this without you.

Secondly, I am incredibly grateful to my committee members, Dr. Kimberly Stroka, Dr. Carson Smith, Dr. Ganesh Sriram, and Dr. Helim Aranda-Espinoza for their valuable insights and critiques of my projects. You have all greatly improved the work presented in this thesis, and I am a better researcher because of you. I owe an additional thank you to Dr. Carson Smith, Dr. Gabriel Pena, and everyone else in the Exercise for Brain Health Laboratory without whom the exercise portion of this work would not exist.

Next, I owe some of my deepest thanks to all the members of the Vascular Kinetics Lab, past and present, who have been some of my best mentors, collaborators, and most importantly, friends over these last five years. To Dr. Samantha Bohlman, thank you for showing me the ropes in the lab and teaching me everything there is to know about Western blotting. To Dr. Bilal Moiz thank you for always acting as my sounding board, assistant cell feeder, and computer/microscope wizard at any (and all) hours of the day- there's nobody I would rather have done this alongside. To Dr. Gurneet Sangha, I cannot thank you enough for your endless mentorship and advice. Even though you don't know how to eat an apple, you do know how to navigate every other situation in life, and I absolutely could not have done this without your help. To Marzyeh Kheradmand, your love and friendship have gotten me through the most difficult parts of this PhD, and it would have been impossible without you. Your requisite French fry and tea breaks have made even the hardest days better. To Lauren Smith, I am forever grateful to you for not letting me take this too seriously. Our gossip sessions and candy breaks have made every day infinitely more fun. And finally, to Jesse Vo, Dr. Ryan Sapp, Dr. Michael Sun, Claire Sissons, Viviana Alpizar, Annie Barnes, Sophia Zic, Brooke Wunderler, and Claire Kettula thank you for always providing feedback, support, and kindness throughout my PhD.

I would also like to thank my incredible friends that have supported me throughout my PhD. Alexa Gittle, Rachel Lobien, Julia Elder, Emily Abrishamkar, Sandy Chesterton, and Maddie Brown- you've supported me in every stage of college and graduate school, and I'm so grateful to always have you all to fall back on. Your texts and phone calls are the highlight of each day, and I can't imagine doing this without you. Timber Kelly, Samantha Johnson, Hailey Hulett, Lucy Brannon, Megan Murphy, Brigette Thomas, Grace Kotara, Ellie Punnett, Olivia Thornton, and Tatum Morell, I'm so grateful to have grown up with you all as the most incredible support system. Thank you for the endless supply of memories, laughs, and hometown gossip.

I would never be where I am today without the infinite love and support of my family- my parents Mike and Annie Weber, my brother Nick Weber-Stout, my sister-in-law Mariah Stout, and my grandma Candyce Weber. Mom and Dad- I can't thank you enough for always letting me follow my dreams. You taught me to always work hard, play hard, and cook great food- some of the most important lessons in life. Nick and Mariah, thank you for the flight benefits, running half marathons with me, and most importantly for always flying across the country to support me. Grandma, thank you forever for all your love and encouragement.

Last, but not least, I owe my greatest thanks to Christian Stano for being the most supportive partner over the last seven years. Without a doubt this dream would not be a reality without you. Thank you for always planning weekends around my cell feeding schedule, cooking dinner when I'm too stressed, agreeing to nightly Below Deck marathons, and going on daily walks with me. It's the little things that matter, and you make all the little things a million times better.

Table of Contents

Abstract ii

Acknowledgements ii

Table of Contents iv

List of Tables xi

List of Figures xii

Chapter 1: Introduction 1

1.1 Thesis Goal 1

1.2. Thesis Organization 1

1.3. Clinical Motivation: Brain endothelial cell dysregulation in Alzheimer's Disease 3

1.4. The Blood-Brain Barrier 5

1.5. Metabolism in the Blood-Brain Barrier 7

1.5.1. BMEC Glucose Metabolism 7

1.5.2. BMEC Glutamine and Glutamate Metabolism 8

1.5.3. Fatty Acid Metabolism in BMEC 10

1.6. Risk Factors for Alzheimer's Disease Impact BMEC Metabolism 12

1.6.1. Female Sex 12

1.6.2. Angiotensin II 14

1.6.3. APOE Genotype 15

1.6.4. Sedentary Lifestyle 17

Chapter 2: Sex differences in response to Angiotensin II 19

2.1. Introduction: 19

2.2. Methods: 20

2.2.1. Cell Culture: 20

2.2.2. RNA Sequencing: 21

2.2.3. ELISA: 22

2.2.4. Endothelial-to-Mesenchymal Transition (EndMT): 22

2.2.5. White Blood Cell (WBC) Adhesion Assay: 22
2.2.6. Oxygen Consumption Rate (OCR): 23
2.2.7. Reactive Oxygen Species: 23
2.2.8. CYBB Gene Expression: 23
2.2.9. NOX2 siRNA knockdown: 24
2.2.10. Fluorescent Image Quantification: 24
2.2.11. Statistics: 24
2.3. Results: 25
2.3.1. Female and male HUVEC had sexually dimorphic gene expression. 25
2.3.2. Female HUVEC altered expression of more genes in response to AngII than male HUVEC. 27
2.3.3. TGF-β2 gene expression, but not protein secretion, was elevated in female HUVEC in response to AngII. 27
2.3.4. AngII increased inflammatory responses in female but not male EC. 28
2.3.5. AngII increased ROS production in female but not male EC. 31
2.3.6. Mitochondrial superoxide production, but not mitochondrial metabolic rate, increased in female HUVEC in response to AngII 35
2.3.7. CYBB gene expression was elevated in female HUVEC and may be partially responsible for increased ROS production in response to AngII. 35
2.4. Discussion: 39
2.6 Limitations 42
2.5. Conclusions 42
Chapter 3: iPSC-BMEC modeling of brain endothelial cell glucose metabolism 44
3.1. Introduction 44
3.2. Methods 45
3.2.1. hiBMEC Differentiation: 45
3.2.2. hpBMEC Culture: 46
3.2.3. Astrocyte Culture: 46
3.2.4. TEER: 46

3.2.5. YSI: 47
3.2.6. Seahorse Assays: 47
3.2.7. Immunofluorescence Microscopy: 48
3.2.8. RNA-Sequencing: 48
3.2.9. Western Blots: 49
3.2.10. Metabolic Mass Spectrometry: 49
3.2.11. Statistics: 50
3.3. Results 51
3.3.1. hiBMEC had higher barrier function but lower glycolytic rate relative to hpBMEC. 51
3.3.2. hpBMEC and hiBMEC metabolomic profiles differed primarily in acylcarnetines 53
3.3.3. Glycolytic enzymes, but not labeled metabolite fractions, differed between hpBMEC and hiBMEC. 56
3.3.4. Mitochondrial metabolic enzymes, but not labeled metabolite fractions, differed between hpBMEC and hiBMEC. 56
3.3.5. hpBMEC and hiBMEC metabolism responded similarly to extracellular stimuli. 57
3.4. Discussion 61
3.5. Limitations: 64
3.6. Conclusions: 64
Chapter 4: iPSC-BMEC modeling of brain endothelial cell glutamine metabolism 65
4.1. Introduction: 65
4.2. Methods: 66
4.2.1. Cell Culture: 66
4.2.2. RNA Sequencing: 66
4.2.3. Metabolite Uptake and Production: 66
4.2.4. Mitochondrial Function: 66
4.2.5. Protein analysis: 67
4.2.6. Mitochondrial imaging and quantification: 67
4.2.7. Metabolic Mass Spectrometry: 68

4.2.8. Statistics: 68
4.3. Results: 68
4.3.1. hiBMEC had lower glutamine uptake relative to hpBMEC and negligible glutamate production. 68
4.3.2. hiBMEC had decreased mitochondrial metabolism and more punctate mitochondria than hpBMEC. 69
4.3.3. hiBMEC metabolic transporter and enzyme levels suggested increased glutamine incorporation into asparagine and fatty acids. 70
4.3.4. Mass spectrometry confirmed that hiBMEC had increased glutamine-derived carbons in fatty acids and increased asparagine and glutathione ion counts compared to hpBMEC. 73
4.3.5. Metabolomic analysis using labeled glutamine reveals hpBMEC and hiBMEC have distinct metabolomic signatures. 75
4.3.6. Metabolomic analysis indicated that hpBMEC incorporated more carbons from glutamine into the TCA cycle. 78
4.3.7. α-KG supplementation restored glutamate efflux in hiBMEC. 79
4.4. Discussion: 80
4.5. Limitations: 83
4.6. Conclusions: 84
Chapter 5: APOE genotype impacts BMEC metabolism and function 85
5.1. Introduction: 85
5.2. Methods: 87
5.2.1. Cell Culture 87
5.2.2. CRISPR/Cas9 87
5.2.3. iPSC expansion and Genotyping 88
5.2.4. TEER 89
5.2.5. Immunostaining and JAnaP 89
5.2.6. YSI 90
5.2.7. Seahorse 90

5.2.8. Western Blotting 90
5.2.9. Membrane Fractionation 90
5.2.10. SIRT1 Activity Assay 91
5.2.11. Mass Spectrometry 91
5.2.12. Statistics 91
5.3. Results 91
5.3.1. hiBMEC with the APOE ε4 genotype had reduced barrier function. 91
5.3.2. APOE ε4 hiBMEC had reduced glucose metabolism relative to APOE ε3 hiBMEC. 92
5.3.3. Glucose transporter and rate limiting glycolytic enzymes were lower in APOE ε4 hiBMEC. 93
5.3.4. APOE ε3 and ε4 hiBMEC had similar metabolite transport and polarization. 94
5.3.5. Impaired insulin signaling may contribute to reduced glycolysis in APOE ε4 hiBMEC 95
5.3.6. Decreased SIRT1 in hiBMEC did not change glycolysis but decreased barrier function. 99
5.3.7. APOE ε4 genotype induced systemic differences in hiBMEC metabolism. 101
5.4. Discussion 102
5.5. Limitations 107
5.6. Conclusions 107
Chapter 6: Exercise training has genotype-dependent impacts on BMEC metabolism and function 109
6.1. Introduction 109
6.2. Methods 110
6.2.1. Exercise training 110
6.2.2. Human serum collection 111
6.2.2. Cell culture 111
6.3.3. APOE ELISA 111
6.2.4. Western blot 112
6.3.5. YSI 112
6.3.6. Seahorse 112
6.3.7. TEER/Permeability assays 112
6.3.8. Immunostaining and Junction Analysis 113

6.3.9. Metabolic Mass Spectrometry 113
6.3.10. Statistics 113
6.3. Results 113
6.3.1. Exercise training did not significantly cardiorespiratory fitness. 114
6.3.2. Exercise training did not alter serum or intracellular APOE. 114
6.3.3. Exercise trained serum did not alter glycolysis in APOE ε3 or ε4 hiBMEC. 115
6.3.4. Serum from exercise trained individuals increased glycolytic enzymes in APOE ε3 hiBMEC but decreased glycolytic enzymes in APOE ε4 hiBMEC relative to serum from sedentary individuals. . 116
6.3.5. SIRT1 was differentially regulated by serum genotype and exercise training. 119
6.3.6. VO2 max is not correlated with changes in glycolysis, but changes in APOE and SIRT1 are positively correlated with changes in some glycolytic enzymes in APOE ε3 and ε4 hiBMEC. 120
6.3.6. Serum systemically altered the hiBMEC metabolome, but exercise training did not. 120
6.3.7. Serum from exercise trained individuals did not significantly impact barrier function. 122
6.3.8. Serum from exercise training may increase tight junction protein continuity. 122
6.4. Discussion 125
6.6. Limitations 127
6.7 Conclusions 128
Chapter 7: Conclusions and Future Work 129
7.1. Thesis Summary 129
7.2. Specific Discoveries 129
7.3. Contributions to the Field 132
7.4 Future Studies 134
7.4.1. Sex differences in response to AngII in BMEC. 134
7.4.2. Development of improved BMEC metabolic models. 134
7.4.3. Multicellular models to investigate the effects of APOE genotype on brain function. 135
7.4.4. Multi-omics analysis of serum and BMEC pre- and post-exercise training. 136
Appendix: 137
Appendix Table 1: Gene expression differences between female and male HUVEC 137

Appendix Table 2: Significantly changed genes in female and male HUVEC following treatment with Angiotensin II 155
Appendix Table 3: KEGG pathways with 3 or more differentially expressed genes in female HUVEC treated with Angiotensin II 166
Appendix Table 4. Hypergeometric analysis of metabolite pathways with differentially expressed metabolites between hpBMEC and hiBMEC 169
Appendix Table 5. Normalized metabolite concentrations in APOE ε3 and ε4 hiBMEC treated with serum from sedentary or exercise trained individuals. 170
Appendix Table 6. Metabolite contributions to PC1 in APOE ε3 and ε4 hiBMEC with and without serum. 172
References: 175

List of Tables

Table 2.1. EC donor characteristics. 20

Table 3.1: Western blot antibodies. 50

Table 4.1: Western blot antibodies 67

Table 5.1. CRISPR/Cas9 and genotyping sequences. 88

Table 5.2. Primary antibodies used for immunofluorescence. 89

Table 6.1. Serum donor demographics 111

List of Figures

Figure 1.1. Overview of BBB degradation with age and disease. 6

Figure 1.2. Hypothesis of APOE ε4-induced reduction in glycolysis. 16

Figure 1.3. Hypothesis of APOE ε4-induced reduction in glycolysis and barrier function. 17

Figure 2.1. Female endothelial cells differentially express more genes in response to AngII treatment.... 26

Figure 2.2. AngII increased TGFβ2 mRNA expression in female as compared to male HUVEC, but TGFβ2 protein and EndMT did not change with AngII or sex. 29

Figure 2.3. Female HUVEC had higher IL-6 mRNA expression than male HUVEC following AngII treatment but required concurrent TNFα exposure to show higher IL-6 protein and inflammation. 30

Figure 2.4. Female HPAEC and HUVEC increased WBC adhesion when treated with TNFα and AngII.. 31

Figure 2.5. Male HPAEC and HUVEC increased WBC adhesion when treated with TNFa and AngII. 32

Figure 2.6. Female HUVEC demonstrate increased ROS production in response to AngII compared to male HUVEC. 33

Figure 2.7. Female HUVEC and HPAEC had elevated ROS following AngII treatment, while male cells did not. 34

Figure 2.8. Male and female HCAEC did not increase ROS production in response to AngII. 35

Figure 2.9. Female HUVEC demonstrate increased superoxide in response to AngII compared to male HUVEC. 37

Figure 2.10. CYBB is upregulated in female, but not male EC, which may contribute to elevated ROS production in AngII-treated female cells. 38

Figure 3.1. Glucose concentrations in cell culture conditions. 48

Figure 3.2. hpBMEC had higher glycolytic and oxidative glucose metabolism than hiBMEC, but similar proportions of glycolytic metabolism. 52

Figure 3.3. hpBMEC had elevated glycolytic and mitochondrial metabolism relative to hiBMEC. 53

Figure 3.4. Metabolomic abundance profiling showed hpBMEC and hiBMEC had distinct metabolomes, largely driven by changed in acyl-carnitines. 55

Figure 3.5. hpBMEC and hiBMEC showed differences in glycolytic enzyme gene and protein levels, but similar U-13C6-glucose labeled metabolite fractions. 58
Figure 3.6. hpBMEC and hiBMEC had different TCA and FAO gene and protein levels, but similar U-13C6-glucose labeled metabolite fractions. 59
Figure 3.7. hpBMEC and hiBMEC had similar glycolytic responses to ACM and high glucose, but not fluvastatin. 60
Figure 4.1. hiBMEC took up less glutamine and secreted almost no glutamate, as compared to hpBMEC and iPSC. 69
Figure 4.2. hiBMEC had decreased mitochondrial metabolism and a punctate mitochondrial morphology. 72
Figure 4.3: hiBMEC had decreased GLS and increased fatty acid and asparagine synthesis genes. 73
Figure 4.4. Mass spectrometry confirmed that hiBMEC had higher fatty acid, asparagine, and glutathione synthesis than hpBMEC. 76
Figure 4.5. hpBMEC and hiBMEC have distinct metabolomes. 77
Figure 4.7. Alpha-ketoglutarate supplementation restored hiBMEC glutamate production. 80
Figure 5.1. Hypothesized mechanism by which APOE ε4 reduces glycolysis via insulin signaling. 86
Figure 5.2. Hypothesized pathway by which APOE ε4 reduces glycolysis and barrier function via SIRT1. 87
Figure 5.3. APOE **ε**4 BMEC had reduced barrier function. 93
Figure 5.4. APOE **ε**4 hiBMEC had reduced glycolysis relative to APOE **ε**3 hiBMEC. 94
Figure 5.5. Glucose transporter and rate limiting glycolytic enzymes were reduced in APOE **ε**4 hiBMEC. 96
Figure 5.6. Glucose transport was lower in APOE **ε**4 hiBMEC. 97
Figure 5.7. Impaired insulin signaling may have contributed to reduced APOE ε4 hiBMEC glycolysis. 98
Figure 5.8. SIRT1 was lower in APOE ε4 hiBMEC. SIRT1 inhibition did not alter glycolysis but decreased barrier function in hiBMEC. 100
Figure 5.9. APOE ε4 genotype led to systemic differences in iPSC-BMEC metabolism. 102

Figure 6.1. Exercise training did not change VO2 max, serum APOE protein level, or intracellular hiBMEC APOE protein level. 115
Figure 6.2. Glycolysis was not changed in APOE ε3 or APOE ε4 hiBMEC with exercise training. 116
Figure 6.3. Serum from exercise trained individuals decreased rate limiting glycolytic enzymes HK2 and PFKFB3 in APOE ε4 hiBMEC relative to serum from sedentary individuals. 118
Figure 6.4. SIRT1 increased with exercise trained serum in APOE ε3 hiBMEC and decreased with exercise trained serum in APOE ε4 hiBMEC, while insulin receptor levels were unchanged with genotype and serum. 119
Figure 6.5. VO2 max is not correlated with changes in glycolysis, but changes in APOE and SIRT1 are positively correlated with changes in some glycolytic enzymes in APOE ε3 and ε4 hiBMEC. 121
Figure 6.6. Serum systemically altered the hiBMEC metabolome, but exercise training did not. 123
Figure 6.7. Barrier integrity was not significantly altered by sedentary or exercise trained serum in APOE ε3 or APOE ε4 hiBMEC. 124

Chapter 1: Introduction

1.1 Thesis Goal

The overarching goal of this thesis is to understand how prominent risk factors for Alzheimer's disease (AD) increase cerebrovascular dysfunction and contribute to AD development. *I hypothesize that female sex, stress hormone exposure, the apolipoprotein (APOE) ε4 genotype, and a sedentary lifestyle alter brain microvascular endothelial cell metabolism, which then results in endothelial dysfunction and blood-brain barrier (BBB) breakdown.* In *Aim 1,* I demonstrated that AngII exposure increased reactive oxygen species (ROS) production and inflammation in female, but not male, endothelial cells (EC). I used RNA sequencing to identify transcriptomic changes induced by AngII exposure in male and female EC. I then validated sex differences in ROS production using fluorescent ROS indicators and in inflammation using a white blood cell (WBC) adhesion assay. In *Aim 2* I identified a mechanism through which the APOE ε4 genotype decreased glycolysis and barrier function of induced pluripotent stem cell (iPSC) derived brain microvascular endothelial cells (hiBMEC). I measured glycolytic activity in APOE ε3 and ε4 hiBMEC using Western blot for glycolytic enzymes, Seahorse glycolytic rate assays, and metabolomics. I also measured barrier function through trans-endothelial resistance and tight junction protein immunofluorescence. In *Aim 3* I quantified the effects of a 6-month aerobic exercise training program on hiBMEC metabolism and function. I applied serum from older adults pre- and post- 6 months of exercise training to hiBMEC of the same APOE genotype. I then measured changes in hiBMEC metabolism and barrier function.

1.2. Thesis Organization

This thesis is composed of seven chapters.

Chapter 1 begins with the goal and the organization of the thesis. This chapter also includes the clinical motivation for my research, as well as the relevant background on BMEC metabolism and AD risk factors including female sex, stress hormone exposure, the APOE ε4 genotype, and sedentary lifestyle.

Chapter 2 examines how angiotensin II (AngII) exposure increases EC dysfunction in female, but not male EC. Male and female EC were exposed to AngII for 24 hours, after which RNA sequencing was used to identify transcriptomic changes that occurred in female, but not male, EC. To determine if gene expression changes from RNA sequencing resulted in EC dysfunction, we then used fluorescent ROS assays to show increased ROS production and WBC adhesion assays to show increased inflammation in female, but not male EC following AngII exposure. Finally, we showed that female EC have elevated expression of NOX2, an enzyme involved in ROS production that escapes X-chromosome inactivation and may contribute to elevated ROS in female EC.

Chapters 3 and 4 use transcriptomics and metabolomics, validated through basic science approaches, to interrogate the ability of hiBMEC to model BMEC metabolism by comparing hiBMEC metabolism to primary BMEC (hpBMEC) metabolism. In Chapter 3, I demonstrated that glucose metabolism was lower in hiBMEC relative to hpBMEC, but that hiBMEC and hpBMEC responded similarly to metabolic stimuli such as high glucose and astrocyte conditioned media. These results indicated that hiBMEC could be used to model BMEC glucose metabolism. In Chapter 4, however, I demonstrated that hpBMEC and hiBMEC have systemic differences in glutamine metabolism. HiBMEC consumed less glutamine and produced negligible glutamate relative to hpBMEC. HiBMEC also had more punctate, immature mitochondrial morphology while the hpBMEC mitochondria were longer and more branched, which may contribute to glutamine metabolic differences. Transcriptomics, metabolomics, and basic science techniques demonstrated that hiBMEC and hpBMEC routed glutamine differently through metabolism; hiBMEC used glutamine to produce more glutathione, fatty acids, and asparagine, while hpBMEC used glutamine to produce more GABA, nucleotides, and aminosugars. The differences in glutamine metabolism between hpBMEC and hiBMEC are important to consider in choosing a BMEC model since the metabolites produced by the cells can influence cell function and cell-cell communication.

Chapter 5 investigates how the APOE ε4 genotype decreased BMEC metabolism and function relative to the APOE ε3 genotype. I showed that APOE ε4 hiBMEC have reduced glycolysis and lower barrier function compared to APOE ε3 hiBMEC. APOE ε4 hiBMEC also had reduced insulin receptor (INSR) and Sirtuin 1 (SIRT1) levels. Using and inhibitor of insulin signaling I showed that reduced insulin signaling in

APOE ε4 hiBMEC contributes to lower levels of glycolysis relative to APOE ε3 hiBMEC. Using an inhibitor of SIRT1, I demonstrated that the low levels of SIRT1 in APOE ε4 hiBMEC contributed to the reduced glucose metabolism and barrier function relative to the APOE ε3 hiBMEC.

Chapter 6 examines the ability of exercise training to improve glucose metabolism and barrier function in APOE ε4 hiBMEC. I showed dimorphic effects of exercise training on SIRT1 in APOE ε3 and ε4 hiBMEC; serum from exercise trained individuals increased SIRT1 in APOE ε3 hiBMEC but decreased SIRT1 in APOE ε4 hiBMEC. Changes in SIRT1 with exercise training correlated with changes in glucose metabolic enzymes, but did not significantly alter overall glycolytic rates and had little effect on barrier function in APOE ε3 or ε4 hiBMEC.

Chapter 7 concludes the thesis by highlighting the major discoveries of this thesis and my contributions to the field and discussing future directions for this work.

1.3. Clinical Motivation: Brain endothelial cell dysregulation in Alzheimer's Disease

One of every three seniors dies of AD or a related dementia, making it the seventh leading cause of death in the United States [1]. AD is a progressive neurodegenerative disease, and the most common form of dementia. AD symptoms begin with small impairments of learning and memory but progress to complete loss of speech and mobility. Following diagnosis with AD, the mean survival time is 5.8 ($\pm$ 2.0) years [2]. Care and treatment of individuals with AD costs the United States about $345 Billion per year, not including the time value of the estimated 11 million Americans providing unpaid care for family and friends with AD [1]. AD is diagnosed through a series of memory tests, laboratory tests, and brain imaging tests. Laboratory tests can include lumbar punctures to withdraw cerebral spinal fluid (CSF) and measure amyloid-β (Aβ) and tau protein levels as AD biomarkers.

AD has no cure; however, there is a large effort to develop therapeutics that prevent AD or slow its progression. Recent advances resulted in approval by the United States Federal Drug Administration for

two drugs to slow disease progression: Aducanumab and Lecanemab. Though the mechanism of action for each drug is different, both therapeutics are designed to slow memory loss by reducing the burden of Aβ plaques in the brain. Both Aducanumab and Lecanemab have been heavily criticized for their lack of efficacy; though the drugs show statistically significant improvements in cognitive and functional measurements, the improvements are extremely small and may not be clinically meaningful [3]. Despite little evidence that reducing Aβ slows cognitive decline, most therapeutics that have progressed to Phase 3 clinical trials for AD are still targeted at Aβ [4]. To develop new therapeutics that effectively prevent or reduce the burden of AD symptoms, we must target other biomarkers of the disease.

While Aβ and tau are the two conventionally measured AD biomarkers, glucose hypometabolism in the brain may be a stronger predictor of AD development [5]. Glucose hypometabolism is clinically assessed using a radiotracer, fluorodeoxyglucose (FDG), in a positron emission tomography (PET) scan. Meta-analysis has revealed FDG PET has a sensitivity of 90% and a specificity of 89% in detecting dementia in patients with AD compared to healthy control subjects [6]. Comparatively, CSF Aβ levels only have a sensitivity of 80% and a specificity of 82% [6]. Spatial FDG distributions in PET scans can also accurately distinguish between AD and other dementias such as frontotemporal dementia and Lewy Body dementia [7]. Early detection of glucose hypometabolism via FDG PET could allow for earlier, and likely more effective intervention to treat or prevent AD.

Brain cells, including EC, astrocytes, and neurons, rely on glucose as a primary energy source. Hypoglycemia, categorized as blood glucose levels lower than 70 mg/dL [8], can induce neuronal death [9] and impair executive function [10]. Brain microvascular endothelial cells (BMEC) line the blood vessels of the brain and are a primary component of the BBB. BMEC selectively transport glucose from the blood into the brain to meet its metabolic demands. Dysfunction of glucose uptake and transport in these BMEC could impair the function of the BMEC themselves and induce neurodegeneration, leading to cognitive decline in AD. As such, EC glucose metabolism and transport may reveal important insights into AD pathogenesis and may be a critical pathology to target for future therapeutic development.

1.4. The Blood-Brain Barrier

The brain has an extensive microvascular network, since metabolic demand requires brain cells be no more than 200 µm from a capillary to survive [11]. The BBB has small intercellular gaps (1.4 - 1.8 nm), which make the BBB essentially impermeable to paracellular transport. Thus, BMEC tightly control nutrient and waste product exchange between the blood and all cell types in the brain. The BBB is formed primarily of BMEC, which are connected via tight junction proteins including claudins, occludins, junction adhesion molecules (JAMs), and zonula occludins (ZO) (Fig. 1.1). Claudin family proteins are considered the primary BBB sealing component, with claudin-5 having the greatest BBB expression compared to other isoforms [12], [13]. Occludins, the first tight junction proteins to be discovered, regulate adhesion between BMEC [14]. JAMs, and specifically JAM-1, are essential for tight junction initiation between BMEC [15]. JAM down-regulation or deletion markedly increased BBB permeability [15], [16]. ZO-1, the primary ZO protein expressed in the BBB, is a cytoplasmic scaffolding protein that tethers transmembrane tight junction proteins to the actin cytoskeleton [17]. Tight junction assembly and function is also influenced by signaling with other adhesion complexes, including adherens junctions and focal adhesions [18].

The BBB is further supported by pericytes and astrocytes. Pericytes are mural cells that surround the brain microvasculature where they stabilize the vascular wall. Pericytes maintain the BBB by releasing signaling factors that impact BMEC tight junction proteins [19], secreting basement membrane proteins [20], regulating neuroinflammation [21], and contracting via proteins such as α-smooth muscle actin to control blood flow in the brain [22]. Astrocyte terminal processes (endfeet) also directly contact BMEC to contribute to BBB strength. Astrocytes secrete factors, including growth factors, that regulate BMEC tight junction formation [23] and transporter expression and polarization [24], [25]. Together, BMEC, pericytes, and astrocytes maintain strict control of molecule movement across the BBB, which is essential to protecting the brain from neurotoxins.

The BBB degrades with increasing age, which promotes inflammation and neurotoxicity. BBB dysregulation is further observed in neurodegenerative diseases such as AD. Though it is debated whether BBB breakdown is causal to or a byproduct of neurodegeneration, it is clear that increased BBB permeability leads to neurotoxin and leukocyte infiltration into the brain, initiating an immune response and propagating cell death. Zhao *et al.* proposed a model of vascular-mediated neurodegeneration in which atypical intercellular BBB signaling results in increased BBB permeability, which in turn leads to brain accumulation of 1) hemoglobin and iron, which increase oxidative stress; 2) fibrinogen, thrombin, and plasminogen, which degrade brain extracellular matrix and activate microglia; and 3) albumin, which leads to cerebral hypoperfusion, hypoxia, and edema [26]. Together, these BBB degradation effects contribute to the neuronal stress and eventual cell death associated with neurodegenerative diseases; however, the events that cause BBB dysfunction have yet to be elucidated.

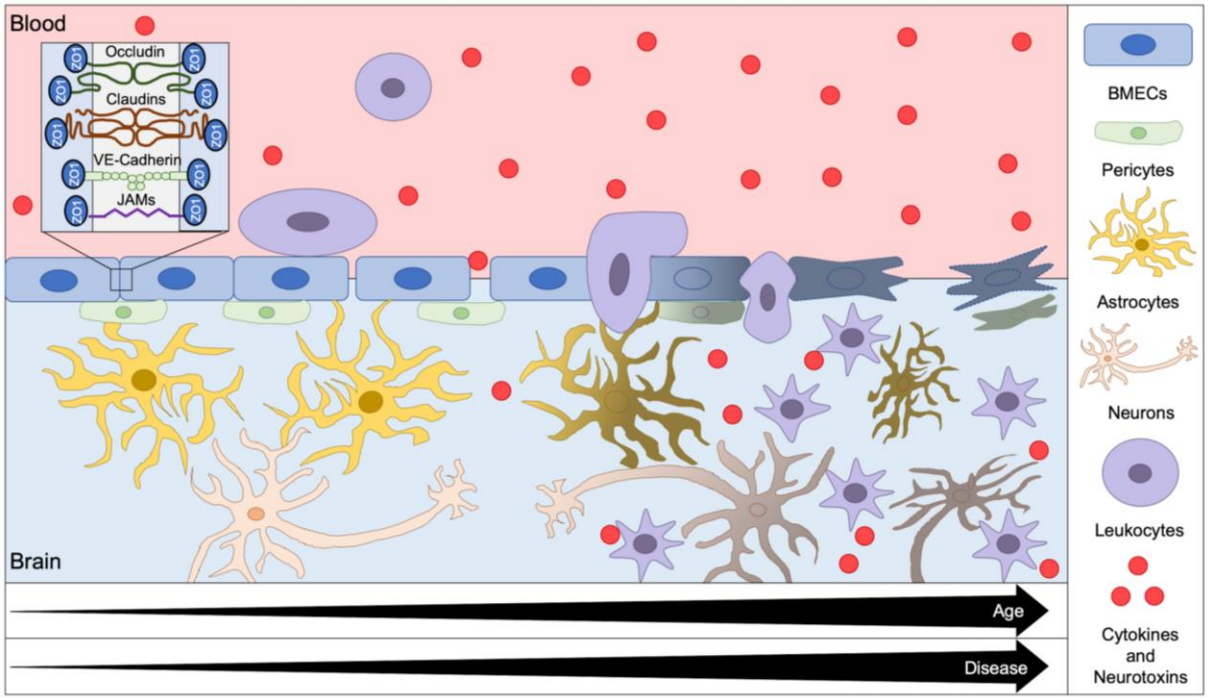


Figure 1.1. Overview of BBB degradation with age and disease. The BBB, which is formed by BMEC and maintained through interactions with pericytes, astrocytes, restricts cell and molecule movement from the blood into the brain. BMEC form impermeable intercellular junctions though tight junction proteins, including occludins, claudins, VE-Cadherin, JAMs, and ZO proteins. With increasing age and disease, tight junction proteins degrade, leading to BBB opening. The leaky BBB allows cytokines, neurotoxins, and leukocytes to infiltrate the brain, which can cause downstream inflammation and neurodegeneration.

1.5. Metabolism in the Blood-Brain Barrier

1.5.1. BMEC Glucose Metabolism

Glucose is the primary energy source in the brain, and therefore its transport has been extensively characterized [27]. Glucose cannot diffuse across the BBB and must enter the brain through BMEC glucose transporters. Glucose transport is regulated so that cerebral glucose levels only reach 20% of blood glucose levels, which is just sufficient for neuronal demand [28]. This tight glucose regulation is hypothesized to balance the reliance of the brain on glucose for energy while simultaneously preventing potential neurotoxic glucose effects [28]. Glucose transported across the BBB is either released into the CSF or diffuses into the gap junctions of astrocytes that are in contact with BMEC.

The most prominent BMEC glucose transporter is GLUT1, a sodium-independent glucose transporter. GLUT1 is found at much higher levels in BMECs than in peripheral endothelial cells [29]. The importance of GLUT1 in cerebral glucose transport was shown by the fact that no glucose was found in the cerebrospinal fluid (CSF) of patients with GLUT1 deficiency syndrome [30]. Approximately 12% of BMEC GLUT1 is on the apical (blood-facing) cell membrane, while 48% of BMEC GLUT1 is on the basolateral cell membrane, and the remaining 40% of BMEC GLUT1 resides in the cytosol [31]. BMEC have other glucose transporters such as GLUT3 and GLUT4, as well as sodium-dependent glucose transporters such as SGLT1; however, these are less important for glucose transport [32]. Glucose movement across all of these glucose transporters occurs through facilitated diffusion due to the glucose concentration gradient across BMEC [33].

Reduced BMEC glucose transport can lead to cerebral glucose hypometabolism, which is associated with neurodegeneration and has even been proposed to be a driver of neuropathology [34], [35]. A murine endothelial GLUT1 knockout triggered severe neuroinflammation and reduced brain-derived neurotrophic factor (BDNF). This effect was exaggerated when the GLUT1 knockout was induced neonatally. Furthermore, murine GLUT1 haploinsufficiency reduced extracellular brain glucose by 90% and also reduced BDNF, which is essential for neuronal survival and growth [36]. Indeed, in another study

endothelial-specific GLUT1-KO mice had reduced neuronal density and widespread brain inflammation [37]. Therefore, dysregulated BMEC glucose transport can have devastating effects for the brain.

Both *in vitro* and *in vivo* evidence suggest that glucose transport via GLUT1 plays an important role in BBB function. Barrier integrity was characterized in hiBMEC with GLUT1 knocked out via CRISPR-Cas9 *in vitro*. GLUT1 KO decreased hiBMEC transendothelial electrical resistance (TEER) compared to control; however, no tight junction morphology differences were observed [38]. Likewise, glucose deprivation diminished hiBMEC barrier integrity. The barrier loss was maintained even following supplementation with ketone bodies, which are used by the brain during glucose deprivation [39]. *In vivo,* GLUT1 KO zebra fish had decreased BMEC tight junction proteins and increased barrier permeability [40]. Global GLUT1 haploinsufficiency reduced tight junction proteins and increased endogenous plasma protein leakage in the brain of 2-week-old mice. In mice overexpressing Aβ as a transgenic AD model, endothelial-specific GLUT1 KO initiated BBB breakdown [29]. However, endothelial-specific GLUT1-KO mice (1-week old) did not show differences in BBB integrity, specifically in terms of brain water content, Evans Blue or gadolinium permeability, or tight junction morphology [37]. The differences in *in vivo* BBB integrity with GLUT1 KO may be age dependent, as a later study found no permeability changes in 5-day endothelial-GLUT1-KO mice but found increased permeability in 10-day old mice [41].

1.5.2. BMEC Glutamine and Glutamate Metabolism

BMEC maintain the concentration of most amino acids tenfold lower in the brain than in the plasma, with the exception of glutamine which is present in a similar concentration in the brain and plasma. Glutamine can be transported into and out of brain endothelial cells through either facilitative or active transport. L-type amino acid transporter 1 (LAT1), the primary facilitative transporter of glutamine, primarily transports neutral amino acids into cells in exchange for transport of glutamine out of cells [42]. Of the active transporters, system N amino acid transporters 1 and 2 (SNAT1/2) both transport glutamine into cells [43], while alanine/serine/cysteine transporter 2 (ASCT2) is a bidirectional transporter that exchanges glutamine for neutral amino acids [44]. Though not the primary energy source for endothelial cells, glutamine metabolism is vital for proliferation and vessel formation of EC [45], [46].

Glutamate, which is derived primarily from glutamine, acts as both a metabolic intermediate that feeds the TCA cycle and as a vital neurotransmitter in the brain. Glutamate concentration usually ranges from 50-100 μM in the plasma and 0.5-2 μM in brain extracellular fluids [47]. The cerebral glutamate concentration is tightly regulated by bidirectional glutamate transporters on BMEC, including SLC1A1, SLC1A2, SLC1A3, and SLC1A6. BMEC can also bind glutamate to ionotropic receptors such as N-methyl-D-aspartate (NMDA) receptors that regulate ion flux and membrane potentials [48], [49] and metabotropic glutamate receptors such as metabotropic glutamate receptor 5 (mGluR5) that initiate intracellular signaling cascades through second messengers [50].

High cerebral extracellular glutamate concentrations cause excitotoxicity resulting in cell death. Glutamate binding to NMDA receptors induces calcium influx into immortalized human BMEC [51]. As cytosolic calcium rises, calcium entry into mitochondria also increases thereby elevating mitochondrial membrane potential. This increased mitochondrial potential drives increased flux through oxidative phosphorylation, a byproduct of which is increased reactive oxygen species (ROS) production leading to oxidative stress and cell death [52]. Though there are few studies to validate this mechanism in human primary BMEC, glutamate concentrations as low as 250 μM decreased transgenic rat BMEC viability, likely as a result of excitotoxicity and downstream oxidative stress [53]. In mouse hippocampal neurons, cellular oxygen consumption, a measure of mitochondrial metabolism, increased following 24-hours of treatment with 4 mM glutamate [54]. In these same cells, tetramethylrhodamine (TMRM) staining indicated that 4 mM extracellular glutamate hyperpolarized the mitochondrial membrane, which in turn elevated ROS production [54].

In mouse BMEC, glutamate-induced increases in intracellular calcium can also increase nitric oxide production (Zuccolo et al., 2019). However, this is likely because glutamate treatment reduces eNOS RNA and increases iNOS RNA [53]. While eNOS is generally considered vasoprotective and produces nitric oxide to initiate vasodilation, iNOS produces large bursts of nitric oxide in oxidative environments. Through this mechanism, iNOS leads to ROS production and downstream inflammation and apoptosis.

BMEC must precisely regulate glutamate concentration to maintain the BBB and protect neurons in the surrounding brain tissue. 30 minutes of exposure to 1 mM extracellular glutamate, which is much higher than the physiological concentration, increased *in vivo* rat BBB permeability by almost 20% [56]. In immortalized

cerebral endothelial cells, 1 mM glutamate and 1 mM NMDA both significantly decreased barrier function, as shown by lower TEER. The barrier loss was inhibited by MK-801, an NMDA receptor antagonist [49]. These studies indicate that glutamate decreases BMEC barrier function through an NMDA receptor-mediated mechanism.

1.5.3. Fatty Acid Metabolism in BMEC

Lipids constitute nearly 50% of the brain's dry weight [57]; yet the brain has a limited capacity to synthesize fatty acids and must instead import them from circulation. Lipids enter the circulation through dietary absorption, through production in the liver, or through release from adipose tissue. Due to their hydrophobic nature, lipids must bind to soluble proteins such as albumin or be integrated into lipoprotein complexes to remain in circulation. Lipoproteins have a hydrophilic outer shell and an internal core composed of cholesterol and triglycerides, which are formed of three fatty acids and glycerol. Lipids form a major part of brain cell membranes, and two key fatty acids, arachidonic acid and docosahexaenoic acid (DHA), play extensive roles in neuroprotection, brain development, synaptogenesis, and neural differentiation [58].

Free fatty acids (FFAs) can passively diffuse across the BMEC membrane even though they are at low concentration close to the endothelium (7.5 nM) [59], [60]. First, the fatty acids dissociate from their carrier proteins through hydrolysis by membrane-associated lipases. The FFAs then adsorb to the endothelium and flip from the outer plasma membrane to the cytosolic plasma membrane. However, the flippase activity that facilitates FFA movement across the membrane is thermodynamically unfavorable, and fatty acid translocase (FAT, CD36) or fatty acid transport proteins (FATP) are needed to make FFA transport into BMEC possible [59]. Once inside the cell, FFAs are ferried through the cytoplasm by fatty acid binding proteins (FABP). For example, FABP5 binds to and carries DHA across BMEC [61]. Once the FFAs reach the basolateral BMEC plasma membrane, they flip across to diffuse to other cerebral cells [60]. FFA transport rate depends on several factors, including the fatty acid/albumin dissociation rate as well as the fatty acid size and lipophilicity. Longer chain fatty acids are less lipophilic and therefore typically have decreased transport [59].

Lipid can also be moved across BMEC by clathrin dependent and caveolae mediated transcytosis. Low-density lipoprotein (LDL) is taken up by BMEC via clathrin dependent transcytosis after binding to the LDL receptor (LDLR) or LDLR-related protein 1 (LRP1). LDL particles are then directed to the lysosome where they are degraded and released as cholesterol and fatty acids. LDL can also be taken up via LDLR in caveolae. These structures are thought to transfer LDL without its degradation [62]. Interestingly, while BMEC internalize LDL, they do not transport the cholesterol into the brain [63].

Finally, lipids can be transported into the brain via transport proteins. FFAs can be incorporated into lysophosphatidylcholine (lysoPC), which is then transported across the plasma membrane by monocarboxylic acid transporters (MCTs) or FATPs. LysoPC can also be transported by Mfsd2a, specifically lysoPC that contains DHA [64]. Mfsd2a appears to be involved in maintaining DHA levels in BMEC and in other brain cells, and therefore Mfsd2a loss inhibited BBB function and caused neuronal loss, cognitive deficits, and microcephaly [65], [66], [67], [68], [69], [70], [71].

While few studies address fatty acid oxidation in BMECs specifically, current evidence suggests an important role for fatty acid oxidation in maintaining barrier function. Fatty acid metabolism byproducts and intermediates can directly mediate BMEC function. Palmitoylation, the covalent attachment of fatty acids to protein cysteine residues, is particularly important for claudin-5, a key tight junction protein. Palmitoylated claudin-5 translocated to cholesterol-rich lipid rafts, where it dimerized and restricted paracellular permeability to enhance BBB function [72], [73].

While fatty acid oxidation may be essential for BBB maintenance, high serum lipids can damage the BBB. BMECs exposed to elevated postprandial triglyceride-rich lipoproteins, a risk factor for vascular dementia, had elevated ROS and increased expression of the stress-responsive protein ATF3 [74]. A follow up study showed that triglyceride-rich lipoprotein treatment increased mitochondrial oxidative stress and protein leakage, but this effect could be reduced by CPT1A1 siRNA knockdown [75].

Disturbances in fatty acid metabolism have been linked to aging and neurodegenerative diseases [76], [77]. Indeed, the brain loses 42% of its phospholipids and 47% of its cholesterol between the ages of 20 and 100 [57]. Cerebral DHA transport was studied in mice with the human apolipoprotein 4 (APOE4) allele,

a main genetic risk factor for late onset Alzheimer's disease. The DHA uptake rate was 24% lower in APOE4 mice [78]. Similarly, in the 3x-TG mouse model of Alzheimer's disease, DHA cerebral transport was 25% lower [79].

1.6. Risk Factors for Alzheimer's Disease Impact BMEC Metabolism

The National Institutes of Health (NIH) awards nearly $8 Billion per year to studies of AD and related dementias [80]; however, the root cause of AD is still unknown. It is likely that disease onset is due to a combination of factors, including genetics and social and environmental determinants of health. Female sex [1], stress hormone exposure [81], the APOE ε4 genotype [82], and a sedentary lifestyle [83] all increase the risk of developing AD.

1.6.1. Female Sex

Almost two thirds of Americans diagnosed with AD are women [84], which could be caused either by increased AD incidence in women vs. men or because women have a longer lifespan than men [85]. Recent studies showed that female subjects with the apolipoprotein (APOE) ε4 allele, which increases AD risk by almost 15% [86], are more likely to be diagnosed with AD than male subjects with the gene [87]. Additional AD risk factors also have sex-specific effects. For example, obesity leads to greater BBB disruption and induces a larger inflammatory response in women than men [88], [89]. I have extensively reviewed the role of sex differences in the BBB in neurodegenerative diseases in *APL Bioengineering* [90].

Many AD sex differences can be tied to the neuroprotective effects of estrogen. *In vitro* studies demonstrate that estrogen regulates BBB glucose transporter expression and membrane translocation [91], [92], which could impact glucose transport into the brain. Indeed, in human studies, brain glucose transport, and thus brain glucose metabolism, decreased following the menopausal transition [93], [94]. Similarly, preclinical studies indicate estrogen decreases brain reactive oxygen species (ROS) production [95], which is tied to decreased tight junction protein expression and BBB dysregulation [96]. Few studies, however, have focused on intrinsic sex differences of cells or sex differences in circulating molecules (apart from estrogen) and their role in AD development.

Recent transcriptomic studies suggest that 14-25% of the EC transcriptome is sex-dependent [97], some of which may occur through increased X-linked gene expression via escape from X-chromosome inactivation (XCI). Approximately 15% of X-linked genes always escape XCI, and an additional 10% of X-linked genes show variable inactivation patterns [98]. Female human umbilical vein endothelial cells (HUVEC) demonstrate increased endothelial nitric oxide synthase (eNOS) expression, proliferation, and migration compared to male HUVEC [99]. These data support the idea that sex differences in the BBB go beyond estrogen.

A master's thesis written by Dakota Kamm addressed sex differences in BBB permeability in the SAMP8 mouse model of accelerated aging [100]. Kamm found female mice to have increased mRNA expression of claudin 1, 5, and 12, occludin, junction adhesion molecule A (JAMA), ZO-1, Major Facilitator Superfamily Domain Containing 2, and BDNF compared to their male counterparts [100]. This study suggests sex-specific differences in tight junction protein expression that could affect BBB function, though notably did not measure estrogen levels or account for estrogen-mediated BBB function. Sex differences in BBB characteristics should be further studied *in vivo* in other rodent models of neurodegenerative disease and *in vitro* using human cells in the absence of estrogen.

In 2020, Oliva *et al.* used the Genotype-Tissue Expression (GTEx) Project to catalogue sex differences across 44 human tissue sources, including brain tissue. 37% of all genes assayed in the GTEx database showed sex-biased gene expression [101]. Building off this work, Lee *et. al* investigated the sex bias of metabolic genes from human brain tissue in the GTEx database and found between 1-2% of all differentially expressed genes between male and female brain tissue samples were metabolic genes [102]. Phosphoglucomutase (PGM1, converts glycogen to glucose-6-phosphate for glycolysis), pyruvate dehydrogenase (PDH; converts pyruvate to acetyl-CoA), isocitrate dehydrogenase 2 (IDH2; converts isocitrate to α-ketoglutarate), glutamate dehydrogenase (GLUD1; converts glutamate to alpha-ketoglutarate), and oxoglutarate dehydrogenase (OGDH; converts alpha-ketoglutarate to succinyl-CoA) were all elevated in female brain tissue. Phosphofructokinase (PFK; converts fructose-6-phosphate to fructose-1,6-phosphate) was the only enzyme in glycolysis or the TCA cycle showing higher expression in male brain tissue [102]. Transcriptomic analysis of female rat brain microvessels showed pathway enrichment of genes involved in

the respiratory chain/respiratory electron transport and chylomicron-mediated lipid transport, while male rat brain microvessels showed enrichment of pathways for cholesterol biosynthesis and glucokinase regulation [103].

Though little *in vitro* research has investigated sexual dimorphisms in BMEC metabolism, studies in other endothelial cell lines demonstrate apparent metabolic differences between male and female cells. Lorenz *et al*. recently showed in HUVEC procured from male-female twin sets that VEGF-stimulated male HUVEC had higher mitochondrial respiration and lower glycolysis:mitochondrial respiration ratios than VEGF-stimulated female HUVEC [104]. Furthermore, female HUVEC had higher intracellular ATP following serum starvation than male HUVEC [104]. HUVEC studies also demonstrated a positive correlation between estradiol binding and phosphofructokinase-2/fructose-2, 6-bisphosphatase 3 (PFKFB3) upregulation, indicating a potential link between sex hormones and a rate-limiting glycolytic enzyme [105]. In the first protocol of hiBMEC differentiation, GLUT1 expression was higher in the female IMR90-4 hiBMEC line than the male DF19-9-11T hiBMEC line [106]. However, statistical analysis was not performed on the expression levels. These preliminary data justify further examination of sexual dimorphisms in BMEC glucose metabolism, since these differences may lead to downstream energetic and functional discrepancies between male and female cells.

1.6.2. Angiotensin II

Angiotensin II (AngII), a circulating stress hormone [107], increases oxidative stress, decreases vascular function, and increases BBB permeability [108], all of which occur in AD pathology. Both *in vitro* and *in vivo* studies support hyperactivity of the renin-angiotensin system (RAS) as a contributor to AD pathology [109]. In the RAS, angiotensinogen is cleaved by renin to form Angiotensin I, which is then cleaved by angiotensin converting enzyme (ACE) to AngII. Angiotensinogen is synthesized in response to gluticocorticoids, thyroid hormone, and estrogen [110]. AngII levels increase in response to both acute and chronic stress [111], which are implicated in AD development and progression [112]. Specifically, AngII binding to the angiotensin type 1 receptor (AT_1R) in the brain increases BBB permeability [113], oxidative stress [114], and neuroinflammation [115], and decreases cerebral blood flow [116], all of which are associated with AD pathogenesis [117], [118], [119], [120].

In vitro, cultured bovine aortic EC treated with AngII increased hydrogen peroxide, decreased mitochondrial membrane potential, and reduced nitric oxide production [121]. These effects were reversed with apocynin, an NADPH oxidase (NOX) inhibitor. In HUVEC, hydrogen peroxide promoted endothelial to mesenchymal transition (EndMT) via transforming growth factor-β2 (TGF-β2) [122], which is associated with decreased barrier function [123]. In the same study, HUVEC treated with hydrogen peroxide activated NF-κB [122], a transcription factor known to increase gene expression of interleukin-6 (IL-6) and other inflammatory cytokines [124]. In animals *in vivo,* cerebral arteries from male mice displayed increased superoxide and hydrogen peroxide and decreased contraction *ex vivo* in response to AngII compared to arteries from female mice [125].

AngII increases endothelial ROS production [121] through NOX [121]. Of the seven NOX isoforms, the genes for NOX1 and NOX2 both lie on the X-chromosome. As previously discussed, approximately 15% of genes on the inactivated X-chromosome escape from inactivation, thereby doubling the gene expression in individuals with two X-chromosomes. Data from B-lymphocytes demonstrates that CYBB, the gene for NOX2, escapes X-chromosome inactivation, indicating that it may be expressed at higher levels in female compared to male cells [126].

1.6.3. APOE Genotype

The APOE ε4 allele (15% allele frequency) presents a higher risk for AD as compared to the APOE ε2 (8% allele frequency) or APOE ε3 (77% allele frequency) alleles [127]. The elevated AD risk in people with the APOE ε4 genotype is likely due to a multitude of interconnected factors, many of which are connected to cell metabolism. In mouse models, the APOE ε4 genotype has been linked to deficient glucose uptake and metabolism in astrocytes and neurons [128], and decreased cerebral vascularization, BBB function, and glucose metabolism and transport [129], [130].

Though transgenic mouse models have demonstrated correlations between the APOE ε4 genotype and decreased glucose metabolism and barrier function, this has not yet been shown in human cells. Additionally, the mechanisms through which the APOE genotype regulates BMEC metabolism and function has not yet been identified. The APOE ε4 allele may regulate BMEC function through multiple pathways. In this work, we focus on two likely contenders.

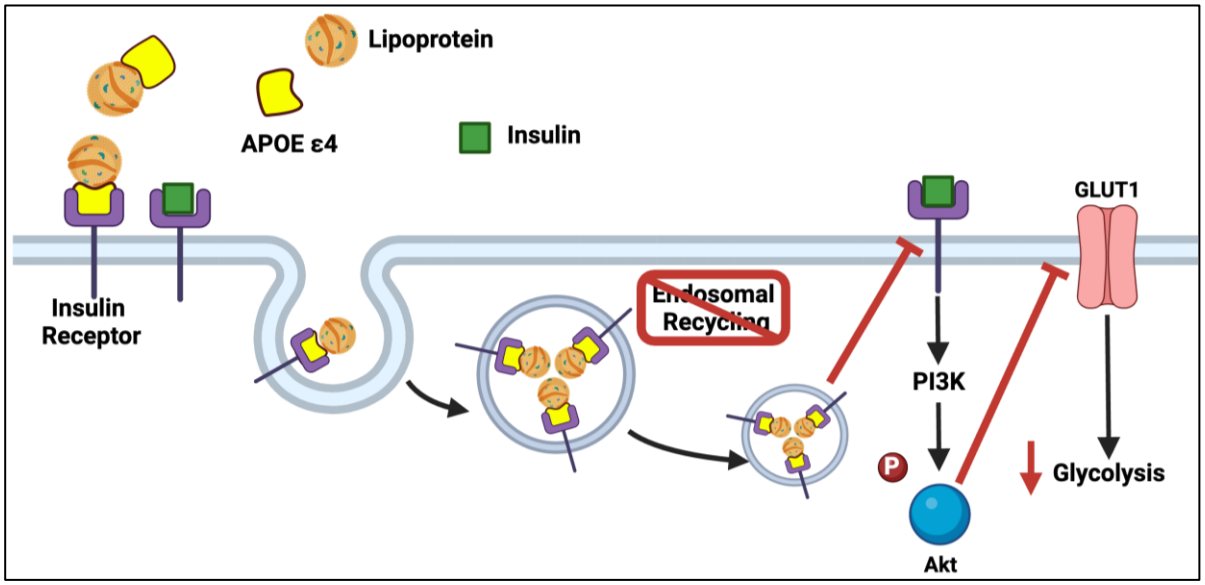


Figure 1.2. Hypothesis of APOE ε4-induced reduction in glycolysis. APOE ε4 proteins bind to lipoproteins in the circulation and then bind competitively to insulin receptors on the cell membrane. These APOE-lipoprotein-insulin receptor complexes are internalized into endosomes where increased binding affinity for APOE ε4 and insulin receptors prevents endosomal recycling of insulin receptors back to the cell membrane, instead targeting them to lysosomes for degradation. This process reduces the amount of insulin receptors available on the cell membrane for insulin signaling, which then impairs GLUT1 transcription and translocation to the membrane and glycolysis.

APOE facilitates cholesterol and phospholipid transfer among cells in the brain [131]. APOE is lipidated when it binds to lipoproteins, after which it acts as a ligand for receptor-mediated endocytosis by binding to low-density lipoprotein receptors (LDLRs), LDL receptor-related proteins (LRPs) [132], or insulin receptors (IR) [133]. Generally, after internalization, the components of the endosome are sorted, the ligand is released, and the receptors are transferred back to the plasma membrane [134]. Recent work in neurons revealed that APOE ε4 has a higher binding affinity to IR than APOE ε3 and leads to overall decreased membrane IR expression and increased endosomal IR, indicative of decreased endosomal recycling [133]. Decreased endosomal recycling of IR may lead to impaired insulin signaling, which can impair glucose

uptake via GLUT1 [135] (Fig. 1.2). In the insulin signaling cascade, insulin binds to the insulin receptor and initiates phosphoinositide 3-kinase (PI3K) activity, which in turn results in downstream phosphorylation of Akt [136]. p-Akt has been shown to increase GLUT1 translocation to the membrane [135]. Reduced endosomal recycling and subsequent insulin signaling is one proposed mechanism through which individuals with the APOE ε4 may be more susceptible to AD, leading to downstream metabolic deficiencies [133] and disrupted lipid homeostasis [137].

The APOE ε4 protein binds to a promotor for and reduces transcription of Sirtuin 1 (SIRT1) [138], a protein deacetylase that may prevent AD-associated neurodegeneration [139]. In brain microvascular endothelial cells (BMEC), SIRT1 promotes barrier strength, decreases inflammation, and attenuates oxidative stress [140]. Furthermore, both APOE ε4 genotype and reduced SIRT1 correlate with decreased glycolysis [130], [141], [142]. SIRT1 increases the transcription of rate limiting glycolytic enzyme hexokinase 2 (HK2) [141] [142](Fig. 3). Reduced SIRT1 levels in APOE ε4 brain endothelial cells could therefore reduce glycolysis and barrier function inducing glucose hypometabolism and BBB dysfunction in AD pathophysiology.

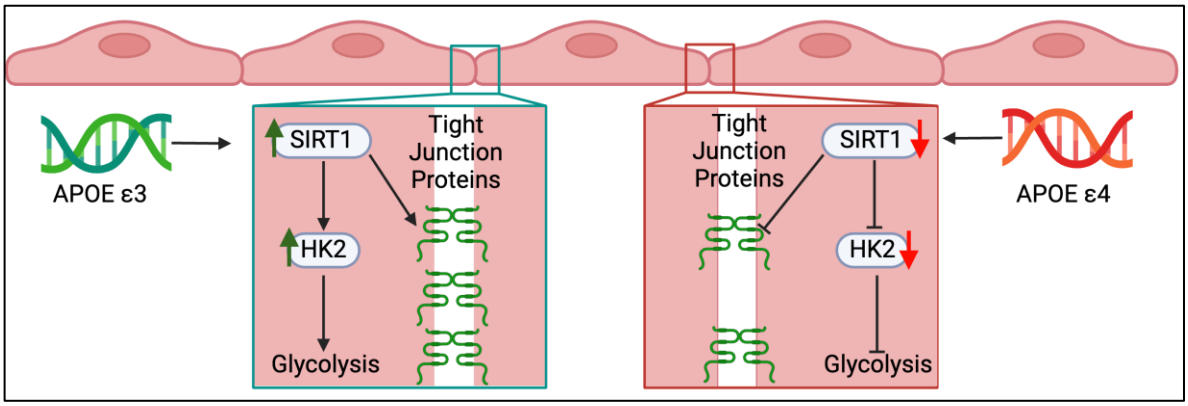


Figure 1.3. Hypothesis of APOE ε4-induced reduction in glycolysis and barrier function. APOE ε4 binds to the SIRT1 promotor and reduces its transcription thereby reducing SIRT1 protein levels. Lower levels of SIRT1 reduce HK2 levels, thereby impairing glycolysis. SIRT1 also reduces junctional expression of tight junction proteins, thereby reducing barrier function.

1.6.4. Sedentary Lifestyle

Exercise training shows promise in delaying the onset and reducing the overall burden of AD symptoms [143], [144]. A 2014 meta-analysis showed that of seven potentially modifiable risk factors

consistently associated with AD (diabetes, midlife hypertension, midlife obesity, physical inactivity, depression, smoking, and low educational attainment), physical inactivity was the single highest population attributable risk for AD [145]. Another meta-analysis found that the relative risk for dementia in adults with high physical activity compared to low physical activity is 0.72, and 0.55 for AD, indicating that in both groups physical inactivity is correlated with risk of disease [146]. In patients diagnosed with mild cognitive impairment (MCI), a disease that often progresses into AD, exercise training improved hippocampal functional connectivity [147], cortical thickness [148], and overall cognitive function [149]. Furthermore, in patients at high risk for developing AD, defined by having at least one copy of the APOE ε4 allele, physical activity was effective in reducing the rate of hippocampal atrophy [150]. Exercise may be beneficial in AD prevention by increasing brain glucose metabolism. In adult Sprague-Dawley rats, treadmill exercise improved mRNA and protein expression of GLUT1, GLUT-3, and metabolic enzymes including phosphofructokinase (PFK), lactate dehydrogenase (LDH), and adenosine monophosphate kinase (AMPK) in cerebral tissue, which indicate increased cerebral glycolysis [151].

Chapter 2: Sex differences in response to Angiotensin II

2.1. Introduction:

The lifetime risk for Alzheimer's disease (AD) is twice as high in women as in men [1]. While studies of AD sex differences historically focused on sex hormones, recent transcriptomic studies suggest that 37% of all genes are sex-biased in one or more tissues. Endothelial cell (EC) dysfunction is an early hallmark of AD, and 14-25% of the EC transcriptome is sex-dependent [152]. These EC sex differences may be a product of increased X-linked gene expression through escape from X-chromosome inactivation (XCI). Approximately 15% of X-linked genes consistently escape XCI, and an additional 10% of X-linked genes show variable inactivation patterns [153]. XCI escape of genes such as *CYBB* [154], which codes for NADPH oxidase-2 (NOX2), could increase oxidative stress in female cells, contributing to EC dysfunction.

Transcriptomic differences in female and male EC may be best studied in human umbilical vein endothelial cells (HUVEC), which exhibit the sex of the newborn [155], [156], [157] and have not been exposed to sex hormones *in vivo.* Indeed, in hormone-naive HUVEC from boy-girl twin pairs, there were more than 2000 differentially expressed genes [152]. Female HUVEC further had higher endothelial nitric oxide synthase (eNOS) expression and intracellular ATP, were more proliferative and migratory, and had lower mitochondrial respiration following VEGF-stimulation compared to male HUVEC [156], [157]. A recent study further showed that female and male HUVEC have different responses to mechanical cues such as shear stress and substrate stiffness [158]. Thus, female and male HUVEC may have different transcriptomes at baseline and in response to external stimuli.

Angiotensin II (AngII) is a circulating stress hormone [159] that contributes to endothelial dysfunction in AD and is elevated in the brains of AD patients [160]. When AngII binds to the angiotensin type 1 receptor (AT1R), it enhances NOX2 activity to increase reactive oxygen species (ROS) production [161], leading to EC dysfunction.

Most studies on the effects of AngII on vascular and EC function were conducted in male rodents [162], [163], [164], [165] or failed to analyze outcomes in a sex-dependent manner [166]. Therefore, in this study

published in *Cellular and Molecular Bioengineering,* I examined how female and male EC responded differently to AngII [167]. I used RNA sequencing to study transcriptomic differences, followed by phenotypic, inflammatory, and oxidative stress assays to measure how the transcriptomic differences affected EC function. My data demonstrate that EC have sexually dimorphic inflammatory and oxidative stress responses to AngII treatment, which could be important in treating AD in female versus male patients.

2.2. Methods:

2.2.1. Cell Culture: Male and female endothelial cells from donors of different sexes and from different vascular beds were used (Table 2.1), as indicated in each experiment. Pooled male and pooled female human umbilical vein endothelial cells (HUVEC; Lonza; 3 donors per sex), individual donor male and female HUVEC (Lonza, 2 donors per sex), and individual donor male and female human coronary artery endothelial cells (HCAEC; Lifeline Cell Technology; 1 donor per sex) were cultured in Endothelial Growth Medium-2 (EGM-2; Lonza) supplemented with 10% fetal bovine serum (FBS; Hyclone), 1% penicillin streptomycin (Thermo Fisher) and 1% L-glutamine (Thermo Fisher). Individual donor human pulmonary artery endothelial cells (HPAEC; Pulmonary Hypertension Breakthrough Initiative; 3 donors per sex) were cultured in Endothelial Growth Medium-2-MV (EGM-2-MV; Lonza) supplemented with 10% FBS, 1% penicillin streptomycin, and 1% L-glutamine. Cells were maintained in an incubator with 5% CO_2 at 37°C and used between passages 4-9.

Table 2.1. EC donor characteristics.

Source Tissue	Cell Sex	Donor Age	Race
Umbilical Vein	Female (3 pooled donors)	Newborn	White
Umbilical Vein	Male (3 pooled donors)	Newborn	White
Umbilical Vein	Female	Newborn	White
Umbilical Vein	Male	Newborn	White
Umbilical Vein	Female	Newborn	Black or African American
Umbilical Vein	Male	Newborn	Black or African American
Pulmonary Artery	Female	36	White
Pulmonary Artery	Male	49	White

Pulmonary Artery	Female	50	White
Pulmonary Artery	Male	51	White
Pulmonary Artery	Female	34	White
Pulmonary Artery	Male	40	White
Coronary Artery	Female	12	Black or African American
Coronary Artery	Male	22	Black or African American

2.2.2. RNA Sequencing: Confluent pooled male and female HUVEC were incubated with 1 µM angiotensin II (AngII; Sigma; SCP0020) or water as a vehicle control for 24 hours. RNA was extracted using phenol/chloroform [168]. Briefly, cells were washed with cold phosphate buffered saline (PBS), scraped, and centrifuged at 17,000 x g and 4°C for 4 minutes. 1 mL TRIzol (ThermoFisher) was added to each sample, after which the cell pellets were resuspended and incubated at room temperature for 5 minutes. 200 µL chloroform (Sigma) was added to each sample, and samples were vortexed and centrifuged at 4°C and 17,000 x g for 30 minutes. Equal volumes of the top RNA sample layer and isopropyl alcohol were combined with a 1:100 dilution of GlycoBlue Co-precipitant (ThermoFisher) and then centrifuged at 4°C and 17,000 x g for 30 minutes. The pellet was washed with ice-cold 70% ethanol and resuspended in RNase-free water. RNA was quantified on a Nanodrop 2000c (Thermo Fisher) and then shipped to Novogene where ribosomal RNA were degraded and a directional RNA library was constructed to extract long non-coding RNA, micro RNA, and circular RNA before the samples were sequenced on an Illumina NovaSeq 6000.

All RNAseq data were processed in Galaxy (https://usegalaxy.org). A FASTQC report was used to verify RNA sequencing quality. Samples were trimmed as paired end reads using Trimmomatic and aligned to the human genome (hg38) using HISAT2. FeatureCounts measured differentially expressed genes (DEG) based on the annotated human genome. EdgeR was then used to compare AngII treated samples to untreated samples for both the male and female HUVEC. A Benjamini and Hochberg p-value adjustment was used for statistical analysis. Genes with a fold change > 0.6 and an adjusted p-value < 0.3 were considered statistically significant. The EdgeR report was uploaded to iPathway Guide [169], [170] (Advaita

Bio) to visualize gene and pathway alterations in response to AngII, and how DEG differed between male and female HUVEC following AngII treatment.

2.2.3. ELISA: Human interleukin-6 (IL-6) and transforming growth factor-β2 (TGF-β2) in cell culture media samples were quantified by ELISA (RayBiotech) as per manufacturer's protocols. For the TGF-β2 ELISA, cells were treated ±1 µM AngII for 24 hours after which 250 µL conditioned media was transferred to microcentrifuge tubes, activated with 50 µL 1N HCl (Sigma) for 10 minutes, and then neutralized with 50 µL 1.2 N NaOH (Sigma)/ 0.5 M HEPES (Sigma). For the IL-6 ELISA, cells were treated ±1 µM AngII and ±1 ng/mL TNFα for 24 hours. Conditioned media was diluted 1:1 in sample dilution buffer. Absorbance was read immediately on a plate reader (Tecan Spark Multimode Microplate Reader) at 450 nm.

2.2.4. Endothelial-to-Mesenchymal Transition (EndMT): Endothelial vs. mesenchymal cell phenotype was measured using an endothelial marker (VE-cadherin) and a mesenchymal marker (α-smooth muscle actin; αSMA). Confluent pooled male and female HUVEC on 18 mm glass coverslips (VWR) were treated ±1 µM AngII for 24 hours, fixed in 4% paraformaldehyde (PFA; Sigma), and then permeabilized and blocked with 0.2% TritonX-100 (Alfa Aesar) and 5% goat serum (Sigma) in phosphate buffered saline (PBS; Thermo Fisher) for 1 hour. Cells were incubated in primary antibodies against VE-cadherin (1:50, Santa Cruz Biotechnology; sc-9989) and αSMA (1:200; Abcam; ab5694) overnight at 4°C in 1% goat serum in PBS. Cells were then incubated in the appropriate secondary antibodies (1:1000; Thermo Fisher) and Hoechst (1:2000; nuclei; Thermo Fisher). Samples were imaged on an ECHO Revolve microscope at 20x magnification.

2.2.5. White Blood Cell (WBC) Adhesion Assay: WBC adhesion was used to determine EC inflammation. Confluent male and female HUVEC and HPAEC were treated ±1 µM AngII and ±1 ng/mL TNFα for 24 hours. WBC were isolated from freshly drawn blood following IRB 1818450-1 using Acrodisc WBC Syringe Filters (Pall). WBC were labeled with Calcein AM (Thermo Fisher) for 30 minutes in EGM-2 media, after which they were washed and resuspended at 2 x 10^6 cells/mL in EGM-2. HUVEC and HPAEC were washed with 1x PBS, then incubated with 1 x 10^6 WBC for 10 minutes. After thorough washing, samples were imaged on an ECHO Revolve microscope at 10x magnification.

2.2.6. Oxygen Consumption Rate (OCR): EC oxidative phosphorylation was measured using a Seahorse ATP Rate Assay (Agilent). Male and female pooled HUVEC were seeded at 40,000 cells/well in a 96-well Seahorse plate (Agilent), allowed to attach overnight, then treated ±1 μM AngII for 24 hours. The ATP Rate Assay was run following manufacturer's protocols. OCR, an approximation of mitochondrial metabolism, was assessed in basal conditions and following oligomycin (ATP synthase inhibitor) and rotenone/antimycin A (mitochondrial electron transport chain inhibitors) treatment. Mitochondrial ATP production was calculated using Seahorse Wave software (Agilent), and proton leak was calculated as the difference between oligomycin and rotenone/antimycin A inhibition of OCR.

2.2.7. Reactive Oxygen Species: Carboxy-H_2DCFDA, which is taken up by a cell and then oxidized by ROS to induce a fluorescent signal, and MitoSOX, which is targeted to the mitochondria then specifically oxidized by superoxide to produce a fluorescent signal, were used to measure EC oxidative stress. Confluent male and female HUVEC and HPAEC were treated ±1 μM AngII (Millipore Sigma; SCP0020) for 24 hours. Cells were washed twice with Hank's Balanced Salt Solution with calcium and magnesium (HBSS/Ca/Mg; Thermo Fisher) and then incubated in 25 μM carboxy-H_2DCFDA (Thermo Fisher) in HBSS/Ca/Mg containing 1 μM Hoechst for 30 minutes at 37°C. HBSS without sodium bicarbonate (Thermo Fisher) was used to wash the cells before mounting them on glass slides and imaging at 10x magnification on an ECHO Revolve microscope. For the MitoSOX assay, HUVEC were washed with HBSS/Ca/Mg and then incubated in HBSS/Ca/Mg containing 5 μM MitoSOX (Thermo Fisher) and 1 μM Hoechst for 15 minutes at 37°C. After washing with HBSS without sodium bicarbonate, samples were mounted on glass slides and immediately imaged on an ECHO Revolve fluorescent microscope.

2.2.8. CYBB Gene Expression: HUVEC, HCAEC, and HPAEC were seeded at 125,000 cells/well in a 12-well plate. RNA was isolated from confluent EC using an RNEasy Mini Kit (Qiagen). Isolated RNA was quantified on a Nanodrop 2000c (Thermo Fisher), and RNA was converted to cDNA using a High-Capacity cDNA Reverse Transcription kit (Thermo Fisher) and a ProFlex Thermal Cycler (Thermo Fisher). I ran qPCR using a Taqman probe for *CYBB* (ThermoFisher; Hs00166163_m1) and *RPLP0,* a ribosomal protein not differentially expressed between male and female EC, as a housekeeper (Thermo Fisher; Hs00420895_gH) using a QuantStudio 7 Flex qPCR System (Thermo Fisher).

2.2.9. NOX2 siRNA knockdown: Pooled HUVEC were seeded at 125,000 cells/well in a 12-well plate in antibiotic-free EGM-2 supplemented with 10% FBS and 1% glutamine. After 24 hours, 18 pmol CYBB siRNA (Thermo Fisher; s531913) or Silencer Select Negative Control #1 (Thermo Fisher) complexed with Lipofectamine RNAiMAX Transfection Reagent (Thermo Fisher) in Opti-MEM I Reduced Serum Medium (Thermo Fisher) was added to the culture medium. After 24 hours of siRNA treatment, cells were treated with 1 μM AngII, and the downstream assay was performed.

NOX2 protein was assessed by Western blot. 6, 24, or 48 hours after *CYBB* siRNA application, cells were lysed. Protein was quantified using a BCA assay (Thermo Fisher), and samples (3.5 μg/μL protein) were separated on 4-12% Bis-Tris gels (Thermo Fisher) and transferred to a nitrocellulose membrane (Thermo Fisher) using an iBlot 2 (Thermo Fisher). Membranes were blocked for 1 hour in 5% bovine serum albumin (Millipore Sigma) in PBS containing 0.5% Tween 20 (Thermo Fisher) and then incubated with primary antibodies for NOX2 (Proteintech; 19013-1-AP; 1:1000) and β-Actin (Santa Cruz Biotechnology; sc-47778; 1:1000) overnight. After thorough washing, membranes were incubated in the appropriate secondary antibodies (Promega; 1:2000) for 2 hours. Western blots were imaged on an Alpha Innotech Fluorchem Imager (Protein Simple), and proteins were quantified using AlphaView software.

2.2.10. Fluorescent Image Quantification: Fluorescent images were quantified in Fiji (ImageJ). For EndMT analysis, rolling ball background subtract was used to remove background fluorescence. Images were then thresholded to remove non-specific labeling before measuring fluorescence intensity. Thresholds were maintained for all images in an experiment, and fluorescence intensity was normalized to cell count by dividing by the number of nuclei in the same image. For WBC adhesion analysis, the number of adhered WBC per frame were counted and averaged between samples. Images shown are representative of the average fluorescence intensity for each treatment group.

2.2.11. Statistics: Statistics were analyzed in GraphPad Prism. Non-parametric Mann-Whitney tests, Kruskal-Wallis tests, and two-way ANOVA with a Tukey's correction for multiple comparisons were used to compare datasets. RNA-seq data were considered biologically significant with an adjusted p-value < 0.3 and a $Log_2FC > 0.6$.

2.3. Results:

2.3.1. Female and male HUVEC had sexually dimorphic gene expression.

AngII is a circulating stress hormone known to have vascular effects. Since the EC transcriptome itself is sexually dimorphic [152], I investigated if AngII has different effects on female versus male EC. I first studied gene expression differences in pooled HUVEC from male and female donors. RNA sequencing showed that male and female HUVEC had 1134 differentially expressed genes. 622 genes were upregulated in female as compared to male HUVEC, and 512 genes were upregulated in male as compared to female HUVEC (Fig. 2.1A, Appendix Table 1A-B). Cell sex was validated through expression of sex-specific transcripts including the female-associated gene X-Inactive Specific Transcript (*XIST),* which was downregulated in male compared to female HUVEC *(*$Log_2FC = 14.16$), and the male-associated gene Ubiquitin specific peptidase 9 Y-Linked (*USP9Y),* which is upregulated in male compared to female HUVEC ($Log_2FC = 14.19$).

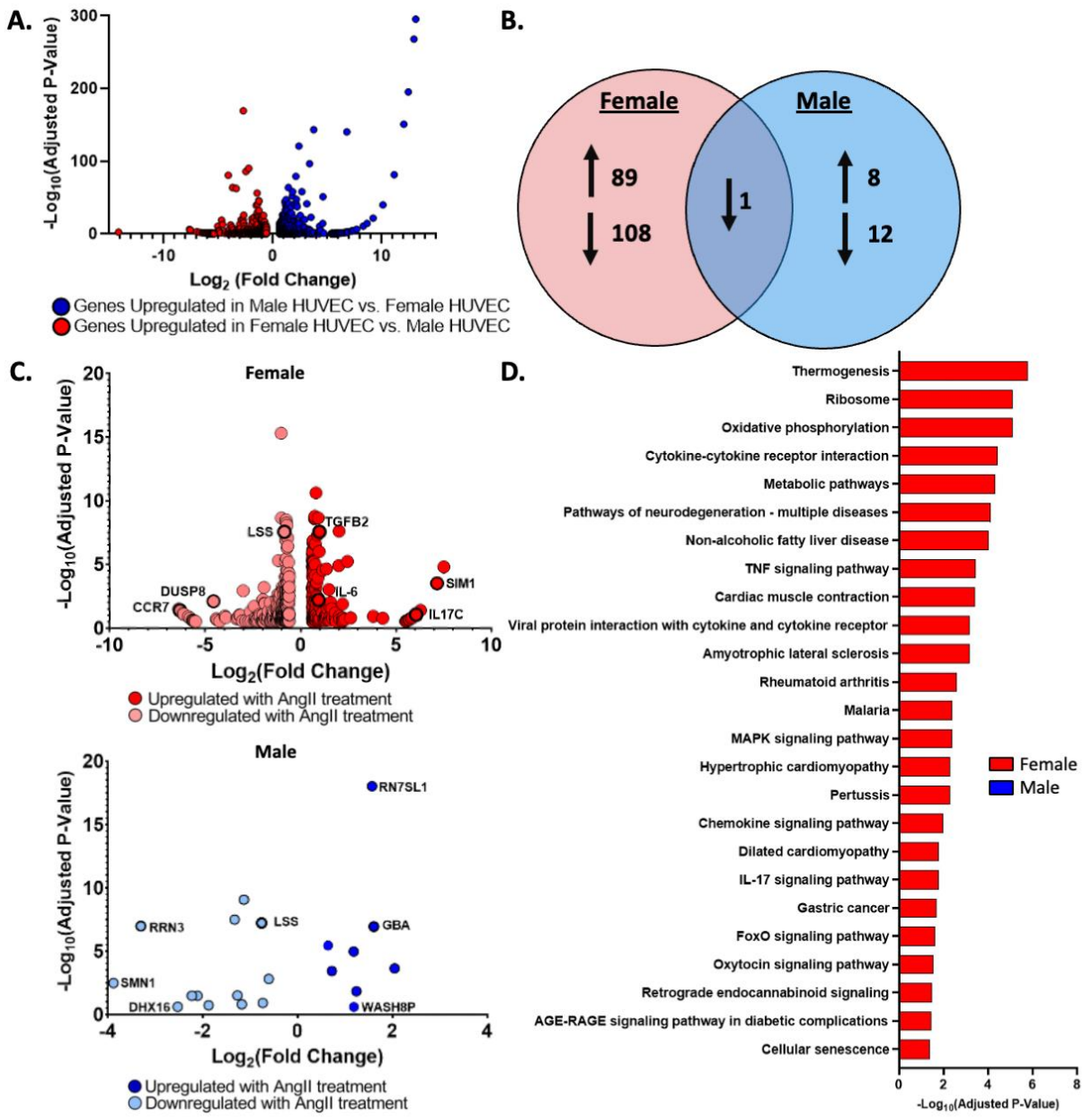


Figure 2.1. Female endothelial cells differentially express more genes in response to AngII treatment. (A) Volcano plot of RNA sequencing data from untreated female and male HUVEC. Blue indicates genes upregulated in male vs. female HUVEC (512 genes), and red indicates genes upregulated in female vs. male HUVEC (622 genes). Graph demonstrates data relative to male HUVEC where a positive Log_2FC indicates upregulation in male HUVEC and a negative Log_2FC indicates downregulation in male HUVEC relative to female. **(B)** Venn Diagram of gene expression changes in female and male HUVEC treated with 1 µM AngII for 24 hours. **(C)** Volcano plots of genes that were differentially expressed genes following 24 hours of AngII treatment in female and male HUVEC. A full table of all differentially expressed genes is in the supplemental data. **(D)** KEGG pathways significantly altered by AngII treatment containing more than three differentially expressed genes. Significant with Log_2FC >0.6, and adjusted p-value <0.05. n = 3 samples for each condition from pooled HUVEC in RNA sequencing data. Female and Male HUVEC were pooled from three donors per sex.

2.3.2. Female HUVEC altered expression of more genes in response to AngII than male HUVEC.

I then treated pooled male and female HUVEC with AngII for 24 hours and analyzed gene expression changes. Female HUVEC differentially expressed 444 genes with AngII treatment, while male HUVEC differentially expressed 21 genes (Fig 2.1B; Appendix Table 2A-B). The 172 upregulated genes in female AngII-treated HUVEC included interleukin-6 (*IL-6*; $p = 0.006$), an inflammatory cytokine, and transforming growth factor β-2 (*TGF-β2*; $p < 0.0001$), a growth factor involved in proliferation, differentiation, and apoptosis. The 272 downregulated genes included dual specificity phosphatase 8 (*DUSP8*; $p = 0.008$), a phosphatase regulating protein responsible for cell proliferation and differentiation. The 8 upregulated genes in AngII-treated male HUVEC included glucosylceramidase β (*GBA*; $p < 0.0001$), a lysosomal protein involved in glycolipid metabolism, while the 13 downregulated genes included RNA polymerase I transcription factor (*RRN3*; $p < 0.0001$; Fig 2.1C), an RNA polymerase regulating apoptosis and transcription. Of the differentially expressed genes, only lanosterol synthase (*LSS*; $p < 0.0001$), an enzyme involved in cholesterol synthesis, was commonly downregulated.

I next used iPathway Guide's KEGG database to understand how these expression changes relate to cell-level functions. Male HUVEC treated with AngII did not have any KEGG pathways with three or more differentially expressed genes. However, female HUVEC treated with AngII had multiple KEGG pathways with more than three differentially expressed genes. Of particular interest were statistically significant changes in pathways that could be important in AngII-related diseases that are more prevalent in women, including tumor necrosis factor (TNF) signaling, advanced glycation end products (AGE)-receptor for advanced glycation end products (RAGE) signaling, cytokine-cytokine receptor interaction, metabolic pathways, oxidative phosphorylation, and pathways of neurodegeneration (Fig. 2.1D, Appendix Table 3).

2.3.3. TGF-β2 gene expression, but not protein secretion, was elevated in female HUVEC in response to AngII.

To determine if gene expression changes resulted in cell function changes, I further investigated several genes that were upregulated in AngII-treated female HUVEC. TGF-β2 is a major molecular player in EndMT [171], which may contribute to loss of BBB integrity in AD [172]. Since TGF-β2 expression was higher in

pooled female, but not significantly altered in male, AngII-treated HUVEC (Fig. 2.2A), I measured TGF-β2 protein and EndMT in female and male HUVEC. TGF-β2 protein did not change after 24 hours of AngII treatment in pooled cells of either sex (Fig. 2.2B). Similarly, VE-cadherin did not decrease and α-smooth muscle actin (αSMA) did not increase with AngII treatment in either male or female cells, suggesting that AngII did not lead to EndMT (Fig. 2.2C). Thus, even though AngII increased *TGF-β2* mRNA expression in female HUVEC, this did not lead to measurable changes in TGF-β2 protein or EndMT.

2.3.4. AngII increased inflammatory responses in female but not male EC.

Expression of IL-6, an inflammatory cytokine implicated in Alzheimer's disease, was also higher in pooled female HUVEC but unchanged in male HUVEC following AngII treatment (Fig. 2.3A). Adhesion protein genes, including E-Selectin (*SELE;* $Log_2FC = 0.601$), vascular cell adhesion protein-1 (*VCAM1;* $Log_2FC = 0.455$), and intercellular adhesion molecule-1 (*ICAM1;* $Log_2FC = 0.399$) were elevated in pooled female, but not male, HUVEC following AngII treatment. IL-6 protein released into the media did not change between cells of differing sex or with AngII treatment (Fig. 2.3B-C). Based on these results, I hypothesized that a second inflammatory stimulus may be needed to change IL-6 release. I therefore treated pooled male and female HUVEC with both AngII and the inflammatory cytokine TNFα. In the presence of TNFα, AngII increased IL-6 protein release by 36% in pooled female but not male HUVEC ($p = 0.0010$; Fig. 2.3B-C). I then determined if the increased IL-6 release enhanced WBC adhesion using the male and female pooled HUVEC, individual donor HUVEC, and individual donor HPAEC. WBC adhesion was elevated by 33% in female, but not male, EC treated with AngII in the presence of TNFα ($p = 0.0224$; Fig. 2.3D-F, Fig. 2.4, Fig. 2.5). These data suggest that AngII exposure in the presence of an additional inflammatory stimuli leads to a cooperative increase in inflammation response in female but not male endothelial cells.

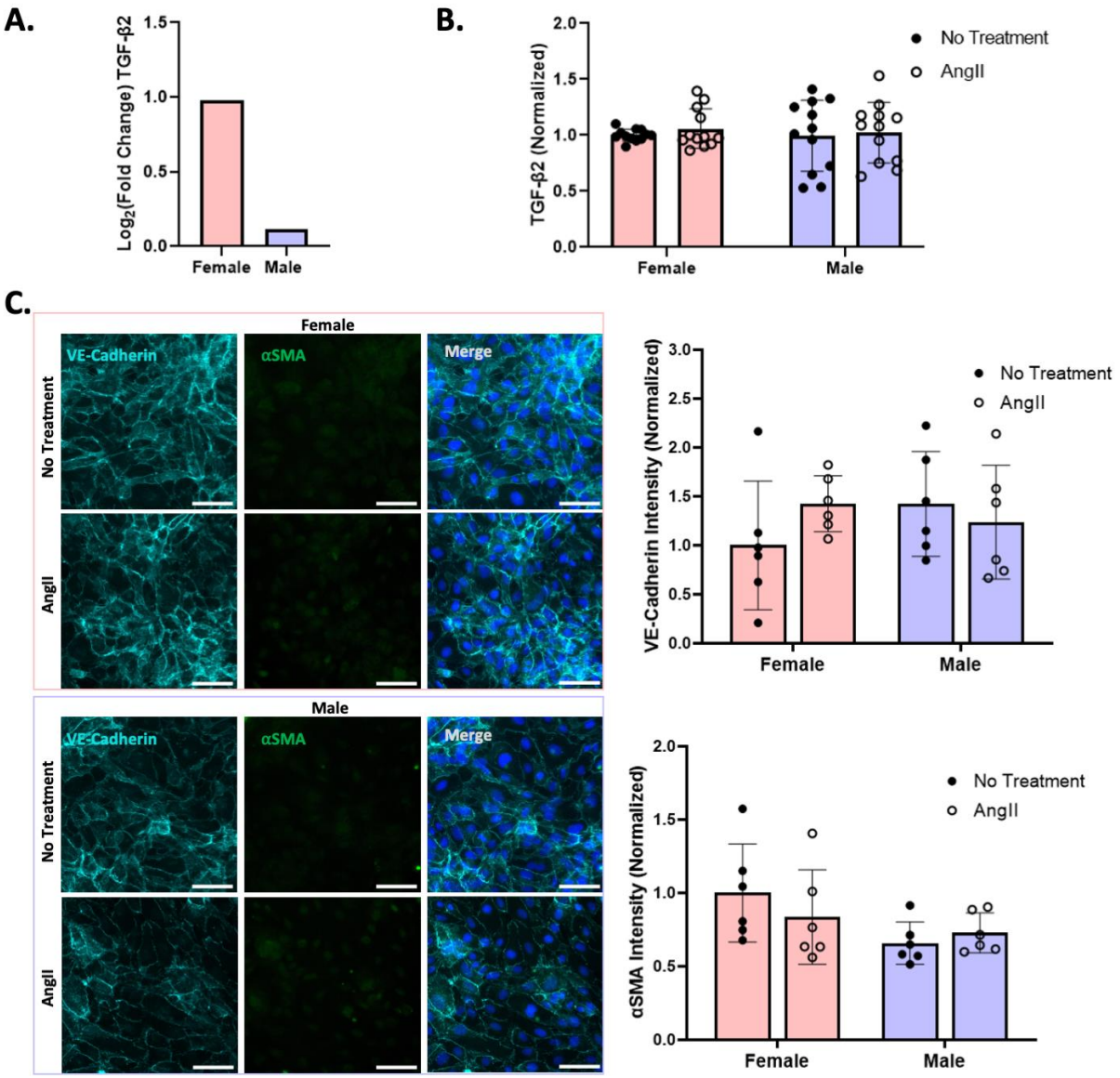


Figure 2.2. AngII increased TGFβ2 mRNA expression in female as compared to male HUVEC, but TGFβ2 protein and EndMT did not change with AngII or sex. (A) RNA-seq of changes in *TGFβ2* gene expression following 24 hours of 1 μM AngII treatment in male and female HUVEC (n = 3 samples per experimental condition from pooled HUVEC). **(B)** TGF-β2 protein after 24 hours of 1 μM AngII treatment in pooled male and female HUVEC, as measured by ELISA (n = 12 samples per condition; 4 experimental repeats, 3 samples per condition in each repeat). **(C)** Representative fluorescent microscopy images of endothelial (VE-cadherin, light blue) and mesenchymal (αSMA, green) markers, with Hoescht-labeled nuclei (dark blue) in female and male HUVEC following 24 hours of 1 μM AngII treatment, with quantification (n = 6 samples per condition; 2 experimental repeats, 3 samples per condition in each repeat). Scale = 50 μm. TGF-β2 protein and fluorescence intensity were normalized to untreated female cells. Female and Male HUVEC were pooled from three donors per sex.

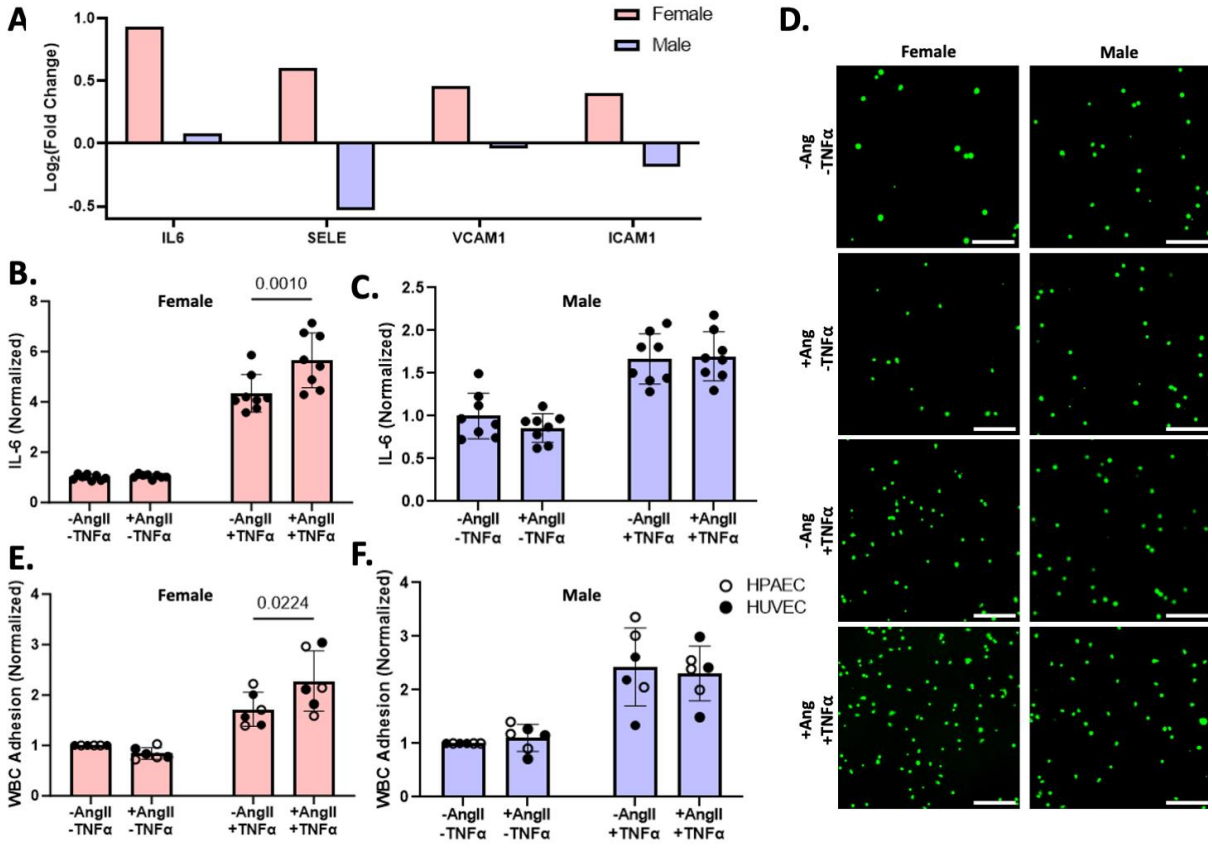


Figure 2.3. Female HUVEC had higher IL-6 mRNA expression than male HUVEC following AngII treatment but required concurrent TNFα exposure to show higher IL-6 protein and inflammation. **(A)** *IL-6, SELE, VCAM1, and ICAM1* gene expression from RNA sequencing in pooled female and male HUVEC following 24 hours of 1 µM AngII treatment (n = 3 samples per condition from pooled HUVEC). IL-6 protein following 24-hour treatment ±1 µM AngII and ± 1 ng/ml TNFα in **(B)** female and **(C)** male HUVEC, measured via ELISA (n = 8 samples per condition; 2 experimental repeats, 4 samples per condition in each repeat). **(D)** WBC adhesion (calcein, green) to male and female HUVEC and HPAEC following 24-hour treatment ±1 µM AngII and ±1 ng/ml TNFα quantified in **(E)** female and **(F)** male EC (n = 6 cell donors per sex; each datapoint averaged from 3 samples per condition). Scale = 100 µm. Data analyzed with Two-way ANOVA. IL6 protein concentration and WBC adhesion were normalized to untreated cells for each sex.

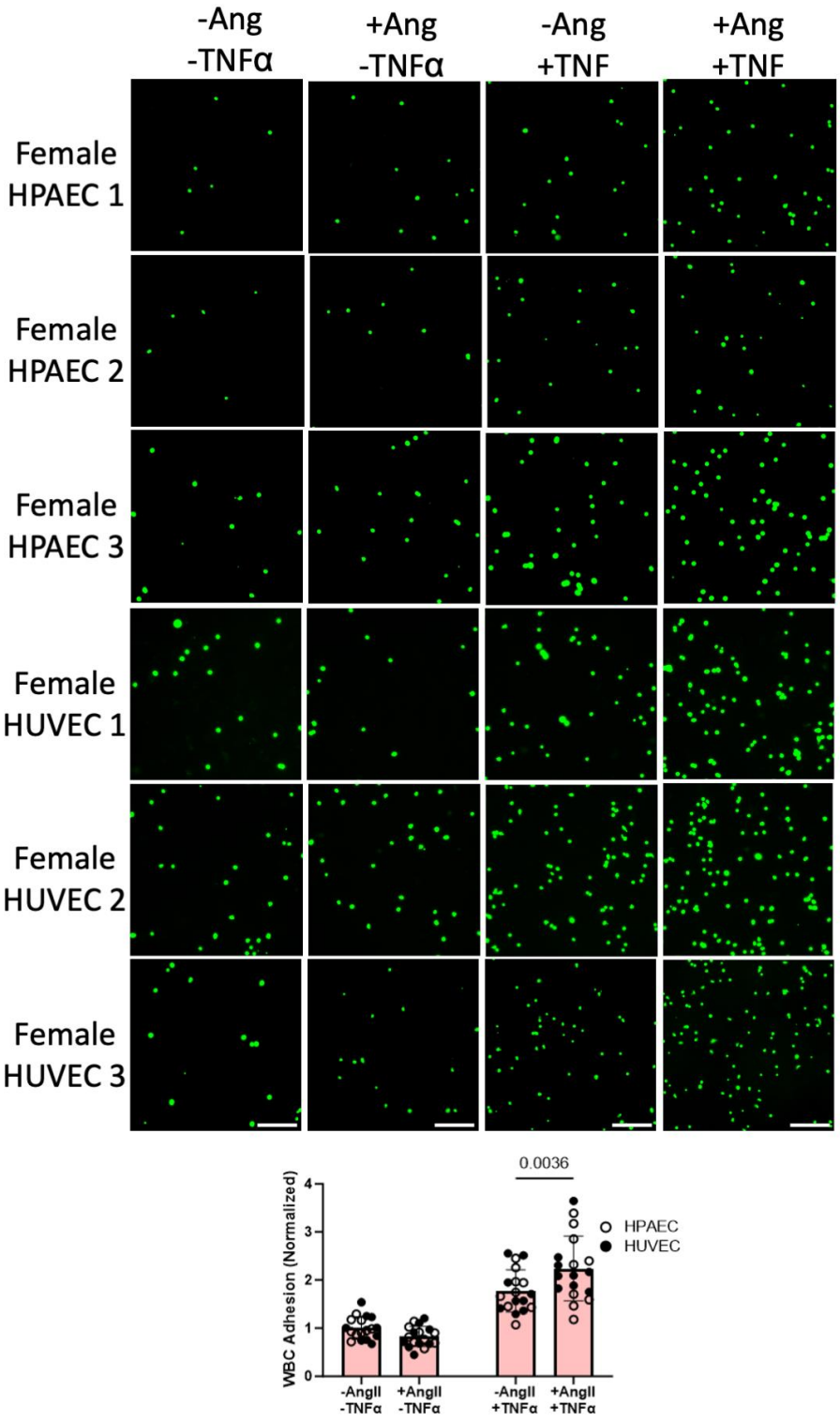


Figure 2.4. Female HPAEC and HUVEC increased WBC adhesion when treated with TNFα and AngII. Female HPAEC and HUVEC from 3 donors each were treated with +/- 1 µM AngII and +/- 1 ng/ml TNFα for 24 hours, followed by a 10-minute incubation with calcein-green labeled WBC (n = 18 samples from 6 donors). Scale bar = 100 µm. Data analyzed with two-way ANOVA. *p<0.05, **p<0.01. WBC adhesion was normalized to –AngII – TNFα.

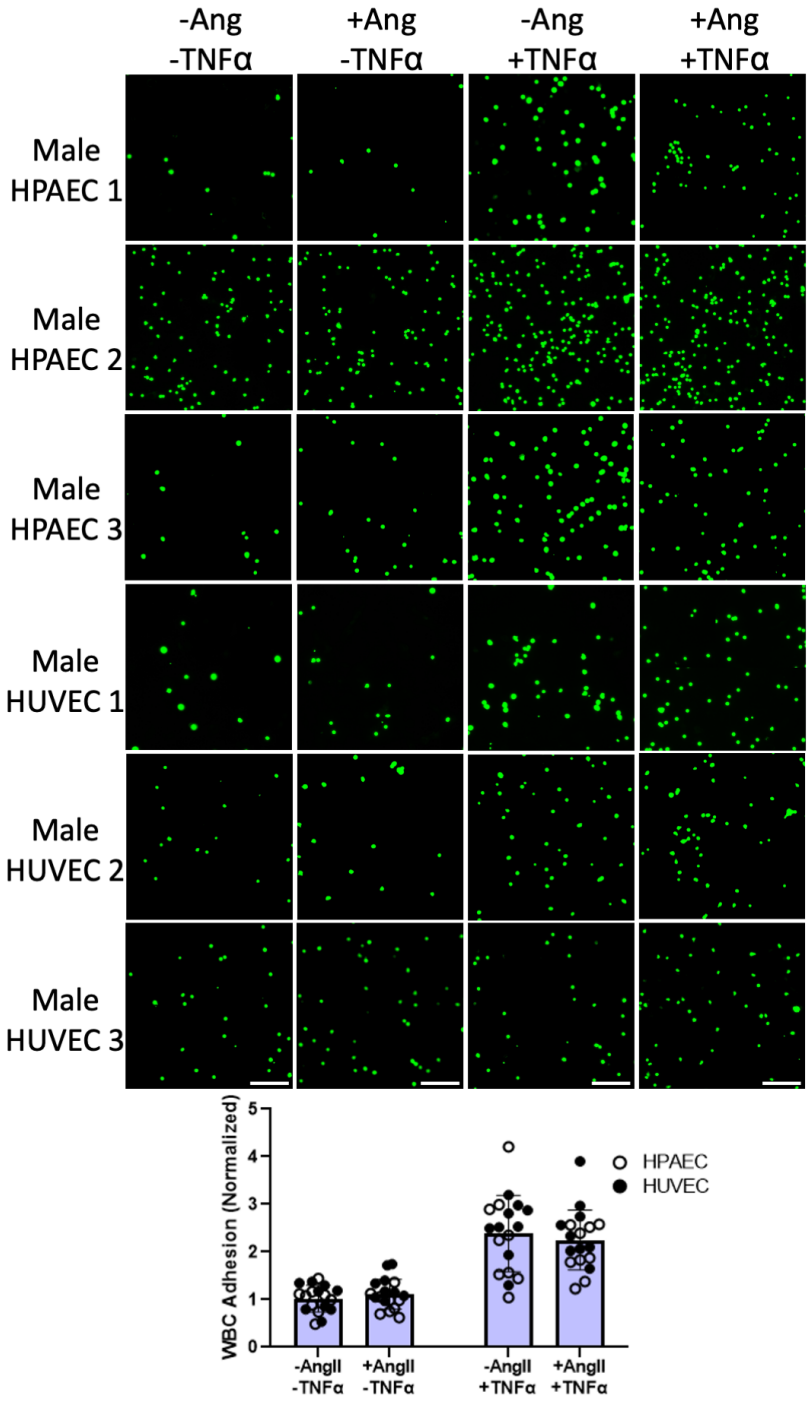


Figure 2.5. Male HPAEC and HUVEC increased WBC adhesion when treated with TNFa and AngII. Male HPAEC and HUVEC from 3 donors each were treated with +/- 1 µM AngII and +/- 1 ng/ml TNFα for 24 hours, followed by a 10-minute incubation with calcein-green labeled WBC (n = 18 samples from 6 donors). Scale = 100 µm. Data analyzed with Two-way ANOVA. WBC adhesion was normalized to – AngII – TNFα.

Indeed, nine genes involved in mitochondrial respiration were upregulated in female, but not male, pooled HUVEC following 24 hours of AngII treatment (Fig. 2.6A). As ROS are a by-product of mitochondrial respiration, and AngII is known to increase endothelial ROS [173], I hypothesized that female EC treated with AngII would have higher ROS than male EC. Female and male pooled HUVEC, individual donor HUVEC, and individual donor HPAEC were treated with ±1 µM AngII for 24 hours and then incubated with

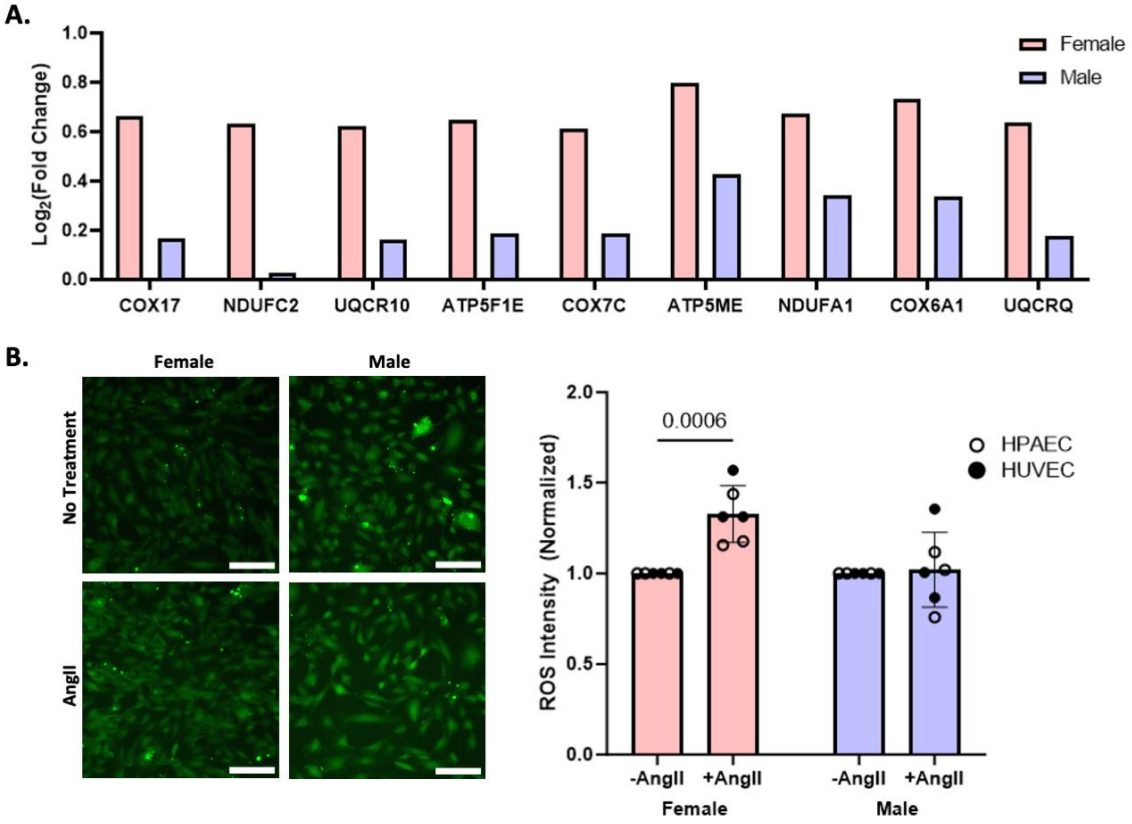


Figure 2.6. Female HUVEC demonstrate increased ROS production in response to AngII compared to male HUVEC. (A) RNA-seq of differentially expressed genes associated with mitochondrial respiration elevated in female but not male HUVEC following AngII treatment (n = 3 samples per condition from pooled HUVEC). **(B)** General ROS production shown via Carboxy-H_2DCFDA in female versus male HUVEC and HPAEC following 24 hours of AngII treatment (n = 6 cell donors per sex; each datapoint averaged from 3 samples per condition).

Carboxy-H_2DCFDA, a general ROS indicator. Female HUVEC and HPAEC demonstrated a 33% increase in ROS following AngII treatment (p =0.0006), while male HUVEC and HPAEC did not show an increase in ROS (Fig. 2.6B; Fig. 2.7). However, individual donor female HCAEC did not increase ROS following AngII treatment (Fig. 2.8).

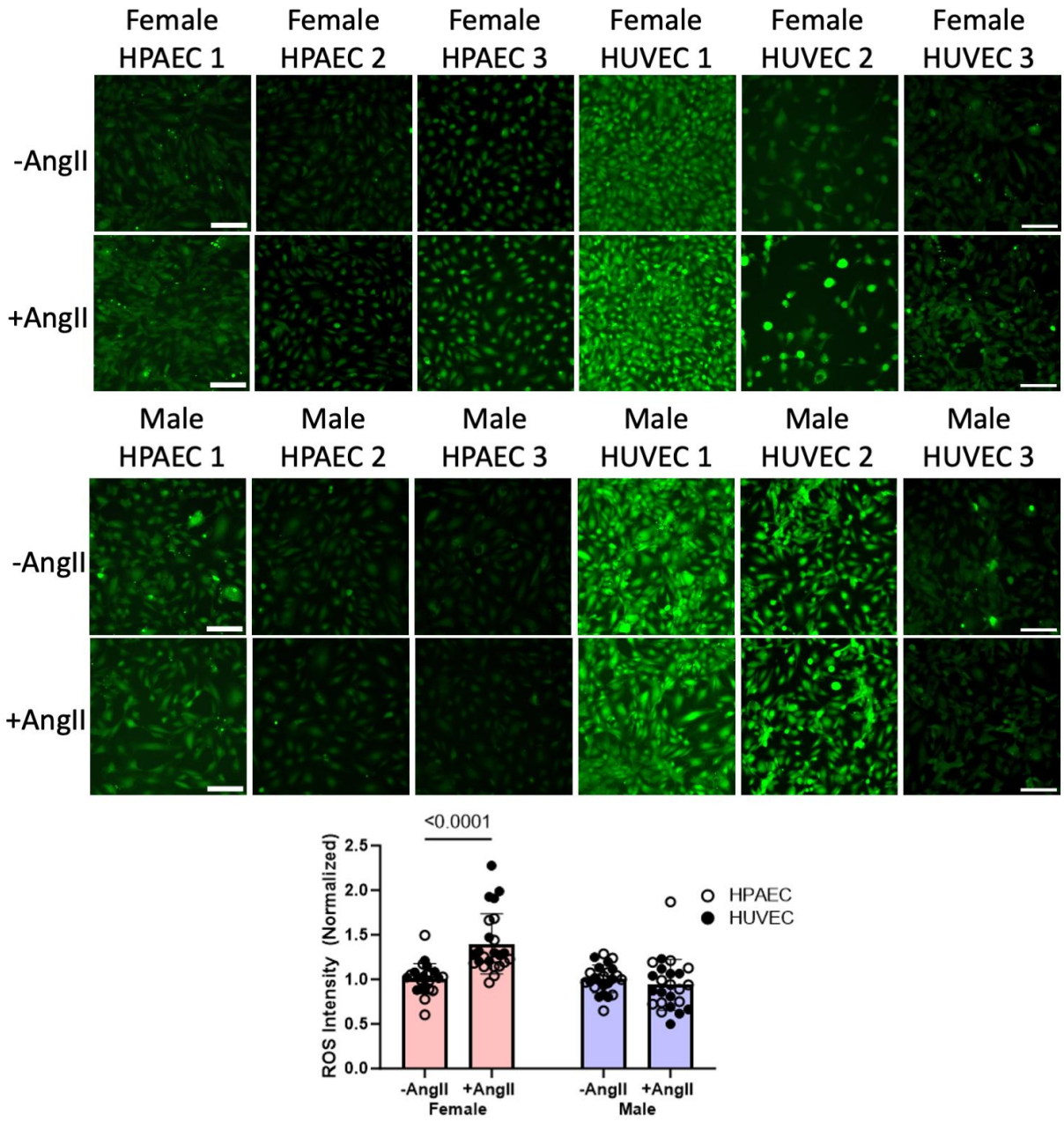


Figure 2.7. Female HUVEC and HPAEC had elevated ROS following AngII treatment, while male cells did not. HUVEC and HPAEC from 3 donors per sex were treated with +/- 1 µM AngII for 24 hours, then labeled with carboxy-H_2DCFDA (green). Scale bar = 100 µm. Data analyzed with two-way ANOVA. ROS intensities were normalized to untreated cells for each sex.

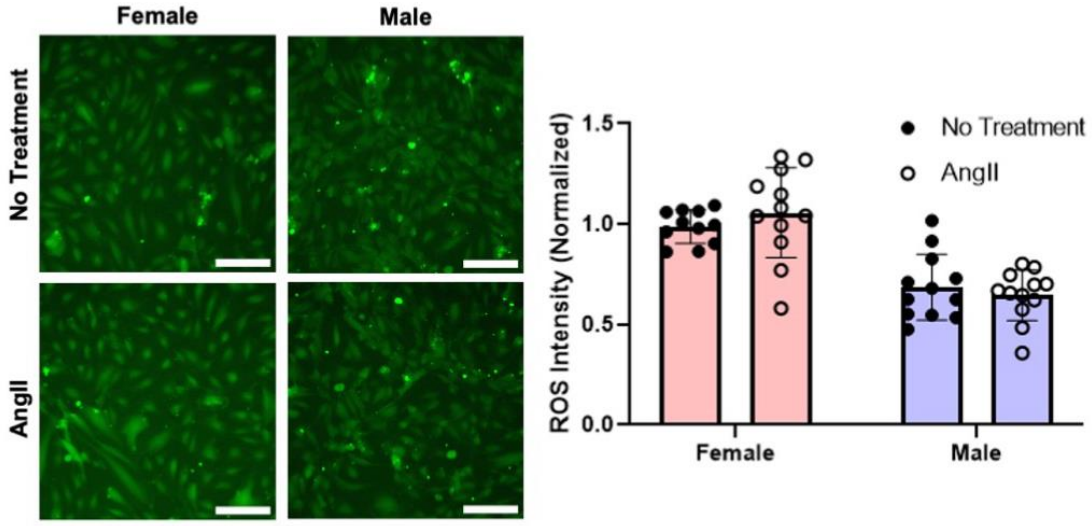


Figure 2.8. Male and female HCAEC did not increase ROS production in response to AngII. Single donor male and female HCEAC were treated with +/- 1 µM AngII for 24 hours, then labeled with carboxy-H_2DCFDA (green). Scale bar = 100 µm. Data analyzed with two-way ANOVA. ROS intensities were normalized to untreated cells for each sex.

2.3.6. Mitochondrial superoxide production, but not mitochondrial metabolic rate, increased in female HUVEC in response to AngII.

I then evaluated if the increase in ROS was due to a rise in superoxide production as a byproduct of mitochondrial metabolism. When I labeled AngII-treated pooled female and male HUVEC with the mitochondrial ROS indicator MitoSOX, I observed that mitochondrial superoxide increased by 19% in the female but not male HUVEC ($p = 0.0017$; Fig. 2.9A). However, while pooled female HUVEC had 17% higher oxygen consumption rate (OCR; oxidative phosphorylation; $p < 0.0001$) and 17% higher mitochondrial ATP production than pooled male HUVEC ($p < 0.0001$) by Seahorse dynamic metabolic measurements, neither OCR nor mitochondrial ATP changed with AngII treatment (Fig. 2.9B-D). Proton leak, defined as respiration that is not coupled to ATP production, was similar across all conditions (Fig. 2.9E). Although female HUVEC had higher mitochondrial metabolism than male HUVEC, this did not appear to relate to the elevated ROS observed in AngII-treated female HUVEC.

2.3.7. CYBB gene expression was elevated in female HUVEC and may be partially responsible for increased ROS production in response to AngII.

I therefore examined an alternative pathway by which ROS production could be elevated in female HUVEC treated with AngII. *CYBB*, the gene for NOX2, escapes from XCI [154]. NOX2 is the catalytic subunit of NADPH oxidase, which produces superoxide when activated and assembled in the cell membrane. RNA-sequencing showed *CYBB* gene expression to be higher in pooled female than male HUVEC, but due to high variability in the data, this was not statistically significant. I therefore repeated gene expression measurements by RT-qPCR and showed that *CYBB* gene expression was 4 times higher in pooled female compared to pooled male HUVEC and in female compared to male HPAEC from one donor ($p < 0.0001$; Fig. 2.10A). I then knocked down *CYBB* via siRNA in pooled HUVEC and confirmed significant NOX2 protein reduction after 24 hours by Western blot ($p = 0.0021$; Fig. 2.10B). Using the more general, cell permeable ROS indicator Carboxy-H_2DCFDA, I again demonstrated elevated ROS in AngII-treated female but not male HUVEC ($p = 0.0098$). However, in HUVEC with NOX2 knocked down, AngII treatment failed to significantly elevate ROS in female or male cells (Fig. 2.10C-D).

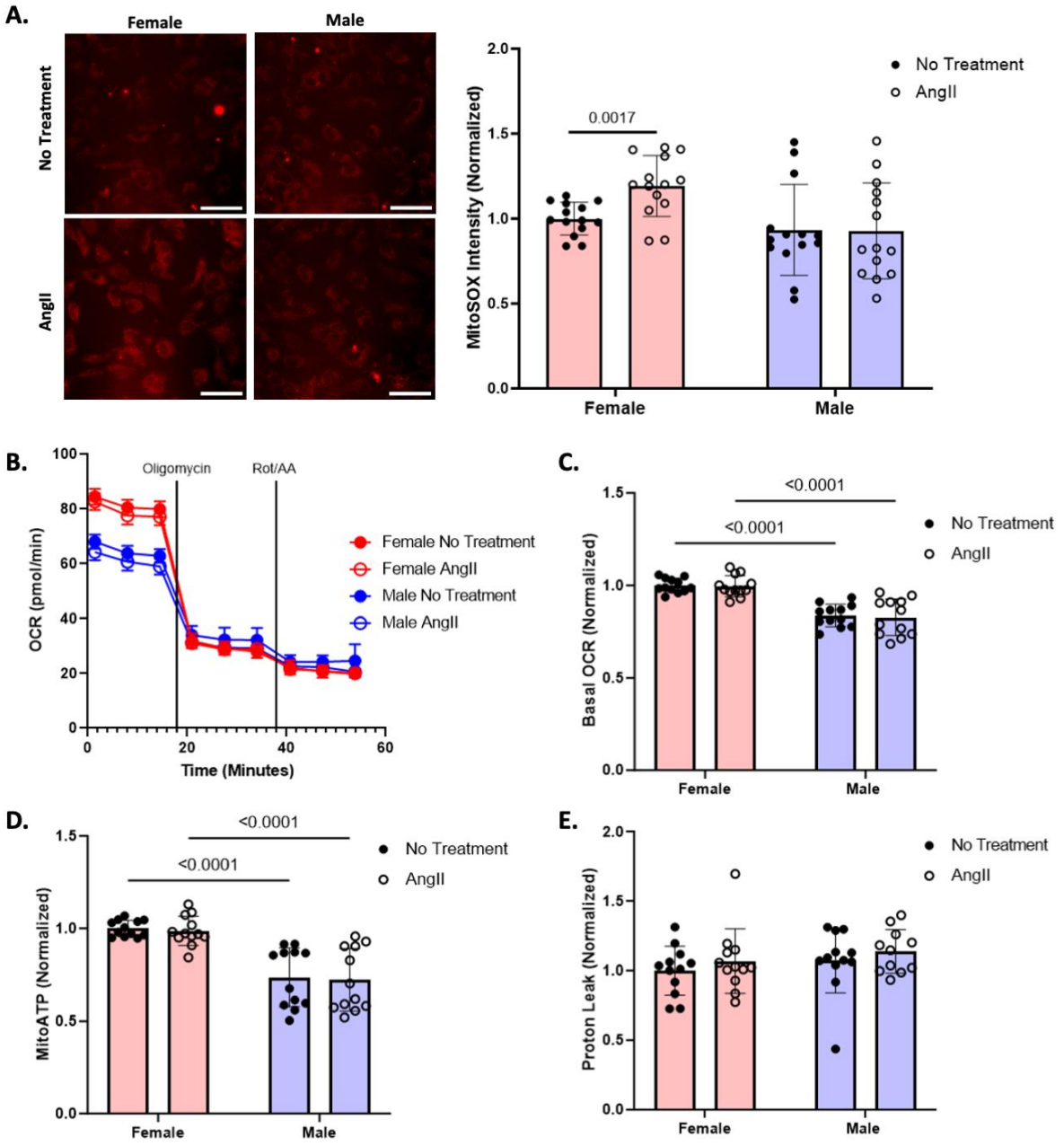


Figure 2.9. Female HUVEC demonstrate increased superoxide in response to AngII compared to male HUVEC. (A) Mitochondrial superoxide production in female versus male HUVEC following 24 hours of AngII treatment measured via MitoSOX (n = 14; 2 experimental repeats, 7 samples per condition from pooled HUVEC). Scale = 100 µm. **(B)** OCR measured by Seahorse ATP Rate assay in male and female HUVEC ±1 µM AngII treatment (n = 12; 2 experimental repeats, 6 samples per condition from pooled HUVEC). **(C)** Basal OCR, **(D)** Mitochondrial ATP production, and **(E)** Proton leak calculated from Seahorse OCR (n = 12; 2 experimental repeats, 6 samples per condition from pooled HUVEC). MitoSOX and seahorse data normalized to the female untreated cells. Data analyzed with two-way ANOVA.

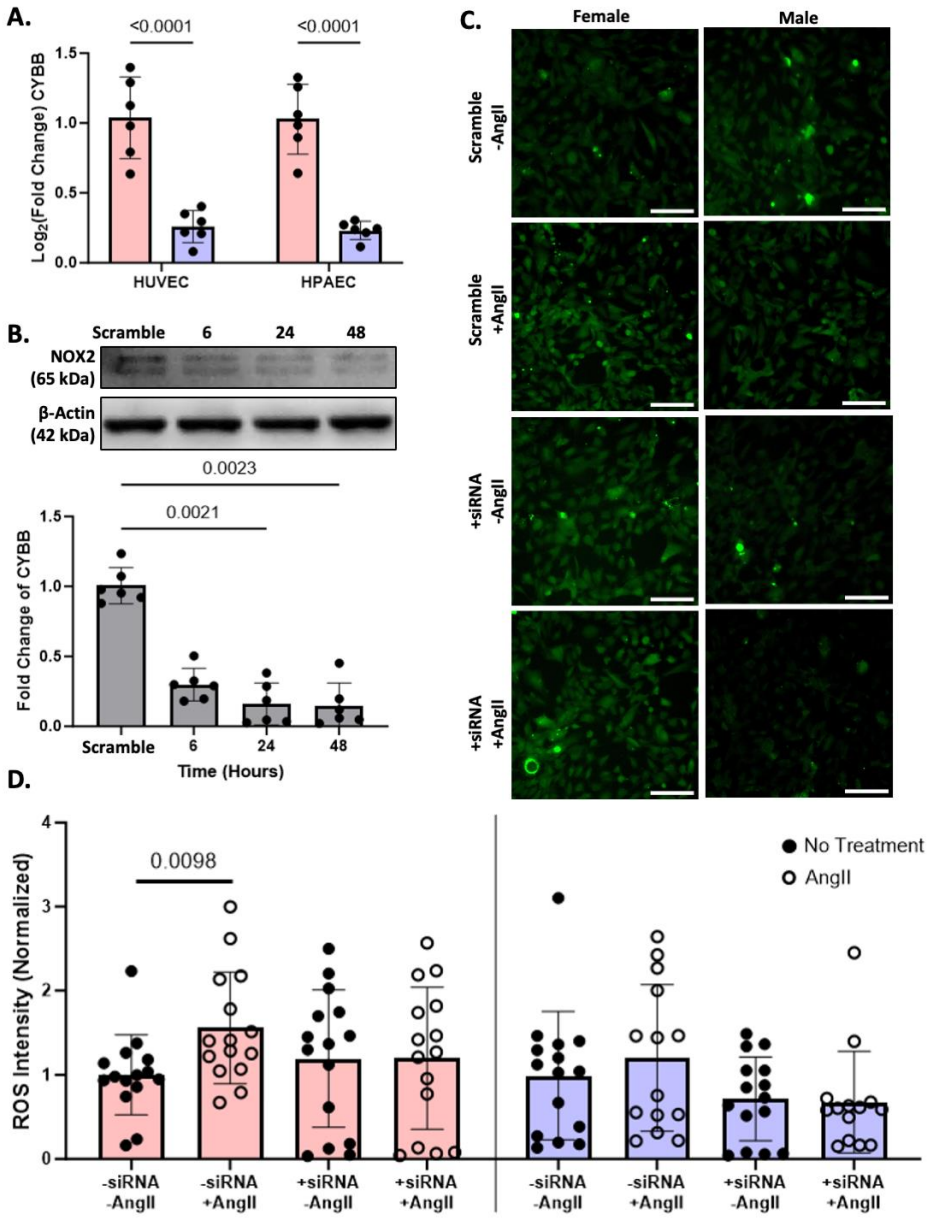


Figure 2.10. CYBB is upregulated in female, but not male EC, which may contribute to elevated ROS production in AngII-treated female cells. (A) *CYBB* gene expression in untreated female and male HUVEC and HPAEC by RT-PCR. Analyzed with a Mann-Whitney test (n =6). **(B)** Western blot of NOX2 and β-Actin, with quantification, in HUVEC treated with scramble siRNA or *CYBB* siRNA for 6-48 hours (n = 6). **(C)** Representative fluorescent microscopy images of carboxy-H_2DCFDA (green) as a ROS indicator in female and male HUVEC following *CYBB* siRNA (or scramble siRNA) and ±1 μM AngII treatment for 24 hours. Scale = 100 μm. **(D)** Quantification of ROS following siRNA knockdown (n = 15). Western blot and ROS intensity were normalized to the untreated female cells.

2.4. Discussion:

Elevated AngII is associated with many sexually dimorphic diseases that disproportionately affect women, including Alzheimer's disease [174], [175]. Since EC have sexually dimorphic transcriptomes [152], I investigated how female and male EC respond differently to AngII. I now show that female EC have more extensive transcriptional changes in response to AngII as compared to male EC. While changes in *TGF-β2* gene expression did not lead to altered EC phenotype *in vitro,* I did observe elevated immune and oxidative stress responses to AngII in female EC as compared to male EC. My study indicates that female EC have a stronger reaction to AngII, which may contribute to higher rates of AngII-related diseases in women.

Most studies of sex differences investigate specifically the impacts of sex hormone (estrogen and testosterone) exposure. However, hormone exposure is not the only differentiating factor between men and women. Phenotypic sex differences between men and women are a combination of the effects of sex chromosomes, genetic variation through copy number variants and single nucleotide polymorphisms, and epigenetic regulation by endogenous factors such as hormones or exogenous factors like environmental exposures [176]. Additionally, through the process of escape from XCI, genes on the second silenced X-chromosome in female cells can be reactivated, essentially doubling their gene expression. In this paper, I examined sex differences in response to AngII in neonatal umbilical vein endothelial cells, which were not exposed to sex hormones. I further validated my findings using adult pulmonary artery endothelial cells to demonstrate that sex differences were maintained regardless of cell age and hormone exposure.

My RNA-sequencing data confirmed prior studies that demonstrated gene expression changes in male and female HUVEC [152]. Indeed, sex differences have been observed in most tissues of the body [101]. A previous study reported 2,528 differentially expressed genes between male and female HUVEC in boy-girl twin pairs [152]; however, an adjusted p-value of <0.1 was considered significant with no required Log_2FC cutoff, whereas I chose a more stringent cutoff of adjusted p-value < 0.3 and $Log_2FC > 0.6$. I now further show that female HUVEC have more differentially expressed genes compared to male HUVEC when treated with AngII. In male HUVEC, none of the differentially expressed genes were in the same KEGG pathway. Female HUVEC, on the other hand, had 25 KEGG pathways with 3 or more differentially expressed genes. Many of the differentially expressed genes were included in multiple KEGG pathways.

For example, thermogenesis, oxidative phosphorylation, and metabolism KEGG pathways had almost entirely overlapping differential gene expression (electron transport chain, specifically cytochrome C reductase, cytochrome C oxidase, NADH dehydrogenase, and F-type ATPase). Seven out of eleven differentially expressed genes associated with the neurodegeneration KEGG pathway also overlapped with oxidative phosphorylation. These synergies suggest that differentially expressed genes in AngII-treated female cells could have wide-reaching cellular effects.

Although TGF-β2 production is known to increase EndMT [177], and female AngII-treated cells showed an increase in *TGF-β2* gene expression, I did not observe an increase in TGF-β2 released from the cells in male or female HUVEC treated with AngII. Generally, TGF-β2 is translated in the endoplasmic reticulum where it dimerizes and binds to latent TGF-β binding proteins (LTBP). The TGF-β2-LTBP complex is secreted, after which activating factors dissociate the complex. Active TGF-β2 then binds to TGF-β receptors on cells [178]. TGF-β2 can be secreted without LTBP [179], although LTBP promotes its folding and secretion [180]. I did not observe increased *LTBP* gene expression in female HUVEC, which could explain why TGF-β2 protein release was not increased in these cells following AngII treatment.

Furthermore, increased *TGF-β2* gene expression in female AngII-treated HUVEC did not induce EndMT, as measured by decreased endothelial markers and increased fibrotic markers. Maleszewska *et al* proposed that elevated IL-1β is necessary for inducing EndMT, while TGF-β2 is essential to sustaining EndMT [171]. *IL-1β* was not differentially expressed in male or female HUVEC following AngII, which could mean that EndMT was not induced. Alternatively, other secondary stimuli such as TNF-α [181] and hydrogen peroxide [182] have been proposed to supplement TGF-β2-related EndMT. Sex differences in valvular interstitial cells were accentuated on soft and stiff hydrogels compared to tissue culture plastic, [183] thus I might have observed functional changes in EndMT on softer substrates. Finally, *TGF-β2* gene expression may take longer to lead to cell functional changes [171], [181], [182], [184]. Although I did not observe cell function changes due to AngII-induced increased *TGF-β2* gene expression in female HUVEC, differences may occur with secondary stimuli, on softer substrates, or at longer times.

I similarly observed increased *IL-6* gene expression in AngII-treated HUVEC with no change in secreted protein or EC inflammatory response. *IL-6* mRNA is relatively unstable, with a 30-minute half-life [185]. *IL-6* mRNA is stabilized by Arid5a [186], and its degradation is accelerated by Regnase-1 (*Zc3h12a)* [187]. Neither *ARID5A* nor *ZC3H12A* were differentially expressed in female EC following AngII treatment; therefore, *IL-6* mRNA may have been too unstable in AngII-treated cells to increase IL-6 protein secretion. TNF-α is an inflammatory stimulus that may increase *IL-6* mRNA stability [188], and in my cells, concurrent AngII and TNF-α treatment increased both IL-6 secretion and WBC adhesion in female HUVEC and HPAEC compared to TNF-α alone. WBC adhere to cell adhesion molecules on EC membranes including intercellular adhesion molecule-1 (ICAM-1), vascular cell adhesion protein-1 (VCAM-1), and E-Selectin. The E-selectin gene was significantly increased in female HUVEC following AngII treatment (Log_2FC = 0.601, p <0.0001). Though *ICAM-1* (Log_2FC = 0.399) and *VCAM-1* (Log_2FC = 0.455) had statistically significant p-values, they did not reach my LogFC threshold for significance but may also be elevated in female HUVEC treated with AngII. Male HUVEC did not increase ICAM-1, VCAM-1, or E-Selectin expression following AngII treatment. Cell adhesion molecule gene upregulation likely contributes to increased WBC adhesion to female, but not male, HUVEC following TNF-α and AngII treatment.

Finally, oxidative phosphorylation genes and ROS increased in female HUVEC treated with AngII, which correlated with elevated mitochondrial superoxide production. Seahorse ATP Rate Assays did not show a corresponding increase in mitochondrial respiration in either female or male HUVEC. Similar to increases in IL-6 following AngII treatment in female HUVEC, it may be that the cells are increasing gene expression of oxidative phosphorylation genes but require a second stimuli to actually increase OCR. I did find that *CYBB*, the gene encoding for NOX2, was overexpressed in female as compared to male cells and when knocked down, abrogated the AngII-induced increase in ROS in female HUVEC. *CYBB* was shown to escape X-chromosome inactivation [154], meaning it was expressed on both X chromosomes in female cells leading to double the gene expression. I similarly observed higher *CYBB* expression in female as compared to male HUVEC and HPAEC, indicating that *CYBB* may escape from X-chromosome inactivation in these cells. Interestingly, *CYBB* knockdown in female HUVEC did not reduce baseline ROS. Thus, NOX2 may be partially responsible for elevated ROS production in female HUVEC treated with AngII.

The HUVEC sex differences were partially replicated in EC from patients who were not neonates. Female HPAEC and HCAEC from donors aged 12-51 demonstrated elevated CYBB gene expression, congruent with my hypothesis that *CYBB* escapes X-chromosome inactivation. However, only female HPAEC had elevated ROS in response to AngII. This could relate to the specific vascular bed. HPAEC dysfunction is associated with pulmonary artery hypertension (PAH) [189], and women are 2-4 times more likely to be diagnosed with PAH compared to men [190]. Indeed, differential gene expression associated with ROS production (including *CYBB*) has been proposed to be partially responsible for these sex differences [191]. Alternatively, age and sex hormone exposure may make sex differences in female EC less pronounced. In another study, ROS production was higher in female vs. male HUVEC at birth, but ROS production was higher in male vs. female human aortic endothelial cells in adults [152]. Additional studies are needed to determine how age and sex hormone exposure may impact female vs. male EC differences.

2.6 Limitations

In this work, sex differences in EC response to AngII were well characterized. However, the EC studied in this work were HUVEC and HPAEC. In AD, brain microvascular endothelial cells (BMEC) are the primary EC of interest; however, procuring primary BMEC from enough donors to study sex differences was not possible for this study. Studies in HUVEC and HPAEC may not apply to all EC beds. Additionally, 1 μM AngII is supraphysiological [192], [193], though large AngII fluctuations occur in disease and may be region-specific [193]. Finally, the EC examined here were grown in static culture on tissue culture polystyrene. Incorporating laminar flow and physiologically relevant growth substrates may alter the results of these experiments.

2.5. Conclusions

Many diseases, including Alzheimer's disease, manifest differently in women than men. Some of these differences may result from cellular transcriptomic differences due to genomic escape from XCI. My data

confirm that female HUVEC are transcriptomically distinct from male HUVEC. I further show that female EC had more extensive transcriptomic, inflammatory, and oxidative stress changes than male EC when exposed to the stress hormone AngII. These data suggest that transcriptomic differences between female and male EC may predispose women to certain vascular diseases by altering the cellular response to a cardiovascular risk factor. Overall, my study supports the examination of sex differences at a cellular level to understand sexual dimorphisms in susceptibility to vascular diseases such as AD. In future chapters, I will examine how other risk factors for AD, including APOE genotype and sedentary lifestyle, lead to endothelial dysfunction. These risk factors will be examined in an induced pluripotent stem cell (iPSC) derived model of BMEC to increase the relevance of the studies to the BBB.

Chapter 3: iPSC-BMEC modeling of brain endothelial cell glucose metabolism

3.1. Introduction

In the previous chapter, I showed that female endothelial cells (EC) increased inflammation and reactive oxygen species (ROS) production when treated with angiotensin II, while male cells did not. In that study, I used human umbilical vein endothelial cells and human pulmonary artery endothelial cells to demonstrate sex differences; however, it is important to use brain microvascular endothelial cells (BMEC) in studies of Alzheimer's disease (AD), since BMEC are distinct from other vascular beds. In this chapter, I evaluated glucose metabolism of induced pluripotent stem cell derived BMEC (hiBMEC) to determine if they can be used as a model for BMEC glucose metabolism since future chapters of this thesis examine how AD risk factors alter BMEC glucose metabolism and function.

Glucose is the primary energy source in the brain [194], [195], and brain glucose hypometabolism has been implicated in neurodegenerative diseases such as AD [196], [197], [198], [199], [200], [201]. Glucose transport into the brain is dynamically regulated by BMEC, which together with pericytes and astrocytes form the neurovascular unit (NVU). BMEC have extensive intercellular tight junctions that block paracellular transport of metabolites such as glucose into the brain, allowing diffusion of only lipophilic compounds with a molecular weight less than 400 Da [202] and less than 8 hydrogen bonds with water [203]. Instead, glucose is transported into the brain transcellularly via glucose transporters such as GLUT1.

Peripheral endothelial cells are thought to rely on glycolysis rather than oxidative phosphorylation for ATP production [204], [205], and as such have a small mitochondrial volume [206]. Elevated glycolytic rates reduce peripheral endothelial cell reliance on oxygen, which may both reduce metabolic stress and enhance lactate signaling as endothelial cells undergo angiogenesis into a hypoxic environment [207], [208], [209]. In contrast, relatively little is known about BMEC metabolism. BMEC likely also use glucose as their primary energy source. However, BMEC may have higher metabolic flexibility, since they maintained viability in the absence of glucose [210], have higher mitochondrial volume than peripheral EC [211], and switched to oxidative phosphorylation of glutamate in hypoglycemia [212]. It is therefore essential to understand how glucose that is taken up by BMEC is metabolized versus transported to the NVU and the rest of the brain.

In vitro blood-brain barrier (BBB) models are an important tool for understanding glucose metabolism and transport since *in vivo* systems are complex and difficult to analyze. Currently, the BBB can be modeled *in vitro* using human primary BMEC (hpBMEC), the immortalized hCMEC/D3 cell line, or hiBMEC. hpBMEC are expensive and difficult to obtain, as their isolation is complicated by low yield, mural cell contamination, and ethical issues. hpBMEC are also prone to donor variability and low barrier integrity [213]. hCMEC/D3 cells were developed to overcome some of the hpBMEC limitations; however, these cells also have low barrier integrity and tight junction protein expression [214]. Previous evaluations of hCMEC/D3 cells show they have similar glycolytic and oxidative metabolism to hpBMEC [215]. hiBMEC offer a renewable BMEC source with high barrier integrity and tight junction protein expression [216]. However, recent studies suggest that these cells retain an epithelial-like transcriptomic profile and may therefore not fully recapture the vascular BMEC phenotype [217], [218].

Little is currently known about glucose metabolism in any of the *in vitro* human BMEC cell lines, and therefore selecting a cell type to use in glucose metabolism and transport studies is challenging. In this study published in *Fluids and Barriers of the CNS*, I compared glucose metabolism between hpBMEC and hiBMEC [219]. I used transcriptomic and metabolomic profiling, together with real-time metabolic analysis, to analyze glucose metabolism in hpBMEC and hiBMEC at baseline and when treated with stimuli known to alter endothelial glucose metabolism. My data show key differences in baseline hpBMEC and hiBMEC glucose metabolic flux and metabolic enzyme expression; however, both cell types had similar baseline glucose metabolomic profiles. I further show that hpBMEC and hiBMEC respond similarly to most of my tested metabolic stimuli. Together, my data suggest that hpBMEC and hiBMEC provide similar results in an *in vitro* model of BMEC glucose metabolism.

3.2. Methods

3.2.1. hiBMEC Differentiation: hiBMEC were differentiated using previously established protocols [216]. IMR90 iPSC [220], a generous gift from Dr. Xiaoming He, were maintained in mTeSR-Plus medium (STEMCELL Technologies, 100-0276) on Matrigel (Corning, 354230) and passaged using Versene (Thermo Fisher, 15040066) at 70% confluence. For differentiation, cells at 70% confluence were detached using Accutase (Thermo Fisher, A1110501) and seeded at 150,000 cells/well on Matrigel-coated plates in

mTESR-Plus medium containing 10 µM Y-27632 (ROCK inhibitor; Tocris, 1254). Over the subsequent 4 days, medium was changed to E6 (STEMCELL Technologies, 05946) and replaced daily. On day 4, cells were changed to either human endothelial serum free media (hESFM; Thermo Fisher, 11111044) or neurobasal medium (Thermo Fisher, 21103049) supplemented with 2% B27 (Thermo Fisher, 17504001), 20 ng/mL basic fibroblast growth factor (bFGF; Peprotech, 100-18B), and 10 µM retinoic acid (RA; Millipore Sigma, R2625-50MG). Media was not changed on day 5. On day 6, the cells were subcultured at 1 x 10^6 cells/cm^2 onto extracellular matrix (ECM) containing 0.4 mg/mL collagen IV (Millipore Sigma, C7521) and 0.1 mg/mL fibronectin (Millipore Sigma, F2006) on 0.4 µm pore Transwell filters (Corning, 3460) or 12-well plates (CELLTREAT, 229112).

3.2.2. hpBMEC Culture: hpBMEC were purchased from Cell Systems (ACBRI 376 V) and only used up to passage 9, since higher passages are associated with decreased proliferation which could alter cell metabolism [221], [222]. Cells were maintained in Endothelial Growth Medium-2 MicroVascular (EGM-2 MV; Lonza, CC-4147) supplemented with 1% glutamine (Thermo Fisher, 25-030-081), 1% penicillin streptomycin (Thermo Fisher, 15140163), and 10% fetal bovine serum (FBS; Cytiva, SH30088.03). For experiments, cells were seeded on 0.4 µm pore Transwell filters or 12-well plates coated with ECM as previously described.

3.2.3. Astrocyte Culture: Primary human astrocytes were a generous gift from Dr. Silvia Muro and used through passage 9. Astrocytes were maintained in Dulbecco's Modified Eagle Medium (DMEM; Thermo Fisher, A1443001) supplemented with 5.5 mM glucose, 15% FBS, 1% penicillin streptomycin, and 1% glutamine. Conditioned media was collected from confluent astrocytes after 24 hours, aliquoted, and frozen at -20°C until use.

3.2.4. TEER: To measure transendothelial electrical resistance (TEER), BMEC were subcultured onto 0.4 µm ECM-coated Transwell filters in hESFM with 2% B27, 20 ng/mL bFGF, and 10 µM RA. Every day post-subculture, TEER was measured in triplicate using STX2-Plus electrodes and the Epithelial Volt/Ohm Meter 3 (EVOM3; World Precision Instruments).

3.2.5. YSI: Media metabolite concentrations were measured using a YSI 2950 Bioanalyzer (Yellow Springs Instruments, 527690). BMEC were subcultured onto 12-well plates in hESFM with 2% B27, 20 ng/mL bFGF, and 10 μM RA. The next day, media was changed to DMEM supplemented with 4.5 mM glutamine, 2% B27, and either 5.5 mM glucose (no treatment), 25 mM glucose, 20% astrocyte conditioned media or 500 nM fluvastatin (Millipore Sigma, SML0038-10MG; Fig. 3.1). 200 μL media samples were taken from each well of the 12-well plates. Glucose, lactate, glutamine, and glutamate concentrations were then quantified using the YSI.

3.2.6. Seahorse Assays: BMEC glycolysis was measured using the Seahorse Glycolytic Rate Assay (Agilent, 103344-100), and oxidative respiration was measured using the Seahorse Mito Stress Test (Agilent, 103015-100). hiBMEC were subcultured at 100,000 cells/well in a 96-well Seahorse Assay plate in hESFM supplemented with 2% B27, 20 ng/mL bFGF, and 10 μM RA. The next day, media was replaced with hESFM supplemented with only B27. hpBMEC were seeded in the Seahorse Assay plate at 10,000 cells/well in EGM-2 MV and cultured for 48 hours. Three days after seeding, all cells were switched to DMEM supplemented with 5.5 mM glucose, 4.5 mM glutamine, and 2% B27. On the day of the assay, media was changed to Seahorse DMEM (Agilent, 103680-100) supplemented with 5.5 mM glucose, 1 mM pyruvate, and 4.5 mM glutamine for 1 hour. For the Glycolytic Rate Assay, rotenone + antimycin A (0.5 μM) and 2 deoxyglucose (50 mM) were added to the drug loading cartridge. For the Mito Stress Test, oligomycin (1.5 μM), FCCP (0.5 μM), and rotenone + antimycin A (0.5 μM) were added to the drug loading cartridge. Glycolytic proton efflux rate (GlycoPER, glycolysis) and oxygen consumption rate (OCR, oxidative respiration) were measured using a Seahorse XF96 (Agilent) and analyzed using Seahorse analytics software.

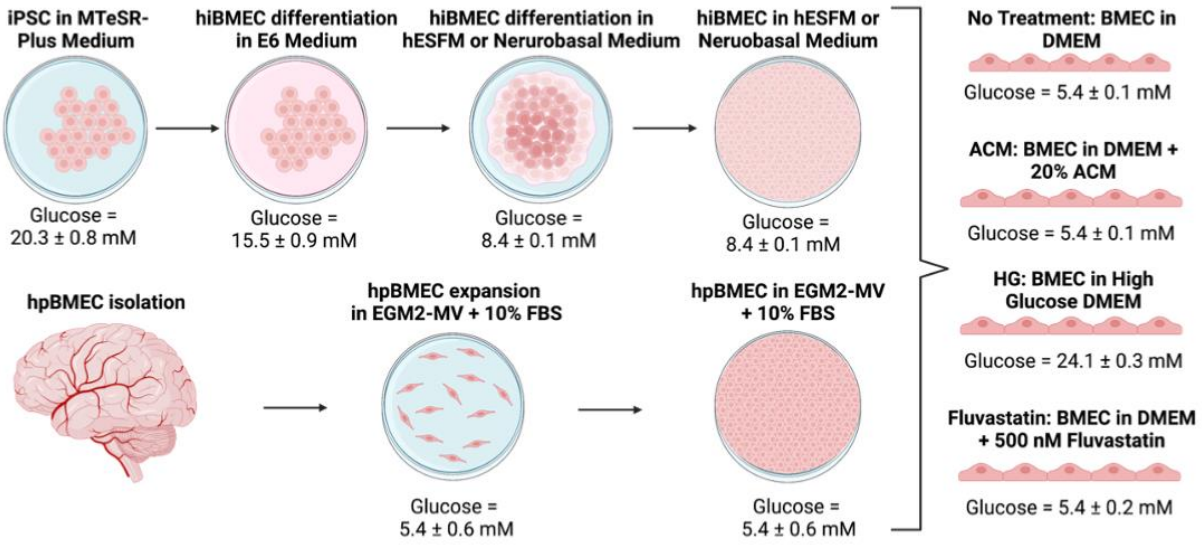


Figure 3.1. Glucose concentrations in cell culture conditions. Glucose concentrations were measured via YSI at each step of the hiBMEC differentiation process, in hpBMEC culture, and in each treatment media. Concentrations are reported as mean ± standard deviation. n = 12 biological replicates.

3.2.7. Immunofluorescence Microscopy: For immunofluorescence, BMEC were subcultured on glass coverslips. Cells were fixed in 4% paraformaldehyde (PFA; Millipore Sigma, P6148) for 20 minutes, after which they were blocked and permeabilized in 5% normal goat serum (Millipore Sigma, S26) with 0.2% TritonX-100 (Alfa Aesar, A16046) in phosphate buffered saline (PBS; Thermo Fisher, 70011069) for 1 hour. Cells were incubated in primary antibodies for GLUT-1 (Thermo Fisher, 21829-1-AP, 1:100), zonula occludins-1 (ZO-1; Cell Signaling Technology, 13663S, 1:100), and occludin (Cell Signaling Technology, 91131S, 1:100) overnight at 4°C. Cells were then incubated in a goat-anti-rabbit secondary antibody (Thermo Fisher, A-11012, 1:1000) with Hoechst (Thermo Fisher, 62249, 1:2000) for 1 hour. Samples were imaged using an Eclipse Ti2 spinning disk confocal microscope (Nikon) with a 60x objective.

3.2.8. RNA-Sequencing: hiBMEC RNA was isolated using a phenol/chloroform isolation protocol [223] and quantified using a Nanodrop 2000c (Thermo Fisher). RNA was sequenced at Novogene (Sacramento, CA) using a NovaSeq 6000 with 105-bp paired end reads. Reads were trimmed and mapped to the human genome and converted to fragments per kilobase of transcript per million mapped reads (FPKM) using

Galaxy open-source software. RNA sequencing data from hpBMEC was accessed using publicly available data [217], [224], [225].

3.2.9. Western Blots: hiBMEC and hpBMEC were grown to confluence in their respective media and then changed to DMEM supplemented with 5.5 mM glucose, 4.5 mM glutamine, and 2% B27 for 24 hours. After treatment, cells were lysed in RIPA buffer (Thermo Fisher, 89901) supplemented with Halt Protease and Phosphatase Inhibitor (Fisher Scientific, PI78440), and protein was quantified via BCA assay (Thermo Fisher, 23225). 3.5 µg/µL protein, 7.5 µL sample buffer (Thermo Fisher, NP0008) and 3 µL reducing agent (Thermo Fisher, NP0009) were combined, heated to 37°C (GLUT1) or 70°C (all other proteins) for 5 minutes, then loaded in 4-12% Bis-Tris gels (Thermo Fisher; NP0323). Samples were transferred to nitrocellulose or polyvinylidene fluoride membranes (Thermo Fisher, IB23001 and IB24001) using an iBlot2 (Thermo Fisher, IBL21001), blocked for 1 hour in 5% bovine serum albumin (Millipore Sigma, 126609) in PBS containing 0.5% Tween 20 (Thermo Fisher, 85113), and incubated in primary antibodies (Table 3.1) overnight. The next day, membranes were incubated for 2 hours in the respective secondary antibody (Table 3.1) and imaged using an Alpha Innotech Fluorchem Imager (Protein Simple). Band intensities were analyzed using AlphaView software.

3.2.10. Metabolic Mass Spectrometry: Both hiBMEC and hpBMEC were cultured for 24 hours in serum-free DMEM (Thermo Fisher, A1443001) supplemented with 2% B27, 200 mM L-glutamine, and 5.5 mM U-$^{13}C_6$-glucose (Fisher Scientific, NC9207695). The medium was then removed, and 80:20 methanol:water (extraction solvent) was added to cells for 15 min at −80°C. Cells were scraped in the extraction solvent, after which cell lysates were centrifuged at 16,000 g for 10 min at 4°C to pellet debris. Cell metabolite extracts and media samples were then shipped to the University of Colorado School of Medicine Metabolomics Core. Samples were randomized and 8 µL was injected onto a Q Exactive mass spectrometer (MS) by a Vanquish ultra-high performance liquid chromatograph (UHPLC; Thermo Fisher, San Jose, CA, USA) as described previously [226]. Electrospray ionization was used to introduce eluent to the MS, which scanned in full MS mode (2 µscans) over 65-950 m/z. Technical mixes were injected approximately every ten samples to determine instrument stability [227]. Metabolites were manually annotated and integrated with Maven (Princeton University) in conjunction with the KEGG database. Peak

quality was determined using blanks, technical mixes, and ^{13}C natural abundance [228]. Isotope labeling was corrected using the IsoCor Python package [229]. Metabolite pool size was analyzed using Metaboanalyst 5.0 [230].

3.2.11. Statistics: Statistics were analyzed in GraphPad Prism. Non-parametric Mann-Whitney tests were used to compare datasets, and data were considered biologically significant if $p < 0.05$ and $Log_2FC > 0.6$. RNA-sequencing fold change was considered biologically significant with $Log_2FC > 0.6$. Significance of metabolomics data was corrected using the Benjamini-Hochberg correction and was considered biologically significant if $Log_2FC > 2.32$.

Table 3.1: Western blot antibodies.

Antibody Name	**Company**	**Catalog Number**
GLUT1	Thermo Fisher	21829-1-AP
HXK I	Santa Cruz Biotechnology	sc-46695
HXK II	Santa Cruz Biotechnology	sc-374091
GPI	Santa Cruz Biotechnology	sc-365066
PFKFB3	Cell Signaling Technology	13123S
PFK1	Santa Cruz Biotechnology	sc-166722
AldoA	Santa Cruz Biotechnology	sc-390733
GAPDH	Cell Signaling Technology	2118S
PGK	Santa Cruz Biotechnology	sc-48342
PGM-1	Santa Cruz Biotechnology	sc-373796
a-Enolase	Santa Cruz Biotechnology	sc-100812
PKM	Santa Cruz Biotechnology	sc-365684
LDH	Santa Cruz Biotechnology	sc-133123
CPT1A	Cell Signaling Technology	12252S
CPT1B	ABCAM	ab134135
Citrate Synthetase	ABCAM	ab96600
IDH1	Cell Signaling Technology	8137S

IDH2	Millipore Sigma	HPA007831
B-Actin	Santa Cruz Biotechnology	sc-47778
Anti-mouse IgG (H+L), HRP Conjugate	Promega	W4021
Anti-rabbit IgG (H+L), HRP Conjugate	Promega	W4011

3.3. Results

hiBMEC are increasingly used as a human *in vitro* BBB model for drug delivery and disease modeling [231], [232]. As brain glucose hypometabolism is a common indicator of neurodegenerative diseases, BMEC could be used to study glucose transport across the BBB *in vitro*. Since glucose is metabolized as well as transported by BMEC, in this chapter I compared hiBMEC and hpBMEC glucose metabolism.

3.3.1. hiBMEC had higher barrier function but lower glycolytic rate relative to hpBMEC.

I first confirmed the glucose transporter and barrier proteins of hpBMEC and hiBMEC using immunofluorescent imaging for GLUT1 and tight junction proteins ZO1 and occludin (Fig. 3.2A). TEER was then used to analyze hpBMEC and hiBMEC barrier function. hiBMEC had a higher maximum TEER (5555 $\Omega \times cm^2$) compared to hpBMEC (283 $\Omega \times cm^2$; $p < 0.0001$; Fig. 3.2B), which is similar to previously reported values [213], [216], [233], [234], [235].

I next measured BMEC glucose metabolism via glycolysis and oxidative respiration. hpBMEC took up more glucose (2.64 mM vs. 1.41 mM; $p = 0.002$) and produced more lactate (4.75 mM vs. 2.19 mM; $p = 0.002$) compared to hiBMEC (Fig. 3.2C). However, the lactate:glucose ratio (~1.6 $\pm$ 0.2) was similar between hpBMEC and hiBMEC, indicating that in both cell types, a similar proportion of glucose was metabolized via glycolysis. Similarly, hpBMEC demonstrated higher basal GlycoPER (glycolysis; 16.80 vs. 1.65 pmol/min/1000 cells; $p < 0.0001$) and OCR (oxidative respiration; 13.07 vs. 5.52 pmol/min/1000 cells; $p < 0.0001$) compared to hiBMEC (Fig. 3.2D-E). Both cell types responded similarly to metabolic manipulation, including oligomycin (inhibits mitochondrial ATP synthase), FCCP (depolarizes mitochondrial membrane potential to maximize mitochondrial respiration), and rotenone/antimycin (shuts down mitochondrial respiration). Both cell types also produced more ATP from glycolysis than from oxidative respiration (Fig. 3.3A-B). However, hpBMEC had higher glycolytic capacity (366%; $p < 0.0001$), maximal

respiration (363%; $p < 0.0001$), proton leak (505%; $p < 0.0001$), spare capacity (528%; $p < 0.0001$), and ATP-linked respiration than hiBMEC (243%; $p < 0.0001$; Fig. 3.3C-G).

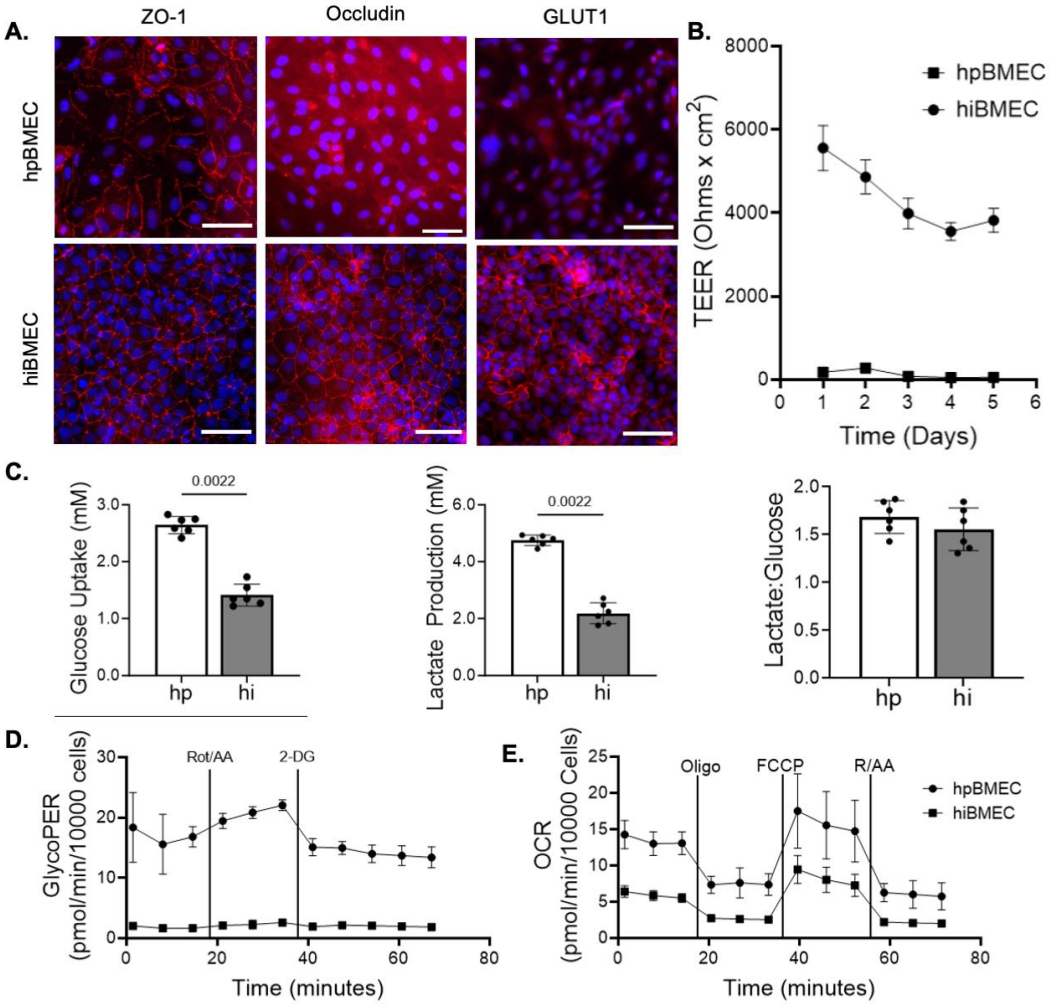


Figure 3.2. hpBMEC had higher glycolytic and oxidative glucose metabolism than hiBMEC, but similar proportions of glycolytic metabolism. (A) Representative confocal images of GLUT1, ZO-1, occludin (all red), and hoechst (nuclei, blue) in hpBMEC and hiBMEC. Scale bar = 100 µm. **(B)** TEER of hpBMEC and hiBMEC measured on confluent monolayers on 0.4 µm pore Transwell filters. **(C)** Glucose uptake, lactate production, and lactate:glucose ratio in hpBMEC and hiBMEC cultured in 5.5 mM glucose over 24 hours, as measured by YSI. **(D)** GlycoPER (glycolysis) and OCR (oxidative respiration) in hpBMEC vs. hiBMEC measured via Seahorse assays, normalized to cell count. n = 6 biological replicates; Data analyzed using a Mann-Whitney test.

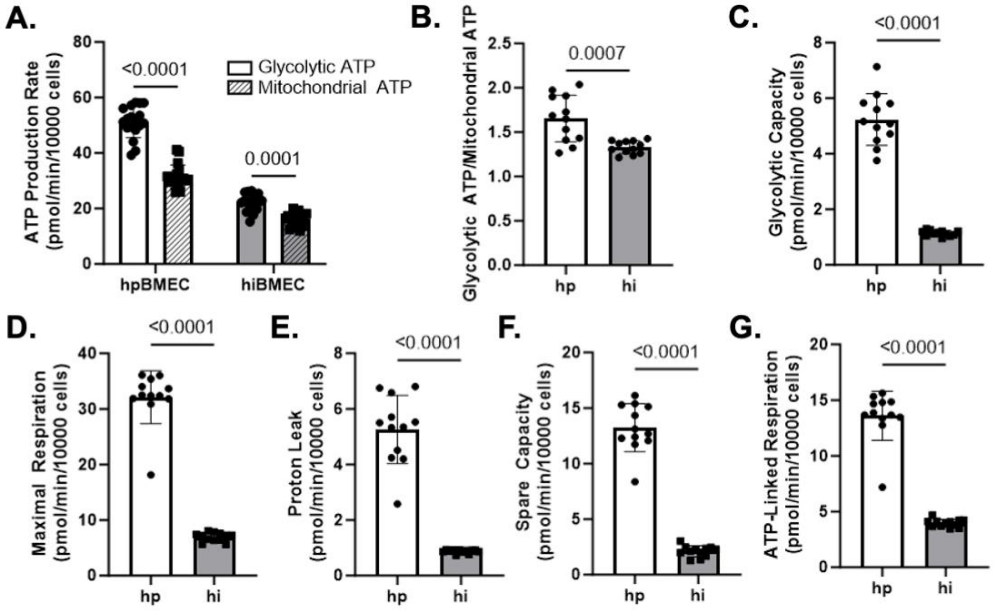


Figure 3.3. hpBMEC had elevated glycolytic and mitochondrial metabolism relative to hiBMEC. (A) ATP Production rate measured via Seahorse ATP Rate Assay in hpBMEC and hiBMEC. **(B)** Quantification of the ratio of glycolytic:mitochondrial ATP production in hpBMEC and hiBMEC. **(C)** Glycolytic capacity quantified via Seahorse Glycolyitic Rate assay**. (D)** measurements of maximal respiration, **(E)** proton leak **(F)** spare capacity, and **(G)** ATP-linked respiration in hpBMEC and hiBMEC quantified using a Seahorse Mito Stress Test. All data are normalized to cell count. n = 12 biological replicates, data analyzed using a Mann-Whitney test.

3.3.2. hpBMEC and hiBMEC metabolomic profiles differed primarily in acylcarnetines

To analyze global similarities and differences in hpBMEC and hiBMEC intracellular metabolites, I labeled cells with uniformly labeled glucose and then examined metabolite pool sizes as well as fractional enrichment patterns with LC-MS. I first used principal component analysis (PCA) to determine whether the hpBMEC and hiBMEC total metabolite pools segregated independently of labeling. hpBMEC and hiBMEC metabolomes separated along both components (Fig. 3.4A, PC1 = 38%, PC2 = 21.4%), indicating key metabolomic differences between the two cell types. Of the 150 metabolites detected, 12 were statistically significantly different and the differences were of biologically relevant scale ($Log_2FC > 2.32$) between hpBMEC and hiBMEC (Fig. 3.4B). Two of these metabolites, argininosuccinate ($Log_2FC = 19.98$ and $p < 0.0001$) and cystathione ($Log_2FC = 17.64$ and $p < 0.0001$), were detected in hiBMEC but not in hpBMEC. Of the remaining metabolites, there were four acylcarnitines, two representatives from nucleotide metabolism and two from glutathione homeostasis, and one each from arginine/proline metabolism and glycolysis. The sole glycolytic metabolite was a phosphohexose glycolytic intermediate (such as glucose-

6-phosphate, glucose-1-phosphate, and/or fructose-6-phosphate); however, its exact identity could not be deciphered due to overlap of signal among these compounds.

Partial-least squares discriminant analysis (PLS-DA), a supervised technique that maximizes variance between classes, was then used to identify variables that drove the glucose metabolic differences between hpBMEC and hiBMEC. Nineteen metabolites had variable importance in projection (VIP) scores greater than 1.5 (Fig. 3.4C); however, none of these metabolites is primarily involved in glycolytic, glycolytic side branch, or TCA cycle pathways. Finally, I used heat maps and hypergeometric analysis to identify statistically significant changes in metabolic pathways (Fig. 3.4D, Appendix Table 4). Metabolite pool sizes were overall similar between the cell types. Twelve metabolic pathways had at least one metabolite that was statistically different between the hpBMEC and hiBMEC; however, I found statistically significant changes only in acylcarnitine ($p = 0.014$) and urea cycle ($p = 0.0245$) pathways.

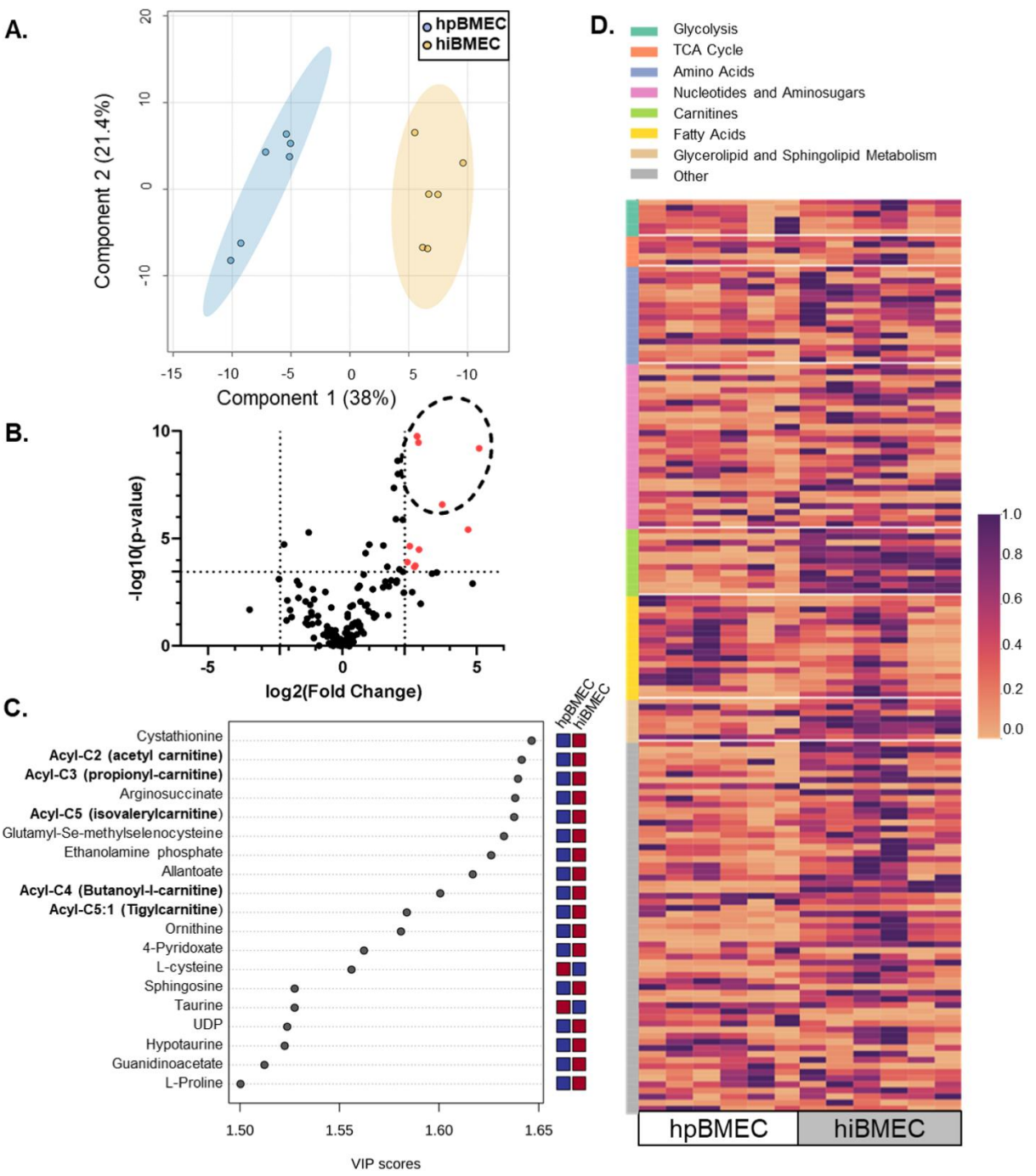


Figure 3.4. Metabolomic abundance profiling showed hpBMEC and hiBMEC had distinct metabolomes, largely driven by changed in acyl-carnitines. (A) Partial least squares discriminant analysis (PLS-DA) of metabolic LC-MS data from hpBMEC and hiBMEC cultured with 5.5 mM U-$^{13}C_6$-glucose for 24 hours. (B) Log2(fold change) versus -log10(p-value), identifying metabolites that are statistically significantly different following Bonferroni correction ($p < 0.0003$) and biologically relevant (fold change > 5). Acyl-carnitines are circled. Plot generated in MetaboAnalyst 5.0. (C) Variable importance in projection (VIP) scores plot, showing metabolites with VIP scores greater than 1.50. Red box = higher and blue box = lower in each cell type. Generated in MetaboAnalyst 5.0. (D) Metabolomic heat map, organized by metabolomic subsystem. n = 6 biological replicates.

3.3.3. Glycolytic enzymes, but not labeled metabolite fractions, differed between hpBMEC and hiBMEC.

Since metabolism is partially driven by glucose transporter and glycolytic enzyme levels, I used RNA sequencing and Western blots to determine differences between hpBMEC and hiBMEC. Glucose transporter GLUT1 was upregulated in hiBMEC compared to hpBMEC ($Log_2FC > 0.6$; Fig. 3.5A). Glycolytic enzymes hexokinase 2 (HK2), glutamine-fructose-6-phosphate transaminase (GFAT), phosphofructokinase, liver (PFKL), phosphofructokinase, muscle (PFKM), phosphoglucomutase (PGM), and lactate dehydrogenase B (LDHB) were also upregulated in the hiBMEC compared to hpBMEC ($Log_2FC > 0.6$). However, hexokinase 1 (HK1), 6-phosphofructo-2-kinase/fructose-2,6-biphosphatase 3 (PFKFB3), phosphofructokinase, platelet (PFKP), and lactate dehydrogenase A (LDHA) were downregulated in hiBMEC compared to hpBMEC ($Log_2FC > 0.6$; Fig. 3.5A). All other enzymes were similar for hiBMEC and hpBMEC. Protein levels overall agreed with the RNA data, although protein changes for G6PDH, GPI, ALDOA, PGK, and PKM reached statistical significance ($p < 0.05$ and $Log_2FC > 0.6$; Fig. 4B, C) while RNA changes did not. GLUT1, HK1 and PGM, which were statistically significantly different in the RNA data, did not significantly change in the protein analysis. Western blots for PFK1 and LDH used non-isoform-specific antibodies and showed that despite differences in RNA expression for the different isoforms, PFK1 protein overall was higher ($p = 0.0012$) while LDH protein overall was lower in hiBMEC compared to hpBMEC ($p < 0.0001$). Only PFKFB3 disagreed between the RNA and protein data, with PFKFB3 RNA lower in hiBMEC ($Log_2FC = -1.37$) and PFKFB3 protein higher in hiBMEC ($Log_2FC = 1.51$; $p < 0.0001$). Overall, glycolytic enzyme RNA and protein levels showed mixed differences between hiBMEC and hpBMEC. Isotope labeling with U-$^{13}C_6$-glucose revealed no significant differences in the labeled enrichment of intracellular glycolytic (Fig. 3.5D) or glycolytic side branch pathway metabolites (Fig. 3.5E) in hpBMEC and hiBMEC.

3.3.4. Mitochondrial metabolic enzymes, but not labeled metabolite fractions, differed between hpBMEC and hiBMEC.

Metabolite pool size data suggested that hpBMEC and hiBMEC had large differences in acyl carnitines, which are important in mitochondrial metabolism. I therefore examined enzymes involved in mitochondrial metabolism, specifically the TCA cycle and fatty acid oxidation (FAO), by RNA sequencing and Western blot. From the RNA sequencing, 12 enzymes associated with the TCA cycle and FAO were upregulated

and 6 were downregulated in hiBMEC compared to hpBMEC (Fig. 3.6A). Two isoforms of the rate-limiting TCA cycle enzyme, isocitrate dehydrogenase 1 and 2 (IDH1, IDH2) were upregulated in hiBMEC as compared to hpBMEC (Log_2FC = 1.66 for IDH1; Log_2FC = 0.67 for IDH1), while IDH3A was downregulated (Log_2FC = -0.84). Carnitine palmitoyltransferase 1A and 1B (CPT1A, CPT1B) are rate limiting FAO enzymes responsible for fatty acid transport from the cytoplasm through the outer mitochondrial membrane. CPT1A gene expression was downregulated in hiBMEC as compared to hpBMEC (Log_2FC = -5.83), while CPT1B gene expression was upregulated in hiBMEC (Log_2FC = 8.44). RNA expression of CPT2, which is responsible for fatty acid transport through the inner mitochondrial membrane, was upregulated in hiBMEC as compared to hpBMEC (Log_2FC = 0.96). Protein levels also largely followed the RNA expression (Fig. 3.6B, C), although CPT1B protein levels were lower while RNA expression was higher in hiBMEC as compared to hpBMEC (Log_2FC = -1.06, $p = 0.0019$). Despite these changes in TCA cycle and FAO enzymes, isotopomer analysis of cells labeled with U-$^{13}C_6$-glucose revealed no significant differences in the glucose labeled fraction of TCA metabolites (Fig. 3.6D).

3.3.5. hpBMEC and hiBMEC metabolism responded similarly to extracellular stimuli.

Finally, I determined if hpBMEC and hiBMEC had similar glucose metabolic responses to external stimuli. Cells were treated for 24 hours with 20% astrocyte conditioned media (ACM), high glucose media (25 mM), or 500 nM fluvastatin, after which metabolism was measured with YSI and Seahorse Mito Stress Test. hpBMEC treated with 20% ACM increased glucose uptake (2.22 mM vs. 4.89 mM; $p < 0.0001$) and lactate production (7.67 mM vs. 5.05 mM; $p < 0.0001$), but the hiBMEC did not (Fig. 3.7A). ACM increased GlycoPER in both hpBMEC (14%; $p = 0.0065$) and hiBMEC (33%; $p < 0.0001$), while ACM decreased OCR in the hiBMEC only (29%; $p < 0.0001$; Fig. 3.7B-C). High glucose increased glucose uptake (2.22 mM vs. 4.42 mM; $p = 0.0032$) and lactate production (7.13 mM vs. 5.05 mM; $p = 0.0009$) in both hpBMEC and hiBMEC (Fig. 3.7D). High glucose also significantly increased GlycoPER (11%, $p < 0.0001$ in hpBMEC; 9%, $p = 0.0001$ in hiBMEC) and decreased OCR (32%, $p = 0.0003$) in hpBMEC; 42%, $p < 0.0001$ in hiBMEC; Fig. 3.7E). Finally, I treated BMEC with a statin since statins have been shown to impair cellular glucose uptake in addition to inhibiting HMG-CoA reductase [236]. Fluvastatin decreased glucose uptake (2.22 mM vs. 1.71 mM; $p = 0.0104$) and lactate production (5.05 mM vs. 3.05 mM; $p < 0.0001$) in hpBMEC

but not in hiBMEC, and GlycoPER similarly decreased in hpBMEC (16%; $p < 0.0001$) but not in hiBMEC. OCR was unaffected in both cell types by fluvastatin treatment.

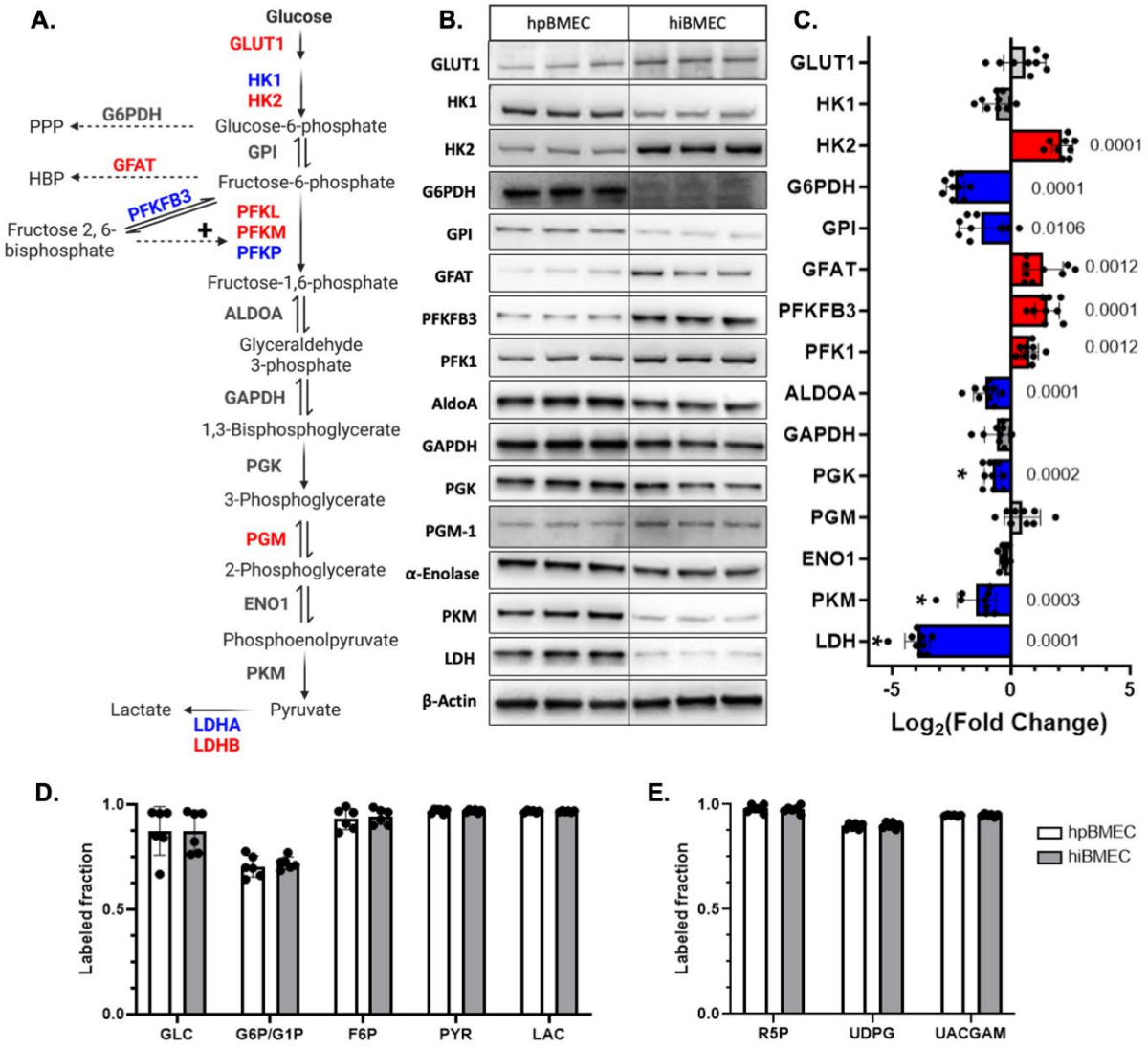


Figure 3.5. hpBMEC and hiBMEC showed differences in glycolytic enzyme gene and protein levels, but similar U-13C6-glucose labeled metabolite fractions. (A) Glucose transporter, glycolysis, and glycolysis side branch pathway enzyme gene expression, measured by RNA sequencing. Red = higher in hiBMEC, blue = higher in hpBMEC (LogFC > 0.6). n = 3 biological replicates**. (B-C)** Western blots with quantification of glucose transporter and glycolytic enzyme protein levels from hpBMEC and hiBMEC. Red = higher in hiBMEC, blue = higher in hpBMEC (significant with $p<0.05$, LogFC>0.6). Blots shown are representative of three separate experiments. n = 9 biological replicates. Glucose labeled fraction of **(D)** glycolytic and **(E)** glycolytic side branch pathway metabolites in hpBMEC and hiBMEC incubated with U-$^{13}C_6$-glucose for 24 hours and then analyzed by LC-MS. n = 6 biological replicates. Data were analyzed using a Mann-Whitney test and considered significant with $p <0.05$ and LogFC >0.6.

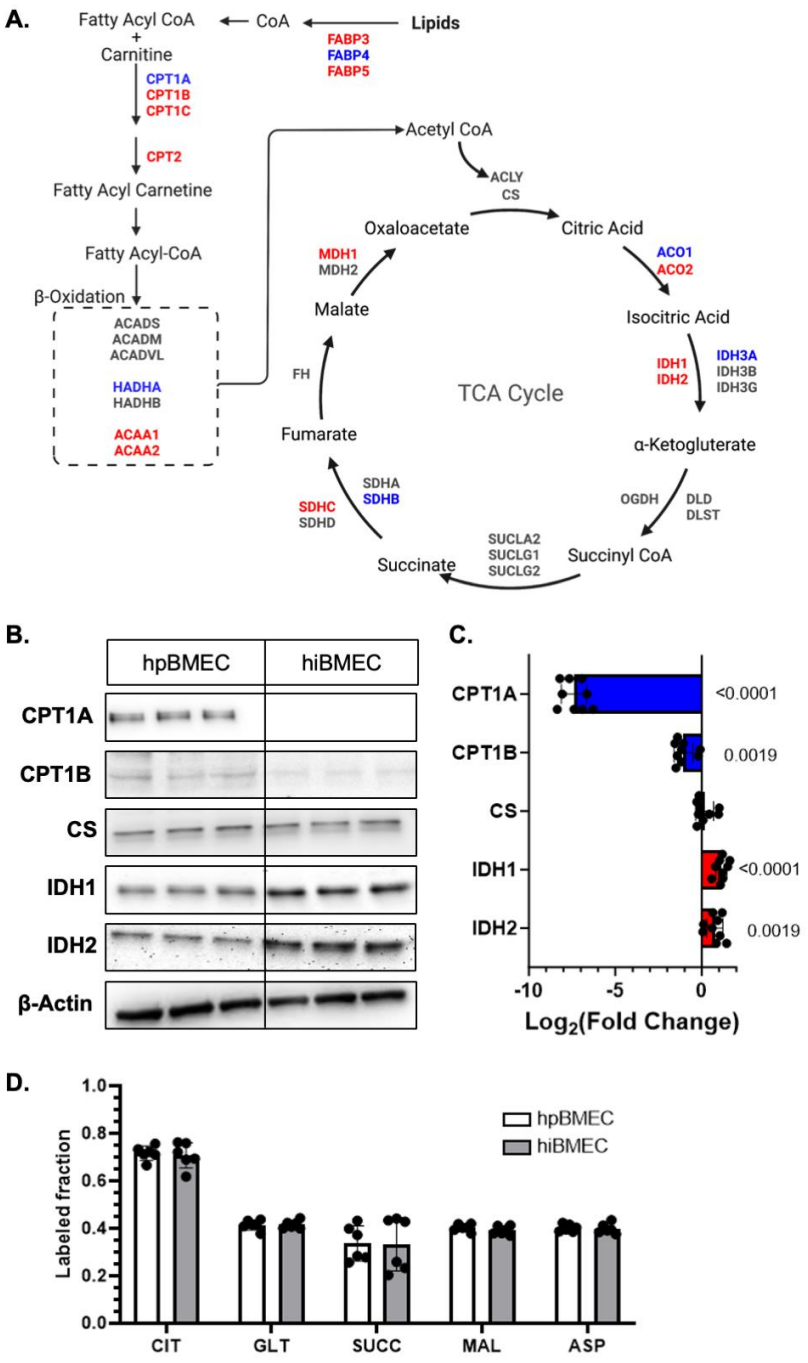


Figure 3.6. hpBMEC and hiBMEC had different TCA and FAO gene and protein levels, but similar U-13C6-glucose labeled metabolite fractions. (A). TCA cycle and FAO enzyme expression, measured by RNA sequencing. Red = higher in hiBMEC, blue = higher in hpBMEC (LogFC>0.6). n = 3 biological replicates. **(B-C)** TCA cycle and FAO enzyme protein levels, measured by Western blot. Red = higher in hiBMEC, blue = higher in hpBMEC (significant with $p < 0.05$, LogFC > 0.6). Blots shown are representative of three separate experiments. n = 9 biological replicates. **(D)** Glucose labeled fraction of TCA metabolites in hpBMEC and hiBMEC incubated with U-$^{13}C_6$-glucose for 24 hours and then analyzed by LC-MS. n = 6 biological replicates. Data were analyzed using a Mann-Whitney test and considered significant with $p < 0.05$ and LogFC >0.6.

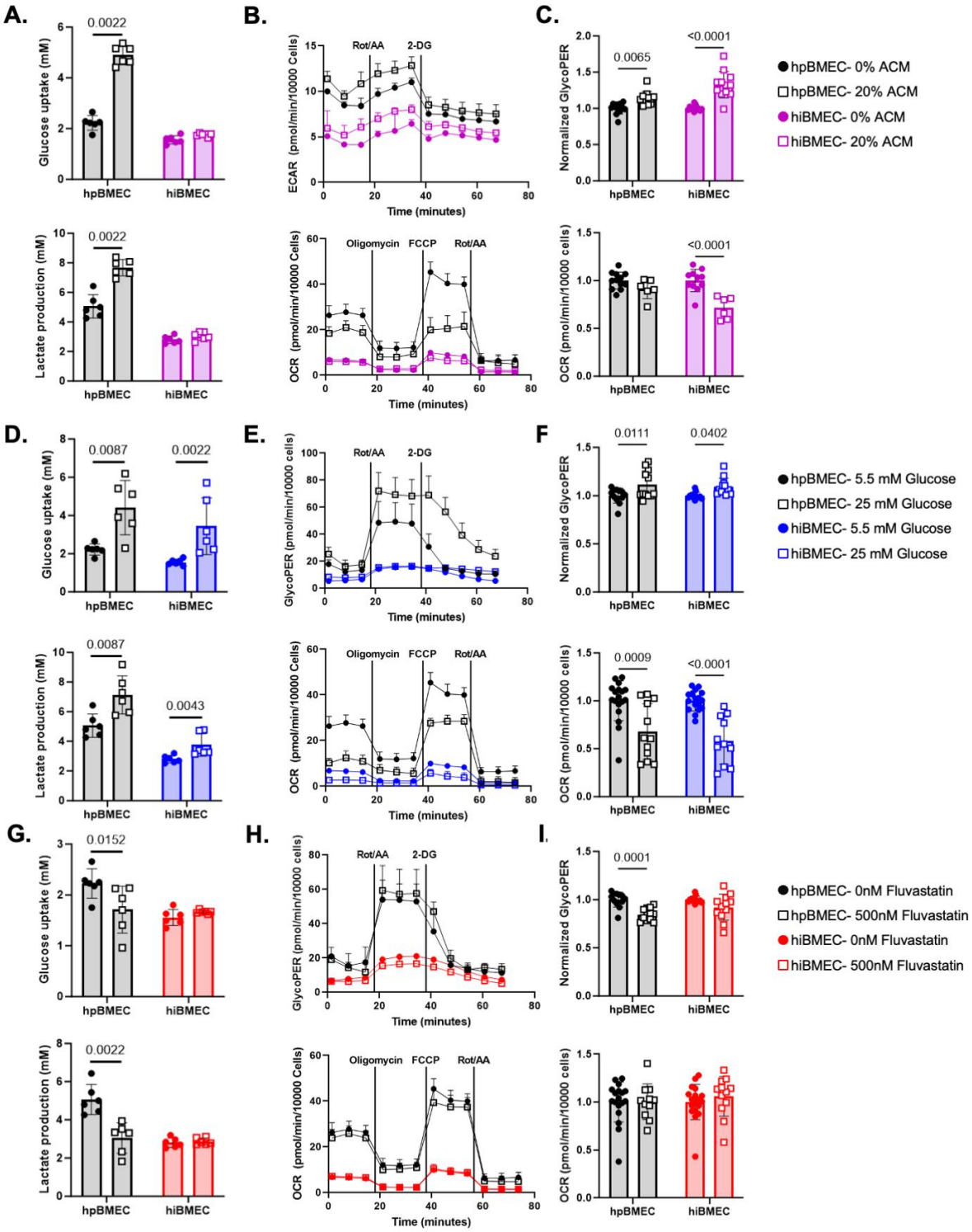


Figure 3.7. hpBMEC and hiBMEC had similar glycolytic responses to ACM and high glucose, but not fluvastatin. Glucose uptake and lactate production of hpBMEC compared to hiBMEC following a 24-hour treatment with **(A)** 0 or 20% ACM, **(D)** 5.5 mM or 25 mM glucose, or **(G)** 0 nM or 500 nM fluvastatin, measured by YSI. n = 6 biological replicates. Seahorse Glycolytic Rate Assay and Mito Stress Test, with analysis of basal GlycoPER and OCR, of hpBMEC compared to hiBMEC following a 24-hour treatment with **(B-C)** 0 or 20% ACM, **(E-F)** 5.5 mM or 25 mM glucose, or **(H-I)** 0 nM or 500 nM Fluvastatin. n = 15 biological replicates. Data analyzed using a Mann-Whitney test.

3.4. Discussion

Cerebral glucose metabolic dysfunction is associated with Alzheimer's [237], Parkinson's [238], and motor neuron diseases [239]. While hpBMEC are used to model BMEC glucose metabolism [215], they are expensive and have limited availability. I therefore compared glucose metabolism in hiBMEC, a renewable BMEC source, and hpBMEC to determine if hiBMEC can be used to model BBB glucose metabolism. I now show that hpBMEC have higher overall glycolytic and oxidative metabolism than hiBMEC, that the metabolomes of the two cell types are distinct, and that the cells differently express glycolytic, TCA cycle, and FAO enzymes. However, the metabolomic differences lie primarily in the acylcarnitine pathway, the two cell types have similar glucose:lactate ratios, and the glucose labeled fractions of glycolytic and TCA cycle metabolites are similar between the two cell types. I thus propose that hiBMEC have similar glucose metabolism as hpBMEC.

hpBMEC had higher glycolytic and oxidative metabolic rates compared to hiBMEC, which is interesting given that stem cells generally have high metabolic rates [240]. Recent work by Williams *et al* further suggests that hiBMEC glycolysis decreased with extended culture, which would have increased metabolic differences between the two cell types [241]. The differences between hpBMEC and hiBMEC glycolytic rates could relate to changes in GLUT1 localization, which was diffuse throughout hpBMEC and localized to cell-cell junctions in hiBMEC, or to changes in metabolic enzymes [242], [243]. The higher glycolytic flux in hpBMEC could also impact the way that these cells interact metabolically with other NVU cells. Thus, glucose metabolism together with transport should be compared between hpBMEC and hiBMEC in NVU models that also contain pericytes and astrocytes.

Despite the difference in overall metabolic flux, the two cell types had similar lactate-to-glucose ratios and glucose-labeled fractions. This indicates that glucose taken up by the cells is similarly consumed in glycolysis, its side branch pathways (e.g., polyol and hexosamine biosynthesis), and the TCA cycle. In preliminary experiments, I further determined that immortalized HCMEC/D3 BMEC have similar glycolytic and oxidative metabolism to hpBMEC (data not shown), which agrees with published studies [215]. All three cell types produced more ATP via glycolysis than via the TCA cycle, confirming what had previously been reported only in hpBMEC [215]. Peripheral endothelial cells have consistently been shown to primarily use

glycolysis for ATP production, and glycolysis is essential to endothelial cell migration and angiogenesis [244]. The reliance of all these cells on glycolysis for ATP production indicates that they likely share fundamental endothelial metabolic characteristics.

Through hypergeometric analysis, I identified a significant difference in the acylcarnitine pathway between hpBMEC and hiBMEC, with five short-chain acylcarnitines significantly elevated in hiBMEC. Acylcarnitines are synthesized when an acyl group is transferred from a fatty acid or an acyl-CoA to free L-carnitine in reactions catalyzed by CPT1A, CPT1B, carnitine acetyltransferase (CrAT), and carnitine octanoyltransferase (CrOT) [245]. Elevated acylcarnitines in hiBMEC may be a remnant metabolic signature of hiBMEC differentiation, since acylcarnitines promoted cardiac and neuronal differentiation [246], [247]. The acylcarnitine with the highest VIP score, acetylcarnitine, is postulated to reduce mitochondrial acetyl-CoA, which could then promote glucose oxidation. Overall, the acylcarnitine changes, and the fact that several of the enzymes that catalyze acylcarnitine formation (CPT1A and CPT1B) were downregulated in hiBMEC as compared to hpBMEC, suggest that there are differences in mitochondrial FAO between hpBMEC and hiBMEC. Additional studies into the source and impact of elevated acylcarnitines in hiBMEC are needed.

Despite differences in gene expression and protein levels of rate-limiting enzymes for glycolysis (HK, PFK/PFKFB3, PKM), pentose phosphate pathway (PPP; G6PDH), hexosamine biosynthetic pathway (HBP; GFAT), and the TCA cycle (IDH) between hpBMEC and hiBMEC, the glucose-labeled metabolite fractions were similar between the two cell types. It is possible that the different isoforms have conflicting effects, or that the enzymes are regulated at a post-translational level (e.g., by phosphorylation). Based on my RNA-sequencing data, HK1 is the predominant hexokinase isoform in hpBMEC and expressed almost equally with HK2 in hiBMEC. Higher HK1 expression is consistent with previously published data showing HK1 is the predominant isoform in brain homogenates [248]. iPSC, however, have elevated HK2 [249], so the higher HK2 expression in hiBMEC may be an artifact from incomplete differentiation. Indeed, prolonged hiBMEC culture (9 days vs. 2 days past subculture) significantly reduced HK2 [241].

PFKFB3 differences in hpBMEC and hiBMEC were in opposite directions for gene expression (lower in hiBMEC) and protein (higher in hiBMEC). PFKFB3 contains AU-rich elements (ARE), which bind to

tristetraproline, a protein that enhances PFKFB3 degradation [250]. My RNA sequencing data indicate that hiBMEC have lower tristetraproline expression compared to hpBMEC, which may decrease PFKFB3 degradation and cause the higher protein levels. Extended BMEC culture decreased PFKFB3 protein [241], suggesting that the lower gene expression does lower PFKFB3 protein over time.

hpBMEC and hiBMEC glucose metabolism increased in similar although not identical ways in response to ACM. ACM was previously shown to increase cerebral endothelial cell glucose uptake by 23% [251], which is similar to what I observed in the increased GlycoPER of both hpBMEC and hiBMEC. While the GlycoPER data agree with the YSI data for the hpBMEC, the hiBMEC did not shown increased glucose uptake by YSI, which could relate to a difference in sensitivity or timescale between the assays. Only hiBMEC had a statistically significant decrease in OCR with ACM. In prior studies, endothelial cells incubated with ACM increased transforming growth factor-β (TGFβ), a cytokine that significantly decreases OCR [252], [253]. Therefore, it is possible that ACM increases hiBMEC TGFβ to decrease OCR.

Hyperglycemia increased glucose uptake, lactate production, and GlycoPER while decreasing OCR in both hpBMEC and hiBMEC. Acute endothelial cell exposure to high glucose increases glycolysis [254] and decreases mitochondrial respiration [255]. Hyperglycemia can lead to enhanced BBB permeability [256], reactive oxygen species production, and apoptosis [257]. These data suggest that hpBMEC and hiBMEC respond similarly to acute hyperglycemia; however, further tests are needed to assess metabolic changes during prolonged hyperglycemia.

In contrast, only hpBMEC but not hiBMEC decreased glycolysis in response to statin treatment. Statins decrease cholesterol production, which could prove therapeutic in restoring BBB function in neurodegenerative diseases associated with dysregulation of cholesterol homeostasis, including Alzheimer's, Parkinson's, and Niemann-Pick type C diseases [258]. My hpBMEC data agree with studies in which statins decrease glycolysis, glycolytic capacity, mitochondrial respiration, and ATP production [259]. Statins may not have decreased glycolysis in hiBMEC due to elevated HMG CoA reductase expression in hiBMEC ($Log_2FC = 2.26$). Thus, the physiologic statin dose that I used might have been too low to induce a measurable effect in hiBMEC.

3.5. Limitations:

Although my data show similarities between hpBMEC and hiBMEC glucose metabolism, my study is not without limitations. I used hpBMEC as the more physiologically relevant cell source; however, hpBMEC cultured *in vitro* also may not accurately model *in vivo* BMEC metabolism [260]. I used hpBMEC from only one donor and hiBMEC derived from only one iPSC line. As a preliminary exploration, I performed RNA-sequencing on hiBMEC derived from DF19-11-T iPSC. I measured metabolic enzyme Log_2FC values that followed the same trend as the IMR90 hiBMEC (data not shown). I also differentiated the iPSC with a single protocol [216]. Thus, my study does not account for donor-to-donor variability or other differentiation strategies, which may change metabolism [261]. Additionally, all cells were cultured in static culture and on stiff substrates, both of which are known to impact endothelial metabolism [262], [263], [264]. Finally, I tested only a single statin dose based on blood statin concentrations from clinical pharmacokinetics studies [265]. However, this dose may not have been the most relevant for BMEC [266].

3.6. Conclusions:

While there are essential differences in hpBMEC and hiBMEC glycolytic and oxidative metabolism, metabolomes, and metabolic enzyme levels, this study suggests that hpBMEC and hiBMEC have similar glucose metabolism and respond similarly to extracellular stimuli known to impact glycolytic activity. Glucose is the primary fuel source for BMEC; however, glutamine also provides carbon and nitrogen molecules essential to biomass formation. In the next chapter, I examine how hiBMEC model hpBMEC glutamine metabolism to further assess the relevance of hiBMEC as a model of hpBMEC metabolism.

Chapter 4: iPSC-BMEC modeling of brain endothelial cell glutamine metabolism

4.1. Introduction:

In the prior chapter, I demonstrated that while hpBMEC metabolize more glucose than hiBMEC, both BMEC cell types use a similar proportion of glucose for glycolysis versus other metabolic pathways and respond similarly to extracellular stimuli, and thus are sufficient models of BMEC glucose metabolism. However, I only examined the role of glucose in BMEC metabolism, and not glutamine, the main fuel source for mitochondrial metabolism. Mitochondrial respiration generates little energy in endothelial cells but is vital to generating metabolites that are essential for cell signaling, regulating vascular tone, and other important physiological functions [267], [268].

Glutamine metabolism is of particular interest, as it is the most abundant amino acid in the human body and is an essential cell source of both carbon and nitrogen. Glutamine can be metabolized in the TCA cycle to produce ATP, and glutamine-derived metabolic intermediates are used for nucleotide and antioxidant synthesis as well as other biosynthetic pathways essential to cell function [269]. While BMEC glutamine metabolism has not been extensively studied, glutamine has been shown to be a vital fuel source for other endothelial cell types. In fact, glutamine catabolism in endothelial cells is thought to be higher than in any other mammalian cell [270], [271], [272], [273]. In human umbilical vein endothelial cells (HUVEC), 90% of glucose that enters the cell is secreted as lactate, indicating that only 10% of glucose carbons enter the TCA cycle [46]. In contrast, only 10% of glutamine that enters endothelial cells is secreted as glutamate, and thus 90% of glutamine carbons and nitrogens are retained to produce metabolic intermediates [46]. HUVEC also have impaired proliferation in glutamine-depleted conditions, since glutamine-derived nitrogen is essential for biomass production [45], [46]. Additionally, glutamine deprivation altered HUVEC redox homeostasis by decreasing intracellular glutathione [45].

Glutamine is essential to endothelial function; thus, it is important to understand how different BMEC models metabolize glutamine to engineer reliable *in vitro* BBB models. Previous work shows other iPSC-derived cells may have distinct mitochondrial morphology and metabolism from the primary cell type they are differentiated to mimic [274]. Therefore, in this chapter I used transcriptomic and metabolomic

approaches to evaluate how hpBMEC and hiBMEC differ in their glutamine metabolism. My data show essential differences in hiBMEC and hpBMEC glutamine metabolism that alter their glutamate secretion and may contribute to functional changes. These key differences between hiBMEC and hpBMEC glutamine metabolism are vital to consider when choosing a BMEC type for *in vitro* models of neurological diseases and cerebral drug delivery.

4.2. Methods:

4.2.1. Cell Culture: hpBMEC and IMR90 iPSC were maintained and differentiated into hiBMEC as described in Chapter 3.

4.2.2. RNA Sequencing: hiBMEC RNA sequencing was completed as previously described (GSE211648) [219]. Briefly, RNA was isolated using a phenol/chloroform isolation protocol [223]. RNA was quantified using a Nanodrop 2000c (Thermo Fisher) and sequenced by Novogene (Sacramento, CA) with a NovaSeq6000 using 105 bp paired end reads. Galaxy open-source software was used to trim and map reads to the human genome, as well as convert reads to fragments per kilobase of transcript per million mapped reads (FPKM). hpBMEC RNA sequencing data were accessed from publicly available datasets [217], [224], [225], [275].

4.2.3. Metabolite Uptake and Production: I used a YSI 2950 Bioanalyzer (Yellow Springs Instruments, 527690) to measure medium metabolite concentrations. hpBMEC and hiBMEC were seeded in 12-well plates and cultured to confluence. For some experiments, cells were treated with 0, 3.5, 7, or 14 mM α-ketoglutarate (α-KG; Millipore Sigma, 349631, pH 7.4). 200 mL medium samples were collected 0 and 24 hours after treatment and analyzed by YSI. Glutamine uptake and glutamate production were calculated as the difference between the medium concentrations at 0 and 24 hours.

4.2.4. Mitochondrial Function: hpBMEC and hiBMEC mitochondrial function was measured using the Seahorse Mito Stress Test (Agilent, 103015-100). hiBMEC were subcultured at 50,000 cells/well and hpBMEC were seeded at 30,000 cells/well in a 96-well Seahorse assay plate. Cells were then incubated

with hESFM supplemented with 2% B27 for 2 days. 1 hour prior to running the assay, the cell culture medium was changed to Seahorse Dulbecco's Modification of Eagles Medium (DMEM; Agilent, 103680-100) supplemented with 10 mM glucose, 1 mM pyruvate, and 2 mM glutamine. During the assay, 1.5 mM oligomycin, 0.5 mM FCCP, and 0.5 mM rotenone + antimycin A were injected. Real-time oxygen consumption rates (OCR) were recorded in the Seahorse XFe96 (Agilent) and analyzed using the Seahorse Wave software (Agilent). Immediately following the assay, cells were fixed in 4% paraformaldehyde (PFA), labeled with Hoescht (1:2000; Thermo Fisher, 62249) and imaged using an Eclipse Ti2 spinning disk confocal microscope (Nikon) at 10x. Nuclei were counted in ImageJ, and OCR was normalized to nuclei count for each sample.

4.2.5. Protein analysis: Western blots were run following the protocol outlined in Chapter 3. Western blots were probed for primary antibodies in Table 4.1.

Table 4.1: Western blot antibodies

Antibody	**Company**	**Catalogue Number**
SLC7A5 (LAT1)	Cell Signaling Technology	5347S
GLS	Thermo Fisher Scientific	701965
SLC1A1 (EAAT3)	Cell Signaling Technology	14501S
ASNS	Santa Cruz Biotechnology	sc-365809
FASN	Santa Cruz Biotechnology	sc-48357

4.2.6. Mitochondrial imaging and quantification: hpBMEC and hiBMEC were cultured for 24 hours in hESFM supplemented with 2% B27. To label mitochondria, cells were washed with pre-warmed PBS and then incubated in Hanks' Balanced Salt Solution (HBSS; Thermo Fisher, 14025092) containing 100 nM MitoTracker Green (Thermo Fisher, M7514) and 100 mM Hoechst (Thermo Fisher, PI62249) for 30 minutes. Cells were washed 3x with warmed HBSS and imaged at 20x on a Revolve microscope (Echo). 4 images were taken (technical replicates) of 9 wells of cells (biological replicates) in 3 separate experiments. Mitochondrial morphology was analyzed using the MitoHacker pipeline [276], in which individual cells were isolated using the Cell Catcher algorithm, mitochondrial networks were segmented using the Mito Catcher

tool, and mitochondrial morphology was analyzed using the MiA tool. The individual data points on the MiA output bar graphs represent the average value of all the cells in each well (biological replicates).

4.2.7. Metabolic Mass Spectrometry: Metabolic mass spectrometry was run as described in Chapter 3, but with hpBMEC and hiBMEC cultured in DMEM (Thermo Fisher; A1443011; no glucose, no glutamine) supplemented with 4.5 mM $^{13}C_5$ L-Glutamine (Cambridge Isotope Laboratories Inc, CLM-1822-H-PK), 5.5 mM glucose (Millipore Sigma, G5767), and 2% B27.

4.2.8. Statistics: Statistics were analyzed in GraphPad PRISM. Non-parametric Mann-Whitney tests were used to compare hpBMEC and hiBMEC, with a p-value < 0.05 considered statistically significant. For RNA-sequencing data, the threshold for biological significance was set at $Log_2FC > 0.6$ and an adjusted p-value < 0.05.

4.3. Results:

While glucose is the main carbon source for glycolytic metabolites, many TCA cycle carbons are derived from glutamine. Glutamine is also an essential source of intracellular nitrogen. Therefore, in this chapter, I compared glutamine metabolism in hpBMEC and hiBMEC to better understand how mitochondrial metabolism impacts the ability of hiBMEC to model BMEC metabolism and produce metabolites critical to BMEC function.

4.3.1. hiBMEC had lower glutamine uptake relative to hpBMEC and negligible glutamate production.

I first assessed hpBMEC and hiBMEC glutamine uptake and glutamate secretion over 24 hours using a YSI Bioanalyzer. As previous reports suggested that hiBMEC maintain iPSC- and epithelial characteristics [217], I also measured glutamine uptake and glutamate secretion in iPSC. Glutamine uptake was 45% ($p = 0.0439$) and 65% ($p < 0.0001$) lower in hiBMEC than hpBMEC and iPSC, respectively (Fig. 4.1A). Both hiBMEC and iPSC had negligible glutamate production (0.01 mM and 0.07 mM, respectively), while hpBMEC produced 0.33 ± 0.11 mM glutamate over 24 hours (Fig. 4.1B). To observe how glutamine uptake and glutamate secretion change during hiBMEC differentiation, media glutamine uptake and glutamate secretion were quantified daily over the 7-day differentiation protocol. Media was replenished daily with the

exception of day 6, when cells did not receive a media change. Glutamine uptake remained fairly stable during differentiation, apart from high glutamine uptake on day 0 and a decline around day 6, when cells were fully confluent and did not receive a media change (Fig. 4.1C). Glutamate secretion declined over the differentiation period, decreasing to nearly zero at day 4 (Fig. 4.1D).

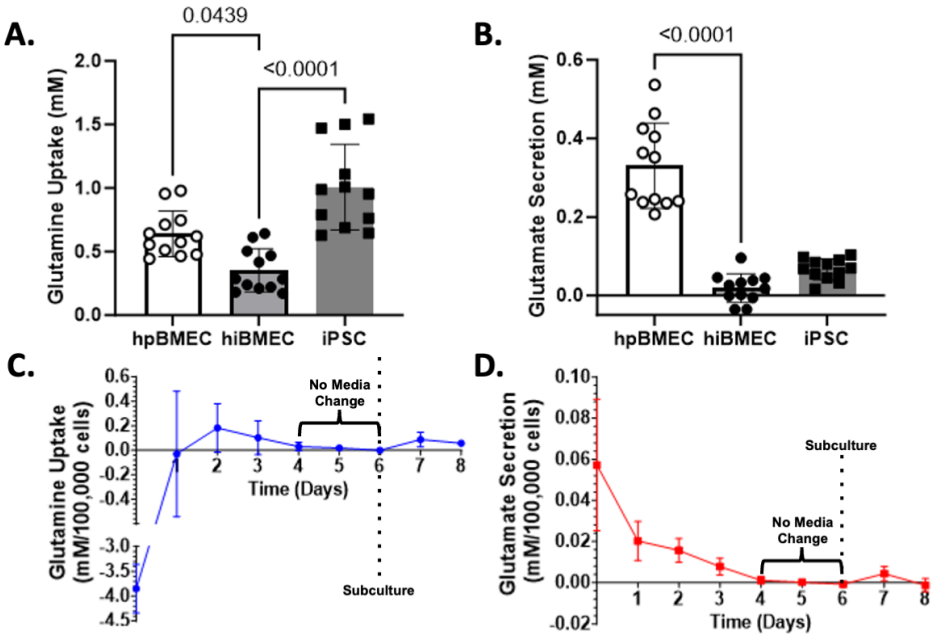


Figure 4.1. hiBMEC took up less glutamine and secreted almost no glutamate, as compared to hpBMEC and iPSC. (A) Glutamine uptake and **(B)** glutamate secretion in hpBMEC, hiBMEC, and iPSC over 24 hours, as measured by YSI. **(C)** Glutamine uptake and **(D)** glutamate secretion over the 7-day hiBMEC differentiation protocol from iPSC, as measured by YSI. Media was not changed between days 4-6, and hiBMEC were subcultured onto a collagen and fibronectin-coated plate on day 6. Data were analyzed using Kruskal-Wallis test with Dunn's multiple comparisons post-hoc analysis. n = 12 biological replicates.

4.3.2. hiBMEC had decreased mitochondrial metabolism and more punctate mitochondria than hpBMEC.

Since glutamine is primarily metabolized in endothelial mitochondria via the TCA cycle, I next compared mitochondrial metabolism and morphology in hpBMEC and hiBMEC. Oxygen consumption rate (OCR), a measure of mitochondrial metabolism from a Seahorse Mito Stress Test, was higher in hpBMEC relative to hiBMEC (Fig. 4.2A). Specifically, basal OCR was 51% higher in hpBMEC than hiBMEC ($p < 0.0001$; Fig. 4.2B), and spare respiratory capacity, interpreted as the difference between the maximal and basal

respiration rates, was 73% higher in hpBMEC than hiBMEC ($p < 0.0001$; Fig 4.2C). Similarly, hpBMEC had higher ATP-linked mitochondrial respiration ($p = 0.0005$), proton leak ($p < 0.0001$), maximal respiration ($p < 0.0001$), and non-mitochondrial oxygen consumption ($p < 0.0001$) than hiBMEC (Fig. 4.2D-G). Taken together, these data indicate hpBMEC have higher mitochondrial metabolic activity than hiBMEC.

I then imaged hpBMEC and hiBMEC mitochondria using MitoTracker (Fig. 4.2H-I) and quantified their morphology using the MitoHacker Pipeline [276]. hiBMEC had 33% more individual mitochondria per cell than hpBMEC ($p = 0.0002$; Fig. 4.2J). hiBMEC mitochondria also had a lower mean mitochondrial area, branch count, and total branch length (Fig. 4.2K-M). These data indicate that hiBMEC mitochondria have a more punctate, fragmented morphology compared to the tubular, networked morphology of hpBMEC mitochondria.

4.3.3. hiBMEC metabolic transporter and enzyme levels suggested increased glutamine incorporation into asparagine and fatty acids.

To investigate further why hiBMEC secreted less glutamate than hpBMEC, I compared glutamine and glutamate transporter and metabolic enzyme expression data from our hiBMEC RNA sequencing with publicly available hpBMEC RNA sequencing data [217], [224], [225], [275] (Fig. 4.3A). I then measured primary glutamine and glutamate transporter and enzyme protein levels via Western blot (Fig. 4.3B-F). Glutamine transporters *SLC1A5, SLC38A1,* and *SLC38A2* had the highest expression levels in hpBMEC, but neither *SLC1A5* nor *SLC38A2* had significantly different gene expression between hpBMEC and hiBMEC. Gene expression of *SLC38A1* was higher in hiBMEC compared to hpBMEC, as was expression of the less expressed glutamine transporter *SLC7A5.* These results were counterintuitive, as glutamine uptake was higher in hpBMEC as compared to hiBMEC. Of note, *SLC7A5* is bidirectional, so its elevated expression may correlate with increased glutamine secretion rather than uptake. Western blotting for SLC7A5 confirmed 1123% higher protein levels in hiBMEC compared to hpBMEC ($p < 0.0001$; Fig. 4.3B).

SLC1A1 (EAAT3) and *SLC7A11* were the most highly expressed glutamate transporters in hpBMEC. Both *SLC1A1* and *SLC7A11* had elevated gene expression in hpBMEC, though these data only reached the threshold for biological but not statistical significance ($p = 0.0778$ and $p = 0.2552$, respectively). However, Western blot showed nearly 70% higher SLC1A1 protein levels in hpBMEC as compared to

hiBMEC ($p < 0.0001$; Fig. 4.3C). Bidirectional membrane glutamate transporters *SLC1A3* and *SLC1A6* were both negligibly expressed in hpBMEC but had significantly higher expression in hiBMEC ($Log_2FC = 10.1418$ and $Log_2FC = 8.1619$, respectively), which again was counterintuitive to lower hiBMEC glutamate secretion. Similarly, *SLC25A18* and *SLC25A22*, transporters responsible for glutamate efflux from mitochondria to cytosol, were more highly expressed in hiBMEC than hpBMEC ($Log_2FC = 2.4301$ and $Log_2FC = 0.8010$, respectively).

Glutaminase (*GLS*) converts mitochondrial glutamine to glutamate, while glutamate-ammonia ligase (*GLUL*) converts glutamate back into glutamine. *GLS* gene expression was elevated in hpBMEC, while *GLUL* gene expression was elevated in hiBMEC, suggesting that hiBMEC may favor glutamine over glutamate in this reaction. I similarly saw 76% lower GLS protein levels in hiBMEC compared to hpBMEC ($p < 0.0001$; Fig. 4.3D).

Glutamine is essential for fatty acid, asparagine, and glutathione synthesis. hiBMEC had elevated fatty acid synthase *(FASN)* gene expression compared to hpBMEC. hiBMEC also had higher gene expression of transporters *SLC25A12/13* and enzyme asparagine synthetase (*ASNS*), all of which are part of asparagine synthesis from TCA cycle metabolites. Similarly, gene expression for g-glutamylcysteine *(GCLC)*, the rate limiting enzyme in glutathione synthesis, was significantly elevated in hiBMEC. I observed 87% higher FASN and 153% higher ASNS protein levels in hiBMEC via Western blot (Figure 4.3E-F; $p = 0.0012$ and $p = 0.0003$, respectively). These data indicate that more glutamate may be used to produce fatty acids and asparagine in hiBMEC compared to hpBMEC.

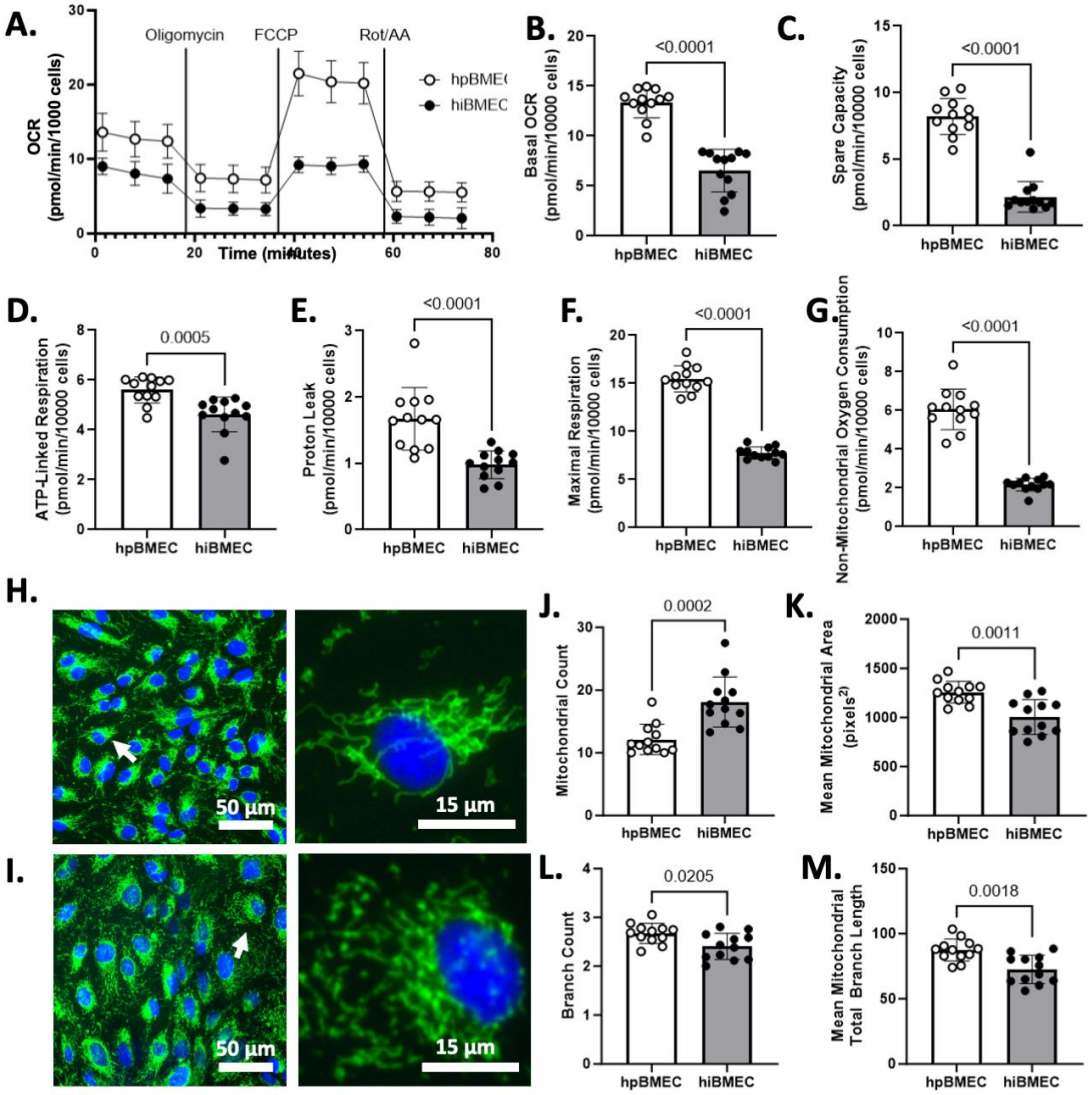


Figure 4.2. hiBMEC had decreased mitochondrial metabolism and a punctate mitochondrial morphology. (A) Oxygen consumption rate (OCR) quantified by Seahorse Mito Stress Test. **(B)** Basal oxygen consumption rate (OCR) in hpBMEC and hiBMEC. **(C)** Spare respiratory capacity calculated by subtracting basal respiration OCR from FCCP induced OCR. **(D)** ATP-linked respiration calculated by subtracting oligomycin-inhibited respiration from basal respiration rates. **(E)** Proton leak calculated by subtracting antimycin/rotenone-inhibited OCR from oligomycin-inhibited respiration rates. **(F)** Maximal respiration calculated by subtracting antimycin/rotenone-inhibited OCR from FCCP induced OCR. **(G)** Non-mitochondrial oxygen consumption equal to the rate of OCR with antimycin/rotenone inhibition (n = 12 biological replicates). Representative immunofluorescence images of **(H)** hpBMEC and **(I)** hiBMEC mitochondria (green) and nuclei (blue), with quantification of **(J)** mitochondrial count, **(K)** mean mitochondrial area, **(L)** branch count, and **(M)** mean mitochondrial total branch length (n = 12 biological replicates). Data were analyzed using a Mann-Whitney test.

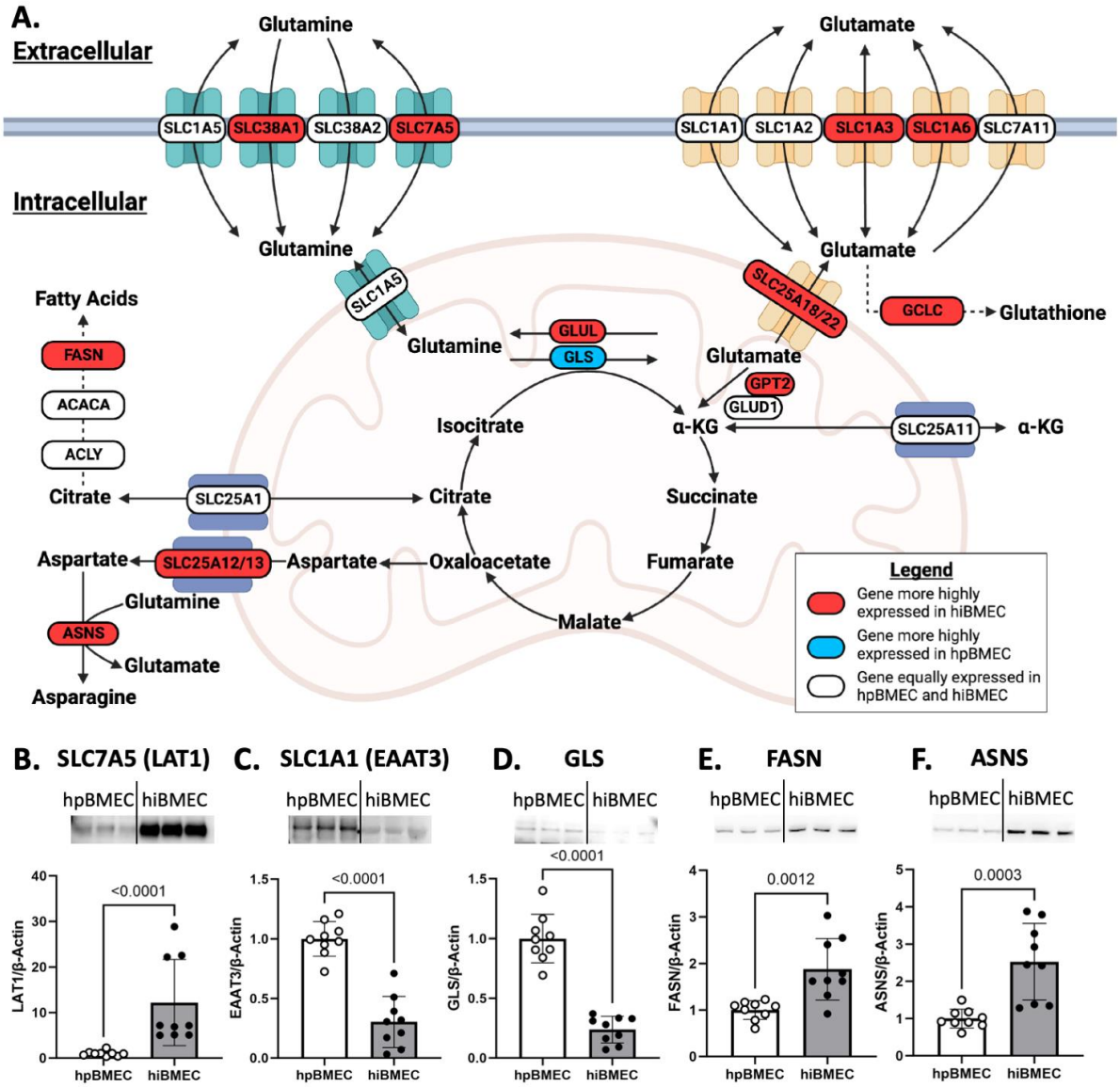


Figure 4.3: hiBMEC had decreased GLS and increased fatty acid and asparagine synthesis genes. **(A)** Glutamine and glutamate metabolism diagram showing genes more highly expressed in hiBMEC (red) or in hpBMEC (blue). Cutoff for elevated expression: $Log_2FC > 6$, $p<0.05$. n = 3 biological replicates. **(B-F)** Representative Western blots with quantification of SLC7A5, GLS, SLC1A1, ASNS, and FASN, key glutamine/glutamate metabolism proteins that differed between hpBMEC and hiBMEC. Data analyzed using Mann-Whitney test. n = 9 biological replicates.

4.3.4. Mass spectrometry confirmed that hiBMEC had increased glutamine-derived carbons in fatty acids and increased asparagine and glutathione ion counts compared to hpBMEC.

To determine if hiBMEC incorporated more glutamine carbons into fatty acids than hpBMEC, I analyzed $^{13}C_5$-glutamine mass spectrometry data for the 10 fatty acids with greater than 10% carbon labeling (Fig.

4.4A). Of these, five were saturated fatty acids, two were mono-unsaturated fatty acids, and three were poly-unsaturated fatty acids. Labeled fractions of saturated fatty acids hexadecanoic acid ($p = 0.0411$), octadecanoic acid ($p = 0.0087$), and tetradecanoic acid ($p = 0.0022$) were higher in hiBMEC compared to hpBMEC. Only dodecanoic acid was higher in hpBMEC ($p = 0.0043$), while there was no significant difference in decanoic acid labeling between hpBMEC and hiBMEC. Both mono-unsaturated fatty acids, octadecenoic acid ($p = 0.0022$) and hexadecenoic acid ($p = 0.0022$), had higher labeled fractions in hiBMEC. Labeled fractions of poly-unsaturated fatty acids linoleic acid ion (-1) ($p = 0.0260$) and eicosatetraenoic acid ($p = 0.0022$) were also higher in hiBMEC while (8Z-11Z-14Z)-icosatrienoic acid had a higher labeled fraction in hpBMEC ($p = 0.0022$). Overall, the majority (7/10) of the most abundant intracellular fatty acids measured had higher labeled fractions in hiBMEC than hpBMEC, demonstrating that glutamine incorporation into fatty acids was higher in hiBMEC than hpBMEC.

Since hiBMEC had elevated expression of *SLC25A12/13* and *ASNS*, I hypothesized that hiBMEC would also incorporate more glutamine carbons into asparagine than hpBMEC. $^{13}C_5$-glutamine mass spectrometry data, however, demonstrated both asparagine and its precursor, aspartate, had lower labeled fractions in hiBMEC relative to the hpBMEC ($p = 0.0022$ and $p = 0.0043$, respectively; (Fig 4.4B-C). As this was unexpected, I investigated if total aspartate and asparagine intracellular ion counts, quantified via mass spectrometry, were different between hpBMEC and hiBMEC. Both aspartate and asparagine had elevated total ion counts in hiBMEC ($p = 0.0022$ and $p = 0.0022$, respectively; Fig. 4.4D-E). This may indicate elevated aspartate and asparagine synthesis in hiBMEC with large pools of unlabeled metabolites leading to decreased labeled fractions but increased total ion counts.

Intracellular glutamate is also readily converted to glutathione via *GCLC*. Elevated *GCLC* gene expression indicated hiBMEC may produce more glutathione compared to hpBMEC, which could better protect hiBMEC from reactive oxygen species. Using metabolic mass spectrometry, I was only able to obtain reliable readings for total ion counts of glutathione, not for incorporation of labeled $^{13}C_5$-labeled glutamine in glutathione, and thus was unable to calculate the labeled fraction. I therefore quantified the labeled fractions of the oxidized form of glutathione, glutathione disulfide. The fraction of labeled carbons in glutathione disulfide was higher in hpBMEC compared to hiBMEC (Fig. 4.4F). Total glutathione and

glutathione disulfide ion counts, however, were elevated in hiBMEC compared to hpBMEC ($p = 0.0022$ and $p = 0.0022$, respectively; Fig. 4.4G-H).

4.3.5. Metabolomic analysis using labeled glutamine reveals hpBMEC and hiBMEC have distinct metabolomic signatures.

While my initial analysis revealed important differences in glutamine metabolism, it did not fully explain why hiBMEC take up less glutamine than hpBMEC and secrete negligible glutamate. I therefore used several metabolomic techniques and our U-$^{13}C_5$ glutamine mass spectrometry data to determine holistic differences in the hiBMEC and hpBMEC glutamine metabolomes. Partial least squares-discriminant analysis (PLS-DA) of the glutamine labeled fraction mass spectrometry data indicated hpBMEC and hiBMEC separate primarily along component 1 (PC1 = 43.9%; Fig. 4.5A). A variable importance projection (VIP) plot was used to determine which metabolite labeled fractions were responsible for hpBMEC and hiBMEC separation in the PLS-DA (Fig. 4.5B). Glutamate had the most different labeled fraction between hpBMEC and hiBMEC, with higher labeling in the hpBMEC. Glutamine and several other amino acids (aspartate, proline, alanine) were also higher in hpBMEC. In contrast, fatty acids including octadecenoic acid, tetradecenoic acid, docosahexaenoic acid, hexadecenoic acid, eicosatetraenoic acid, and tetradecanoic acid had higher labeling in hiBMEC. A heatmap of the glutamine-labeled fractions of all metabolites further indicated that hpBMEC may incorporate more glutamine carbons into specific nucleotides including ATP, GTP, NAD+, and NADH; aminosugars such as UDP-glucose and UDP-N-acetyl glucosamine; and amino acids such as glutamine, glutamate, alanine, and leucine, while hiBMEC incorporate more glutamine into fatty acids (Fig. 4.5C). The heatmap also demonstrated several metabolites with elevated labeled fractions in hpBMEC compared to hiBMEC that did not fit into any specific metabolite category. These were folate, glutathione disulfide, GABA, N-acetyl aspartate, 3-phospho-serine, N-acetyl glutamate, and D-gluconate.

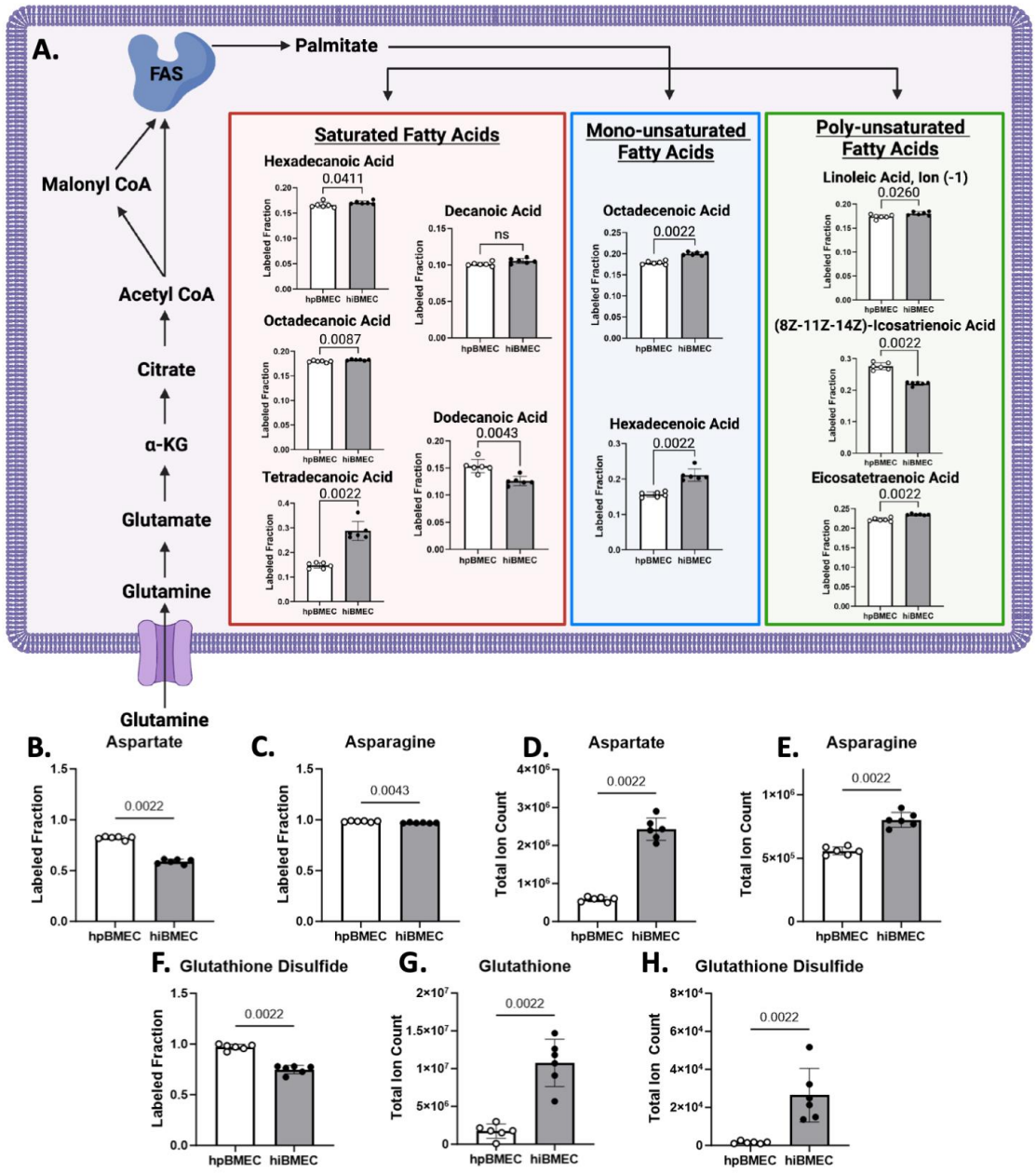


Figure 4.4. Mass spectrometry confirmed that hiBMEC had higher fatty acid, asparagine, and glutathione synthesis than hpBMEC. (A). hpBMEC and hiBMEC were treated with 4.5 mM U-$^{13}C_5$ glutamine for 24 hours, and labeled fractions of intracellular saturated, mono-unsaturated, and poly-unsaturated fatty acids were quantified. Labeled fractions of **(B)** aspartate **(C)** asparagine, and **(F)** glutathione disulfide were quantified by dividing the intracellular labeled ion counts by the total labeled and unlabeled ion counts. From the same dataset, total ion counts of both labeled and unlabeled intracellular **(B)** aspartate, **(C)** asparagine, **(D)** glutathione, and **(E)** glutathione disulfide were quantified. Data analyzed using Mann-Whitney tests. n = 6 biological replicates.

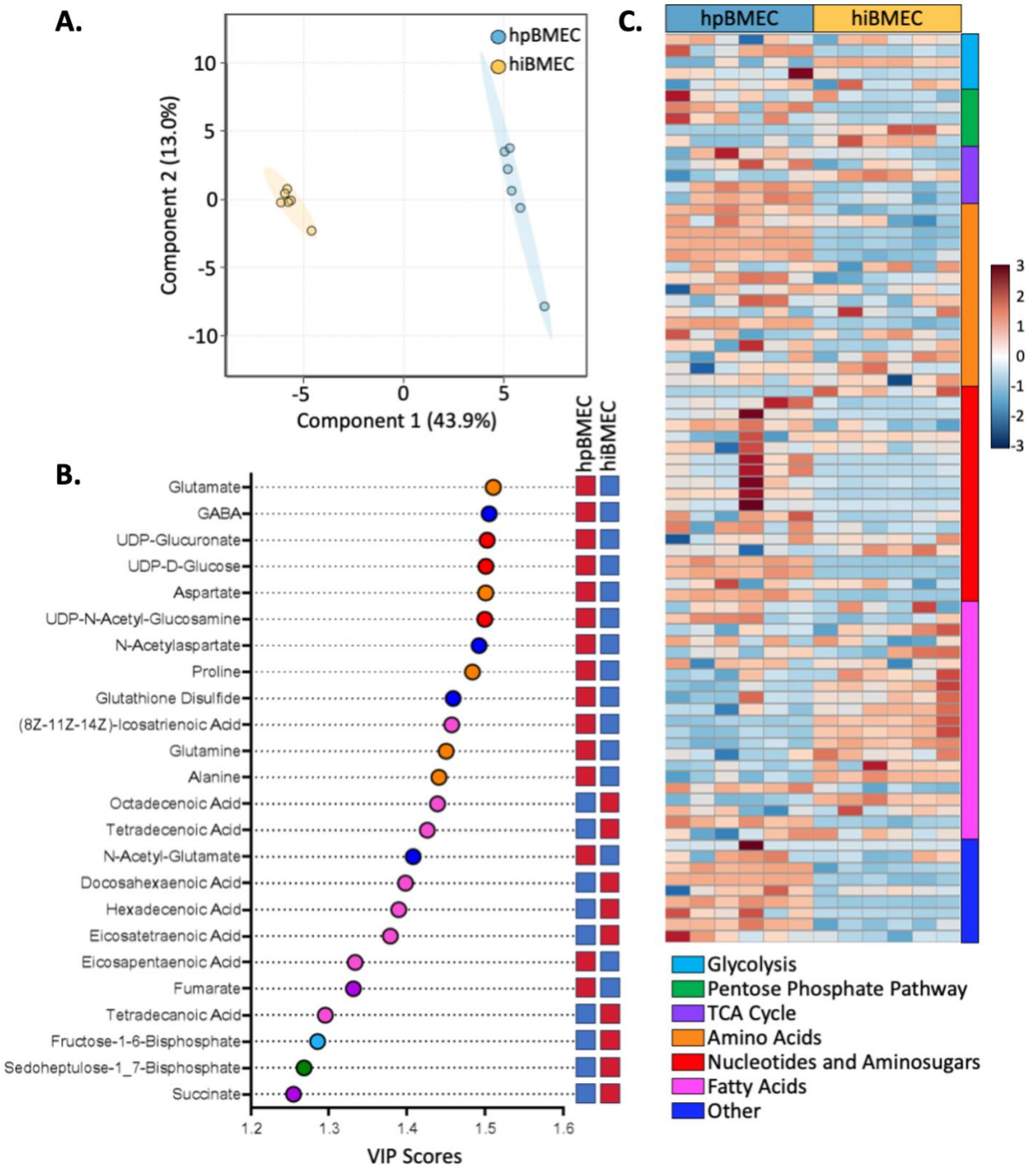


Figure 4.5. hpBMEC and hiBMEC have distinct metabolomes. (A) PLS-DA of intracellular metabolites analyzed by LC-MS/MS from hpBMEC and hiBMEC cultured in U-$^{13}C_5$ glutamine for 24 hours. **(B)** VIP scores of metabolites that most contributed to the hpBMEC and hiBMEC separation in the PLS-DA. Red indicates higher labeled fraction, blue indicates lower labeled fraction. **(C)** Heatmap showing differences in intracellular metabolites in hpBMEC and hiBMEC. n = 6 biological replicates.

4.3.6. Metabolomic analysis indicated that hpBMEC incorporated more carbons from glutamine into the TCA cycle.

I then examined glutamine labeled fractions for TCA cycle metabolites, since our Seahorse and mitochondrial labeling data indicated lower oxidative respiration in hiBMEC (Fig. 4.6). Glutamate and almost all TCA metabolites (α-KG, fumarate, malate, citrate) had higher glutamine-labeled fractions in hpBMEC as compared to hiBMEC, indicating higher glutamine-derived carbon incorporation. Specifically, the m+4 fractions were higher for fumarate, malate, and citrate in hpBMEC, indicative of one forward TCA cycle. The m+5 fraction of citrate, indicative of carbons moving through the TCA cycle in reverse, was also elevated in hpBMEC relative to hiBMEC. However, the m+2 fractions for fumarate, malate, and citrate were higher in hiBMEC, which may come from the incorporation of labeled acetyl-coA back into the TCA cycle. Only succinate showed a higher glutamine carbon labeled fraction in hiBMEC than hpBMEC, along with a lower unlabeled fraction in hiBMEC. A large unlabeled succinate pool was also seen in human umbilical vein endothelial cells (HUVEC) [277] and may be a product of cytosolic succinate that is pooled and stored prior to the labeling experiment.

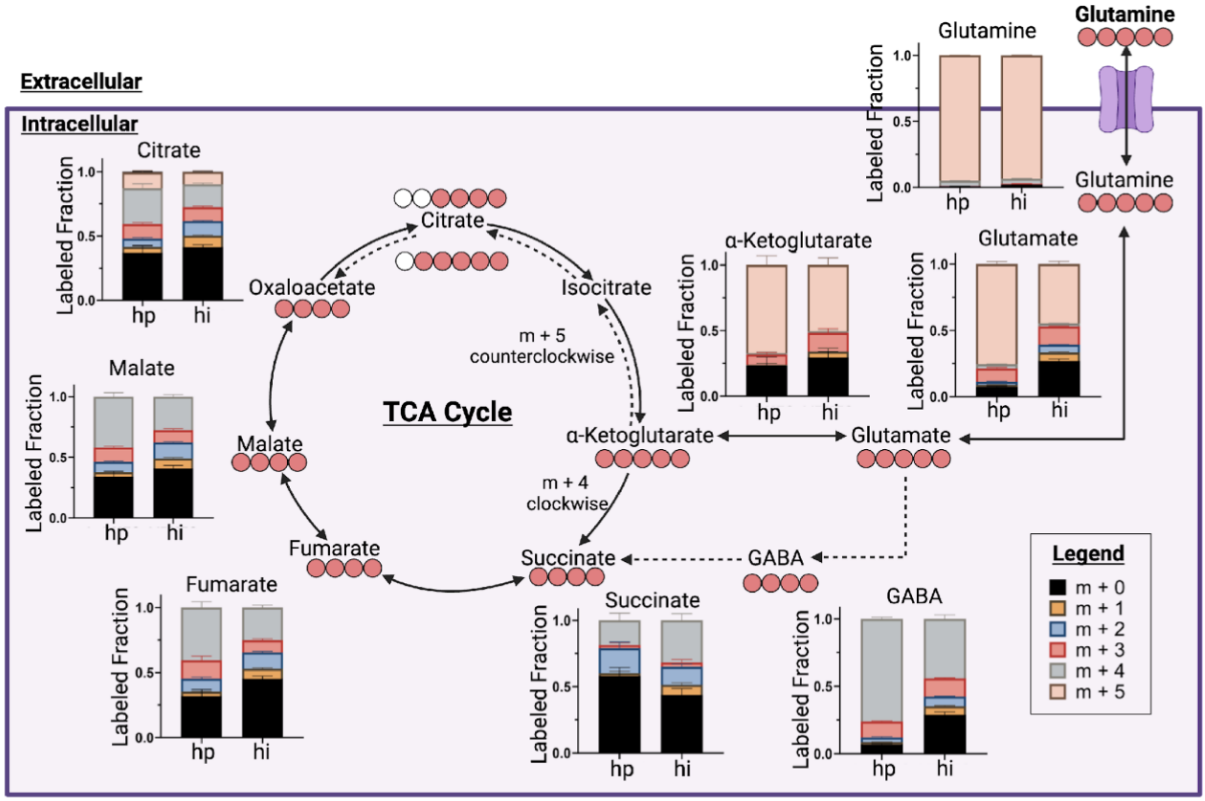


Figure 4.6. Isotope labeling and 13C metabolic flux analysis demonstrated higher TCA metabolite labeling in hpBMEC. Intracellular TCA cycle metabolite labeled fractions following 24 hours of 4.5 mM U-$^{13}C_5$ glutamine (n = 6 biological replicates). Carbon labeling patterns through the first turn of the TCA cycle are shown in red circles. Bar graphs represent the distribution of labeled carbons from each metabolite.

4.3.7. α-KG supplementation restored glutamate efflux in hiBMEC.

BMEC glutamate secretion may be essential to BBB models, since glutamate is the most abundant free amino acid in the brain and can act both a neurotransmitter and a fuel source. I therefore wanted to restore hiBMEC glutamate secretion so that these cells could more effectively be used to model the brain endothelium. I hypothesized that supplementing hiBMEC with α-KG would replenish the intracellular glutamate pool and enable hiBMEC glutamate secretion. hpBMEC and hiBMEC media were supplemented with 0, 3.5, 7, and 14 mM α-KG, and metabolite uptake and secretion were measured by YSI. α-KG supplementation reduced hpBMEC glutamine uptake ($p < 0.05$) and trended toward decreasing hiBMEC glutamine uptake (Fig. 4.7A). 7 and 14 mM α-KG supplementation significantly increased hiBMEC glutamate secretion ($p < 0.05$) to hpBMEC levels (Fig. 4.7B). When as little as 3.5 mM α-KG was added to

the media, hpBMEC and hiBMEC glucose uptake and lactate production were significantly reduced ($p < 0.05$; Fig. 4.7C-D).

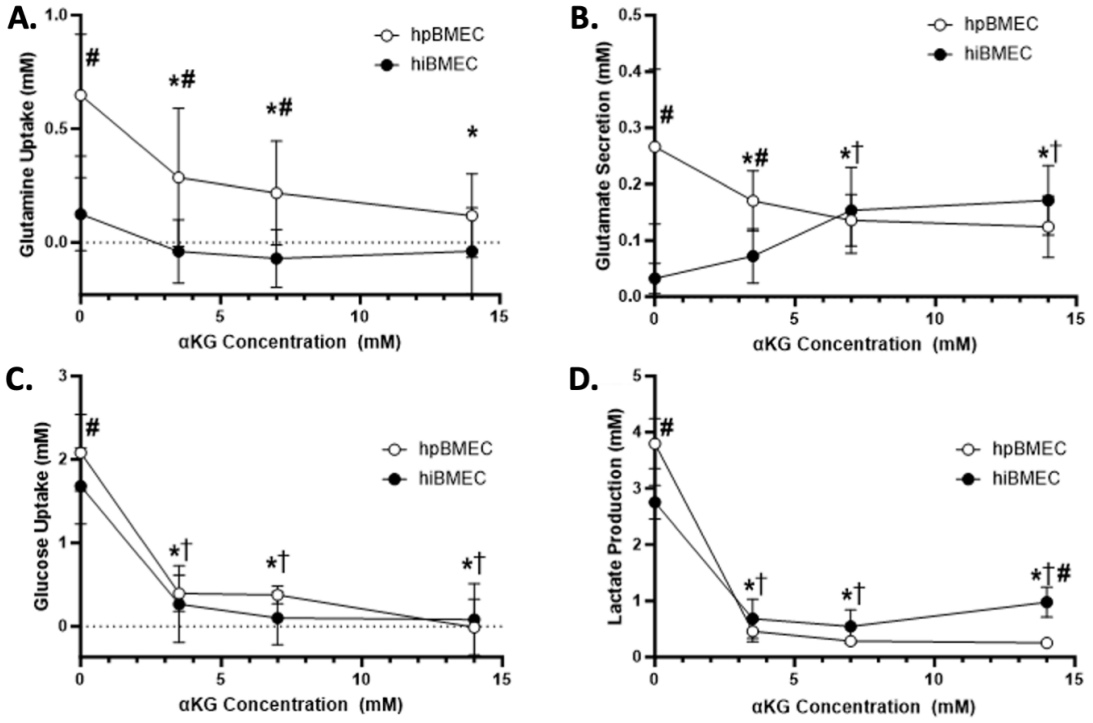


Figure 4.7. Alpha-ketoglutarate supplementation restored hiBMEC glutamate production. (A) Glutamine uptake, **(B)** glutamate secretion, **(C)** glucose uptake, and **(D)** lactate secretion of hpBMEC and hiBMEC cultured in 5.5 mM glucose, 4.5 mM glutamine, and 0, 3.5, 7 or 14 mM αKG for 24 hours as measured by YSI. Data analyzed using two-way ANOVA with Tukey's multiple comparisons post-hoc analysis. n = 9 biological replicates. # indicates significant difference ($p < 0.05$) between hpBMEC and hiBMEC. * indicates significant difference ($p < 0.05$) in hpBMEC compared to 0 mM αKG. † indicates significant difference ($p < 0.05$) in hiBMEC compared to 0 mM αKG.

4.4. Discussion:

Endothelial glutamine metabolism produces metabolites necessary to facilitate both cell-cell communication and biomass production [46]. hiBMEC are increasingly used as a renewable, cost-effective cell choice in BBB models to study neurodegenerative diseases and drug delivery to the brain, both of which are impacted by or can themselves alter cell metabolism. I now show that hpBMEC take up more glutamine and secrete more glutamate than hiBMEC. Glutamine taken up by hiBMEC is routed toward fatty acid, asparagine, and glutathione synthesis pathways, while glutamine taken up by hpBMEC is used to

produce amino acids, nucleotides, and GABA. The differences in metabolite production between hpBMEC and hiBMEC can impact BMEC function and communication with other brain cells, and thus are crucial to evaluate when choosing a cell type to model the brain vasculature for *in vitro* studies.

My data indicate that hpBMEC take up more glutamine and secrete more glutamate than hiBMEC. One potential reason for this difference could be due to cell proliferation rates since glutamine fuels biomass production and is vital for proliferation in peripheral endothelial cells [46]. All my measurements were taken while BMEC were confluent, but hiBMEC were seeded for experiments at confluence, whereas hpBMEC were seeded subconfluent and proliferated until they reached confluence. If hpBMEC were still in a proliferative state during the experiments, they could take up more glutamine to fuel that proliferation. The hpBMEC also demonstrated elevated spare respiratory capacity, which may indicate they have more metabolic flexibility, allowing them to switch nutrient sources more easily in response to altered circulating metabolite levels [278], [279]

Alternatively, hiBMEC may differ in their glutamine metabolism because they are not fully differentiated. I demonstrated that hpBMEC mitochondria are more mature due to their elongated structure and numerous branch points. Conversely, hiBMEC have a larger mitochondrial volume per cell, but these mitochondria are more punctate, a morphology more similar to that of the immature iPSC mitochondria [280], [281]. iPSC-derived cardiomyocytes similarly have a more punctate, immature morphology following differentiation, though mitochondrial fusion occurs over extended culture periods leading to more mature mitochondrial morphology [274]. Gene expression of glutamine transporters SLC38A1 and SLC7A5 and glutamate transporters SLC1A3 and SLC1A6 were elevated in hiBMEC compared to hpBMEC, and these expression levels were similar to those seen in my iPSC (data not shown). These data further support the idea that hiBMEC may retain an iPSC phenotype following differentiation.

The differences in glutamine metabolism in hpBMEC and hiBMEC go far beyond glutamine update and glutamate secretion. PLS-DA showed that hpBMEC and hiBMEC metabolic differences were largely driven by amino acids, fatty acids, and nucleotides and aminosugars. Glutamate and GABA were the largest drivers of this separation. In the brain, disruption of the balance of excitatory (glutamate) and inhibitory (GABA) neurotransmitters is associated with neurological disorders including Alzheimer's disease,

epilepsy, and stroke [282]. The glutamate:GABA ratio may be of particular importance to studies investigating neuron firing in neuron-endothelial co-culture models since the lack of glutamate secretion from hiBMEC may alter neuronal function.

Transcriptomic and metabolomic analysis further showed elevated fatty acid production in hiBMEC relative to hpBMEC. Both saturated and unsaturated fatty acid production in the brain have been heavily studied for their contributions to pathological conditions. Post-mortem tissue samples from the brains of individuals with Alzheimer's disease have reduced octadecanoic acid, and increased octadecenoic acid and hexadecenoic acid [283]. Octadecanoic acid protected brain slices against oxygen-glucose deprivation and glutamate injury, both of which are implicated in the pathophysiology of stroke and traumatic brain injury [284]. Tetradecanoic acid, another saturated fatty acid, increased spatial memory and reduced hippocampal degeneration in aged mice, indicating tetradecanoic acid may be important in slowing memory decline associated with aging [285]. As these fatty acids are implicated in the pathogenesis of neurodegenerative disease, BMEC fatty acid production should be considered when designing BBB models.

Our transcriptomic data also predicted increased asparagine synthesis in hiBMEC compared to hpBMEC. Using metabolomics, I demonstrated that hiBMEC had higher ion counts of asparagine and its precursor aspartate. However, $^{13}C_5$-glutamine labeling results showed higher labeled aspartate and asparagine fractions in hpBMEC. hiBMEC had a much larger unlabeled pool of both metabolites, which diluted the labeled pool and resulted in lower labeled fractions of aspartate and asparagine. Elevated aspartate and asparagine in hiBMEC may be important because asparagine synthesis is vital to vessel sprouting for angiogenesis [45]. Mutations in ASNS, the gene responsible for conversion of aspartate to asparagine, leads to microcephaly and intellectual disability, which is mimicked in ASNS knockout mice. ASNS, and thus asparagine, are important in brain development and function [286].

Similar to aspartate and asparagine labeling, hiBMEC had decreased glutathione disulfide labeled fraction but elevated total ion count. Again, a large unlabeled pool of glutathione disulfide decreased the labeled fraction despite hiBMEC making more glutathione disulfide. These data were supported by elevated hiBMEC *GCLC* expression, which converts glutamate to glutathione. Glutathione is an antioxidant, so

elevated hiBMEC glutathione may indicate these cells are better able to protect themselves from oxidative stress. iPSC also had significantly elevated glutathione compared to some other primary cell lines, indicating elevated glutathione production may be a factor of incomplete differentiation [287]. As glutathione deficiency is a key pathology of many neurological diseases including Alzheimer's disease [288], multiple sclerosis [289], and Parkinson's disease [290], the elevated hiBMEC glutathione may be important to consider in future models of these diseases.

While some glutamate must enter the TCA cycle to produce TCA intermediates [46], metabolomic data suggests hpBMEC keep more carbons from glutamate in the TCA cycle, while hiBMEC draw on glutamate pools to produce other metabolites. Indeed, hiBMEC α-KG treatment increased glutamate secretion in hiBMEC in a dose-dependent manner. This demonstrates that by providing the hiBMEC with another TCA fuel source, glutamate pools could be restored, and excess glutamate was secreted from the cells. However, α-KG decreased hpBMEC glutamate secretion and decreased glycolysis in both cell types. hpBMEC may prevent glutamate overproduction to protect against excitotoxicity. It is not clear how the added α-KG decreased glycolysis in both cell types. Activity of glutamate dehydrogenase (GDH), the enzyme that converts glutamate to α-KG, regulates glycolytic levels by modulating transcription of GLUT1 [291]. Elevated GDH activity increases glycolysis [291]. Therefore, when BMEC are supplemented with α-KG, GDH activity may decrease, thereby decreasing glycolysis.

4.5. Limitations:

My data show clear distinctions in glutamine metabolism between hpBMEC and hiBMEC; however, this study is not without limitations. I compared hpBMEC and hiBMEC, each from one donor. Transcriptomic data for both were compared to publicly available data for cells from other donors to ensure their validity in cells from other donors; however, metabolomic data were only used from our cells and assumed to be representative of cells from other donors. Our metabolomic data was collected using a $^{13}C_5$-glutamine tracer, which limited predictions of which glutamine carbons were metabolized into which downstream metabolites. This tracer also did not provide information on glutamine nitrogen molecule movement through

the TCA cycle and downstream metabolites. In the future, non-uniformly labeled tracers should be used for both carbon and nitrogen to provide more detailed insight into atom movements.

While hpBMEC are assumed to be more similar to *in vivo* human BMEC, hpBMEC may also not be a good model of *in vivo* human BMEC metabolism. hpBMEC and hiBMEC in this study were cultured in static conditions and on tissue culture polystyrene. Both flow [292], [293], [294], [295] and substrate stiffness [296] are known to impact endothelial cell metabolism, and thus may impact our models.

4.6. Conclusions:

hiBMEC have elevated glutamine flux through fatty acid, asparagine, and glutathione synthesis pathways and reduced glutamate secretion compared to hpBMEC. These essential differences in glutamine metabolism between the two BMEC types may alter their function in disease models, and therefore are essential to take into consideration when choosing a cellular model of the BBB. In this chapter and the previous chapter, I examined the limitations of using hiBMEC as a model for BMEC glucose and glutamine metabolism. hiBMEC have similar glucose metabolism, but significantly altered glutamine metabolism compared to hpBMEC. This knowledge is used to inform the interpretation of the results in the next two chapters as I use hiBMEC to examine the effects of APOE genotype and sedentary lifestyle on BMEC metabolism and barrier function.

Chapter 5: APOE genotype impacts BMEC metabolism and function

5.1. Introduction:

In previous chapters, I demonstrated that the stress hormone angiotensin II increased endothelial dysfunction in female endothelial cells, and that induced pluripotent stem cell derived brain microvascular endothelial-like cells (hiBMEC) are a good model of BMEC glucose metabolism but have different glutamine metabolism than primary BMEC (hpBMEC). In this chapter, I build on that work to examine how another risk factor for Alzheimer's disease (AD), the APOE ε4 genotype, impacts hiBMEC metabolism and function.

The APOE ε4 genotype is the highest genetic risk factor for AD. Individuals homozygous for the APOE ε4 allele have a ten-fold higher risk for AD compared to individuals homozygous for the APOE ε3 allele [297]. In humans, the APOE ε4 genotype is correlated with many AD biomarkers, including decreased brain glucose metabolism [298], blood-brain barrier [299], and increased amyloid-β and tau accumulation [300]. In mice, the APOE ε4 genotype reduced BMEC barrier function [130], [301], [302], with one study implicating accelerated matrix degradation [302]. *In vitro,* APOE ε4 astrocytes had decreased glycolysis, but increased pentose phosphate pathway activity as compared to APOE ε3 astrocytes, leading to increased lipid and nucleotide biosynthesis [303]. In transgenic mouse BMEC, APOE ε4 BMEC also had reduced glycolysis and lipid levels compared to APOE ε3 BMEC [130]. Notably, none of these studies examined mechanisms through which the APOE genotype itself regulates barrier function or cellular metabolism.

In this chapter, I focus on two mechanisms through which APOE ε4 regulates glucose metabolism and barrier function: reduced insulin signaling and reduced sirtuin 1 (SIRT1). The first mechanism investigated, reduced insulin signaling, is based on extensive work in neurons, which shows the APOE ε4 protein has a higher binding affinity for insulin receptors (INSR) compared to the APOE ε3 protein. INSR then remains bound to APOE ε4 in the endosome, which reduces INSR endosomal recycling. Reduced INSR recycling leads to reduced INSR on the cell membrane, which can then decrease insulin binding and thus impair insulin signaling [304]. One of the intracellular insulin signaling pathways includes phosphoinositide 3-kinase (PI3K) activation, which leads to Akt phosphorylation. Akt then regulates translocation of the primary

glucose transporter GLUT1 to the cell membrane [305], [306] and, therefore, glycolysis (Fig. 5.1). The second mechanism focuses on SIRT1, a protein deacetylase whose transcription is inhibited by the APOE ε4 protein [138], [307]. Reductions in SIRT1 are associated with reduced GLUT1 [308] and the rate limiting glycolytic enzyme hexokinase 2 (HK2) [141]. Similarly, increasing SIRT1 activity increases tight junction proteins zonulus occludins 1 (ZO-1) [309] and claudin-5 [310]. Therefore, I investigated whether the APOE ε4 genotype leads to low SIRT1, which in turn decreases glycolysis and barrier function in hiBMEC (Fig. 5.2).

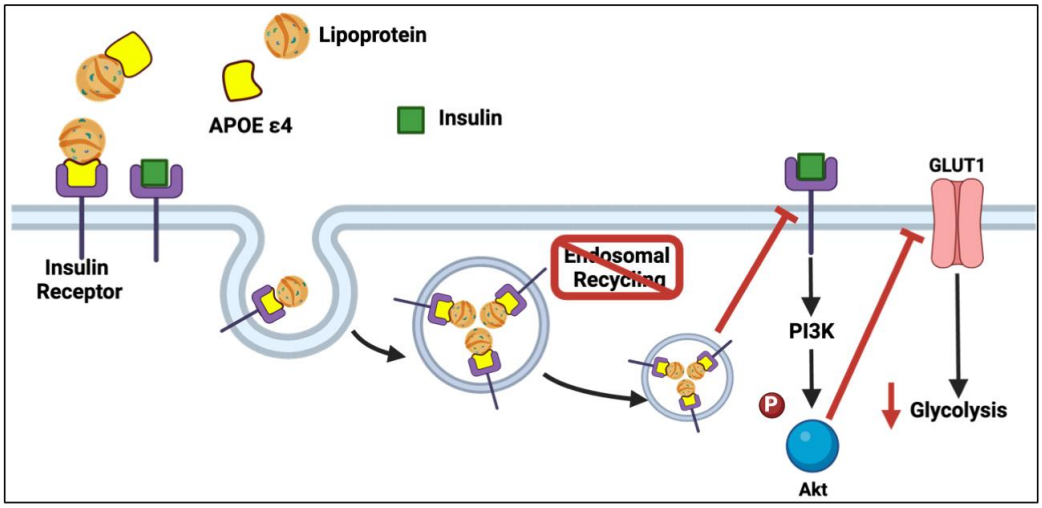


Figure 5.1. Hypothesized mechanism by which APOE ε4 reduces glycolysis via insulin signaling. APOE ε4 proteins bind to lipoproteins in the circulation and then bind competitively to insulin receptors on the cell membrane. These APOE-lipoprotein-insulin receptor complexes are internalized into endosomes. Increased binding affinity between APOE ε4 and insulin receptors prevents endosomal recycling of insulin receptors back to the cell membrane, instead targeting them to lysosomes for degradation. This process reduces the insulin receptors available on the cell membrane for insulin signaling, which then impairs GLUT1 transcription and translocation to the membrane and glycolysis.

BMEC function as a protective barrier between the blood and the brain and specifically transport metabolites to meet the energy demands of surrounding cells. As such, in this chapter I examined the role of the APOE ε4 genotype in glucose hypometabolism and BBB breakdown using hiBMEC as a cellular model. I hypothesized that the APOE ε4 genotype would reduce glycolysis through reduced insulin and SIRT1 signaling, and that the reduction in SIRT1 would also decrease barrier function. I used CRISPR/Cas9 to generate iPSC homozygous for the APOE ε3 and ε4 alleles, differentiated them into hiBMEC, and then measured barrier function using transendothelial resistance (TEER) and immunofluorescent labeling. I

measured differences in glycolysis between APOE ε3 and ε4 hiBMEC using YSI, Seahorse Glycolytic Rate Assay, Western blotting for glycolytic enzymes, and metabolic mass spectrometry. Finally, I probed both the insulin signaling and SIRT1 mechanisms to demonstrate their involvement in reducing glycolysis and barrier function in APOE ε4 hiBMEC.

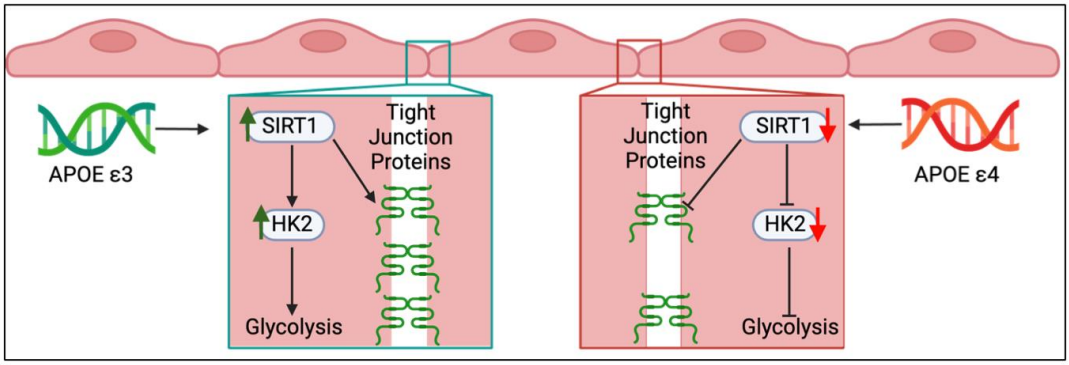


Figure 5.2. Hypothesized pathway by which APOE ε4 reduces glycolysis and barrier function via SIRT1. APOE ε4 binds to the SIRT1 promotor and reduces its transcription, thereby reducing SIRT1 protein. Lower SIRT1 reduces HK2, thereby impairing glycolysis. SIRT1 also reduces expression of tight junction proteins, thereby reducing barrier function.

5.2. Methods:

5.2.1. Cell Culture*:* IMR90 iPSC were maintained as described in Chapter 3. iPSC were also differentiated into hiBMEC as described in Chapter 3; however, to enhance control over media components, Neurobasal medium (NB; Thermo Fisher, 21103049) supplemented with 8.5 mM glucose and 4.5 mM glutamine was substituted for the human endothelial cell serum free medium (hESFM) [311].

5.2.2. CRISPR/Cas9*:* IMR90 iPSC are homozygous for the APOE ε3 allele [312]. Clustered regularly interspaced short palindromic repeats (CRISPR)/Cas9 technology was used to induce a point mutation and alter the iPSC to be homozygous for the APOE ε4 allele based on previously established protocols [313]. Small guide RNA (sgRNA; Table 5.1) targeting rs429358 (IDT) was resuspended to 100 µM in Resuspension Buffer R (Thermo Fisher, MPK10096). Single-stranded oligodeoxynucleotides (ssODN)

were also resuspended to 200 μM in Resuspension Buffer R. iPSC at 80% confluence were dissociated using TrypLE (Thermo Fisher, 12605010), centrifuged at 300 x g for 5 minutes, then resuspended at 13.5 x 10^6 cells/mL in 100 µL of Resuspension Buffer R. 3 µL sgRNA, 2 µL ssODN, 3 µL Alt-R Cas9 Nuclease V3 (IDT), and 7 µL cell suspension were combined and electroporated using a Neon Transfection Instrument (Thermo Fisher) at 1100 V, with 2 pulses of 30 ms each. Following electroporation cells were replated on Matrigel (Corning, 354230) coated plates in mTeSR-Plus medium (STEMCELL Technologies, 100-0276) supplemented with 10 µM Y-27632 (Tocris, 1254) and 1:1000 Alt-R HDR Enhancer (IDT, 1081072).

Table 5.1. CRISPR/Cas9 and genotyping sequences.

Item	**Sequence**
sgRNA	GCGGACATGGAGGACGTG**T**GCGG
ssODN	AGGAGCTGCAGGCGGCGCAGGCCCGGCTGGGCGCGGACATGGAGGAT GTA**C**GTGGCCGCCTGGTGCAGTACCGCGGCGAGGTGCAGGCCATGCTC GGCCAG
APOE ε3 Forward	GTAAAACGACGGCCAGTGTCTCTGTCTCCTTCTCTC
APOE ε3 Reverse	AGGTCATCGGCATCGCGGA
APOE ε4 Forward	GTAAAACGACGGCCAGACGAGACCATGAAGGAGTTG
APOE ε4 Reverse	ACACTGCCAGGCGCTTCTG

5.2.3. iPSC expansion and Genotyping*:* Following the CRISPR/Cas9 process, iPSC were cultured to 80% confluence, passaged using Accutase (Thermo Fisher, A1110501), replated at 15,000 cells/well, and allowed to grow from single cells into colonies in which each cell was a replicate of a single cell. Individual colonies were expanded, and DNA was sequenced to find successfully edited colonies. DNA was isolated using a Quick-DNA Miniprep Plus Kit (Zymo Research; D4068) following manufacturer's protocol. PCR reactions were run using AmpliTaq Gold 360 Master Mix (Thermo Fisher; 4398881) and associated protocols. Samples were thermally cycled using a Pro Flex Thermal Cycler (Thermo Fisher) with an initial 10-minute activation at 95°C followed by 40 cycles of 30 seconds denaturing at 95°C, 30 seconds of annealing at 70°C, and 60 seconds/kb at 72°C. A final extension was performed at 72°C for 7 minutes before cooling back to 4°C. Samples were then sent to Genewiz (Azenta Life Sciences) for sequencing.

Sequencing results were processed through the Synthego ICE CRISPR Analysis tool and successful homozygous APOE ε3 (isogenic controls) and ε4 (edited samples) were expanded and frozen in liquid nitrogen for future use.

5.2.4. TEER*:* To measure trans-endothelial electrical resistance (TEER), APOE ε3 and ε4 hiBMEC were subcultured onto 0.4 µm ECM-coated Transwell filters in NB medium with 2% B27 (Thermo Fisher, 17504001), 20 ng/mL basic fibroblast growth factor (bFGF; Peprotech, 100-18B), and 10 µM retinoic acid (RA; Millipore Sigma, R2625-50MG). Two days post-subculture, TEER was measured in triplicate using STX2-Plus electrodes and the Epithelial Volt/Ohm Meter 3 (EVOM3; World Precision Instruments). Data points shown are individual wells averaged from triplicate technical replicates measured in each well.

5.2.5. Immunostaining and JAnaP: hiBMEC in 96-well plates were washed twice with PBS and fixed with either 4% paraformaldehyde (PFA; Millipore Sigma, P6148) (GLUT1, ZO-1, occludin) or ice-cold 100% methanol (Millipore Sigma, 646377) (claudin-5) for 20 minutes. Cells were washed 2x for 5 minutes in PBS and then blocked and permeabilized for 1 hour at room temperature in 5% normal goat serum (Millipore Sigma, S26) in PBS supplemented with 0.2% Triton X-100 (Alfa Aesar, A16046). Cells were washed 2x for 5 min in PBS and then incubated overnight at 4°C in primary antibodies (Table 5.2). The next day, cells were washed 3x in PBS and then incubated in either Alexa Fluor 594 goat anti-rabbit or Alexa Fluor 488 goat anti-mouse secondary antibodies (1:1000) and Hoechst (1:2000) for 1 hour at room temperature. The cells were then washed 3 times for 5 minutes each in PBS before imaging Z-stacks of the junctions on an Eclipse Ti2 spinning disk confocal microscope (Nikon) at 60X magnification. 3 images were taken per well, and 9 wells were imaged per treatment group. Maximum intensity projections were created in Fiji of each image. The Junction Analyzer Program (JAnaP) [314] was then used to characterize the percent of continuous junctions surrounding each cell. Continuous junctions were classified as areas along the traced edge of the cell with > 15 pixels of continuous labeling. 5 cells were quantified per image.

Table 5.2. Primary antibodies used for immunofluorescence.

Antibody	Manufacturer	Catalogue Number	Dilution
ZO-1	Cell Signaling Technology	13663S	1:100 (Immunostaining)
Occludin	Cell Signaling Technology	91131S	1:100 (Immunostaining)

Claudin 5	Thermo Fisher Scientific	35-2500	1:100 (Immunostaining)
GLUT1	Thermo Fisher Scientific	21829-1-AP	1:100 (Immunostaining) 1:4000 (Western Blot)

5.2.6. YSI*:* Glucose and glutamine uptake and lactate and glutamate secretion, as well as transport of each metabolite, were measured using a YSI 2950 (Yellow Springs Instruments, 527690). 2 days after subculture, media samples were collected from either 12 well plates or both the apical and basolateral chambers of Transwell inserts at 0- and 24-hours. Glucose, lactate, glutamine, and glutamate measurements were measured on the YSI. Metabolite uptake was calculated by subtracting metabolite concentrations at 24 hours from the initial concentrations. Metabolite secretion was calculated by subtracting initial concentrations from the 24-hour metabolite concentrations.

5.2.7. Seahorse*:* A Seahorse glycolytic rate assay (GRA; Agilent, 103344-100) was used to evaluate glycolytic rate in APOE ε3 and ε4 hiBMEC. hiBMEC were seeded at 50,000 cells/well in 96-well Seahorse assay plates. In experiments with Ex-527 (Millipore Sigma, E7034), cells were treated with 10 μM Ex-527 for 24 hours. On the day of the assay, cells were washed once with fresh Seahorse DMEM, and then incubated for 1 hour in Seahorse DMEM supplemented with 10 mM glucose, 2 mM glutamine, 1 mM pyruvate, and 1% B27 before running the GRA in a Seahorse XFe96 following manufacturer's instructions.

5.2.8. Western Blotting*:* 2 days after subculture, cells were lysed in RIPA buffer (Thermo Fisher, 89901) supplemented with Halt Protease and Phosphatase Inhibitor (Fisher Scientific, PI78440) and Deacetylation Inhibition Cocktail (Santa Cruz Biotechonology, sc-362323). Protein levels were evaluated in APOE 3 and ε4 hiBMEC as described in Chapter 3.

5.2.9. Membrane Fractionation*:* To quantify GLUT1 levels in the cell membrane of APOE ε3 and ε4 hiBMEC, a Mem-PER Plus Membrane Protein Extraction Kit (Thermo Fisher, 89842) was used. APOE ε3 and ε4 hiBMEC cultured in 12-well plates were lysed in membrane permeabilization buffer supplemented with Halt Protease and Phosphatase Inhibitor. Samples were agitated for 10 minutes at 4°C and then centrifuged at 17,000 x g for 10 minutes at 4°C. Supernatant containing the cytosolic proteins was removed

and stored on ice. The pellet was then resuspended in membrane solubilization buffer, agitated for 30 minutes at 4°C, and then centrifuged at 17,000 x g for 30 min at 4°C. Protein was quantified, and western blot was run following previously described protocols.

5.2.10. SIRT1 Activity Assay*:* SIRT1 activity was quantified using a fluoremetric SIRT1 activity assay (abcam, ab156065) run according to manufacturer's protocols. 2 technical replicates were run for each sample. Protein concentrations from APOE ε3 and ε4 hiBMEC were quantified using a BCA assay (Thermo Fisher, 23225). SIRT1 fluorescence readings were normalized to total protein levels for each biological replicate.

5.2.11. Mass Spectrometry: APOE ε3 and ε4 hiBMEC were cultured in NB medium supplemented with 8.5 mM glucose, 4.5 mM glutamine, and 2% B27 for 2 days following subculture. Cells were then incubated for 24 hours in NB medium supplemented with 4.5 mM glutamine and 8.5 mM U-$^{13}C_6$-glucose (Fisher Scientific, NC9207695). Metabolites were extracted and mass spectrometry was run by the University of Colorado School of Medicine Metabolomics Core as described in Chapter 3.

5.2.12. Statistics*:* Statistics were analyzed in GraphPad Prism. Non-parametric Mann-Whitney tests were used to compare APOE ε3 and ε4 hiBMEC. In experiments with Ex-527 and SRT1720, Two-Way ANOVA with Fisher's Least Significant Difference test was used.

5.3. Results

The APOE ε4 genotype is associated with BBB breakdown and brain glucose hypometabolism. I therefore explored how the APOE ε4 genotype decreases barrier strength and glucose metabolism in BMEC. I also explored other metabolic alterations that occur as a result of changing APOE genotype to understand how systemic BMEC metabolism may be altered by the APOE ε4 genotype.

5.3.1. hiBMEC with the APOE ε4 genotype had reduced barrier function.

APOE ε4 carriers have elevated BBB permeability relative to APOE ε3 homozygotes [315]. I began by validating this phenotype in hiBMEC. CRISPR/Cas9 was used to insert a point mutation and thereby change iPSC homozygous for the APOE ε3 allele to iPSC homozygous for the APOE ε4 allele (Fig. 5.3A). These

iPSC were then differentiated to hiBMEC [216], [311] and barrier function was assessed using TEER and immunofluorescence. TEER was 36% lower in APOE ε4 hiBMEC compared to ε3 hiBMEC ($p < 0.0001$; Fig 5.3B). Tight junction protein ZO-1 continuity was 8.7% lower in APOE ε4 hiBMEC compared to ε3 hiBMEC ($p < 0.0001$), suggesting that loss of ZO-1 may contribute to BBB breakdown in APOE ε4 BMEC. Continuity of tight junction proteins occludin and claudin-5 did not significantly differ by genotype (Fig. 5.3C-D).

5.3.2. APOE ε4 hiBMEC had reduced glucose metabolism relative to APOE ε3 hiBMEC.

Since brain glucose metabolism is reduced in individuals with the APOE ε4 genotype, and BMEC transport glucose from the blood into the brain, I next investigated how the APOE ε4 genotype alters BMEC glucose metabolism. APOE ε4 hiBMEC had 31% lower glucose uptake than APOE ε3 hiBMEC ($p < 0.0001$; Fig. 5.4A), as measured by YSI. Lactate secretion was 9% lower in APOE ε4 hiBMEC, although this was not statistically significant ($p = 0.0780$; Fig. 5.4B). The lactate:glucose ratio, which indicates how much glucose is metabolized via glycolysis versus through oxidative respiration, was 31% higher in APOE ε4 hiBMEC ($p < 0.0001$; Fig. 5.4C). The basal glycolytic rate, measured by the Seahorse glycolytic proton efflux rate (GlycoPER), was 20% lower in APOE ε4 hiBMEC than ε3 hiBMEC ($p < 0.0001$; Fig. 5.4D-E). Compensatory glycolysis, calculated as the glycolytic rate when mitochondrial metabolism is inhibited, was 24% lower in APOE ε4 hiBMEC compared to APOE ε3 hiBMEC ($p < 0.0001$; Fig. 5.4F). Overall, these data indicate APOE ε4 hiBMEC have a decreased glycolytic rate compared to APOE ε3 hiBMEC, but that APOE ε4 hiBMEC may metabolize more glucose through glycolysis than oxidative phosphorylation compared to APOE ε4 hiBMEC.

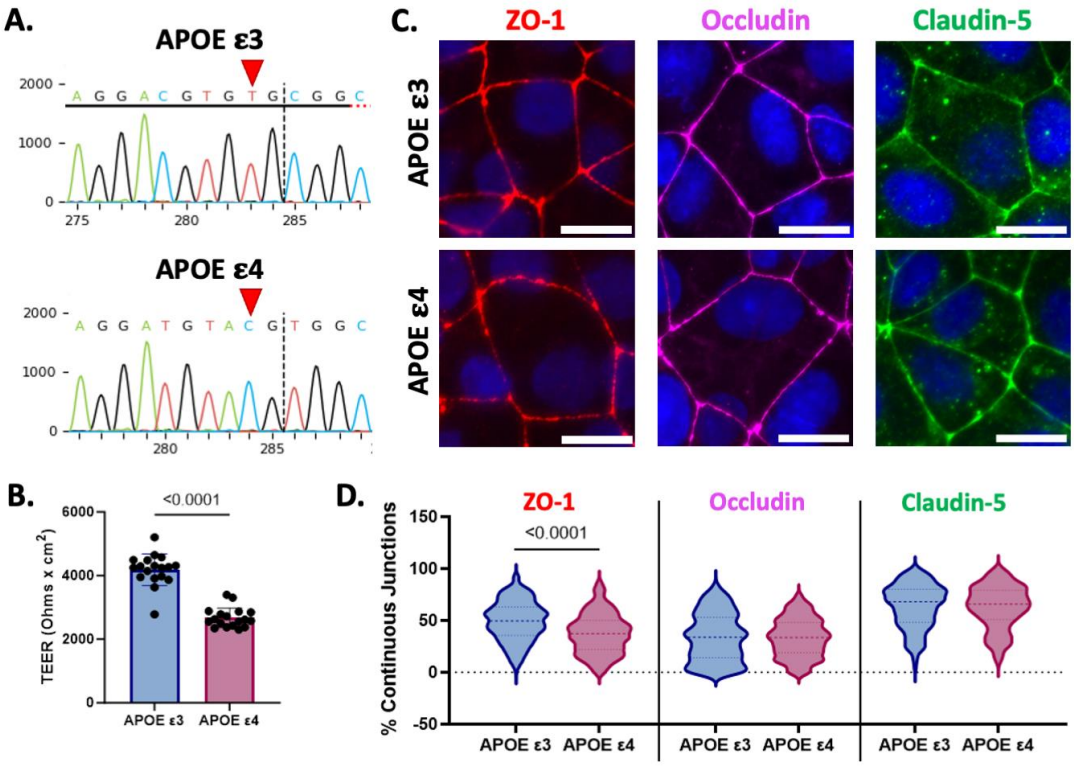


Figure 5.3. APOE ε4 BMEC had reduced barrier function. (A) Sequencing electropherograms of iPSC edited with CRISPR/Cas9 targeting the APOE gene. Red arrows indicate the nucleotide that determines the APOE genotype in APOE ε3 isogenic control iPSC and edited APOE ε4 iPSC. **(B)** TEER measured on APOE e3 and e4 hiBMEC (n = 18 samples per genotype). **(C)** Immunofluorescent labeling of tight junction proteins in APOE ε3 vs. APOE ε4 hiBMEC. ZO-1 (red), occludin (magenta), and claudin-5 (green). **(D)** Percent of continuous junctions quantified via Junction Analyzer Program. Scale bar = 20 μm (n = 176 - 327 cells from 16 biological replicates). Data analyzed using Mann-Whitney tests.

5.3.3. Glucose transporter and rate limiting glycolytic enzymes were lower in APOE ε4 hiBMEC.

To evaluate why glucose metabolism was lower in APOE ε4 compared to APOE ε3 hiBMEC, I measured glucose transporter and glycolytic enzymes via Western blot (representative blots in Fig. 5.5A). I first measured APOE protein levels via Western blot. APOE ε4 protein levels were 330% higher in APOE ε4 hiBMEC compared to APOE ε3 hiBMEC ($p < 0.0001$; Fig. 5.5B). Glucose entry into BMEC primarily occurs through the glucose transporter GLUT1. GLUT1 levels were 38% lower in APOE ε4 hiBMEC compared to ε3 hiBMEC ($p = 0.0003$; Fig. 5.5C). Glycolytic enzymes include hexokinase (HK) 1 and 2, 6-phosphofructo-2-kinase/fructose-2,6-biphosphatase 3 (PFKFB3), glyceraldehyde 3-phosphate dehydrogenase (GAPDH), and lactate dehydrogenase (LDH) (Fig. 5.5D-H). Of these enzymes, HK2 and

PFKFB3, both of which are rate limiting glycolytic enzymes, were 20% and 24% lower, respectively, in APOE ε4 compared to APOE ε3 hiBMEC (p = 0.0188 and p = 0.0106). In addition, I measured levels of glucose-6-phosphate dehydrogenase (G6PD), the rate limiting enzyme for glucose entry into the pentose-phosphate pathway (PPP), and glutamine fructose-6-phosphate amidotransferase (GFAT), the rate limiting enzyme for glucose entry into the hexosamine biosynthesis pathway (HBP). Neither G6PD nor GFAT levels were different between APOE ε3 and ε4 hiBMEC (Fig. 5.5I-J). Lower protein levels of GLUT1 and rate limiting enzymes HK2 and PFKFB3 correlate with the previously measured reduced glycolysis in APOE ε4 hiBMEC.

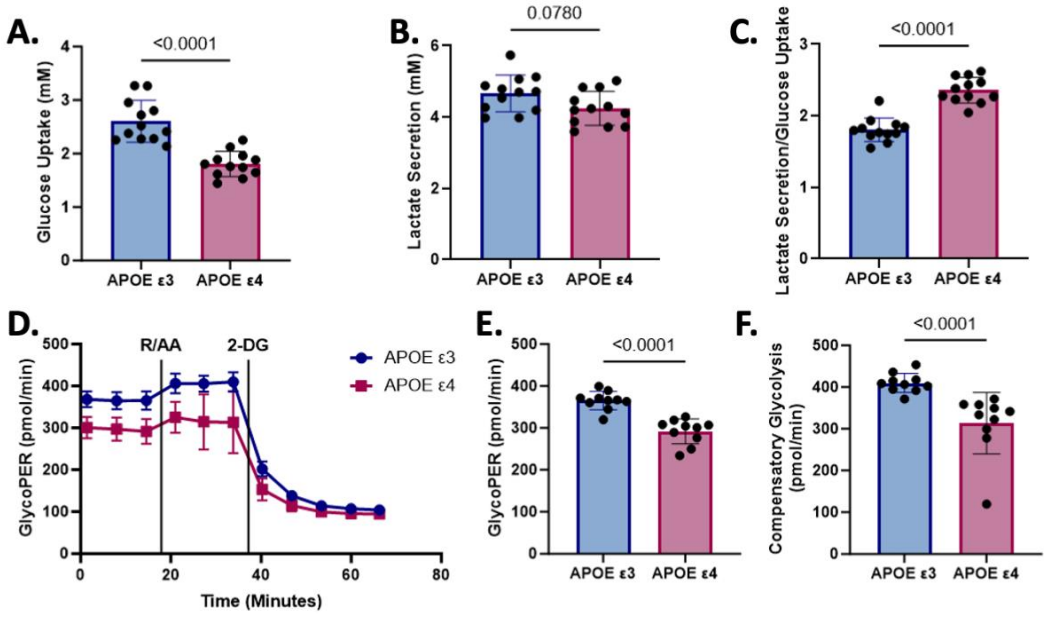


Figure 5.4. APOE ε4 hiBMEC had reduced glycolysis relative to APOE ε3 hiBMEC. YSI measurements of **(A)** glucose uptake, **(B)** lactate secretion, and **(C) l**actate-to-glucose ratio over 24 hours (n = 12 samples per genotype). **(D)** GlycoPER measured via Seahorse Glycolytic Rate Assay in APOE ε3 vs. APOE ε4 hiBMEC. **(E)** basal GlycoPER and **(F)** compensatory glycolysis (n = 10 samples per genotype). Data analyzed using Mann-Whitney tests.

5.3.4. APOE ε3 and ε4 hiBMEC had similar metabolite transport and polarization.

While glucose metabolism is important for energy production in BMEC themselves, BMEC are also responsible for transporting glucose from the blood into the brain for parenchymal brain cells to use as an energy source. To measure hiBMEC metabolite transport and polarization, APOE ε3 and ε4 hiBMEC were seeded on Transwell inserts and then treated with 8.5 mM glucose on the apical side and 0 mM glucose

(8.5 mM mannitol as an osmotic control) on the basolateral side (Fig. 5.6A). After 24 hours, both APOE ε3 and ε4 hiBMEC transported 0.78 ± 0.04 mM glucose from the apical side to the basolateral side (Fig. 5.6B). Lactate secretion was polarized, with both cell types secreting 0.53 ± 0.03 mM lactate on the basolateral side, and 2.60 ± 0.12 mM lactate on the apical side (Fig 5.6C). Therefore, despite reduced glucose metabolism in APOE ε4 hiBMEC, glucose transport is unchanged indicating the cells are able to consistently control metabolite transport regardless of differences in their own metabolic demands.

5.3.5. Impaired insulin signaling may contribute to reduced glycolysis in APOE ε4 hiBMEC.

APOE ε4 protein inhibits INSR recycling and glycolysis in neurons [133]. I hypothesized that APOE ε4 hiBMEC would also have reduced INSR recycling, leading to decreased GLUT1 translocation to the cell membrane, and thereby decreasing glycolytic rate (Fig. 5.1). I first investigated how INSR levels differed between APOE ε3 and ε4 hiBMEC by Western blot. APOE ε4 hiBMEC had 36% lower INSR protein levels than APOE ε3 hiBMEC ($p = 0.0002$; Fig. 5.7A-B). Next, I determined how insulin signaling differed in APOE ε3 and ε4 hiBMEC by treating cells with insulin and probing for phosphorylated-Akt (p-Akt) by Western blot (Fig. 5.7C). APOE ε4 hiBMEC had a 37% lower p-Akt:Akt ratio without insulin stimulation ($p = 0.0186$), and an 82% lower p-Akt:Akt ratio with insulin stimulation ($p = 0.0029$). While APOE ε3 hiBMEC increased the p-Akt:Akt ratio by 30% following insulin stimulation ($p = 0.0340$), APOE ε4 hiBMEC did not significantly increase p-Akt:Akt ratio with insulin stimulation (Fig. 5.7D). These data suggest that insulin signaling is reduced in APOE ε4 hiBMEC, possibly through reduced INSR levels.

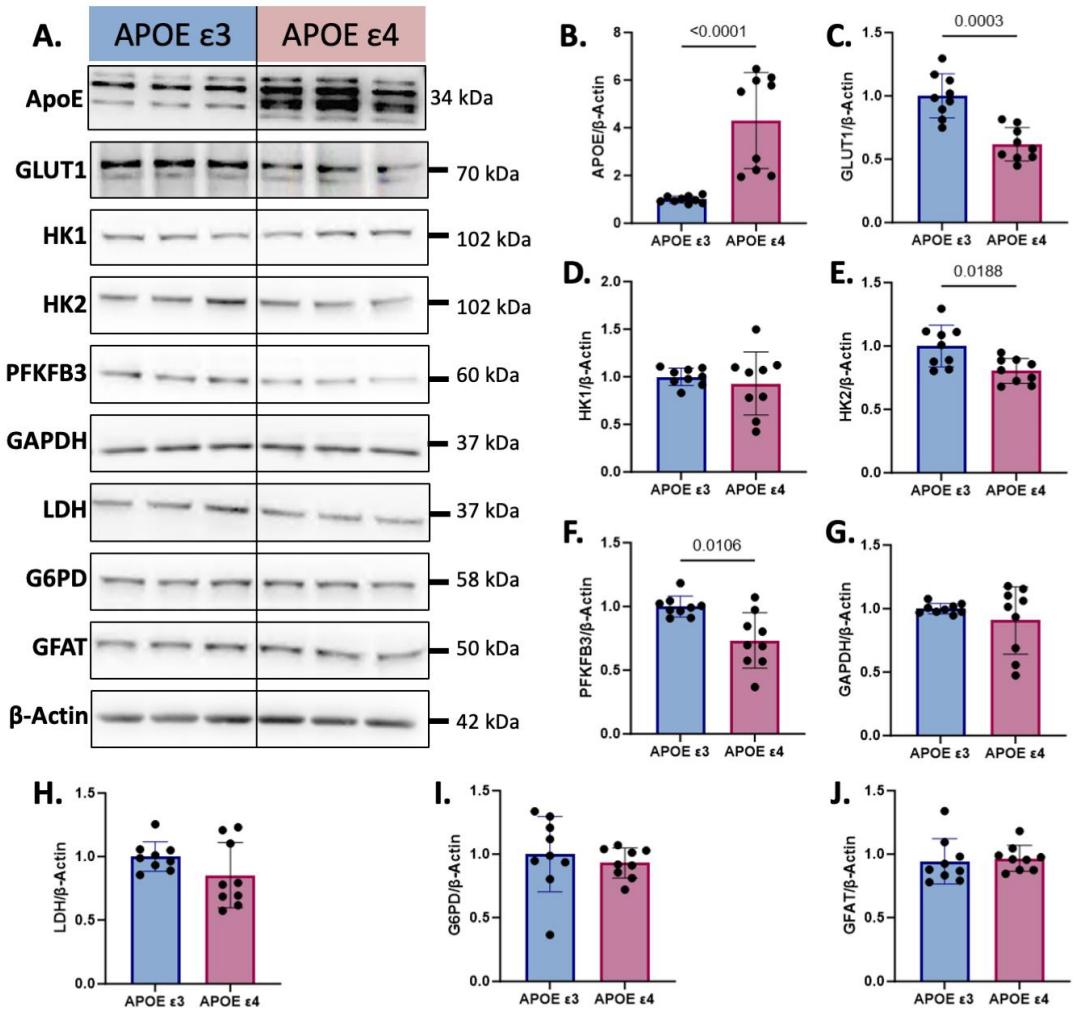


Figure 5.5. Glucose transporter and rate limiting glycolytic enzymes were reduced in APOE ε4 hiBMEC. **(A)** Representative Western blots with quantifications of **(B)** APOE **(C)** GLUT1 **(D)** hexokinase I (HK1), **(E)** hexokinase 2 (HK2), **(F)** 6-phosphofructo-2-kinase/fructose-2,6-biphosphatase 3 (PFKFB3), **(G)** glyceraldehyde 3-phosphate dehydrogenase (GAPDH), **(H)** lactate dehydrogenase (LDH), **(I)** glucose-6-phosphate dehydrogenase (G6PD), and **(J)** glutamine fructose-6-phosphate amidotransferase (GFAT) relative to housekeeper protein β-Actin (n = 9 samples per genotype). Data were normalized to APOE ε3 protein levels in each experiment and analyzed using Mann-Whitney test.

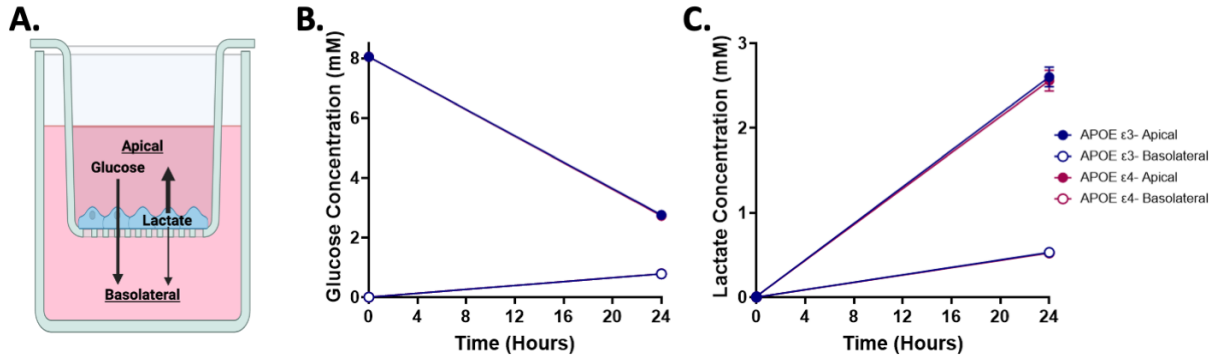


Figure 5.6. Glucose transport was lower in APOE ε4 hiBMEC. (A) APOE ε3 and ε4 hiBMEC were seeded on Transwell inserts in NB medium containing 8.5 mM glucose in the apical chamber and 0 mM glucose in the basolateral chamber (8.5 mM mannitol as an osmotic control) for 24 hours. Media samples were collected from both chambers at 0- and 24 hours and YSI was used to quantify **(B)** glucose and **(C)** lactate concentrations (n = 12 samples per genotype). Data were analyzed with Two-way ANOVA with Fishers Least Significant Difference Test.

I hypothesized that reduced insulin signaling in APOE ε4 cells would reduce GLUT1 translocation to the membrane. Indeed, membrane GLUT1 was 31% lower in APOE ε4 hiBMEC relative to APOE ε3 hiBMEC ($p = 0.0017$; Fig. 5.7E, F). Then, I treated APOE ε4 hiBMEC with 10 µg/mL insulin to stimulate insulin signaling and promote GLUT1 translocation to the membrane, and 1 µM Wortmannin to inhibit PI3K in the insulin signaling pathway, and thus GLUT1 translocation to the membrane (Fig. 5.7G). Insulin treatment did not increase GLUT1 translocation to the membrane. Wortmannin, however, decreased membrane GLUT1 by 32% ($p = 0.0213$; Fig. 5.5H), indicating that inhibition of the insulin signaling pathway decreased membrane. Finally, to determine how reduced insulin signaling and membrane GLUT1 corresponded with reduced hiBMEC glycolysis, I ran a Seahorse Glycolytic Rate Assay in which APOE ε4 hiBMEC were pretreated with insulin or Wortmannin for 30 minutes (Fig. 5.7I). Basal GlycoPER was not significantly elevated by with insulin but decreased by 8.4% with Wortmannin ($p = 0.0089$; Fig. 5.7J).

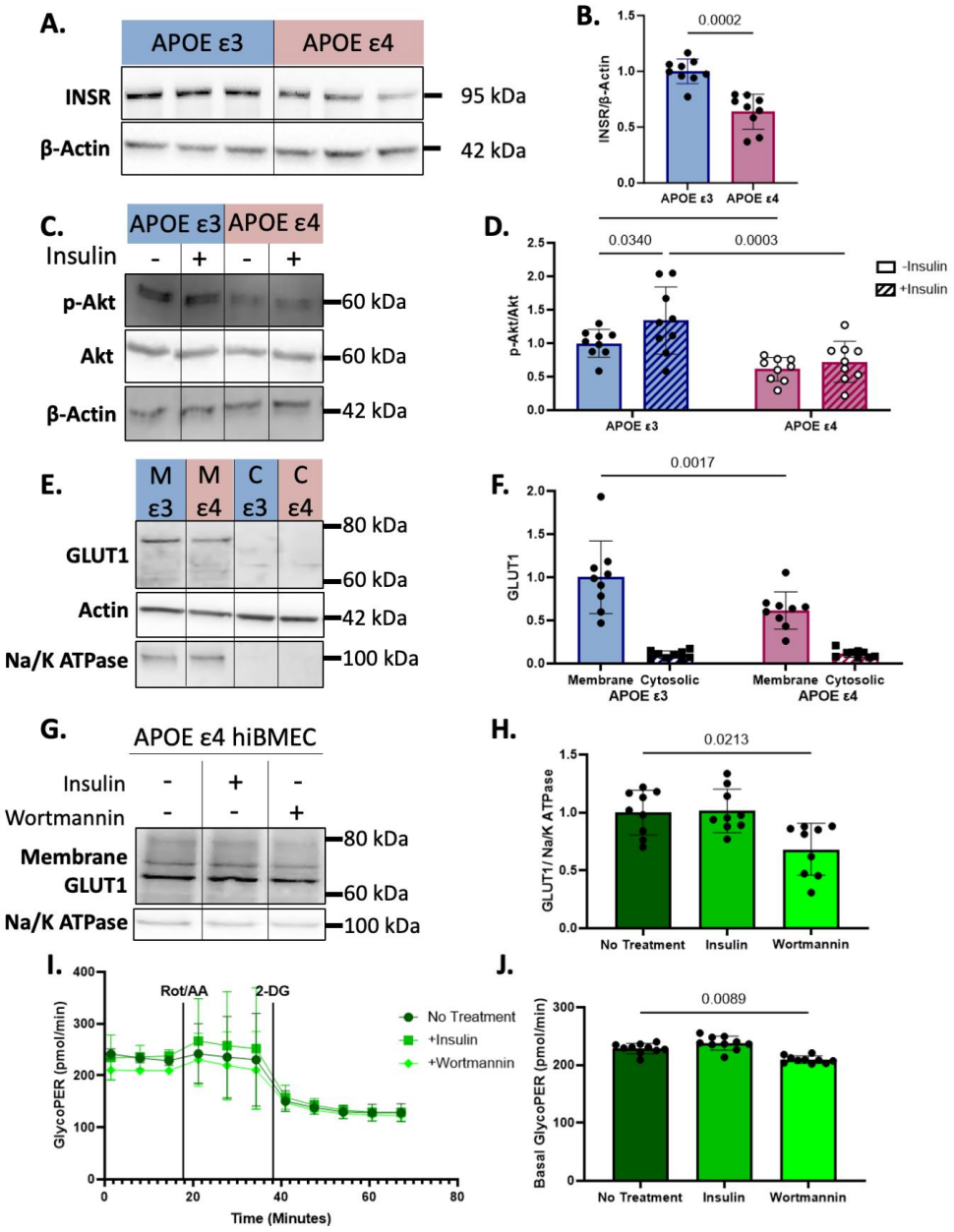


Figure 5.7. Impaired insulin signaling may have contributed to reduced APOE ε4 hiBMEC glycolysis. (A) Representative Western blots with **(B)** quantification of insulin receptor (INSR) protein levels in APOE ε3 and APOE ε4 hiBMEC (n = 9 samples per genotype). **(C)** Representative Western blots with **(D)** quantification of p-Akt and Akt in APOE ε3 and ε4 hiBMEC treated with 10 µg/mL insulin for 30 minutes (n = 9 samples per genotype). **(E)** Representative Western blots with **(F)** quantification of membrane and cytosolic GLUT1 in APOE ε3 and ε4 hiBMEC (n = 9 samples per genotype). **(G)** Representative Western blots with **(H)** quantification of membrane GLUT1 in APOE ε4 hiBMEC treated with 10 µg/mL insulin and 1 µM Wortmannin for 30 minutes (n = 9 samples per genotype). **(I)** Seahorse Glycolytic Rate Assay and **(J)** basal GlycoPER in APOE ε4 hiBMEC following treatment with 10 µg/mL and 1 µM Wortmannin for 30 minutes (n = 10 samples per treatment group). Data were analyzed using (**B)** Mann-Whitney test, **(D,F)** Two-way ANOVA with Fishers Least Significant Difference Test, and **(H,J)** Kruskall-Wallis with Dunn's multiple comparison test.

5.3.6. Decreased SIRT1 in hiBMEC did not change glycolysis but decreased barrier function.

APOE ε4 may impair glycolysis and barrier function through more than one mechanism. Since APOE ε4 is a suppressor of SIRT1 [138], [307], and low SIRT1 can decrease both glycolysis [141], [316] and barrier function [317], I next investigated if decreased SIRT1 impaired glycolysis and barrier function in APOE ε4 hiBMEC. I first measured SIRT1 protein levels via Western blot (Fig. 5.8A). SIRT1 was 27% lower in APOE ε4 hiBMEC than APOE ε3 hiBMEC ($p = 0.0188$; Fig. 5.8B). I then measured SIRT1 activity using a SIRT1 activity assay. SIRT1 activity was 10% lower in APOE ε4 hiBMEC compared to APOE ε3 hiBMEC ($p = 0.0030$; Fig. 5.8C). Next, I used the SIRT1 inhibitor EX-527 to investigate how reducing SIRT1 changed APOE ε4 hiBMEC glycolysis and barrier function. EX-527 decreased SIRT1 activity by 12% ($p = 0.0570$; Fig. 5.8D). However, EX-527 did not significantly alter GlycoPER (Fig. 5.8E-F). EX-527 decreased ZO-1 continuity by 26% ($p < 0.0001$; Fig. 5.8G-H) but did not significantly alter claudin-5 continuity (Fig 5.8I-J).

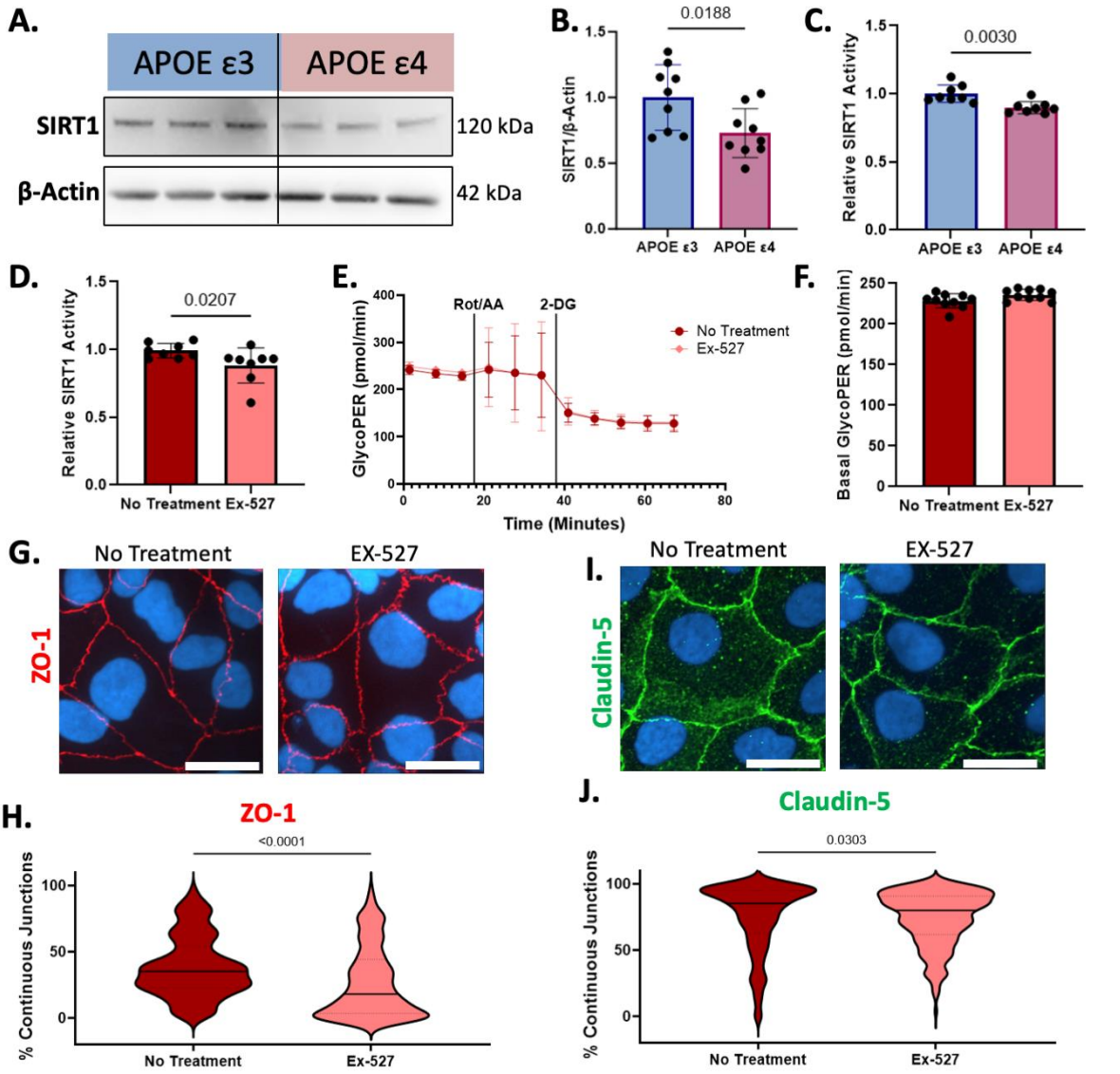


Figure 5.8. SIRT1 was lower in APOE ε4 hiBMEC. SIRT1 inhibition did not alter glycolysis but decreased barrier function in hiBMEC. (A) Representative Western blot and **(B)** quantification of SIRT1 relative to β-Actin protein levels in APOE ε3 and ε4 hiBMEC. Data were normalized to APOE ε3 (n = 9 samples per genotype) **(C)** Relative SIRT1 activity measured using a SIRT1 activity assay and normalized to APOE ε3 cells (n = 12 samples per genotype). **(D)** SIRT1 activity in APOE ε4 hiBMEC treated with 10 μM EX-527 for 24 hours relative to untreated hiBMEC (n = 16 samples per condition). **(E)** Seahorse Glycolytic Rate Assay and **(F)** quantified basal GlycoPER in APOE ε4 following treatment with 10 μM EX-527 for 24 hours (n = 10 samples per condition). Representative confocal microscopy images of APOE ε4 tight junction proteins **(G)** ZO-1 (red) and **(I)** claudin-5 with **(H, J)** quantification of junction continuity by the Junction Analyzer program (n = 225 – 251 cells per condition). Data analyzed using a Mann-Whitney Test.

5.3.7. APOE ε4 genotype induced systemic differences in hiBMEC metabolism.

Finally, I investigated how the complex metabolic network is altered in APOE ε3 versus APOE ε4 hiBMEC using metabolomics. APOE ε3 and ε4 hiBMEC were labeled with $^{13}C_6$-glucose for 24 hours, and then metabolic mass spectrometry was used to identify changes in metabolite abundance and labeling patterns between the genotypes. Partial least squares-discriminant analysis (PLS-DA) indicated that APOE ε3 and ε4 hiBMEC separated primarily along component 1 (33.8%; Fig. 5.9A). A variable importance plot (VIP) was then used to identify which metabolites most contributed to the PLS-DA separation (Fig. 5.9B). The metabolite with the highest VIP score was UDP-N-Acetyl-D-Glucosamine (UDP-GlcNAc), the primary product of the hexosamine biosynthetic pathway (HBP). Nucleotides including adenosine triphosphate (ATP), uridine diphosphate (UDP), cytidine triphosphate (CTP), adenosine diphosphate (ADP), and uridine triphosphate (UTP) were also elevated in APOE ε4 hiBMEC. Amino acids glutamine, serine, aspartate, alanine, and glutamate were all elevated in APOE ε3 hiBMEC, as were tricarboxylic acid (TCA) cycle metabolites α-ketoglutarate, succinate, and fumarate.

I then ran a metabolic pathway analysis using the labeled fraction metabolomics data to explore which pathways were most impacted by APOE genotype. Pathways with p-values < 0.1 ($\log_{10}$(p-value) > 1) and impact scores > 0.1 were considered significant with the pathways in the upper right corner being the most significantly impacted by APOE genotype. The most significantly perturbed pathways included starch and sucrose metabolism, alanine aspartate and glutamate metabolism, glycine metabolism, pyrimidine metabolism, the TCA cycle, and glycolysis/gluconeogenesis.

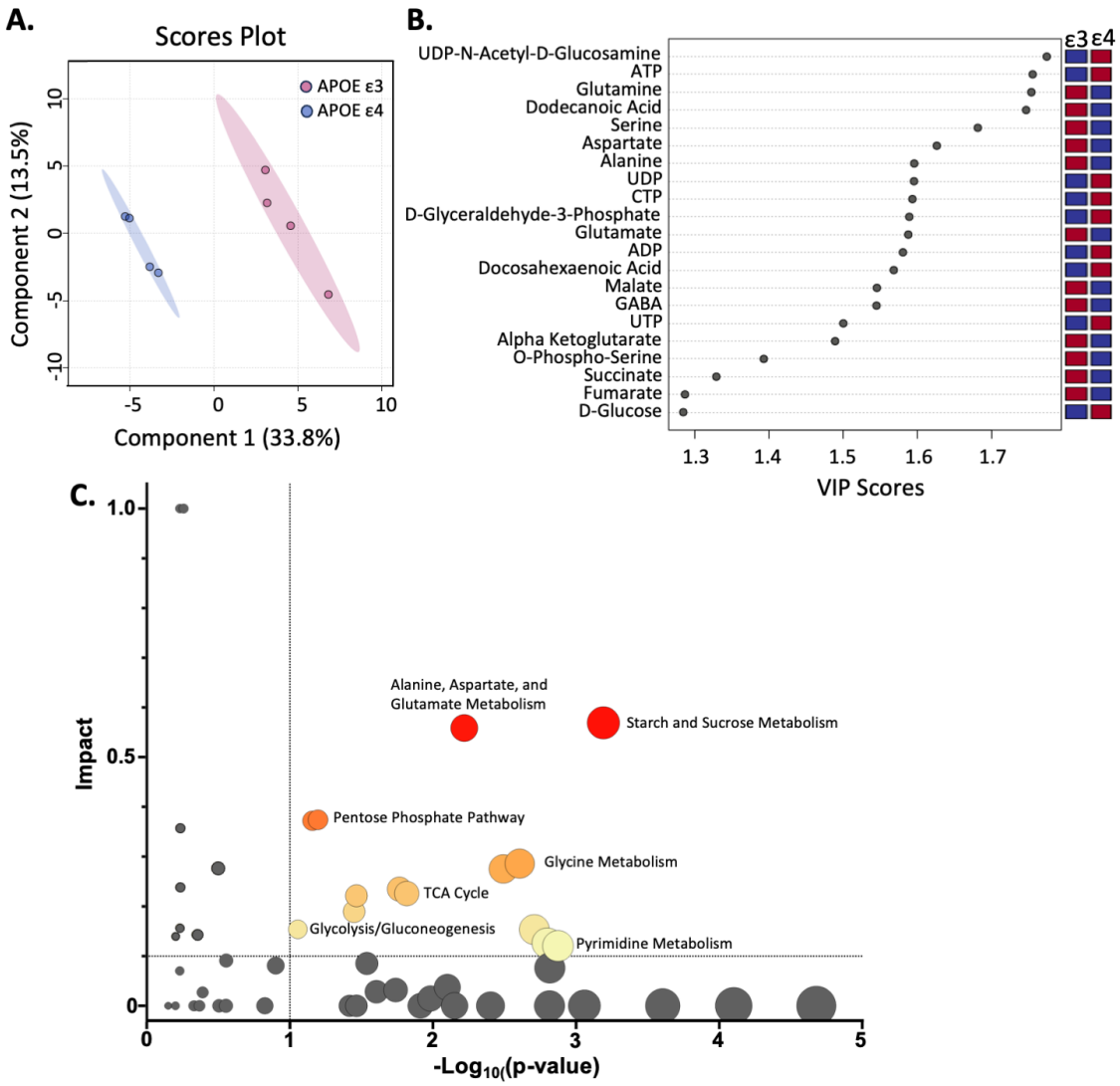


Figure 5.9. APOE ε4 genotype led to systemic differences in iPSC-BMEC metabolism. (A) PLS-DA of APOE ε3 and ε4 iPSC-BMEC based on metabolite labeling with $^{13}C_6$-glucose. (B) Variable importance plot (VIP) of the top 21 metabolites contributing to the separation in the PLS-DA. Red indicates higher metabolite concentrations, blue indicates lower metabolite concentrations. (C) Pathway analysis of intracellular metabolites in APOE ε3 and ε4 iPSC-BMEC. $-Log_{10}(p) > 1$ and Impact > 0.1 indicates metabolites in the pathway were significantly different in the two cell types. Impact score considers the number of nodes for the metabolites involved in the pathway and the number of shortest paths going through the node. (n = 4 samples per genotype).

5.4. Discussion

The APOE ε4 genotype is one of the largest risk factors for AD and is associated with reduced whole brain glucose metabolism and BMEC barrier function. Despite these correlations, there are few if any identified direct mechanisms through which the APOE genotype alters metabolism and barrier function.

Here, I demonstrated that APOE ε4 hiBMEC have reduced barrier function and glucose metabolism compared to APOE ε3 hiBMEC, and that reduced insulin signaling and SIRT1 may reduce glycolysis and barrier function in APOE ε4 hiBMEC. These findings indicate the APOE ε4 genotype induces glucose hypometabolism and BBB breakdown through insulin and SIRT1 signaling, which contribute to AD pathophysiology.

APOE ε4 hiBMEC had reduced barrier function, as measured through TEER and ZO-1 continuity, relative to the APOE ε3 hiBMEC. This agrees with past reports of reduced TEER in BMEC isolated from APOE ε4 transgenic mice [130]; increased permeability with reduced ZO-1 and occludin in brain vessels of transgenic mice [302]; and increased BBB permeability in the hippocampus and parahippocampal gyrus of adults who are carriers of the APOE ε4 allele [315]. While APOE ε4 may reduce barrier function through multiple mechanisms, APOE ε4 cells had lower SIRT1. SIRT1 increased ZO-1 in human pulmonary microvascular endothelial cells [309] and claudin-5 in mouse [317] and primary human BMEC [310]. Though the mechanism has not been examined in BMEC, in ovarian cancer cells, SIRT1 deacetylates Krüppel-like factor 4 (KLF4) which promotes claudin-5 transcription [318]. KLF4 can also interact with promotor regions on ZO-1 and occludin to increase their transcription [319]. Therefore, it is possible the low SIRT1 in APOE ε4 hiBMEC increased KLF4 acetylation, which reduced ZO-1 transcription to reduce overall barrier function in APOE ε4 hiBMEC.

ZO-1 tethers tight junction proteins to actin in the cytoskeleton, so decreased ZO-1 continuity should also impair other tight junction proteins. However, in my work, occludin and claudin-5 junction continuity was not impaired by the APOE ε4 genotype. Research in canine epithelial cells have demonstrated that knockout of ZO-1 delays the formation of tight junctions by occludin and claudin-5, but in long term culture does not affect occludin or claudin-5 junctions or barrier function [320]. The lower TEER seen in my APOE ε4 hiBMEC compared to the APOE ε3 hiBMEC may, therefore, be due to reductions in other tight junction proteins not measured here. For example, VE-Cadherin continuity has been shown to be reduced in ZO-1 knockout human dermal endothelial cells [321], and could contribute to lower TEER in APOE ε4 hiBMEC.

The APOE ε4 genotype is associated with reduced glucose metabolism in transgenic mouse BMEC [130], astrocytes [303], and neurons [322]. Here, I showed that these same changes occurred in hiBMEC. My data suggest that reduced glycolysis may relate to INSR recycling. In neurons, APOE ε4 similarly reduced endosomal INSR recycling, which in turn reduced insulin signaling and glycolysis [304]. Neuronal glucose transport is primarily regulated by GLUT3 [323], while hiBMEC glucose transport is primarily regulated by GLUT1. Both GLUT1 and GLUT3 are categorized as insulin independent glucose transporters because they are highly expressed on the cell membrane even in the absence of insulin [324], [325]. Conversely, the insulin-dependent glucose transporter, GLUT4, is primarily localized in intracellular vesicles until the cells are stimulated with insulin, at which point the vesicles fuse with the cell membrane and take up glucose [326], [327], [328]. However, increased INSR and insulin signaling can increase both transcription of GLUT1 and GLUT3 and trafficking of the transporters to the cell membrane [305], [306], [329], [330]. Interestingly, in my experiments insulin did not significantly increase membrane GLUT1 or glycolytic rate in hiBMEC. It is therefore possible that the cell membrane is already saturated with GLUT1, and thus GLUT1 translocation cannot increase with additional insulin.

Reduced glycolysis could also relate to decreased SIRT1 and hexokinase-2 (HK2) in APOE ε4 hiBMEC. In neuroblastoma and glioblastoma cell lines, APOE ε4 decreases SIRT1 transcription [138], [307]. In neurons and whole brain lysates, the APOE ε4 genotype correlated with reduced HK2 compared to the APOE ε3 genotype, which contributed to lower glycolysis [322], [331]. SIRT1 regulates HK2 [141]. Therefore, the APOE ε4 protein could decrease SIRT1, which in turn decreases HK2. Since EX-527 did not decrease glycolysis in APOE ε4 hiBMEC, I was unable to show in hiBMEC that decreased SIRT1 and HK2 decreased glycolysis. Likely, SIRT1 alone does not regulate glycolysis. Interestingly, I also noted reduced PFKFB3 in APOE ε4 hiBMEC, which has not, to my knowledge, been reported. Transcription factors including Krüppel-like factor 2 (KLF2) [332], hypoxia inducible factor 1-α (HIF-1α) [333], and myocyte enhancer factor 2A (Mef2a) [334] regulate PFKFB3. In microglia, Mef2a expression is inhibited by APOE signaling [335], and since the APOE ε4 hiBMEC had elevated intracellular APOE, this may be one mechanism through which PFKFB3 expression decreased in APOE ε4 hiBMEC.

In a euglycemic individual, brain glucose concentrations range between 1-2.5 mM glucose depending on activity levels [336]. Despite differences in basal rates of glucose metabolism, my data demonstrate that APOE ε3 and ε4 hiBMEC had similar glucose transport for their apical to basolateral sides. Since APOE genotype did not alter hiBMEC glucose transport, it is likely that APOE ε4-induced glycolytic deficiency in all other brain cell types is not due to reduced glucose transport by BMEC. Instead, inhibition of glucose uptake in parenchymal brain cells may also be partially caused by reduced insulin and SIRT1 signaling.

$^{13}C_6$-glucose metabolomics revealed systemic metabolomic differences between APOE ε3 and ε4 hiBMEC. Interestingly, the top driver of separation via PLS-DA was UDP-GlcNAc which was elevated in APOE ε4 hiBMEC. UDP-GlcNAc is added to serine and threonine residues by O-GlcNAc transferase and removed by O-GlcNAcase. Protein GlcNAcylation regulates various cellular processes including gene expression, signal transduction, and cellular stress responses [337]. Counterintuitive to my data, high protein GlcNAcylation is largely neuroprotective and can reduce necroptosis [338], amyloid-β plaque formation [339], and tau hyperphosphorylation [340]. It is possible, however, that the activity of O-GlcNActransferase is lower or O-GlcNAcase is higher in APOE ε4 hiBMEC relative to APOE ε3 hiBMEC, which would mean that regardless of the UDP-GlcNAc concentration in the cell, fewer proteins are being GlcNAcylated.

The decreased TCA metabolites labeling in my study is supported by similar results from a metabolomic-based study in astrocytes wherein APOE ε3 and ε4 immortalized astrocytes isolated from transgenic mice were cultured with $^{13}C_6$-glucose for 24 hours before mass spectrometry was run to measure metabolomic changes [303]. Since my study examined only the labeled fraction of TCA metabolites from $^{13}C_6$-glucose, not other carbon sources, lower glucose-derived TCA metabolites in APOE ε4 hiBMEC may be counteracted by elevated use of other carbon sources that feed the TCA cycle, such as glutamine and fatty acids. However, as discussed in Chapter 4, hiBMEC may not accurately represent the glutamine metabolism of BMEC, and therefore we cannot draw conclusions based on this data. In future studies, primary BMEC (hpBMEC) from APOE ε3 and ε4 donors could be used to more accurately assess the impact of APOE genotype on glutamine metabolism.

I also showed increased labeling of nucleotides from $^{13}C_6$-glucose in APOE ε4 hiBMEC, which has also been noted in astrocytes [303]. Nucleotide synthesis, specifically ATP, CTP, UTP, and their precursor molecules were increased in APOE ε4 hiBMEC, likely due to increased activity of the PPP which generates ribose-5-phosphate, a metabolite critical to nucleotide synthesis. Due to large variability in the data, I was unable to detect differences in ribose-5-phosphate levels in these experiments. Elevated ATP in APOE ε4 hiBMEC is unexpected as glucose metabolism through glycolysis and the TCA cycle are the main methods of ATP production, and both are decreased in the APOE ε4 hiBMEC. It is, however, possible that APOE ε4 hiBMEC perform fewer ATP-consuming reactions such as protein phosphorylation or active ion transport. Since ATP is also an allosteric inhibitor of glycolytic enzyme phosphofructokinase (PFK), a high ATP:ADP ratio can indicate inhibition of glycolysis through PFK [341]. The ratio of $^{13}C_6$-glucose labeled ATP:ADP in the APOE ε3 and ε4 hiBMEC was the same indicating this is likely not a mechanism through which APOE genotype alters glycolysis in APOE ε3 and ε4 hiBMEC. Elevated UTP levels likely contribute to the previously described elevations of UDP-GlcNAc in APOE ε4 hiBMEC, as UTP binding to N-acetylglucosamine-1-phosphate leads to the UDP-GlcNAc formation.

Based on the $^{13}C_6$-glucose metabolomics, I assessed which metabolic pathways are most impacted by hiBMEC APOE genotype. Expectedly, both glycolysis and the TCA cycle were significantly impacted by genotype differences. The starch and sucrose pathway, which had both a significant impact and $\log_{10}$(p-value), contains glycolysis and the HBP, which are the main contributors to its differential metabolism between APOE ε3 and ε4 hiBMEC. The alanine, aspartate, and glutamate metabolic pathway include N-Acetyl-Aspartate, L-aspartate, citrate, 2-oxoglutarate, 4-aminobutanoate, L-glutamine, and succinate, all of which were elevated in APOE ε3 hiBMEC. An analysis of post-mortem brain tissue of AD patients vs. control subjects demonstrated similar dysregulation of glycine metabolism, purine metabolism, and alanine, aspartate and glutamate metabolic pathways [342]. These data indicate that disruptions of BMEC metabolism in these pathways may be a predictor of AD disease risk and contribute to AD progression.

Here, I demonstrated that intracellular APOE protein levels were significantly higher in APOE ε4 hiBMEC compared to APOE ε3 hiBMEC. Previous reports conflict in whether intracellular APOE protein levels are higher in APOE ε3 or APOE ε4 cells. In mouse transgenic BMEC [130] and astrocytes [343],

APOE levels were higher in APOE ε3 cells, while our data and data from microglia [344] showed higher APOE levels in APOE ε4 cells. The APOE ε4 protein can have several direct intracellular effects, so elevated intracellular APOE concentrations in APOE ε4 hiBMEC may enhance some of these transcriptional effects. For example, in neurons the APOE ε4 protein induces translocation of histone deacetylases 4 and 6 to the cell nucleus, which decreases expression of brain derived neurotrophic factor (BNDF), a protein that enhances survival, growth, and differentiation of neurons [345]. More broadly, in neurons the APOE ε4 protein binds to nearly 1,700 gene promotor regions encoding for 76 proteins and can impact glucose metabolism and energy homeostasis, inflammation, and neuronal signaling [138]. Overall, elevated intracellular APOE ε4 may enhance these effects and potentiate the neurodegenerative impacts of the APOE ε4 allele.

5.5. Limitations

The results presented in this chapter show two mechanisms through which APOE genotype regulates hiBMEC glucose metabolism and barrier function. However, this study does have limitations. First, hiBMEC have incomplete differentiation, leading to retention of an epithelial-like transcriptomic profile, which decreases their physiological relevance for brain vasculature [217]. Furthermore, in Chapters 3 and 4, I demonstrate that although glucose metabolism is similar between hiBMEC and hpBMEC, they are not the same. These studies were also only performed on hiBMEC differentiated from one iPSC cell line (IMR90). Future studies should use hiBMEC from multiple iPSC lines to ensure the results are not iPSC specific. Finally, the BBB is simplified in these studies to only use BMEC. The addition of other brain cell types, as well as more physiological substrate stiffnesses and flow, would increase the physiological relevance of this study.

5.6. Conclusions

The APOE ε4 genotype is associated with glucose hypometabolism and BBB breakdown in humans. Here, I showed that the APOE ε4 hiBMEC had lower glucose metabolism through reduced insulin signaling.

Furthermore, I demonstrated that reducing SIRT1 in hiBMEC reduced tight junction protein continuity indicative of BBB breakdown. In the next chapter, I build on this work to investigate how sedentary lifestyle, another AD risk factor, impacts hiBMEC metabolism and barrier function in a genotype-dependent manner.

Chapter 6: Exercise training has genotype-dependent impacts on BMEC metabolism and function

6.1. Introduction

In the last chapter, I demonstrated that the APOE ε4 genotype, the largest genetic risk factor for Alzheimer's disease (AD) development, reduced glucose metabolism and barrier function in induced pluripotent stem cell derived brain microvascular endothelial-like cells (hiBMEC). I also demonstrated that these processes are, at least in part, mediated through reduced insulin signaling and SIRT1 activity in APOE ε4 hiBMEC relative to APOE ε3 hiBMEC. In this chapter, I examine how sedentary lifestyle, another risk factor for AD, alters hiBMEC metabolism and barrier function and how exercise training counteracts these effects.

Consistent exercise training is estimated to reduce AD risk by 45% [346]. Exercise training in healthy older adults increases cerebral blood flow [347], reduces hippocampal atrophy [348], and increases brain glucose metabolism [349], each of which reduces AD risk. Exercise training also improves amyloid-β (Aβ) clearance in rodents [350] and may reduce plasma Aβ levels in humans as well [351]. From a mechanistic standpoint, exercise elevates circulating levels of irisin, lactate, and cathepsin B, which are all hypothesized to increase brain derived neurotrophic factor (BDNF) [352], [353], [354], [355], a molecule that supports neuronal growth, synaptic plasticity, learning, and memory [356], [357]. Past studies primarily focused on how exercise training improves neuronal signaling to improve cognition. However, little is known of how exercise alters BMEC function, which is of particular importance because BMEC are directly in contact with the circulation, and therefore act as first responders to the benefits of exercise training.

One mechanism through which exercise training may benefit BMEC function and metabolism is by increasing SIRT1 protein levels. As previously discussed in Chapter 5, SIRT1 may increase BMEC function and metabolism. Male rats with access to wheel running for 14 days had higher levels of SIRT1 in the hippocampus compared to those without access to wheel running [358]. SIRT1 levels can likely be controlled by many circulating factors that change with exercise. For example, mice with access to voluntary

wheel running for 1 month had higher concentrations of lactate in the hippocampus compared to sedentary mice, and both exercise and lactate injections were shown to increase SIRT1 protein levels in the hippocampus [354]. Therefore, exercise induced elevations in lactate may cause increases in SIRT1 in the brain. In addition to increasing SIRT1 protein levels, exercise training can also increase SIRT1 activity through elevation of AMP-activated protein kinase (AMPK). In human endothelial cells increases in laminar shear stress, similar to those that occur with exercise training, increase AMPK activation, which in turn increase NAD+ production and SIRT1 activity [359], [360]. Overall, these may be two mechanisms through which exercise supports BMEC metabolism and function via SIRT1.

In this chapter, I used human serum samples collected from sedentary healthy older adults before and after six months of exercise training to examine how exercise training alters hiBMEC metabolism and barrier function. I treated APOE ε3 and ε4 hiBMEC with genotype-matched serum samples and examined how serum from sedentary versus trained individuals altered glycolytic rates, glycolytic enzyme levels, SIRT1, and barrier function. I demonstrate that exercise training differentially impacts APOE ε3 and ε4 hiBMEC SIRT1 and metabolic enzymes, which should be considered in the development of exercise training regimens to support brain health of older adults at risk for AD.

6.2. Methods

6.2.1. Exercise training*:* Adults between the ages of 60 and 80 years old were recruited in compliance with clinical trial NCT03727360. Participant demographics are shown in Table 6.1. All participants were deemed healthy and showed no signs of mild cognitive impairment, dementia, or neurological illness. Participants were also classified as physically inactive, meaning they did not partake in physical activity more than 2 days a week during the past 6 months. During the 6-month clinical trial, each participant was randomly assigned to either the exercise training intervention (ET) or a low intensity flexibility exercise control condition (FC). At the start of the trial, each participant underwent a VO_2 max test to quantify their cardiorespiratory fitness. All ET and FC participants began each workout with the same 20-minute warmup.

Following the warmup, the ET group completed a moderate intensity interval training exercise while FC participants completed a set of stretching and strength training exercises. For both the ET and FC groups, exercise duration and frequency increased over the course of the study, starting with 10 minutes of exercise one day a week and finishing with 30 minutes of exercise four days per week. A VO_2 max test was then repeated at the end of the 6-month trial.

Table 6.1. Serum donor demographics

	Donor Sex		**Race**				**Age at consent**
	Male	Female	Undisclosed	White	Black/African American	Asian	Average (± Standard Deviation)
APOE e3 (n = 9)	0 (0%)	9 (100%)	0 (0%)	6 (67%)	2 (22%)	1 (11%)	65.3 ± 5.0
APOE e4 (n = 9)	3 (33%)	6 (66%)	1 (11%)	5 (56%)	3 (33%)	0 (0%)	65.1 ± 3.9

6.2.2. Human serum collection*:* At the start and finish of the trial, 8 mL of blood was drawn from each participant in Vacutainer Serum Separator Tubes (SST; BD, 367989). To isolate serum from the whole blood, SST tubes were centrifuged at 15,000 x g for 15 minutes at 4°C. Serum was then aliquoted and stored at -80°C until use.

6.2.2. Cell culture*:* CRISPR/Cas9 was used to generate iPSC homozygous for the APOE ε4 allele and isogenic APOE ε3 controls, after which iPSC were differentiated into hiBMEC as described in Chapter 5. hiBMEC were cultured in Neurobasal medium (NB; Thermo Fisher 21103049) supplemented with 8.5 mM glucose, 4.5 mM glutamine, and 2% B27 for 2 days following differentiation prior to serum treatment. For serum treatment, APOE ε3 and ε4 hiBMEC were treated with 20% genotype-matched human serum from participants pre- and post- 6 months of exercise training for 24 hours before downstream assays were completed.

6.3.3. APOE ELISA*:* To quantify APOE protein in human serum samples, a Human APOE enzyme linked immunosorbent assay (ELISA) kit (Thermo Fisher, EHAPOE) was used. All serum samples were diluted

1:1000 in the ELISA Assay Diluent, and the ELISA was run following the manufacturer's protocol. Absorbances were read at 450 nm, and concentrations were calculated based on the standard curve.

6.2.4. Western blot*:* After 24 hours of serum treatment, protein levels were analyzed by Western blot as described in Chapter 3. Each Western blot shown is a representative blot including 3 replicates treated with serum from one single donor per genotype.

6.3.5. YSI*:* Glucose and glutamine uptake and lactate and glutamate secretion were measured using a YSI 2950 (Yellow Springs Instruments, 527690). APOE ε3 and ε4 hiBMEC were treated with 20% genotype-matched serum. 200 μL media aliquots were then collected for YSI analysis at 0 and 24 hours. For each metabolite, uptake was calculated by subtracting metabolite concentrations at 24 hours from the concentrations at 0 hours. Secretion was calculated by subtracting the 0-hour metabolite concentration from the 24-hour concentration.

6.3.6. Seahorse*:* Seahorse Glycolytic Rate Assays (Agilent, 103344-100) were used as described in Chapter 5 to evaluate differences in glycolysis following 24 hours of serum treatment in genotype-matched hiBMEC.

6.3.7. TEER/Permeability assays*:* Trans-endothelial electrical resistance (TEER) was measured as described in Chapter 5 with some modifications. Two days post-subculture, TEER was measured. Cells were then treated with 20% human serum in the apical compartment only. Basolateral medium was exchanged with fresh NB medium supplemented with 8.5 mM glucose, 4.5 mM glutamine, and 2% B27. 24 hours after serum treatment, TEER was measured again. Reported results include both the TEER after 24 hours of treatment and the change in TEER between the 0- and 24- hour recordings.

Permeability was also assessed using a sodium fluorescein permeability assay after 24 hours of serum treatment. Sodium fluorescein (Millipore Sigma, F6377) was resuspended to 10 μM in NB medium supplemented with 8.5 mM glucose, 4.5 mM glutamine and 2% B27. Medium in the apical chamber was replaced with the pre-warmed medium containing sodium fluorescein. 50 μL medium samples were

collected from the basolateral chamber after 0, 5, 15, 30, 45, and 60 minutes with replacement. The sample fluorescence intensity was measured on a Spark Multimode Plate Reader (Tecan) at 485 nm excitation and 530 nm emission. Sodium fluorescein permeability was calculated by subtracting off background fluorescence of the media, accounting for signal loss from media sampling in the basolateral chamber, using the linear slope of the clearance volume vs. time to calculate the permeability coefficient of the hiBMEC monolayer [361].

6.3.8. Immunostaining and Junction Analysis*:* To measure junction continuity following 24 hours of treatment with genotype-matched serum, APOE ε3 and ε4 hiBMEC were labeled for ZO-1 and claudin-5 as described in Chapter 5. Junction continuity was quantified using the Junction Analyzer Program [314]. Junction continuity was quantified on a per cell basis, wherein junction continuity was analyzed for every cell in each serum treatment group, and on a per donor basis wherein junction continuity of all the cells from each donor in each serum treatment group was averaged.

6.3.9. Metabolic Mass Spectrometry*:* Metabolomic changes between APOE ε3 and ε4 hiBMEC following serum treatment were assessed via liquid chromatography mass spectrometry mass spectrometry/mass spectrometry (LC-MS/MS) as described in Chapter 3 with some modifications. Samples were incubated for 24 hours in NB medium supplemented with 8.5 mM U-$^{13}C_6$-glucose, 4.5 mM glutamine, 2% B27, and 20% human serum prior to collecting the cells for metabolomics. Data were analyzed using Metaboanalyst 6.0 [230].

6.3.10. Statistics*:* All statistics were analyzed in GraphPad Prism using repeated measures two-way ANOVA with Fisher's Least Significant Difference test.

6.3. Results

Exercise training reduces brain hypertrophy and increases cerebral glucose metabolism associated with AD. I therefore examined how serum from exercise trained individuals alters hiBMEC metabolism and barrier function to explore the molecular mechanisms by which exercise benefits the brain.

6.3.1. Exercise training did not significantly cardiorespiratory fitness.

I first examined how cardiorespiratory fitness, measured using VO_2 max, changed in study participants from the start to the end of the trial (Fig. 6.1A). Since the VO_2 max change was statistically similar between the FC and ET groups, the data were combined. Overall, study participants did not have a significant change in VO_2 max following exercise training. However, VO_2 max increased by 18% in APOE ε4 participants ($p = 0.0678$).

6.3.2. Exercise training did not alter serum or intracellular APOE.

To assess if exercise training altered APOE levels, serum and intracellular APOE was measured via ELISA and Western blot, respectively. Serum APOE concentrations did not change with genotype or exercise training (Fig. 6.1B). APOE ε4 hiBMEC had ~400% higher intracellular APOE protein than APOE

ε3 hiBMEC (p = 0.0007 for sedentary and p = 0.0018 for trained). There were no significant changes in intracellular APOE protein levels with exercise training.

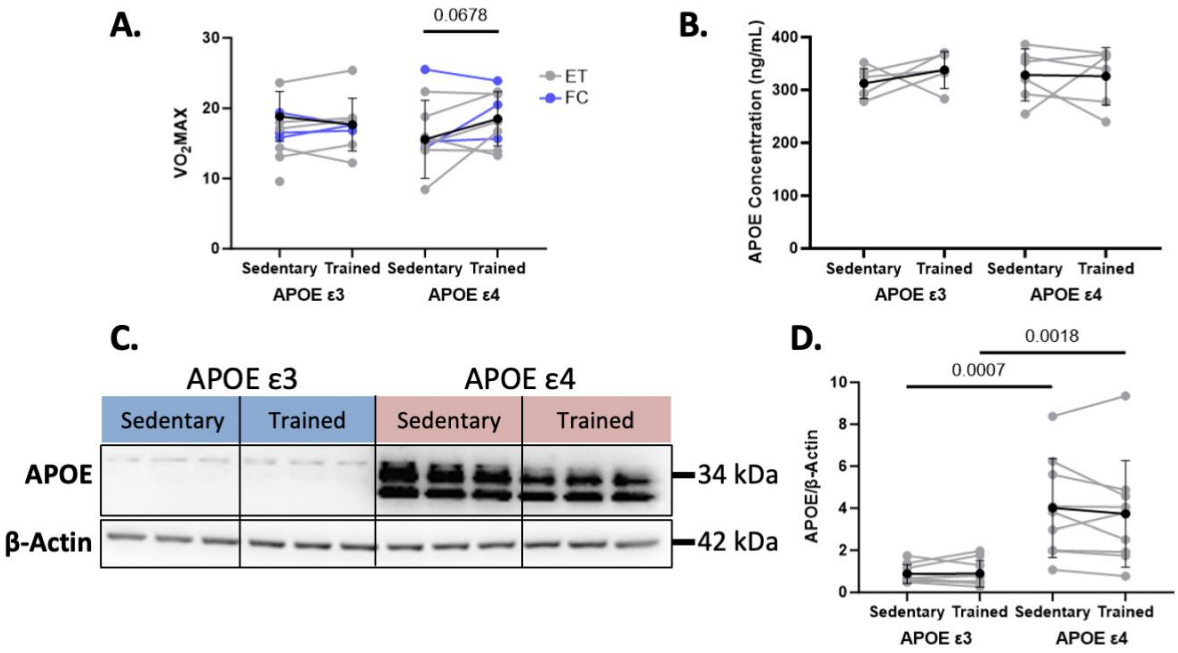


Figure 6.1. Exercise training did not change VO2 max, serum APOE protein level, or intracellular hiBMEC APOE protein level. (A) Cardiorespiratory fitness in individuals with the APOE ε3 and ε4 genotypes was measured before and after 6 months of aerobic (grey) or flexibility (blue) exercise training (n = 9 participants per genotype). **(B)** APOE concentrations were measured via ELISA in serum collected from APOE ε3 and ε4 individuals before and after exercise training (n = 6 donors per genotype). Intracellular APOE protein levels were **(C)** measured via Western blot and **(D)** quantified relative to β-Actin in APOE ε3 and ε4 hiBMEC following 24 hours of treatment with 20% serum from genotype-matched participants pre- and post- exercise training (n = 9 donors per genotype). Data were analyzed using repeated measures two-way ANOVA with Fisher's Least Significant Difference Test.

6.3.3. Exercise trained serum did not alter glycolysis in APOE ε3 or ε4 hiBMEC.

I next investigated how glycolytic rate changed with serum from sedentary vs. exercise-trained individuals using a YSI 2950 and Seahorse Glycolytic Rate Assay. In Chapter 5, I demonstrated that in the absence of serum treatment APOE ε4 hiBMEC had lower rates of glycolysis compared to APOE ε3 hiBMEC. Here, YSI measurements showed APOE ε3 and ε4 hiBMEC had similar levels of glucose uptake with both sedentary and exercise trained serum (Fig. 6.2A). Lactate secretion was similar between APOE ε3 and ε4 hiBMEC with serum treatment, but exercise trained serum did increase lactate secretion in APOE ε4 hiBMEC by 5% (p = 0.0218; Fig. 6.2B). Glutamine uptake increased with exercise trained serum in APOE

ε3 hiBMEC by 7% (p = 0.0379) but decreased with exercise trained serum in APOE ε4 hiBMEC by 14% (p = 0.0084; Fig. 6.2C). In Chapter 4, I demonstrated that hiBMEC do not secrete measurable glutamate. With the addition of serum, glutamate secretion was still minimal; however, compared to APOE ε3 hiBMEC, APOE ε4 hiBMEC secreted 77% more glutamate when treated with sedentary serum (p = 0.0003) and 72% more glutamate when treated with serum from exercise trained individuals (p = 0.0007; Fig. 6.2D). A Seahorse Glycolytic Rate Assay was used as a secondary measure of glycolysis (Fig. 6.2E). There was no difference in basal or compensatory glycolysis rates between APOE ε3 and ε4 hiBMEC treated with sedentary or exercise trained serum (Fig. 6.2F-G).

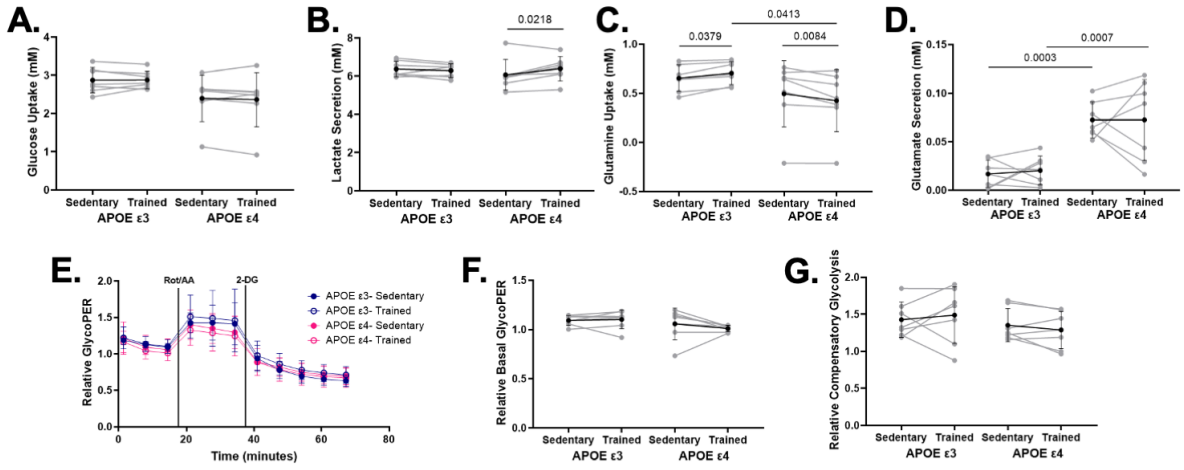


Figure 6.2. Glycolysis was not changed in APOE ε3 or APOE ε4 hiBMEC with exercise training. YSI measurements of **(A)** glucose uptake, **(B)** lactate secretion, **(C)** glutamine uptake, and **(D)** glutamate secretion by APOE ε3 and ε4 hiBMEC following 24 hours of treatment with 20% serum from genotype matched sedentary and exercise-trained individuals. **(E)** Real-time measurements of glycolytic rates measured using Seahorse glycolytic rate assay in APOE ε3 and ε4 hiBMEC following 24 hours of serum treatment and quantifications of **(F)** basal GlycoPER and **(G)** compensatory glycolysis. All GlycoPER data is presented relative to APOE ε3 hiBMEC in each Seahorse plate to allow for comparison among plates (n = 7 donors per genotype). Data were analyzed using repeated measures two-way ANOVA with Fisher's Least Significant Difference Test.

6.3.4. Serum from exercise trained individuals increased glycolytic enzymes in APOE ε3 hiBMEC but decreased glycolytic enzymes in APOE ε4 hiBMEC relative to serum from sedentary individuals.

Since glycolytic enzymes were different in APOE ε3 and ε4 hiBMEC in chapter 5, I next measured how serum from sedentary vs. exercised APOE ε3 and APOE ε4 individuals impacted glycolytic enzymes via Western blot (Fig. 6.3A). In Chapter 5, I demonstrated that APOE ε4 hiBMEC had lower levels of GLUT1

than APOE ε3 hiBMEC. With the addition of serum, GLUT1 levels were similar between APOE ε3 and ε4 hiBMEC. Serum from exercise trained individuals did not significantly change GLUT1 levels compared to serum from sedentary individuals in APOE ε3 or ε4 hiBMEC (Fig. 6.3B). Rate limiting glycolytic enzyme hexokinase 1 (HK1) was also unchanged by exercise training or genotype (Fig. 6.3C). However, levels of the more highly expressed hexokinase isoform, hexokinase 2 (HK2), were similar between APOE ε3 and ε4 hiBMEC. This is different from results without serum presented in Chapter 5, which showed APOE ε4 hiBMEC had lower levels of HK2 compared to APOE ε3 hiBMEC. APOE ε3 hiBMEC treated with exercise trained serum had 27% higher HK2 ($p = 0.0307$), while APOE ε4 hiBMEC treated with exercise trained serum had 15% lower HK2 ($p = 0.0246$; Fig. 6.3D). 6-phosphofructo-2-kinase/fructose-2,6-biphosphatase 3 (PFKFB3), which regulates glycolysis via phosphofructokinase (PFK) activity, was shown in Chapter 5 to be lower in APOE ε4 hiBMEC than APOE ε3 hiBMEC. However, with the addition of serum, there were similar levels of PFKFB3 between APOE ε3 and ε4 hiBMEC. PFKFB3 levels were 23% lower in APOE ε4 hiBMEC treated with exercise trained as compared to sedentary serum ($p = 0.0171$; Fig. 6.3E). Levels of other glycolytic enzymes, including glyceraldehyde 3-phosphate dehydrogenase (GAPDH) and lactate dehydrogenase (LDH), were unchanged by genotype or serum from exercise training (Fig. 6.3F-G). Glucose-6-phosphate dehydrogenase (G6PD), which regulates glucose entry into the pentose phosphate pathway, and glutamine fructose-6-phosphate amidotransferase (GFAT), which regulates glucose entry to the hexosamine biosynthetic pathway, were also unaffected by genotype and serum from exercise training (Fig. 6.3H-I).

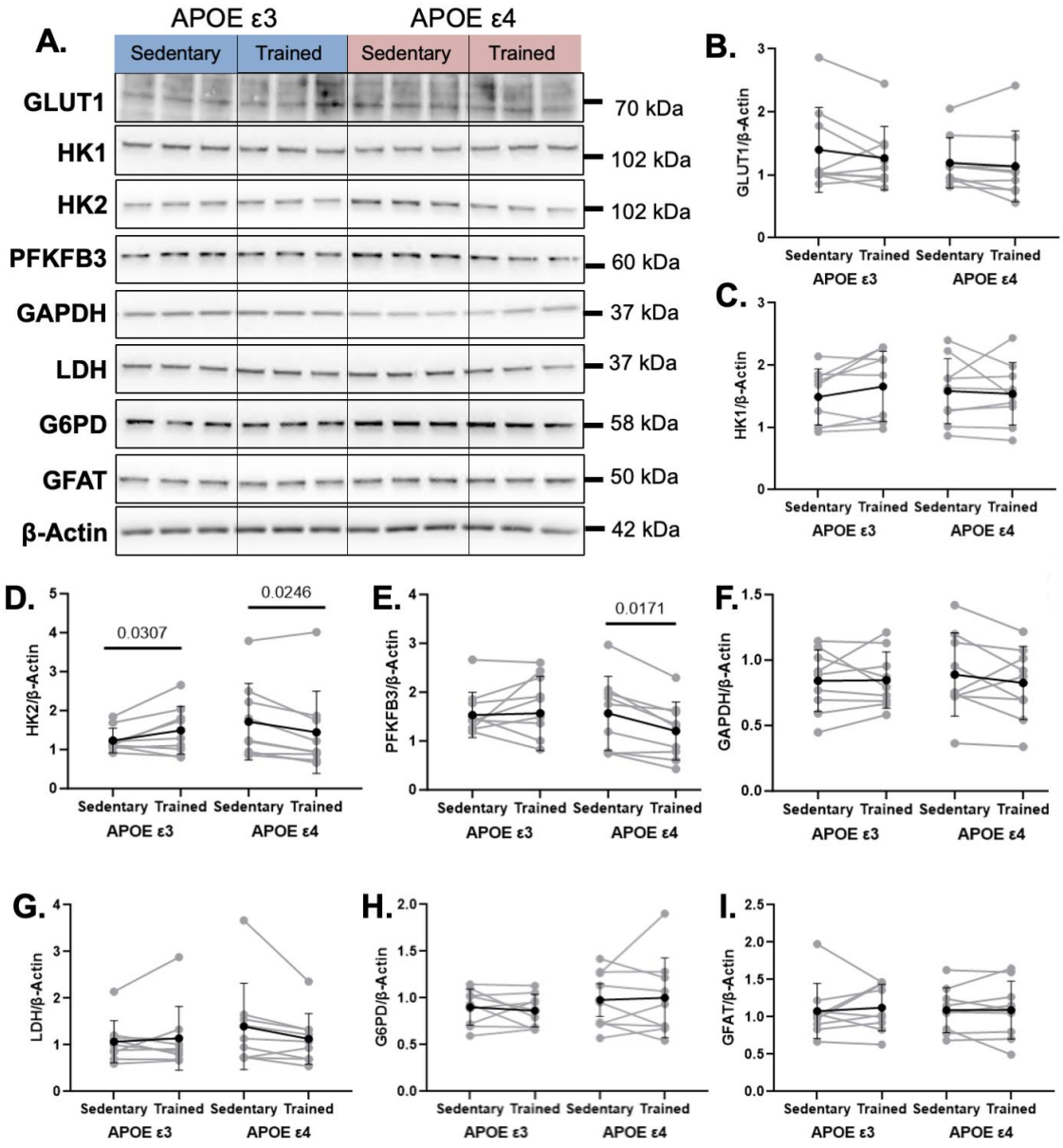


Figure 6.3. Serum from exercise trained individuals decreased rate limiting glycolytic enzymes HK2 and PFKFB3 in APOE ε4 hiBMEC relative to serum from sedentary individuals. (A) Representative Western blots of GLUT1 and glycolytic enzymes in APOE ε3 and ε4 hiBMEC following 24 hours of treatment with 20% serum from genotype matched sedentary and exercise-trained individuals. Quantification of Western blots for **(B)** GLUT1, **(C)** HK1, **(D)** HK2, **(E)** PFKFB3, **(F)** GAPDH, **(G)** LDH, **(H)** G6PD, and **(I)** GFAT relative to housekeeper β-actin (n = 9 donors per genotype). Data were analyzed using repeated measures two-way ANOVA with Fisher's Least Significant Difference Test.

6.3.5. SIRT1 was differentially regulated by serum genotype and exercise training.

Since SIRT1 and insulin signaling were found to be upstream regulators of glycolytic enzyme levels and glycolysis in Chapter 5, I next examined how serum from exercise-trained participants altered SIRT1 and insulin receptor levels in APOE ε3 and ε4 hiBMEC by Western blot (Fig. 6.4A). SIRT1 was 71% higher in APOE ε4 hiBMEC treated with sedentary serum compared to APOE ε3 hiBMEC treated with sedentary serum ($p = 0.0013$). In APOE ε3 hiBMEC, SIRT1 was 33% higher when cells were treated with exercise trained serum relative to cells treated with sedentary serum ($p = 0.0043$). However, APOE ε4 hiBMEC treated with exercise trained serum had 22% lower SIRT1 compared to those treated with sedentary serum ($p = 0.0004$; Fig. 6.4B). Insulin receptor protein levels were not changed with hiBMEC genotype or serum treatment (Fig. 6.4C).

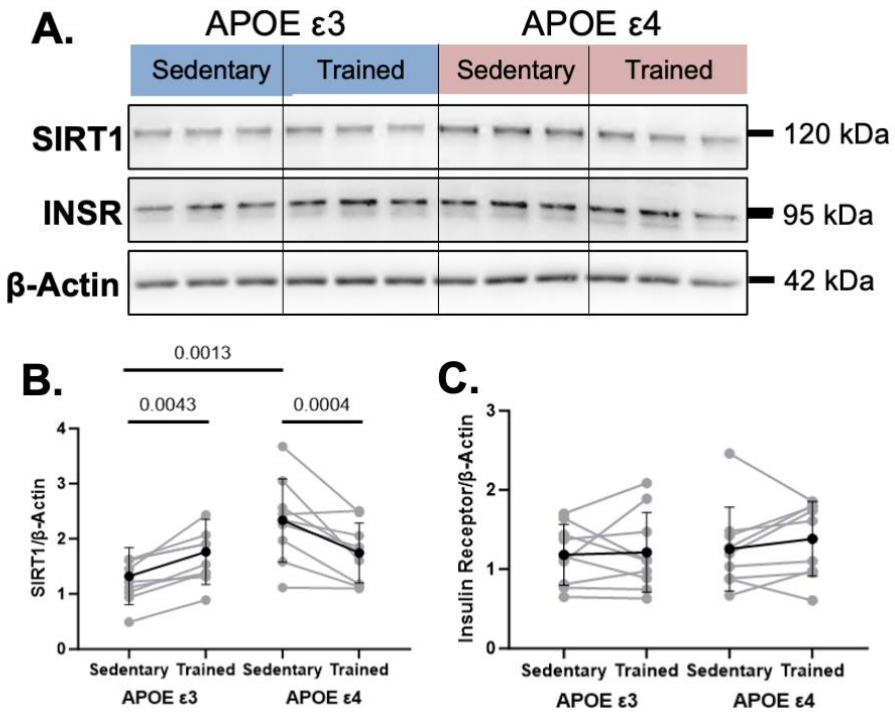


Figure 6.4. SIRT1 increased with exercise trained serum in APOE ε3 hiBMEC and decreased with exercise trained serum in APOE ε4 hiBMEC, while insulin receptor levels were unchanged with genotype and serum. (A) Representative Western blots with quantification of **(B)** SIRT1 and **(C)** insulin receptor levels in hiBMEC treated with 20% genotype-matched serum for 24 hours (n = 9 donors per genotype). Data were analyzed using repeated measures two-way ANOVA with Fisher's Least Significant Difference Test.

6.3.6. VO2 max is not correlated with changes in glycolysis, but changes in APOE and SIRT1 are positively correlated with changes in some glycolytic enzymes in APOE ε3 and ε4 hiBMEC.

Because changes in VO_2 max varied among participants, I next ran a Spearman Rank correlation analysis to determine if VO_2 max changes correlated with other glycolytic measures or protein levels, including: glucose uptake, lactate secretion, glutamine uptake, glutamate secretion, lactate:glucose ratio, basal glycolysis, compensatory glycolysis, GLUT1, HK1, HK2, PFKFB3, GAPDH, LDH, G6PD, GFAT, SIRT1, INSR, and APOE (Fig. 6.5A-B). In APOE ε3 hiBMEC, VO_2 max did not correlate with any of the measured glycolytic markers. In APOE ε4 hiBMEC, however, changes in VO_2 max with exercise training were positively correlated with changes in glutamate secretion ($r_s = 0.738$, $p = 0.046$).

In Chapter 5 APOE, SIRT1, and INSR were hypothesized to be upstream regulators of glycolysis. Therefore, I examined the correlations between these proteins and glycolytic measures. In APOE ε3 hiBMEC, APOE protein levels were positively correlated with HK2 ($r_s = 0.817$, $p = 0.012$), LDH ($r_s = 0.867$, $p = 0.005$), and INSR ($r_s = 0.717$, $p = 0.037$). SIRT1 was negatively correlated with lactate: glucose ($r_s = -0.833$, $p = 0.015$), and positively correlated with HK2 ($r_s = 0.85$, $p = 0.006$), and INSR was positively correlated with HK2 ($r_s = 0.733$, $p = 0.031$) and APOE as previously noted. In APOE ε4 hiBMEC, APOE protein levels were positively correlated with glutamate production ($r_s = 0.738$, $p = 0.046$) and LDH ($r_s = 0.767$, $p = 0.021$). SIRT1 was positively correlated with HK2 ($r_s = 717$, $p = 0.037$), and INSR was negatively correlated with glutamine uptake ($r_s = -0.738$, $p = 0.046$).

6.3.6. Serum systemically altered the hiBMEC metabolome, but exercise training did not.

In Chapter 5, metabolomics analysis revealed systemic differences in hiBMEC metabolism between APOE ε3 and ε4 hiBMEC. I therefore next used LC-MS to examine systemic metabolomic changes in APOE ε3 and ε4 hiBMEC treated with sedentary and exercise-trained serum (Appendix 5). Partial least squares-discriminant analysis (PLS-DA) demonstrated no clear separation of APOE ε3 or ε4 hiBMEC treated with sedentary or exercise trained serum (Fig. 6.6A). However, in 3/4 of APOE ε3 hiBMEC, the addition of exercise trained serum resulted in a rightward shift along PC1 relative to sedentary serum, whereas the addition of exercise trained serum was associated with a leftward shift along PC1 in all the APOE ε4 hiBMEC. Additionally, 3/4 APOE ε4 hiBMEC treated with exercise trained serum were shifted upwards

along PC2 compared to those treated with sedentary serum. A heat map of the metabolites analyzed did not show clear differences in individual metabolites between APOE ε3 and ε4 hiBMEC with sedentary or exercise trained serum (Fig. 6.6B).

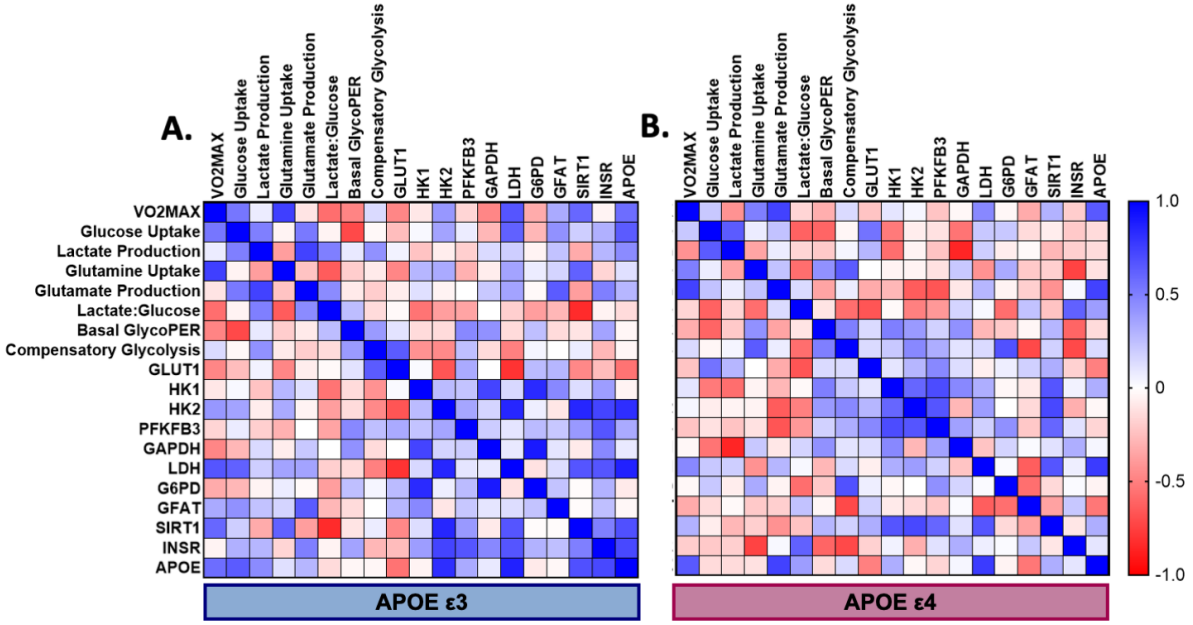


Figure 6.5. VO2 max is not correlated with changes in glycolysis, but changes in APOE and SIRT1 are positively correlated with changes in some glycolytic enzymes in APOE ε3 and ε4 hiBMEC. Spearman Rank Correlation plots generated from the calculated percent change in measured VO_2 max, glycolytic, and protein changes in **(A)** APOE ε3 and **(B)** APOE ε4 hiBMEC (n = 7 - 9 donors for each measured output). Blue indicates a positive correlation, while red indicates a negative correlation.

Because the trends seen between APOE ε3 and APOE ε4 hiBMEC metabolomes in Chapter 5 were not as apparent with the addition of serum, I next analyzed how APOE ε3 and ε4 hiBMEC metabolomes differed with the addition of serum. For this analysis, samples with either sedentary or trained serum were compared to serum-free APOE ε3 and ε4 hiBMEC. APOE ε3 and ε4 hiBMEC did not separate by genotype, as demonstrated by PLS-DA (Fig. 6.6C). However, serum addition led to a large separation of hiBMEC along component 1 (PC1 = 44%). The metabolites that were the largest drivers of this separation are reported in Appendix 6 and include lactate, alanine, pyruvate, (4Z-7Z-10Z-13Z-16Z-19Z)-Docosahexaenoic acid, (9Z)-Octadecenoic acid, fructose 1,6-bisphosphate, and citrate, all of which decreased in hiBMEC treated with serum compared to serum-free hiBMEC cultures. The metabolites with the largest contributions

to the separation along component 1 largely belonged to glycolysis, fatty acid metabolism, and the TCA cycle.

6.3.7. Serum from exercise trained individuals did not significantly impact barrier function.

To assess BMEC permeability, I measured changes in barrier function in APOE ε3 and ε4 hiBMEC treated with sedentary or exercise trained serum. There was no difference in TEER for APOE ε3 and ε4 hiBMEC treated with sedentary or exercise trained serum (Fig. 6.7A). However, the increase in TEER after addition of sedentary serum was 55% higher in APOE ε3 hiBMEC as compared to APOE ε4 hiBMEC ($p = 0.0542$), and the increase in TEER after addition of exercise trained serum was 65% higher in APOE ε3 relative to APOE ε4 hiBMEC ($p = 0.0568$; Fig. 6.7B). The increase in TEER after addition of serum was higher in both APOE ε3 and ε4 hiBMEC when treated with sedentary serum compared to exercise trained serum. The increase in TEER after addition of serum was 17% higher in APOE ε3 hiBMEC treated with sedentary serum compared to those treated with exercise trained serum ($p = 0.0721$). Similarly, the increase in TEER after addition of serum was 38% higher in APOE ε4 hiBMEC treated with sedentary serum treatment compared to APOE ε4 hiBMEC treated with exercise trained serum ($p = 0.0817$).

Sodium fluorescein permeability, normalized to the APOE ε3 hiBMEC treated with sedentary serum permeability, demonstrated no differences among APOE ε3 and ε4 hiBMEC with sedentary or exercise trained serum (Fig. 6.7C).

6.3.8. Serum from exercise training may increase tight junction protein continuity.

Finally, I assessed ZO-1 and claudin-5 tight junctions in APOE ε3 and ε4 hiBMEC treated with genotype-matched serum. In Chapter 5, I demonstrated that APOE ε4 hiBMEC had lower ZO-1 continuity compared to APOE ε3 hiBMEC. With serum, there was no difference in ZO-1 continuity between APOE ε3 and ε4 hiBMEC (Fig. 6.7D). However, APOE ε4 hiBMEC treated with exercise-trained serum had 8.2% higher continuity than APOE ε4 hiBMEC treated with sedentary serum ($p = 0.0014$; Fig. 6.7E). When these data were analyzed by donor rather than per cell, there were no significant differences in junction continuity with genotype or serum type (Fig. 6.7F).

When analyzed on a per-cell basis, APOE ε4 hiBMEC treated with sedentary serum had 15% higher claudin-5 continuity than APOE ε3 hiBMEC treated with sedentary serum ($p < 0.0001$; Fig. 6.7G-H). APOE ε4 hiBMEC also had 9% higher claudin-5 continuity when treated with exercise trained serum compared to APOE ε3 hiBMEC ($p < 0.0001$). Exercise trained serum decreased claudin-5 junction continuity by 6% in APOE ε3 hiBMEC ($p = 0.0008$), while claudin-5 continuity in APOE ε4 hiBMEC was unchanged. However, similar to the ZO-1 measurements, when the claudin-5 continuity was analyzed by serum donor, there was no significant difference in the percent of continuous junctions from genotype or serum type (Fig. 6.7I).

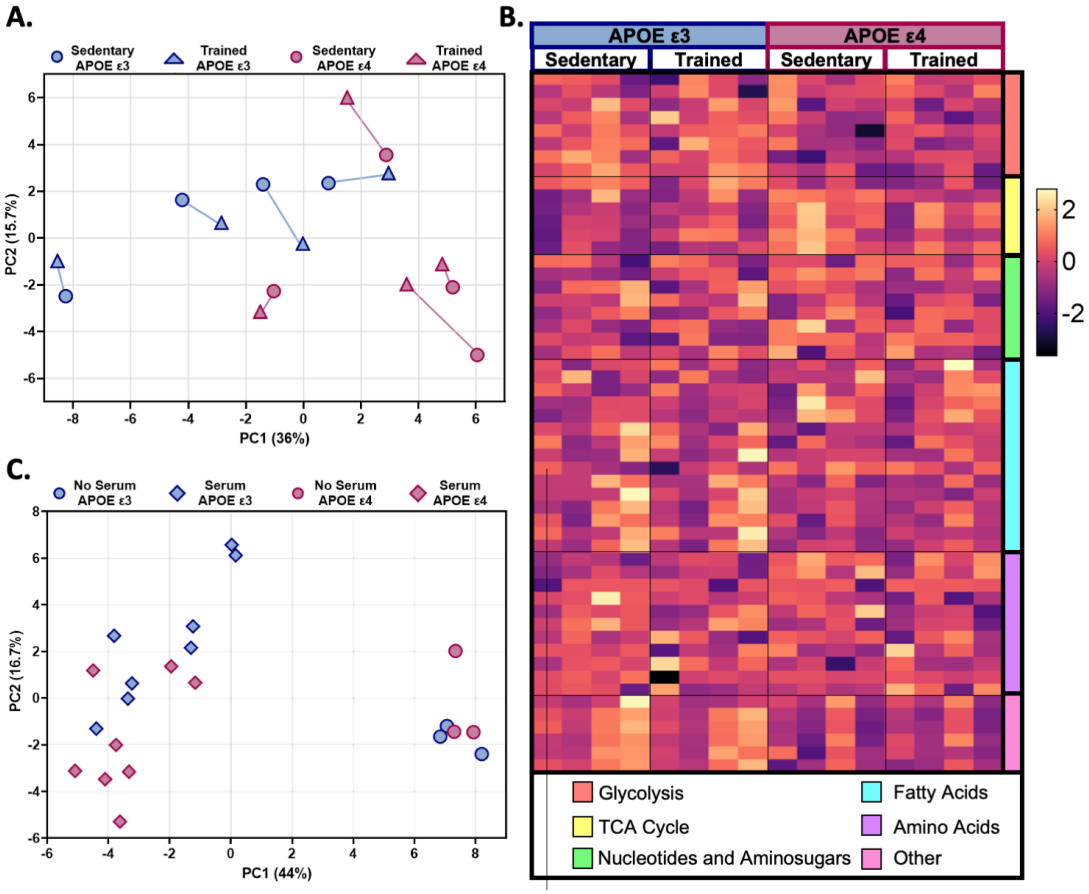


Figure 6.6. Serum systemically altered the hiBMEC metabolome, but exercise training did not. **(A)** PLS-DA of APOE ε3 (blue) and ε4 (pink) hiBMEC treated for 24 hours with 20% serum from genotype-matched sedentary (circle) and exercise trained (triangle) individuals and $^{13}C_6$-glucose. A line connects hiBMEC treated with serum samples from the same donor (n = 4 donors per genotype). Data analyzed are based on the labeled fraction of each metabolite. **(B)** Heat map of the metabolite labeled fractions in APOE ε3 and ε4 hiBMEC treated with serum from sedentary and exercise trained individuals clustered by metabolic pathway. **(C)** PLS-DA of the metabolite labeled fraction of APOE ε3 (blue) and ε4 (pink) hiBMEC treated for 24 hours with no serum (circle) or serum (diamond). Serum effects were analyzed for combined sedentary and trained serum samples and compared to hiBMEC not treated with serum (n = 8 donors per genotype with serum, n = 3 donors per genotype without serum).

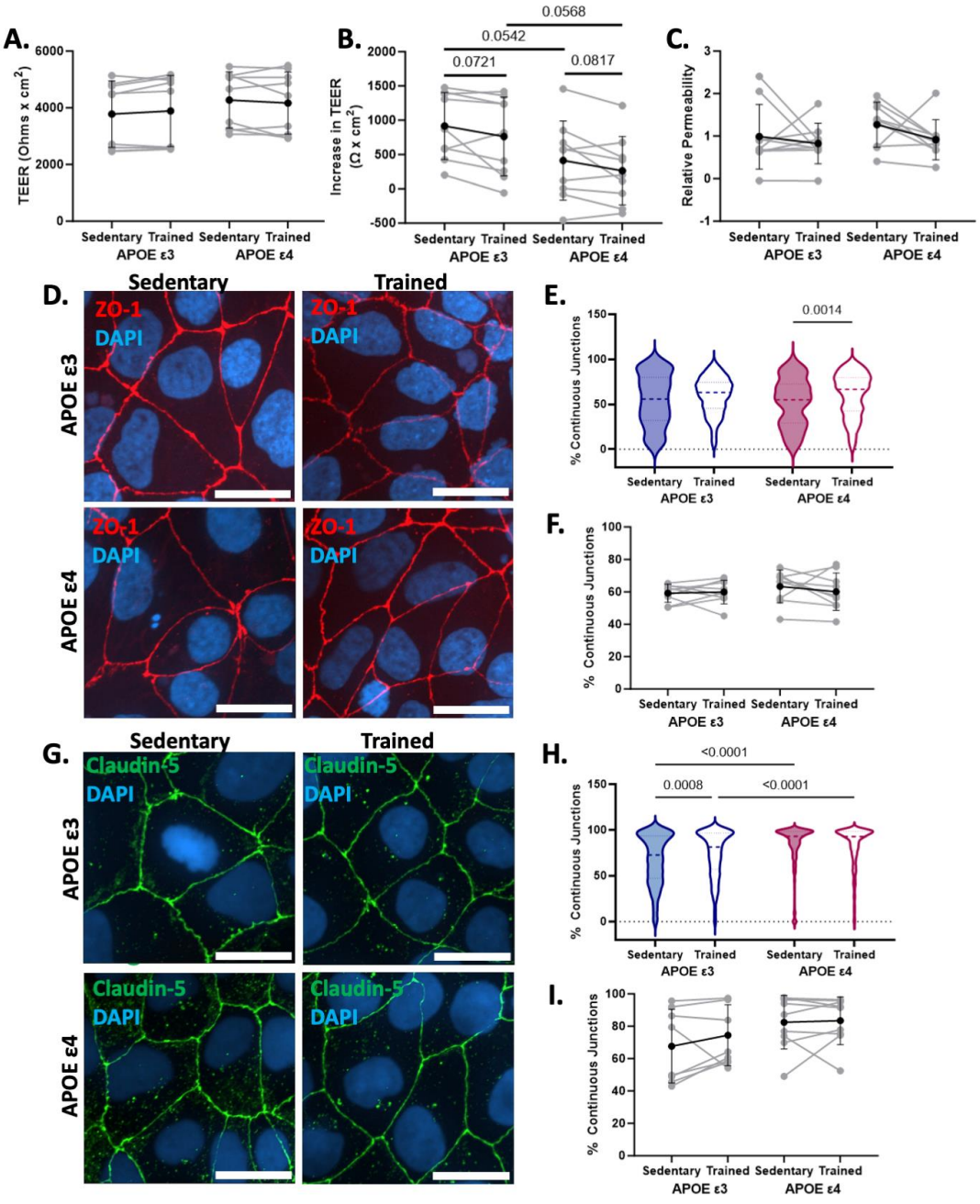


Figure 6.7. Barrier integrity was not significantly altered by sedentary or exercise trained serum in APOE ε3 or APOE ε4 hiBMEC. (A) TEER measurements in APOE ε3 and ε4 hiBMEC following 24 hours of treatment with 20% genotype-matched serum, and **(B)** the change in TEER values over the 24-hour serum treatment period. **(C)** Permeability coefficient calculated based on sodium fluorescein permeability after 24 hours of serum treatment. Immunostaining was used to visualize tight junction proteins **(D)** ZO-1 and **(G)** claudin-5 following serum treatment, with junction continuity was quantified on a **(E,H)** per-cell (n = 356 – 407 cells per treatment group) and **(F,I)** per-serum donor basis (n = 9 donors per genotype). **(A,B,C,F,I)** analyzed using repeated measures two-way ANOVA with Fisher's Least Significant Difference Test. **(E,H)** analyzed using two-way ANOVA with Fisher's Least Significant Difference Test.

6.4. Discussion

Sedentary lifestyle is a modifiable AD risk factor, and exercise training has been shown to reduce brain atrophy with age [348], increase brain glucose metabolism [349], [362], and improve cognition [363]. Despite ample evidence that exercise training reduces AD risk, few studies have examined how exercise training modifies BMEC metabolism and function to support brain health. Here, I demonstrated that serum from exercise trained individuals decreased rate-limiting glycolytic enzymes HK2 and PFKFB3 in APOE ε4 hiBMEC but not APOE ε3 hiBMEC. However, exercise trained serum did not significantly alter glycolytic rates in APOE ε3 or APOE ε4 hiBMEC. Furthermore, exercise trained serum increased SIRT1 in APOE ε3 hiBMEC and decreased SIRT1 in APOE ε4 hiBMEC. Despite these changes, exercise trained serum did not significantly impact barrier function in either APOE ε3 or ε4 hiBMEC. The lack of significant effects of exercise training on barrier function or metabolism may indicate that the benefits of exercise on BMEC are conferred through other means not tested here, such as changes in blood flow or inflammation.

VO_2 max did not significantly increase following 6 months of exercise training in APOE ε3 or ε4 participants. A meta-analysis of 41 past studies of exercise training in 2,102 individuals showed VO_2 max can increase by 3.50 ± 0.84 $mL*kg^{-1}*min^{-1}$ in older adults [364]. It is, however, possible that physical fitness was improved in other measures of this study not reported here such as grip strength or 6-minute walk test.

Exercise trained serum increased SIRT1 in APOE ε3 hiBMEC but decreased SIRT1 in APOE ε4 hiBMEC. A meta-analysis of SIRT1 changes with exercise training demonstrates that acute exercise elevates SIRT1 in skeletal muscle and consistent exercise can elevate circulating SIRT1[365]. In general, exercise regulates SIRT1 via lactate concentration. Mice with access to wheel running for 30 days had elevated hippocampal lactate, which increased hippocampal SIRT1 [366]. Serum samples from APOE ε3 and ε4 participants could have had different lactate concentrations, which would have differentially modulated SIRT1 levels in the APOE ε3 and ε4 hiBMEC. Additionally, caloric restriction has been shown to increase SIRT1 [367]. Human embryonic kidney cells treated with 10% serum from calorie restricted mice had increased SIRT1, which was inhibited upon treatment with insulin or insulin-like growth factor-1 (IGF-1). Caloric intake was not measured in this study. However, serum insulin or IGF-1 could have changed with exercise training in a genotype-dependent manner to differentially regulate SIRT1 in APOE

ε3 versus APOE ε4 hiBMEC. Future studies should examine insulin and IGF-1 in exercise-trained cohorts stratified by APOE genotype to determine if these are upstream differential regulators of SIRT1 in APOE ε3 and ε4 individuals.

HK2 followed the same trend as SIRT1, increasing in APOE ε3 hiBMEC treated with exercise trained serum and decreasing in APOE ε4 hiBMEC treated with exercise trained serum. As discussed in Chapter 5, SIRT1 can regulate HK2 transcription, so it is likely the dimorphic effects of exercise on SIRT1 also impact HK2. PFKFB3, another glycolytic rate limiting enzyme, also decreased in APOE ε4 hiBMEC following exercise training. PFKFB3 is decreased by Krüppel-like factor 2 (KLF2) [332], which increases with exercise training [368]. KLF2 may therefore be one mechanism through which exercise decreases PFKFB3 in APOE ε4 hiBMEC, though it is unclear why the same reduction in PFKFB3 is not observed in APOE ε3 hiBMEC. Additional serum profiling would be necessary to uncover how APOE ε4 differentially regulates PFKFB3 compared to APOE ε3.

Although HK2 and PFKFB3 both decreased in APOE ε4 hiBMEC following treatment with exercise trained serum, glycolysis did not change with exercise trained serum treatment. In leukemia cells, HK2 knockdown increased carbon flux into the pentose phosphate pathway (PPP) and TCA cycle but did not significantly impact glycolysis [369]. Therefore, reduced HK2 in APOE ε4 hiBMEC treated with exercise trained serum may alter PPP and TCA pathway activity more than glycolysis, though metabolites in these pathways were not consistently altered in my dataset. In APOE ε3 hiBMEC, HK2 protein levels increased, but glycolysis was unchanged. Glycolytic rates are modulated by many metabolites and proteins outside of the direct glycolytic pathway including ATP bioavailability [369], so likely other serum or intracellular factors are overriding the changes in HK2 to modulate glycolytic rates.

Here, I demonstrated that changes in APOE, SIRT1, and INSR were positively correlated with changes in some glycolytic enzymes including HK2 in APOE ε3 hiBMEC, but only changes in SIRT1 were positively correlated with changes in HK2 in APOE ε4 hiBMEC. In Chapter 5 I demonstrated that decreased INSR signaling decreased glycolysis, and that decreased SIRT1 correlated with decreased glycolytic enzyme levels. It therefore follows that increases in SIRT1 was positively correlated with increases in HK2 in both

cell types. Brain cortical APOE protein levels have been shown to increase in mice following 8 weeks of treadmill running [370], so it is unsurprising that changes in APOE are positively correlated with changes in other proteins that increase with exercise training.

In Chapter 5, PLS-DA revealed a clear separation of serum-free APOE ε3 and APOE ε4 hiBMEC metabolites; however, this separation was no longer apparent when cells were treated with serum from sedentary and exercise-trained individuals. Though the lack of separation could be due to the larger inherent variability involved when using human serum samples, it is also possible that the addition of human serum reduced metabolomic differences between APOE ε3 and ε4 hiBMEC. Serum decreased intracellular fatty acid synthesis, which may be due to the presence of fatty acids in serum that are not generally present in serum-free cell culture experiments. Overall, the reduction in metabolomic separation between APOE ε3 and ε4 hiBMEC in the presence of serum reveals that despite intracellular differences, other cells in the body may be secreting metabolites and proteins to naturally regulate genotype-dependent differences in BMEC.

I hypothesized that serum from exercise-trained individuals would increase tight junction protein continuity. In these experiments, I did not see consistent changes in barrier function in response to serum from exercise trained individuals. Aerobic exercise increases cerebral blood flow [371], and shear stress can increase claudin-5 and ZO-1 levels in human BMEC [372], [373]. Thus, it is possible that changes in BBB function are more a factor of increased shear stress exposure than from modifications of serum in response to exercise.

6.6. Limitations

The results presented here indicate that exercise trained serum impacts hiBMEC glucose metabolism and SIRT1 differently depending on APOE genotype. However, the results of this study are limited by testing serum effects on only one set of APOE ε3 and ε4 hiBMEC. The results could be better generalized if the serum was tested on multiple hiBMEC lines from each genotype. Additionally, as discussed in Chapters 3-5, the use of hiBMEC is limiting itself since hiBMEC are not a perfect model of BMEC function

and metabolism. In addition to altering serum components, exercise training can also initiation extracellular matrix remodeling [374] and inflammatory responses [375], which may also have larger impacts on BMEC metabolism and function. I could not measure shear stress response or inflammation in this study, as the hiBMEC generated using this protocol do not respond to shear stress in the same manner as most microvascular endothelial cells [376] and lack endothelial markers of inflammation [377]. Finally, the studies performed in this chapter examined the effects of serum from exercise trained individuals on hiBMEC metabolism and function only. A multicellular model including circulating immune cells and other brain cells would give more insight into modifications of BMEC function and metabolism in response to exercise training.

6.7 Conclusions

Exercise training improves brain glucose metabolism and slows cognitive decline. In this chapter, I demonstrated that serum from exercise trained individuals has dimorphic effects on hiBMEC dependent on APOE genotype. In APOE ε3 hiBMEC, rate limiting glycolytic enzyme levels increased with exercise trained serum, while the same enzyme protein levels decreased in APOE ε4 hiBMEC with exercise trained serum. These changes correlated with SIRT1, an upstream regulator of glycolysis, but not with overall glycolytic rates which were unchanged in APOE ε3 and ε4 hiBMEC. Finally, serum from exercise training had little impact on hiBMEC barrier function. Overall, these data suggest exercise training may have different impacts on BMEC depending on APOE genotype, indicating a need for future studies of exercise benefits on brain health to be stratified by genotype and perhaps genotype-dependent exercise recommendations.

Chapter 7: Conclusions and Future Work

7.1. Thesis Summary

One out of every three seniors dies from Alzheimer's disease (AD) or a related dementia, yet to date, scientists have been unable to identify a cause, cure, or even highly effective treatments to slow AD. Brain microvascular endothelial cells (BMEC) line the blood vessels of the brain and are the primary components of the blood-brain barrier (BBB). Breakdown of the BBB is a hallmark of AD and allows cytokines and neurotoxins from the blood to infiltrate the brain to induce neuroinflammation and neurodegeneration. Additionally, BMEC are responsible for glucose transport from the blood to the brain. In AD, brain glucose metabolism is reduced, which may be due to reduced BMEC glucose uptake and transport. In this thesis, I examined how AD risk factors, including female sex, stress hormone exposure, APOE ε4 genotype, and sedentary lifestyle, impact BMEC metabolism and function. I discovered novel mechanisms of how the aforementioned AD risk factors alter BMEC metabolism and reduce BMEC function, which may contribute to AD pathogenesis.

7.2. Specific Discoveries

The overarching goal of this thesis was to understand how prominent AD risk factors increase cerebrovascular dysfunction, which may contribute to AD development. I hypothesized that female sex, stress hormone exposure, APOE ε4 genotype, and sedentary lifestyle alter BMEC metabolism, which then results in endothelial dysfunction and BBB breakdown. The impact of these risk factors on BMEC is of particular importance because most therapeutics are designed to reach their target tissue through the circulatory system, so in the brain, BMEC are the first cell type that will interact with a therapeutic. BMEC may, therefore, be the easiest cell type to target to prevent metabolic dysfunction and BBB breakdown in AD. Based on the work presented in this thesis, each of the aforementioned risk factors for AD also has different impacts on glucose metabolism and BBB function. Therefore, in designing future therapeutics to reduce AD risk or progression, it may be important to consider these risk factors and design personalized medical treatments to confer the highest benefits to each patient.

In Chapter 2, I examined how endothelial cell inflammation and oxidative stress in response to angiotensin II (AngII) were sex dependent. I used transcriptomic analysis of male and female endothelial cells (EC) treated with AngII for 24 hours to show that female EC increased expression of genes associated with inflammation and oxidative stress while male cells did not. I then showed that inflammation did not increase from AngII alone but did increase in conjunction with a secondary inflammatory stimulus only in female EC. I also discovered that AngII increased reactive oxygen species production in female, but not male, EC. Finally, I showed that female EC had higher NADPH oxidase gene expression, likely due to escape from X-chromosome inactivation (XCI). Elevated NADPH oxidates contributes to the higher reactive oxygen species production in female EC in response to AngII. Overall, my discoveries indicate that female EC become more dysfunctional in response to AngII than male EC, which may contribute to the increased prevalence of AD in women compared to men.

In Chapter 3, I used transcriptomic and metabolomic approaches to interrogate the ability of induced pluripotent stem cell derived BMEC (hiBMEC) to model BMEC metabolism by comparing hiBMEC glucose metabolism to primary BMEC (hpBMEC) glucose metabolism. I demonstrated that hpBMEC had higher glycolytic flux compared to hiBMEC. hpBMEC and hiBMEC had significantly different glycolytic enzyme gene expression and protein levels, but metabolomics showed nearly identical glucose labeled fractions of glycolytic metabolites. These data indicate that hiBMEC and hpBMEC have similar glucose metabolism. I also discovered that hpBMEC and hiBMEC respond similarly to metabolic stimuli such as high glucose and astrocyte conditioned media. This study demonstrated that hiBMEC can be used to model BMEC glucose metabolism.

Chapter 4 built on Chapter 3 to evaluate if hiBMEC glutamine metabolism is similar to hpBMEC glutamine metabolism. In contrast to my results on glucose metabolism, I showed that hiBMEC and hpBMEC had systemically different glutamine metabolism. HiBMEC used glutamine to produce more glutathione, fatty acids, and asparagine, and did not secrete any glutamate. HpBMEC used glutamine to produce more GABA, nucleotides, and aminosugars. hiBMEC also had more punctate, immature mitochondrial morphology compared to the elongated, branched hpBMEC mitochondrial networks, which may contribute to mitochondrial metabolism differences. These differences in hpBMEC and hiBMEC

glutamine metabolism may impact cell-cell communication and BMEC function. My discoveries from Chapters 3 and 4 highlight the necessity of fully characterizing a cellular model before its use to understand model strengths and limitations, in particular which results may not applicable to humans.

In Chapter 5, I evaluated how the APOE ε4 genotype, the highest genetic AD risk factor, alters hiBMEC metabolism and function compared to the more neutral APOE ε3 genotype. I used CRISPR/Cas9 to create induced pluripotent stem cells (iPSC) homozygous for the APOE ε3 or APOE ε4 alleles. After differentiating these cells in hiBMEC, I evaluated their glucose metabolism and barrier function. I discovered that APOE ε4 hiBMEC had reduced barrier function and glucose metabolism compared to APOE ε3 hiBMEC. Reduced glucose metabolism in APOE ε4 hiBMEC was likely due to decreased levels of the primary glucose transporter, GLUT1, as well as lower levels of key glycolytic enzymes hexokinase 2 (HK2) and 6-phosphofructo-2-kinase/fructose-2,6-biphosphatase 3 (PFKFB3). I discovered a mechanism that may contribute to reduced glycolysis in APOE ε4 hiBMEC. APOE ε4 hiBMEC had reduced insulin signaling, which decreased GLUT1 translocation to the cell membrane and thus reduced glycolysis. I also discovered a second mechanism through which APOE genotype decreases barrier function in BMEC. APOE ε4 hiBMEC had decreased Sirtuin 1 (SIRT1), a protein deacetylase that reduced the continuity of zonula occludins 1 (ZO-1), which likely contributes to the reduced barrier function of APOE ε4 hiBMEC. These discoveries overall demonstrate that the APOE ε4 genotype can detrimentally change BMEC metabolism and function, which may contribute to AD pathogenesis.

In Chapter 6, I treated APOE ε3 and ε4 hiBMEC with serum from genotype-matched sedentary older adults collected before and after 6 months of exercise training to evaluate how a sedentary lifestyle contributes to BBB dysfunction and how exercise training can counteract the dysfunction. I discovered that serum from exercise trained individuals decreased HK2 and PFKFB3 protein levels in APOE ε4 hiBMEC but did not decrease overall rates of glycolysis. I also discovered that exercise training increased SIRT1 in APOE ε3 hiBMEC but decreased SIRT1 in APOE ε4 hiBMEC. The dimorphic response of SIRT1 to exercise training may have implications in lipid metabolism, cholesterol homeostasis, and inflammation. Finally, I demonstrated that exercise training increased claudin-5 continuity in APOE ε3 but not APOE ε4 hiBMEC.

Due to inherent human variability, many of the discoveries in this chapter were small and had significant variance. However, I demonstrated that exercise training can significantly impact glycolytic enzyme levels and SIRT1 differently in APOE ε3 and ε4 hiBMEC, which may indicate that recommendations for exercise training in older adults need to be further evaluated, and perhaps differentiated by APOE genotype, to best benefit individuals with the APOE ε3 and APOE ε4 genotypes.

7.3. Contributions to the Field

Female sex, stress hormone exposure, APOE ε4 genotype, and sedentary lifestyle are all known AD risk factors. Almost every *in vitro* study of these risk factors focuses on neurons, as their dysfunction most directly causes reduced cognition. However, BMEC dysfunction can impact the brain. BMEC also directly interface with the circulatory system, and thus interact directly with circulating proteins and metabolites that influence AD risk (e.g., AngII, APOE). BMEC also may feel the effects of exercise more directly than other cells since consistent exercise training regiments increase cerebral blood flow [347]. Thus, understanding the impacts of these risk factors on BMEC is vital to understanding how they modify AD risk.

I demonstrated for the first time that female EC are more sensitive to AngII independent of sex hormone exposure. Estrogen is a neuroprotective biomolecule, and sex differences in AD (and other vascular diseases) are often attributed to reduced estrogen following the menopausal transition in women. I used human umbilical vein endothelial cells (HUVEC), which are hormone naive, and showed widespread differences in AngII response in male and female cells. The presence of sex differences in the absence of sex hormones indicate hormone replacement therapies may not be sufficient to address sex differences in AD progression. These sex differences may instead be attributed to escape from X chromosome inactivation (XCI), which may impact cellular function and disease risk [183]. The results of this study may also be more broadly applicable to other vascular diseases, such as pulmonary arterial hypertension and vascular complications of diabetes, which are both more prevalent in women than in men.

I also showed for the first time that iPSC derived BMEC had similar glucose metabolism to hpBMEC but systemic differences in glutamine metabolism. In the context of BMEC, these data indicate that hiBMEC can adequately be used to model glycolysis but are limited in their ability to model oxidative respiration. More broadly, these studies suggest that iPSC-derived cell metabolism may be intrinsically different from *in vivo* cells. Similar results have been demonstrated in cardiomyocytes, which have different mitochondrial morphology in iPSC derived cells compared to primary cells unless the cells undergo additional maturation steps in the differentiation [274], [378]. It is therefore vital to characterize and account for these differences when using iPSC derived cells for disease modeling, as the results of such studies may not directly apply to the human condition. Further, the differences in systemic glutamine metabolism between hpBMEC and hiBMEC underscore the importance of analyzing entire metabolic networks rather than individual metabolic pathways since the metabolic pathways are interdependent and changes may compound upon one another.

This is also the first study to show that reduced insulin signaling and SIRT1 activity in APOE ε4 hiBMEC contributes to their reduced glucose metabolism and barrier function, respectively. Reduced insulin signaling and SIRT1 have both been demonstrated in APOE ε4 neural cell lines, but this was the first study to show these mechanisms are also reduced in BMEC. These pathways may also be dysregulated in glial cells and pericytes, leading to widespread reductions in brain glucose metabolism. Furthermore, the APOE ε4 genotype may reduce glucose metabolism and EC barrier function in other tissue beds, which may contribute to the known elevated risk of cardiovascular disease and diabetes in individuals with the APOE ε4 genotype.

Finally, this is the first study examining how serum from sedentary and exercise trained individuals impacts hiBMEC metabolism and function. I found that the most prominent serum effect was to increase SIRT1 in APOE ε3 hiBMEC and reduce SIRT1 in APOE ε4 hiBMEC. My data are the first to show that changes in SIRT1 with exercise training are dimorphic based on APOE genotype. Though these SIRT1 changes did not correlate with large changes in glycolysis or barrier function, SIRT1 can also impact neuroinflammation, lipid metabolism, and cholesterol sensing. Exercise modulation of SIRT1 in a genotype-

dependent manner indicates that APOE ε3 populations may see more benefits from exercise training than APOE ε4 populations, in particular as it related to AD risk.

7.4 Future Studies

7.4.1. Sex differences in response to AngII in BMEC.

In this thesis, I demonstrated that female HUVEC and human pulmonary artery endothelial cells (HCAEC) increased inflammation and oxidative stress in response to AngII, while male HUVEC and HCAEC did not. Although many functions are conserved among EC of different tissue beds, not all functions are. Male and female BMEC may have different responses to AngII than was seen in HUVEC and HCAEC. Therefore, it would be worthwhile to examine how male and female BMEC respond to AngII treatment. Further, it would be interesting to investigate how sex differences in BMEC response to AngII propagate to other brain cell types in both *in vitro* and *in vivo* studies. *In vitro*, 3D neurovascular units could be patterned with an endothelialized channel surrounded by neurons and astrocytes [379], [380], [381], [382], [383], [384], [385], [386], [387], [388], [389], [390], [391], [392], [393], [394], [395], [396], [397], but with exclusively male or female cells. AngII could then be perfused through the vessel and barrier permeability, inflammation, and neuron and astrocyte metabolism and function could be measured. *In vivo*, similar measurements could be collected but with male and female rodents that are treated with AngII. The results of these studies would give more insight into how AngII, as a circulating stress hormone, alters BMEC function as well as the function of surrounding brain cells, differently in men and women.

7.4.2. Development of improved BMEC metabolic models.

My studies demonstrated that while hiBMEC have similar glucose metabolism to hpBMEC, they have systemically different glutamine metabolism than hpBMEC. In this work, we compared hiBMEC to hpBMEC and considered hpBMEC to be the gold standard model of BMEC. The hpBMEC, however, had been expanded for 7-9 passages before they were used in these experiments, which provided ample time for the hpBMEC to lose characteristics of their *in vivo* phenotype. If they were more readily available,

comparing hiBMEC to freshly isolated hpBMEC may provide different results. Perhaps hiBMEC have a metabolic signature more similar to BMEC in the brain than hpBMEC after expansion.

Recent efforts have focused on improving the hiBMEC differentiation protocol to remove the underlying epithelial transcriptomic signature and produce more cells with a more endothelial phenotype through upregulation of ETS transcription factors during differentiation [217] or through extended culture [377]. In a similar manner, a new hiBMEC differentiation protocol could be developed with a focus on improving metabolic similarities between hiBMEC and BMEC *in vivo*. In fact, iPSC-derived cardiomyocytes have immature mitochondria similar to the hiBMEC, and extended cardiomyocyte culture following differentiation leads to mitochondrial maturation [274]. Therefore, the newer extended hiBMEC culture differentiation protocol [377] may also improve hiBMEC metabolism and should be investigated. Overall, improving hiBMEC differentiation techniques to generate cells with a more similar metabolome to BMEC *in vivo* would greatly increase the ability of these cells to model BMEC function, communication, and metabolite transport.

7.4.3. Multicellular models to investigate the effects of APOE genotype on brain function.

In this work, I showed that the APOE ε4 genotype reduced hiBMEC glucose metabolism and barrier function, which are in part due to reduced insulin and SIRT1 signaling. The reductions in glucose metabolism noted in Chapter 5 were small, and may not, on their own, be biologically meaningful. However, in the brain, all other cells will also have the APOE ε4 genotype, which could lead to larger scale differences in glucose metabolism and therefore larger biological impact. APOE ε3 and ε4 iPSC could be used to generate multiple brain cell types, including hiBMEC, pericytes, astrocytes, and neurons. These cells could then be combined to create a 3D neurovascular unit. In this multicellular model, one could measure glucose metabolism changes to determine if the inclusion of more cell types leads to more extensive glucose hypometabolism. Additionally, the insulin and SIRT1 pathways could be modulated using activators and inhibitors perfused through a fabricated endothelialized channel to investigate how potential new therapeutics targeted towards these pathways may improve BMEC glucose metabolism and barrier function, and how these improvements could be transmitted to surrounding brain cells.

7.4.4. Multi-omics analysis of serum and BMEC pre- and post-exercise training.

In this thesis, I used Seahorse assays, YSI analysis, Western blotting, and metabolomics to evaluate the metabolic impacts of serum from sedentary and exercise trained individuals on APOE ε3 and ε4 hiBMEC. Omics-based approaches would give more insight into how both serum and hiBMEC treated with serum are altered by exercise training. For example, proteomic and metabolomic analysis of serum pre- and post- exercise training would allow researchers to see what proteins and metabolites change with exercise training. This would enable us to develop mechanistic hypotheses of how exercise modulates BMEC barrier function and metabolism. Furthermore, proteomic, metabolomic, and transcriptomic analysis of hiBMEC treated with sedentary and exercise trained serum may highlight changes in pathways vital for BMEC function and metabolism that were not considered in this study. These future studies could enable development of better exercise training recommendations or therapeutics to prevent BBB breakdown and glucose hypometabolism in AD.

Appendix:

Appendix Table 1: Gene expression differences between female and male HUVEC

Appendix Table 1A. Genes upregulated in female compared to male HUVEC.

Gene Symbol	Log_2FC	Adjusted p-value
A2M	1.24672339	0.00019819
AADAC	1.36153476	1.97E-05
AADACL2-AS1	5.87184532	0.1244803
AADACP1	1.25873704	0.0011903
ABCG2	0.7353726	2.70E-07
AC003957.1	0.85851706	0.01046968
AC004490.1	2.60062776	0.16576626
AC005594.1	2.24333087	0.16049219
AC005618.1	1.93497149	0.19868911
AC005674.1	0.71200025	0.05671822
AC005699.1	1.08053824	0.00280841
AC005757.1	6.10735762	0.04542852
AC005840.2	1.3913691	0.0226773
AC006504.1	1.40320553	0.0640434
AC007384.1	1.67049225	0.08793831
AC008149.2	1.01705637	0.07108459
AC008438.1	2.55561666	0.18078871
AC008764.6	0.83862055	0.17119855
AC008868.1	2.54537404	0.18460546
AC008969.1	0.65833403	0.00874604
AC008993.1	6.05280702	0.06797364
AC009078.3	0.63992584	0.00871668
AC009509.1	3.63960768	0.00796216
AC009630.4	5.9077114	0.11074019
AC009962.1	1.07396394	0.05860975
AC009994.1	3.43484858	0.11377842
AC010422.8	0.76085909	0.24132888
AC010536.1	1.51490615	0.25727401
AC010536.2	5.05159801	3.04E-11

Appendix Table 1B. Genes upregulated in male compared to female HUVEC.

Gene Symbol	Log_2FC	Adjusted p-value
ABCA6	1.2000335	1.48E-23
ABCA8	3.36482479	2.27E-97
ABCB11	1.55859037	0.06700713
ABCC3	1.45536734	4.64E-12
ABI3BP	0.91955873	1.45E-24
ABLIM1	0.6507505	0.00331243
AC002059.3	2.38263308	0.17340714
AC004130.2	1.15124702	0.0911878
AC004466.3	0.90166052	0.15396412
AC005520.2	1.02485542	0.12389601
AC007182.2	1.39211717	0.06562912
AC009977.1	6.5751955	0.00876967
AC010737.1	11.1445288	3.94E-82
AC010889.1	8.28598829	1.16E-11
AC010889.2	5.62878912	0.19535641
AC011287.1	6.82530466	0.00213007
AC011379.1	5.59510073	0.20252223
AC011444.4	5.82460589	0.15970338
AC011451.4	5.4319229	0.27830625
AC012625.1	3.3733937	0.22110291
AC013452.2	3.04008652	0.27755747
AC025154.2	3.77887731	0.19815286
AC026341.1	6.02416068	0.1054951
AC073130.3	1.19125519	0.02281344
AC078850.1	1.10962002	0.12870122
AC079140.2	1.48043039	0.09123961
AC083862.2	1.17536076	0.1444589
AC089983.1	1.33726225	0.18890686
AC092295.2	1.63505296	0.14467628

AC010761.1	0.70735262	0.27310602
AC010809.2	1.4503487	0.22151473
AC010913.1	1.59237747	0.22938444
AC011447.7	1.20763829	0.03225423
AC011491.2	5.44385484	0.26713236
AC011498.7	0.76286925	0.24798172
AC011510.1	1.55890733	0.20194767
AC011767.1	3.53087947	0.27459908
AC012213.1	5.84468039	0.11967529
AC012443.2	0.7317746	0.23977504
AC012531.1	3.30265038	0.00060182
AC012615.6	0.72723153	0.21722361
AC013731.1	5.56480363	0.23775793
AC015712.2	0.8318829	0.16759502
AC016586.1	1.53500569	0.06595857
AC016597.1	3.43625893	0.03214944
AC018521.5	1.03037968	0.26607684
AC018665.1	1.09490214	0.00595053
AC018695.9	1.20301089	0.22122922
AC019205.1	0.76358686	0.22304026
AC020659.1	2.53804269	0.00121762
AC020907.4	0.9698838	0.14366881
AC022137.3	0.85962355	0.2966863
AC022150.2	1.57989151	0.03043208
AC022336.3	1.92926239	0.28054044
AC022400.1	3.22005928	0.01063959
AC022440.1	5.55533181	0.23977504
AC024267.4	3.37368646	0.04108873
AC025614.2	1.69375618	0.00012141
AC025774.1	0.75976347	0.22434087
AC026407.1	5.62041915	0.20889411
AC026474.1	5.67714571	0.18110315
AC026741.1	1.67539974	0.16645167
AC027290.2	0.8666686	4.37E-05
AC027601.1	1.49768438	0.01495464
AC027601.4	1.38321375	0.07544719

AC092490.1	1.54146928	0.09355193
AC105942.1	0.68543648	0.15582181
AC108519.1	1.654247	0.02534689
AC108941.3	4.58155709	2.73E-15
AC123023.1	2.89127891	0.00234515
AC239859.5	1.43145736	0.03582424
AC245407.2	2.41311423	0.14360171
ACKR1	3.49500445	6.77E-24
ACKR4	1.90444183	4.74E-19
ACOT1	1.64357645	0.00010448
ACSM3	0.72096262	2.50E-05
ADA2	1.81497527	4.23E-59
ADAM23	0.63591601	3.34E-11
ADAMTS18	1.02939731	3.12E-16
ADM2	1.04944397	0.16019159
AGAP10P	2.0914856	0.01706323
AGPAT1	1.38968073	0.00122128
AHCYL2	0.60289627	2.17E-06
AK3P5	1.47993294	0.1312157
AK5	0.79902102	0.0005443
AKR1C1	1.01902	0.04542852
AKR1C2	1.74809632	0.12053799
AKR1C3	1.33986362	2.17E-12
AL118511.1	5.86616412	0.13870707
AL121757.1	3.60871488	0.25748719
AL353748.3	0.9276591	0.29185026
AL513550.1	0.62914771	0.22529545
AL592148.3	0.95765573	0.1678126
AL627309.7	1.30777328	0.020385
AL662795.2	4.6694886	0.07083475
AL713998.1	5.45484206	0.29879928
ALDH1A2	0.61434754	5.97E-08
ALDOC	0.64184258	0.01514874
ALX1	1.06807323	0.0875976
AMPH	1.28664885	1.42E-10
AMZ2P1	0.64378634	0.00893325

AC027601.5	0.70636399	0.04168395
AC063960.2	2.86945524	0.08728646
AC068647.2	1.82307351	0.00388762
AC068790.5	2.13293902	0.08566451
AC068831.6	0.65281596	0.00600312
AC073107.2	2.5280495	0.08728646
AC073840.1	5.78658735	0.13753516
AC078983.1	5.6409531	0.20487288
AC079140.3	1.30860683	0.20227993
AC079322.1	5.67000136	0.18218064
AC079921.2	1.30863571	0.23983848
AC079922.2	0.63817473	0.21220811
AC090826.1	2.9521683	0.22109578
AC091057.1	1.67701521	5.14E-10
AC091167.4	3.13375801	0.12732016
AC092135.2	5.68547329	0.17941363
AC092279.1	0.78872719	6.39E-06
AC092279.2	0.94247726	0.23007289
AC092375.2	1.03037744	0.23876853
AC092821.1	4.61351932	6.44E-14
AC093510.2	5.8005216	0.15785338
AC093909.1	3.02596714	4.30E-06
AC093909.6	0.69530453	0.24403076
AC104561.4	4.05642072	0.23353172
AC107027.3	1.25863067	0.0722578
AC107959.3	1.5181715	0.12777478
AC112484.5	2.49676926	0.01814249
AC112777.1	0.67975643	0.08545386
AC122688.3	0.7586341	0.13482347
AC122718.2	2.15312406	0.28327579
AC124283.4	1.70454552	0.11535998
AC124944.3	0.68026558	0.14280402
AC131009.4	1.63371063	0.00447188
AC131235.3	5.5083938	0.27133699
AC137630.5	1.53695648	0.06368443
AC137932.1	0.67692347	0.00908538

ANKRD1	0.97041339	8.23E-26
ANKRD20A3P	5.40690885	0.28375427
ANKRD20A4P	4.18450919	0.00030937
ANKRD24	2.45837752	0.00935456
ANO5	1.16455153	0.01052467
ANOS2P	7.25038042	6.32E-05
AP002957.1	5.69293512	0.15295597
AP005018.2	3.19515472	0.0018644
APCDD1	1.94477547	0.00782939
APCDD1L	2.44751829	3.02E-14
APOBEC3G	1.25398349	7.54E-07
APOE	1.7556916	4.00E-14
AQP5	2.79007172	9.53E-11
AQP7P1	1.10730461	0.24266529
ARHGAP6	1.19073344	0.14730371
ARHGEF6	0.62131192	5.98E-05
ARL4A	0.62979539	2.59E-09
ARRDC4	0.65497617	0.22499152
ART4	1.06513335	1.05E-23
ASAH2B	0.80144318	0.00144371
ASIC1	1.10759014	0.04280734
ASS1	0.90563795	0.00094417
ATP6AP1L	1.18631326	0.00852851
B3GNT9	0.72163727	0.00867785
BAMBI	0.74213849	0.02951711
BCL2L10	1.47981448	0.06739922
BCORP1	8.64523405	2.59E-15
BDNF	0.88524993	0.00546625
BGN	1.08645607	3.92E-45
BMP4	0.90026621	8.37E-27
BMPER	2.15042948	0.04280734
BMPR1B	1.28850416	0.00701835
BMS1P10	1.6342383	1.99E-06
BRD2	1.30509698	2.20E-08
BST2	1.15235041	3.75E-34
BTBD7P1	6.24095136	0.04532271

AC138028.2	0.9000351	0.1244803
AC138649.1	1.62358396	0.01149549
AC139795.3	5.47801286	0.25822356
AC141557.1	1.13562607	0.22382186
AC141557.2	1.91443879	0.00146602
AC146944.2	2.99526855	0.11356143
AC243964.3	1.12172708	0.00020106
AC245060.6	0.62654196	0.11967529
ACACA	0.71229044	0.0124102
ACOT11	0.86904927	0.00222767
ACRV1	1.80445144	0.15919986
ADAMTS12	3.04265144	4.14E-14
ADAMTS2	4.13570603	0.02087146
ADAMTS4	0.86042896	2.07E-14
ADAMTS9	0.71004485	8.71E-13
ADAMTSL4-AS1	2.82598435	0.19815286
ADCY10	5.55533181	0.23977504
ADCY7	0.64608089	0.00914387
ADGRE5	0.67011278	0.00442317
ADGRF3	1.71746149	0.29788996
ADGRF5P1	4.34285245	0.00030399
ADRB2	2.11874432	0.00464101
AFF2	2.87972166	0.29767044
AGAP13P	3.01913716	0.00280841
AGAP7P	1.43136677	0.05448659
AHRR	1.77664782	0.09862994
AIDAP2	0.84041576	0.13977128
AL021707.8	1.83056367	0.14280402
AL021937.3	1.97599327	0.03087647
AL022069.1	3.67056244	0.1911154
AL022069.2	5.59807461	0.23011575
AL022328.2	1.04372962	0.22016124
AL022331.1	5.45852491	0.26340558
AL031186.1	1.12473056	0.24976765
AL031658.1	1.07762004	0.0376756

C12orf60	0.77646386	0.04974876
CA11	0.78837951	0.04194101
CA12	1.16209211	0.00084767
CADM3	3.73529076	3.75E-144
CADM3-AS1	3.41802519	1.19E-05
CAMK2N1	0.6570129	1.35E-06
CAMK4	0.77882648	0.03389245
CAMTA1-DT	1.92855421	0.1673931
CASP1	0.84042966	0.00119204
CATSPERG	2.23287443	0.02229354
CCBE1	2.22581143	3.04E-38
CCDC110	1.43969447	0.17241269
CCDC144NL	6.74251526	0.00447734
CCDC3	0.96237086	0.23007289
CCDC92	0.64865687	0.00348607
CCL23	2.43302836	0.02292546
CCN2	0.62672179	7.23E-16
CD14	2.60797176	0.00025156
CD200	1.09389485	2.66E-08
CELP	5.85765783	0.1270993
CEP20	1.05268207	0.00030265
CFH	0.627751	2.67E-11
CGREF1	1.07520341	0.00010152
CHRNA1	1.29267422	7.55E-06
CHRNA6	6.56041163	0.00633783
CHRNB1	0.68466517	0.00190507
CHRNB3	3.10092593	0.2329173
CLDN10	1.00514208	0.02220652
CLPSL2	5.36445645	0.29431783
CLSTN2	2.49127151	0.05975202
COL12A1	0.74972116	4.21E-18
COL13A1	0.6538726	2.81E-12
COL1A2	2.39165009	1.07E-121
COL3A1	1.6754133	4.66E-38
COL8A1	0.86807602	1.35E-26

AL031670.1	0.86497351	0.19337992
AL033543.1	1.29844883	0.16179831
AL118558.3	1.47083663	0.2869166
AL132655.1	5.53199814	0.22777868
AL133445.3	6.09944108	0.05107764
AL138689.2	0.81749268	0.11460671
AL161935.1	5.38885072	0.28054044
AL353622.1	2.05581189	6.17E-05
AL355334.2	5.83006947	0.13059129
AL355612.1	5.69013703	0.16550684
AL356489.2	5.87743455	0.12389601
AL357079.1	1.73707774	0.04864154
AL357874.2	5.90831109	0.10231431
AL442067.3	2.76595216	0.13289326
AL442125.1	0.79433161	0.00071664
AL445931.1	1.21400219	0.03854473
AL451064.2	1.57576593	0.16550684
AL512625.1	0.75300867	0.22843137
AL590004.3	1.41961596	0.14301795
AL591848.3	0.87861246	0.18110415
AL592301.1	0.85141	0.21997688
AL645608.7	1.12918192	0.17340714
AL731566.2	0.75200503	0.21259722
AL807752.5	3.85896312	0.09013066
AMIGO1	0.94072595	0.22222674
ANK3	1.47276221	1.36E-11
ANKLE1	1.21958046	1.63E-06
ANKRD13B	0.64034347	7.08E-08
ANKRD18A	2.96717648	8.81E-09
ANKRD20A1	1.4711236	0.06966043
ANKRD36B	0.71969741	9.81E-05
ANKRD36C	0.67833344	3.38E-07
AP000873.2	0.8496319	0.15924011
AP000889.1	5.64273988	0.18773495
AP001625.2	3.01158643	0.01558034
AP002800.1	1.71024388	0.04752286
COL8A2	0.77793411	0.00153861
COLEC12	0.96601125	8.06E-26
CPA3	0.91887746	0.00642453
CSMD1	1.7319772	3.99E-29
CSPG4BP	1.10299817	9.48E-06
CSPG4P12	1.35794333	0.0161705
CU633906.1	1.89017303	0.00807639
CU634019.1	1.43570654	0.02450857
CU638689.4	1.96686564	0.01033053
CUTALP	0.67546188	1.49E-05
CYB5A	0.73469927	1.53E-06
CYSLTR2	1.19238173	0.15057218
DACT3	2.07642644	5.68E-05
DAPK2	0.75659848	0.00505216
DCAF12L1	1.11449288	2.44E-16
DCN	1.39652248	0.0240857
DDX3Y	15.1740287	0
DDX43	2.09419751	6.21E-05
DHX16	4.31529634	0.00037331
DIO2	1.7565109	0.23116594
DIRC3-AS1	2.03878113	0.12111435
DISP2	2.07214178	3.03E-11
DMD	0.91317321	7.21E-10
DNAH5	0.93139905	0.15941174
DNAH8	0.88630241	4.03E-09
DNALI1	0.80597139	0.00134013
DPY19L2	0.74220315	0.03519877
DUSP23	0.79785498	3.75E-14
DYNC1I1	1.52380737	0.00017075
EBF4	0.65271271	0.02947451
EDA	0.74039958	0.28054044
EDIL3	0.76144602	3.35E-17
EDNRB	0.77691015	0.00141233
EEF1AKMT1	0.63831501	0.01470468
EFCAB2	1.32065718	1.12E-10
EFHB	1.81537044	0.2966863

AP003068.2	1.17553699	0.03278093
ARAP1-AS2	1.07021146	0.10132622
ARHGAP11B	2.155018	0.10785478
ARHGEF4	5.89479074	0.12111435
ARSD	0.67371999	1.31E-07
ATAD3C	2.614455	0.20601015
ATG12P2	5.54925218	0.24125252
ATP6V1E2	0.61389224	0.2703255
AUTS2	1.19331779	8.61E-09
B3GALT1	5.88213226	0.10599197
B4GALNT4	0.73589975	2.94E-05
BDH1	2.17656366	0.25600953
BEGAIN	1.88572187	0.29879928
BMS1P1	0.76380772	0.00390407
BX005266.2	1.65554324	0.21776002
BX255925.1	1.18111769	0.13968967
BX842570.1	1.26945889	3.61E-08
BX890604.1	1.46378309	4.73E-30
C13orf46	1.44346702	0.04349442
C1RL-AS1	0.86567693	0.00490803
C21orf58	0.60604899	7.85E-06
C2CD4A	1.46437318	0.01935066
C3orf62	0.72638371	0.09005682
C6orf141	1.01695444	7.48E-20
CA5BP1	0.81157487	0.00689011
CACHD1	0.61978416	5.47E-05
CACNG8	0.83449284	3.46E-11
CACTIN-AS1	1.71568801	0.08901919
CARS1	3.36436937	2.45E-63
CARS1-AS1	6.07474103	0.06564496
CASC9	5.89917905	0.10336913
CBWD1	0.77818246	1.21E-08
CCDC17	0.70469371	0.2585193
CCDC32	0.62229766	0.00286004
CCDC57	0.60538841	1.09E-06
CCHCR1	1.95138776	6.71E-15
EIF1AY	12.4422516	5.03E-196
ELN	1.40257503	0.02233417
EMILIN1	1.47015478	1.72E-42
EPB41L1	0.82622068	1.56E-07
EPSTI1	1.44075247	0.00019096
EZH2P1	5.72436803	0.21528163
FAM228A	1.46583438	0.19808909
FAM53A	0.81611639	0.27572226
FAM74A3	2.16295025	0.02886166
FAM86B3P	1.01883991	0.00039355
FAT1	0.71605317	0.00056213
FBLN2	0.75749575	0.11856487
FBLN5	1.36773913	2.11E-41
FBXO32	1.10450922	2.42E-19
FCHO1	0.62120267	0.1898018
FHIT	1.2653353	0.12960547
FLVCR1-DT	2.91671454	1.76E-09
FMN2	5.43681654	0.2774901
FMOD	2.09170299	0.15717473
FP236383.3	1.32997828	0.07190131
FP236383.5	0.70655453	3.51E-06
FP565260.1	0.61474614	0.00026806
FSTL3	0.68513683	5.88E-06
FXYD6	1.63792985	0.11376056
GADD45B	1.08621084	2.63E-26
GALNT15	2.11399858	7.62E-80
GBP4	0.81774145	7.06E-08
GCNT1	0.74524236	4.21E-14
GDF3	0.61873974	0.03409377
GDF6	2.32499425	1.37E-14
GDF7	2.15217192	1.72E-48
GIPC3	0.80547238	2.03E-05
GIPR	3.61374764	0.25616197
GLT8D2	0.79563729	0.23775793
GNG8	6.1761658	0.03991178
GOLGA2P7	0.87282207	0.24632965

CCNA1	1.35092118	0.00634662
CCNT2-AS1	1.10820326	0.0796274
CDC42EP3	0.78703337	1.80E-16
CDCP1	1.06753289	0.1155783
CDH4	2.41172278	0.00199995
CDKN2B	0.91291637	0.15165127
CECR2	2.27037915	1.50E-05
CEND1	1.4833604	0.21456284
CHADL	1.25260451	0.28227757
CLN6	0.65901314	4.91E-07
CLUHP3	0.82171212	0.06804041
COL18A1-AS1	1.18226622	0.00595053
COL18A1-AS2	1.59612238	0.10866755
COL1A1	3.69765653	1.50E-64
COL4A6	0.86951338	9.01E-06
COL6A3	3.87780082	2.95E-13
CORO1A	0.68625724	0.09580185
COX20P1	2.18968424	0.03998678
CPM	0.90858914	0.28967054
CRACR2A	0.67532131	0.0006778
CREG2	0.90506197	0.0704052
CRHR2	3.60377349	0.04387448
CRLF1	1.36979731	0.10232585
CSF3	1.5067902	0.00141369
CSNK1G2-AS1	1.57055667	0.08513315
CST1	1.41110245	0.1909927
CTAGE7P	1.52075717	0.25727401
CTC-338M12.4	1.252756	0.01494274
CTD-2350J17.1	4.12912639	0.24363919
CXADR	0.76933372	8.94E-12
CYP4V2	2.73260834	1.89E-20
CYTL1	1.12095431	1.72E-23
DCLK1	1.9334608	1.43E-21
DCLK2	0.73450584	0.04151652
DDAH2	3.99963527	3.87E-07

GOLGA8O	1.98451424	0.00071833
GOLGA8R	2.93485468	0.00839336
GPR137C	0.67485835	0.01849378
GPR146	0.76584424	0.13910218
GRAMD2B	0.66824583	0.2842276
GRIK5	1.67503474	1.92E-25
GSTM1	3.25210143	1.48E-07
GSTM3	0.90768013	5.04E-12
GSTO2	1.26669865	0.00516572
GSTT2B	2.38129445	7.93E-17
GTF2H2C	1.47056789	0.01066696
GULP1	0.65528185	4.39E-10
HAS2	1.52558893	0.02984029
HERC2P3	3.10907049	3.05E-42
HLA-A	12.154979	0
HLA-B	1.27235709	1.28E-37
HLA-F	7.68784103	3.01E-07
HOPX	1.32111947	2.92E-06
HPSE	0.69910758	1.83E-07
HSPA2	0.68865182	8.08E-07
HSPE1P27	4.2863623	0.28735933
HTR1D	0.7916081	0.00585672
ICOSLG	1.96038087	2.27E-05
IFI44	0.7127589	1.03E-06
IFI44L	1.56983639	1.28E-29
IFI6	1.24935248	5.63E-23
IFITM1	0.77470862	0.0321478
IGF2	1.09579302	0.17668509
IGFBP2	0.91575127	8.41E-24
IL17D	0.60229287	0.06937854
IL18	1.11893697	0.03540029
IL6	0.71042119	0.0704052
IQCH-AS1	1.18413879	0.01777019
IRF6	1.23678201	4.09E-33
IRS2	1.30596092	7.47E-17

DDX11	0.62080842	1.65E-08
DDX11L2	1.46849898	0.00295902
DDX12P	0.72341699	3.04E-06
DHRS11	3.83276929	0.09320774
DLK2	0.96361964	0.15733799
DMRTA1	2.9100067	2.68E-20
DNAH6	2.03237437	0.11569921
DOCK8	1.81629121	4.70E-18
DPP4	0.62684269	0.0001372
DPYSL4	2.46682692	1.18E-86
DRP2	1.25920795	0.01943331
DUSP4	0.79050108	2.20E-08
DUSP8	6.98665846	0.00069786
EBF3	1.97525979	1.87E-09
ECHDC3	0.83090581	0.00013687
EFNB1	0.71041922	1.87E-09
EIF1AX	0.76211394	1.51E-17
EIF1AXP1	0.93044351	0.00018305
EIF4A1	0.64054152	0.00536262
ELMOD1	1.14684913	6.64E-06
EMC3-AS1	0.69271034	0.14737727
EME2	0.70461691	3.97E-06
EPHX4	0.66349221	0.00968535
ERAP2	1.30389708	1.74E-46
ERVW-1	1.63118473	0.03696714
ETV4	0.67883203	6.80E-07
EYA1	3.02017638	0.04373859
FAHD1	0.67759767	5.75E-09
FAM107A	0.64977941	0.00039375
FAM118A	1.45810788	4.52E-57
FAM120B	2.26462071	0.01485063
FAM169A	1.17128633	0.26602405
FAM172BP	5.9066105	0.1024403
FAM201A	2.91990867	0.00468227
FAM227A	0.60432693	0.10231431
FAM95C	3.20532779	0.0379285

ISG15	0.72119983	2.01E-08
ITGA1	0.83347504	0.00030327
ITGB4	0.71879071	2.88E-06
ITGBL1	0.62183265	0.15644945
JAK3	0.65382525	0.00011984
JDP2	0.64180668	0.16585077
KCCAT198	2.12548975	0.18866622
KCNAB2	0.65815618	0.00254595
KCNK6	0.82327441	1.77E-10
KCNMB4	0.97468367	0.0006971
KCNT2	1.02257253	0.00037101
KCTD4	5.41528451	0.28163571
KDM5D	14.0619022	0
KHDRBS3	0.84141852	0.00040827
KIAA0825	0.95977161	0.15045635
KLF4	1.0162164	0.02514082
KLHL13	0.71342536	1.09E-10
KLRD1	1.2328466	0.10231431
KLRF1	3.07440999	0.29482674
KRT8P41	5.63870863	0.23152521
LGALS3	0.74214724	6.88E-11
LGALS4	4.17684336	0.25915041
LIMCH1	1.76679949	9.26E-53
LIMS2	0.67486613	5.90E-10
LIMS4	1.61982195	0.27832022
LIN7A	0.7607667	5.70E-05
LINC00173	2.59426027	0.01867451
LINC01013	0.78171946	4.65E-17
LINC01137	1.16831916	0.10311871
LINC01291	9.20260205	1.31E-22
LINC01293	5.53341422	0.25418243
LINC01537	1.93592715	0.03275142
LINC01719	1.26024673	0.17651866
LINC01811	1.69528565	0.06396747
LINC02026	5.52717191	0.25643478
LINC02154	2.09388162	0.02628056

FAP	1.62581592	0.06852248
FAS	0.78465004	0.05997279
FBXO39	1.98303547	0.00192694
FERMT1	1.15081348	0.00606005
FGF12	1.22295825	0.09264427
FGF13	2.22701639	0.29879928
FGF5	1.94690901	0.08364469
FIRRE	1.41194519	0.00416862
FLJ31104	1.74862678	0.22588027
FOXA1	2.09721395	0.2422129
FOXF1	1.16392912	5.22E-07
FP565260.3	0.86032296	0.13892356
FSIP2	2.38563551	9.98E-06
FST	1.1310412	0.13127105
FUT8-AS1	2.49468096	0.07595443
GAGE12G	7.64787023	5.04E-07
GAGE12H	6.4815989	0.01305641
GAGE13	5.69333524	0.17803251
GAGE2E	5.77516301	0.16227078
GAL	0.72146586	0.01734036
GALNT12	1.41992695	0.12557108
GALNT16	1.43444118	0.06942147
GALNT18	2.60095187	4.40E-08
GALNT8	6.7298454	0.00322411
GAPDHP1	0.75599573	0.03650822
GAS6-AS1	0.72098608	0.29329231
GAS8-AS1	2.00990996	0.14559922
GATD3A	0.90248917	3.47E-08
GFOD1	0.6734184	6.65E-12
GJA5	1.96865254	1.31E-07
GNB3	0.80588037	2.37E-05
GOLGA2P10	1.23782683	0.03886361
GOLGA2P8	6.08861684	0.0641429
GOLGA6L5P	0.94845412	0.01271577
GPAT3	1.04829983	0.00464101
GPR157	0.71771556	0.00104277
LINC02649	1.70164461	0.20853615
LINC02701	1.27201916	0.0095746
LINGO2	2.83988068	0.00455206
LIPA	0.72173925	3.40E-12
LMCD1	1.64389097	3.44E-21
LRMDA	0.84719053	0.02335406
LRP1	0.74296194	8.01E-09
LRRC19	4.11232545	0.04550487
LRRC23	0.8521976	0.03168269
LRRC75A	0.67206287	0.00528947
LUM	1.30730971	0.00070178
LYNX1	0.98586489	0.17119855
LYVE1	1.4961585	2.59E-28
MAFB	1.24692708	0.00134326
MAL2	1.47629966	0.04381788
MAN1C1	0.74475014	0.25776263
MAOA	1.02145386	7.44E-24
MARF1	1.27908362	0.15660533
MBOAT7	2.66335083	3.17E-59
MEIS2	0.86118507	9.81E-12
MEST	0.97122267	3.52E-19
METRNL	3.24433031	0.01967093
METTL25	0.76486724	0.00868817
MGARP	1.5973531	5.22E-21
MGMT	1.53354099	2.99E-22
MGP	1.15080535	1.99E-40
MICE	5.97328926	0.09352268
MILR1	1.17909706	8.22E-05
MKX	5.96977617	0.09366117
MLF1	0.77994644	0.00217717
MLLT6	2.1249856	1.73E-11
MMP19	1.17426945	0.00386676
MN1	0.72813832	0.0042296
MRPL45	2.41901566	0.22047941
MS4A2	1.41023105	0.00018687
MS4A6A	0.97023062	1.28E-11

GPRACR	5.62242698	0.19211502
GPRIN3	0.74055926	0.00014688
GREB1L	1.57480009	0.00455748
GRIK4	1.24219137	0.09334076
GSTT2	1.30947931	0.12535624
GTF2H2	0.86778087	0.01456898
GTF2H2B	1.68990751	8.38E-05
GTF2IP14	1.71346823	0.05997279
HAGLROS	0.61833079	0.08078099
HAPLN1	1.23978725	0.06550156
HEATR4	1.33139501	0.01645597
HELLPAR	0.74183292	0.01102735
HES2	0.88103798	0.00010073
HEY1	0.67676122	0.17200917
HEY2	4.10299856	0.02841822
HIF1A-AS3	1.31265088	0.01234873
HLA-C	4.77084085	#NUM!
HOXB-AS2	0.74742865	0.09462129
HOXB-AS3	0.81823856	8.60E-05
HOXB6	0.68329243	2.25E-05
HOXB8	1.24164007	6.54E-07
HOXB9	1.1066639	0.01407029
HOXC-AS1	5.60271381	0.22930654
HOXC-AS2	5.53049712	0.24573479
HOXC4	2.37156659	0.00986122
HOXC6	1.56351038	0.0051705
HOXC9	2.20682605	0.00049512
HOXD4	0.88956208	1.83E-08
HPDL	1.05187759	0.00278951
HRCT1	1.43419842	1.84E-05
HS6ST2	1.05147421	0.05183435
HSD17B2	1.76165498	0.00245828
HTATSF1P2	2.95496098	0.01045236
HTR7P1	0.67350443	0.00175382
ICA1L	0.60168376	0.03582771
IFIT5	1.09625222	9.15E-07

MYO15B	0.91044512	2.09E-17
MYO16	3.77952769	0.00728524
MYO7A	0.72250856	0.04937538
MYZAP	0.67910343	0.23116594
NACAD	0.83451182	2.01E-05
NAP1L2	1.20363378	0.07200499
NDRG2	1.95943538	0.03756938
NDRG4	1.157587	5.58E-34
NEK11	0.71887645	0.06484317
NEXN	0.72548846	4.58E-08
NID2	0.80429336	0.00263995
NLGN4Y	13.1306018	2.84E-296
NMRK1	0.67262834	1.25E-09
NOMO1	2.91102899	1.68E-20
NOTCH2NLA	2.7200893	0.09907223
NOTCH3	1.35495482	1.26E-13
NPIPA1	2.83478323	2.45E-08
NR5A2	0.77159758	1.16E-09
NRG3	0.76784192	0.00596463
NRK	1.23579388	2.53E-14
NXN	0.86709871	1.65E-20
OAS1	1.90070592	5.36E-23
OAS2	2.15915622	1.52E-41
OASL	1.56471851	0.15410492
OCLN	1.21008234	0.14765018
OLFM2	1.26871254	0.09737909
OSGIN2	0.60152474	7.34E-08
OXCT2P1	1.07036554	0.04338231
P2RX4	0.93992063	1.98E-22
P2RX7	1.90923383	1.22E-17
P3H2	1.66623737	9.24E-09
PALM	0.60880761	6.44E-05
PAX8	1.34781586	0.03551025
PAX8-AS1	1.39463394	4.19E-23
PAX9	3.10470267	0.0127097
PCDH10	0.70718451	2.45E-15

IL17RA	0.72810489	7.51E-12
IL1A	1.40065235	0.01071348
IMPG2	0.90381246	0.18354277
INE1	1.06529886	0.00732694
ITGAX	1.42797462	0.08572047
JAZF1-AS1	5.39921923	0.29835469
JPH1	1.77662874	0.26183812
KANSL1	2.20141891	0.00070801
KCNA6	2.81511145	0.02662322
KCNAB1	0.75104763	5.22E-07
KCNJ12	1.78028295	0.02105327
KCNK1	1.14102484	0.0155779
KDM5C	0.6365282	9.91E-13
KIAA0040	0.94551415	4.57E-16
KIAA1217	1.53415719	3.48E-40
LAMC1-AS1	1.12640932	0.10132622
LAMC2	2.23073523	8.56E-91
LERFS	3.01963092	4.72E-07
LGALS3BP	1.3192812	0.07295713
LGALSL-DT	2.91881846	0.29010075
LINC00265	0.92408113	0.03950363
LINC00271	1.63113117	0.19679027
LINC00431	3.23634373	3.46E-07
LINC00649	0.9613159	0.15508641
LINC00705	0.60576765	0.04371185
LINC01117	1.5030474	0.14407469
LINC01239	3.96312971	0.04798586
LINC01776	1.30360191	0.0072327
LINC02381	1.64634511	0.00600171
LINC02454	0.7667597	0.23351156
LINC02610	3.73910928	4.97E-10
LINC02795	1.10709714	0.16449831
LIPG	1.2861107	3.33E-46
LRRC45	0.93092367	1.04E-12
LRRC69	0.88453974	0.26486064
MAGEE1	0.87600295	0.12428511

PCDH17	1.08135896	0.00202536
PCDHB10	1.55691928	0.14995474
PCLO	1.30754936	0.29623601
PCSK1	1.08060717	1.09E-07
PDCD1LG2	0.97809766	2.07E-10
PDE2A	0.82697409	3.85E-15
PDK4	0.86266331	4.07E-05
PDPR	0.63208574	3.25E-10
PDXDC1	1.18580101	4.28E-11
PDZRN3	5.36445645	0.29431783
PER3	0.84676144	0.00396244
PIANP	1.2331951	0.17200917
PIEZO2	0.763471	0.08078099
PIM1	0.61089102	0.00013848
PLAC4	0.61254917	0.25804549
PLEK	2.20127312	0.13848297
PLEKHA4	0.70316764	2.55E-05
PLSCR4	1.2145104	3.80E-48
PMS2P2	2.9574379	0.0237376
PNMA8A	1.45988731	1.86E-07
POLE4	0.70710592	0.0007991
PPP1R11	4.39640564	1.58E-05
PPP1R14A	1.87082225	0.0002784
PPP1R3C	1.24271655	6.55E-05
PRKCZ	1.4760151	0.11376056
PRKY	6.79327289	4.77E-141
PRR15	1.34534716	0.0042296
PSORS1C2	5.72079924	0.16179831
PTER	0.75481241	0.01407751
PTGIR	1.48014264	6.66E-08
PTGIS	0.7692067	3.31E-10
PTGS1	0.97533104	7.31E-28
PTPRR	1.70333579	0.12053799
PYCARD	0.63436075	0.03379088
RAD17	0.82366855	0.03583689
RAI2	1.02172411	0.24494199

MANSC4	2.12045635	0.06498409
MAP3K21	0.85597771	0.11908433
MAP6	2.26307674	0.00267447
MAPK6-DT	6.3007831	0.02910999
MDGA1	0.80881321	0.02823833
MEG3	0.85263352	2.01E-26
MEG8	0.8104186	0.00015211
MEG9	0.65281082	0.01403256
MFSD2A	1.00927398	0.00372925
MFSD4A	0.91994107	0.14631393
MICA	0.8103147	0.29911007
MIR3136	4.40217469	0.10894896
MIR3142HG	0.7625607	0.00108717
MIR3657	5.66484917	0.18302752
MIR5587	1.8609354	0.17999704
MIR646HG	3.21888461	2.98E-06
MISP3	1.21869364	0.20853615
MMP1	2.70630514	4.63E-170
MMP10	1.4759328	2.01E-26
MMP16	0.61742542	2.37E-10
MPL	1.97519202	0.12171282
MRPL23	0.78520927	1.22E-07
MSX1	0.83279931	0.00701305
MTARC1	1.03347821	0.12271533
MTND2P28	1.39759357	3.89E-25
MYEOV	1.05986855	0.02137511
MYH16	1.61312685	0.22342882
MYH7B	0.74528443	0.05505526
MYO1B	0.77539557	3.56E-17
NAP1L4	2.71836945	0.14918298
NBPF26	1.08298435	6.35E-06
NDN	0.7424013	2.49E-08
NDUFA3P1	4.02119231	0.28054044
NEK10	1.0330386	0.14720929
NHP2P1	5.82432803	0.13154401
NKAIN1	5.5921486	0.23161105
RAMP2	0.71079247	1.48E-08
RAP1GAP2	0.80799292	0.00033384
RARB	0.785147	1.26E-13
RASD1	0.80795565	0.10231431
RASGRP2	0.92233658	0.12604578
RBM26-AS1	0.86423484	0.18658537
RBP1	1.39121517	1.77E-10
RCSD1	2.7158362	0.0376756
REPS2	0.72624484	0.00126359
RFK	0.63462128	8.58E-12
RGL3	1.33425124	0.00092881
RGPD6	1.8570665	0.01547631
RLIMP1	1.4972302	0.18147449
RNASE1	0.66330565	2.54E-13
RND3	0.85162472	2.62E-21
RPH3AL	0.96282569	0.23626835
RPL26P27	3.42566877	0.18535422
RPS26	0.72079795	2.11E-17
RPS4Y1	15.9619289	0
RPS6KA5	0.77106793	1.84E-07
RPS9	2.21741075	6.15E-09
RTP4	5.85327138	0.12777881
SAMSN1	0.71437846	0.02886166
SDAD1P1	0.93854822	0.12245555
SDK1	0.75996654	0.04106896
SEC24AP1	1.39212334	0.00015164
SEMA3A	0.64784085	0.00899562
SEMA3B	2.0746006	1.38E-12
SEMA3D	0.62055321	0.01919417
SEMA6D	0.63120895	4.18E-07
SERINC2	0.7893901	3.53E-06
SERPING1	1.94216389	0.20853615
SFTA1P	2.38161297	0.00348707
SGIP1	0.6084148	2.41E-07
SHC2	1.17876471	9.90E-08
SIK1	2.39521825	8.74E-08

NLRP12	1.66774342	0.01966377
NOG	2.66382836	0.0025225
NOL12	0.7647509	0.00423545
NOP2	1.26634348	0.11640432
NPEPPSP1	1.91852353	0.14737727
NPIPB15	0.83878775	0.00467068
NPTX2	2.39049975	2.23E-05
NRN1	0.63198629	1.02E-06
NSG1	1.47747873	0.03406894
NTNG1	3.51987745	0.21739526
NUDT13	0.95035776	0.00619015
NUS1P1	2.09182668	0.04585259
OCLNP1	3.15268093	0.00244224
P2RY2	0.75912196	0.03818068
PAG1	5.8648303	0.1254261
PAQR4	0.67415702	0.00023483
PARP15	1.03788258	0.01350804
PATL2	2.78239674	0.2462753
PCSK5	0.75354453	0.00022461
PCSK6	1.55932207	0.12503642
PDCL3P5	1.48214752	0.10760709
PDE10A	1.10967437	1.78E-19
PDE1C	0.83261187	0.00265514
PDE3B	1.3877621	3.10E-07
PDXDC2P-NPIPB14P	0.67143306	0.01095261
PDZD2	1.73882207	7.68E-24
PEAK3	2.4913633	0.15220426
PET100	1.03394846	0.23757382
PGAP4	0.9392415	0.02818096
PHRF1	4.70175669	7.42E-20
PIF1	0.72260494	5.57E-11
PIGZ	0.78368567	0.00025865
PITX1	3.05817929	0.00645143
PKD1P2	1.73591541	0.00106918
PKD1P4	0.93178052	0.00048423
SIM1	7.20540452	8.88E-05
SLC12A5	1.50238709	0.19127468
SLC15A3	0.74931394	0.01740093
SLC16A4	0.61230226	0.00619328
SLC2A14	2.70757302	0.0366198
SLC30A3	1.18675771	2.31E-09
SLC40A1	1.32491304	1.04E-32
SLC6A16	0.86449823	0.03772446
SLC7A8	0.8875228	0.03720301
SLITRK4	1.63808458	1.22E-07
SMG1P2	1.20720485	5.52E-07
SMIM14	0.72360602	2.06E-11
SMOC1	2.34012805	0.01645597
SNAP25	0.77349591	0.01750164
SNAP91	1.12771939	0.22005966
SNHG18	1.87691066	0.01016675
SNHG5	0.8117192	2.27E-18
SOCS3	0.61534242	1.69E-07
SP140	4.26827098	2.37E-11
SP8	2.5001999	1.98E-26
SPEG	1.23401199	9.67E-06
SPESP1	0.87492214	0.1465683
SPINT2	1.07054199	1.71E-05
SRPX2	0.62033461	4.02E-12
SRRM3	0.64174006	0.01908041
SSC5D	1.33458421	0.00147223
ST3GAL6-AS1	0.85638283	0.09853297
STON1	0.80375806	3.88E-12
SULF1	1.42049162	1.43E-64
SULT1B1	0.65901602	1.30E-13
SULT1E1	3.83747836	#NUM!
SUPT3H	0.63974174	0.04881247
SV2A	1.06827293	1.49E-13
SVIL2P	1.64390267	0.12423473
SYNGR1	0.79694142	0.000648

PKD1P5	4.09923719	2.08E-81
PKNOX2	1.90983281	7.65E-05
PLAC8	1.02896027	0.00061074
PLCG1-AS1	0.67022302	0.25113001
PLEK2	1.53670288	2.71E-10
PLEKHA8P1	0.84203826	0.07100341
PLEKHG1	0.99319545	1.65E-20
PLEKHH2	0.99107139	2.40E-07
PLPP2	1.10161782	1.29E-10
PLVAP	0.60512097	0.16866968
PLXNA1	0.60872123	5.80E-10
PMS2P3	0.73635404	0.02814075
POLR1G	0.63066773	0.07624191
POLR2J4	0.85607942	0.03111583
POP1	0.7000311	2.77E-07
POSTN	1.07501413	1.81E-21
PPM1F-AS1	0.72301055	0.0002507
PRECSIT	0.8660438	0.26655384
PRELID1P5	1.69287861	0.16543706
PRELID1P6	0.74235257	0.00217537
PRORSD1P	0.75956454	0.26410126
PRRT3-AS1	3.14060087	0.00778745
PTMAP9	2.92483526	0.02216615
PTOV1-AS1	1.13362811	0.09853297
PTPN22	1.5919566	3.60E-06
PTPRD	0.67269814	1.03E-05
PTPRD-AS1	6.04296723	0.06906983
PWP2	2.68175508	6.24E-27
PYCR3	2.84976875	0.15091802
RAB11FIP3	0.74562686	5.22E-07
RAET1K	5.7191535	0.15976493
RASGRF2	1.68238529	5.92E-09
RASGRP3	0.8193431	1.09E-08
RBM12B-AS1	1.07929471	0.29595918
RBP5	0.85466637	0.18157233
RELN	1.1989865	0.00295134
SYNPO	0.68471913	8.97E-16
TACSTD2	0.6625105	3.39E-11
TAGLN	0.64863253	1.76E-05
TCAP	1.73914859	0.1244405
TCEAL7	0.8708673	0.0004038
TCIM	0.6698996	5.26E-08
TF	1.65075021	0.09005682
TGFB2	2.02173479	2.73E-15
TIMP3	1.96316132	1.29E-41
TJP1	0.74641017	0.00010186
TMC8	2.48785921	2.00E-07
TMEM159	0.6419313	3.41E-06
TMEM200A	4.58821302	4.06E-52
TMEM254-AS1	2.11047241	0.04190872
TMEM37	0.71554994	0.00117391
TMEM38A	0.91557454	0.03541163
TMSB4Y	6.89445285	0.00197671
TNFSF15	0.92345113	9.30E-26
TRAPPC6A	0.60960624	0.00695276
TRIM26	6.10303369	0.05644631
TRIQK	0.61715136	5.48E-06
TRPC4	1.95254815	0.00654116
TSC22D3	0.60073377	1.12E-08
TSPAN2	1.25197445	3.61E-05
TSPAN8	3.36366866	2.05E-06
TSSC2	0.90834002	0.0313643
TSTD1	0.93257447	0.00016602
TTTY10	6.36758647	0.02527173
TTTY14	10.1160276	6.25E-41
TUFT1	0.94349713	0.00028593
TXLNGY	14.4478677	0
U82695.1	1.15346895	0.13220392
UBE2L6	0.99568486	4.00E-15
UGCG	0.66778745	4.02E-12
ULBP1	1.15275346	0.00132028
USP44	0.63050898	0.1580714

RFX8	1.74274544	0.03020239
RGS17	0.70258935	0.03712125
RHD	1.09994982	0.11788261
RHOV	1.91655217	0.15621078
RIMS2	2.62264623	1.16E-11
RMI2	0.65436564	0.00028634
RN7SKP239	6.21987383	0.03401654
RN7SL1	1.43376885	5.34E-14
RN7SL116P	5.68292703	0.19504295
RN7SL3	1.55422085	0.10547068
RN7SL434P	5.46614856	0.28122875
RNASET2	0.6916223	0.04156713
RNF14P3	3.46876866	0.02222918
RNF207	0.77465333	0.00010527
RNF32	1.19404129	0.13566169
RNH1	0.76516751	0.11303892
RPL7P49	2.89834108	0.29950923
RPS15AP30	5.53529804	0.24466508
RRN3P1	0.6790826	1.02E-06
RTEL1-TNFRSF6B	0.6292018	0.08568553
SAPCD2	0.97858402	8.31E-15
SAXO1	2.02423451	0.08859536
SAXO2	2.24300817	0.17862969
SCLY	0.73934968	0.01172785
SCN10A	2.28919906	0.09545175
SCN5A	0.62344898	5.94E-06
SDC1	1.51234278	4.20E-13
SEC22B2P	4.91496015	4.04E-05
SEC22B3P	3.57776671	0.25727401
SELE	0.73625464	1.24E-05
SERF1A	3.11360083	0.13550104
SERPIND1	1.83720296	4.49E-05
SERPINF1	1.06561141	0.09225793
SH2D4A	2.42003736	2.98E-06
SH3RF2	2.17780787	0.00060182
USP9Y	14.1919591	0
UTY	12.9509297	6.37E-269
VSTM4	1.87841602	1.83E-08
WDR46	6.8285833	0.00185091
YBX2	1.85138368	0.03514616
ZFAND4	0.64081239	0.03451232
ZFY	12.0333185	1.31E-151
ZIK1	1.06393608	0.13387957
ZNF135	1.19450033	0.27917181
ZNF284	0.71953352	0.14796892
ZNF415	2.07279426	0.00645143
ZNF420	0.60711976	0.1907556
ZNF429	0.78316098	0.23460582
ZNF503	0.7159089	0.26799048
ZNF667	1.31260336	0.03400388
ZNF667-AS1	0.95926272	0.11405591
ZNF773	0.82389476	0.05876681
ZNF793	0.98578561	0.06813584
ZNRD1ASP	7.4178319	1.06E-05

SH3TC2	0.82205233	0.00161577
SHANK1	0.61250161	0.03392592
SHISA2	0.69637474	0.10231431
SIK1B	0.80578466	0.09047562
SINHCAF	1.32188689	0.04035276
SKAP1	1.82312943	0.05664995
SLC16A14	1.09240922	0.18773609
SLC16A9	7.58204698	1.90E-06
SLC35G6	3.73548656	0.00413663
SLC39A1	1.14722204	0.1585968
SLC45A4	1.04241389	2.06E-06
SLC46A3	0.94611426	1.90E-06
SLC5A4	1.09572355	0.06691184
SLC5A4-AS1	1.27279151	0.18510761
SLC9A3	1.5064332	0.00435849
SLC9A3-AS1	1.49481532	1.89E-20
SLFNL1-AS1	0.74164291	0.28360621
SMG1P3	0.63306496	0.00261978
SMIM5	1.28627097	0.14962047
SMN1	1.07151043	0.20025861
SMYD2	0.91774438	7.51E-12
SNHG20	0.63671291	6.60E-05
SNORA80E	4.06271339	0.26583006
SNORD113-3	4.81255237	0.02055742
SNX18P12	5.620742	0.22588027
SNX18P3	3.170514	0.00054246
SORBS2	0.64735856	9.74E-09
SPATA13	0.74017867	1.94E-06
SPATA20	0.62856414	2.71E-10
SPC25	2.33702572	1.63E-05
SPTA1	2.21102604	1.54E-07
SPTBN5	1.40822889	4.97E-42
SSBP3-AS1	0.85066702	0.17527212
STAG3L1	1.89839747	1.91E-06
STC1	1.77055284	0.00017336
STK33	1.13152679	0.00369115

STMN3	0.79034585	0.11961836
STS	0.76615932	3.78E-07
STX1A	0.63054912	0.01394303
SULT4A1	1.49764468	0.20853615
SYN2	2.52582714	0.00062741
SYT1	0.63217902	0.01216576
SYT3	1.07463213	0.18298994
TBC1D3E	1.05299401	0.25565289
TBX1	0.81836039	3.66E-11
TBXAS1	0.7112027	0.21285205
TCF19	2.68751533	2.13E-16
TEX21P	1.02548833	0.25113001
TJP2	0.73848114	1.48E-05
TLL1	1.29775776	4.74E-33
TLR5	2.55608496	0.13258725
TLX1	6.39170999	0.01955622
TMEM156	1.06100377	0.20475023
TMEM158	1.13341407	0.2774901
TMEM163	0.91542385	0.03265807
TMEM233	3.62280991	9.18E-07
TMEM273	1.43503722	2.35E-09
TMEM82	1.30321364	0.01828307
TNFRSF25	0.71955764	1.30E-09
TPTEP1	2.09871701	0.0424084
TRAV13-2	5.58699595	0.1999239
TRIB1	0.70312607	0.0001372
TRIM7	1.02530321	0.08766683
TSIX	5.00739212	1.88E-05
TSPAN11	0.600162	0.03650822
TSPEAR-AS2	2.9761355	0.05415921
TXLNG	0.72076503	4.63E-08
U73169.1	1.47868722	0.00778745
UBR7	2.15621246	0.16642085
UCKL1-AS1	0.98347786	0.00935456
UNC5B	1.14371442	0.00050843
UTS2	5.46937058	0.28054044

VLDLR	0.96085652	1.09E-07
WASH5P	1.34942741	0.00238305
WASH7P	0.78466197	0.00437882
WASHC1	0.61611438	0.0220093
WDR97	1.94898457	0.00068506
WNK4	0.67976958	0.25346927
XIRP2	1.64598423	0.04167255
XIST	14.1577392	0.00261216
XKRX	1.12727003	0.02599804
Z97192.3	1.71760483	0.06095132
ZFHX4	0.78379173	0.2227315
ZFX	0.7355633	4.88E-13
ZNF239	1.57813697	0.0936281
ZNF366	0.91768547	1.68E-05
ZNF37BP	0.61763301	6.96E-07
ZNF66	1.70559765	0.00127246
ZNF714	1.28754448	4.47E-24
ZNF804A	1.51384228	0.09587953
ZSWIM5	0.80692234	0.08765237

Appendix Table 2: Significantly changed genes in female and male HUVEC following treatment with Angiotensin II

Appendix Table 2A. Significant differentially expressed genes in female HUVEC following AngII treatment.

Gene Symbol	Log_2FC (Female AngII vs. Female Control)	Adjusted p-value (Female AngII vs. Female Control)
A2M	-1.0845016	0.00461051
AADAC	-0.685663	0.1641468
ABCA9	-1.16655	5.12E-06
ACAD11	-1.1625478	0.10899578
ACCS	-0.7721288	0.00212469
ACE	-0.7493271	5.68E-09
ACSM3	-0.7188332	0.00834217
ACTBP7	-2.4226385	0.24692973
ACTC1	5.81196678	0.16189432
ADAMTS18	-0.6246223	0.00419682
ADAMTSL4	-0.966214	0.0006119
ADCY4	-0.6725236	3.79E-07
AGAP13P	-1.5673358	0.22564725
AIDAP2	-1.2117583	0.01220575
ALKBH6	-0.8200032	0.24626071
AMH	-1.1719845	0.08459542
ANAPC1P2	0.64949042	0.17812526
ANGPTL8	-0.9142436	0.2469154
ANKK1	-5.5468994	0.28593408
ANKRD1	0.73131687	2.27E-09
ANKRD36B	-0.6891649	0.00774687
ANKS1B	-2.3393046	0.26056548
AP2A2	-0.6884366	0.00391615
APBA2	0.7188027	0.19314964
ARAP1-AS2	-1.2608577	0.03939562
ARL4AP4	-1.7051584	0.1399985
ATP5F1E	0.64937396	1.92E-07
ATP5MD	0.60122215	1.48E-05
ATP5ME	0.79713345	0.02020675
BAG6	2.00920001	2.50E-08
BDH1	-2.2977717	0.18652127
BDNF	0.70874694	0.12964062
BGLAP	-3.1556488	0.09982317

Appendix Table 2B. Significant differentially expressed genes in male HUVEC following AngII treatment.

Gene Symbol	Log_2FC (Male AngII vs. Male Control)	Adjusted p-value (Male AngII vs. Male Control)
SMN1	-3.8746046	0.00339506
RRN3	-3.2988863	1.08E-07
DHX16	-2.5219966	0.24602585
RGPD6	-2.2227501	0.03417551
MARF1	-2.1093736	0.03417551
CDNF	-1.8740033	0.18860392
BRD2	-1.3257267	3.27E-08
ABCA10	-1.2643395	0.03218911
GTF2H2	-1.172781	0.15777317
TJP1	-1.1288555	8.66E-10
LSS	-0.7583602	6.14E-08
SMG1P5	-0.7337094	0.12341125
IFI44L	-0.6082605	0.00160673
ADI1	0.64150494	3.65E-06
GATD3A	0.72258328	0.00037739
PTMAP5	1.18320622	1.09E-05
WASH8P	1.18721546	0.2569676
MTX1P1	1.2399098	0.01509032
RN7SL1	1.56919644	9.47E-19
GBA	1.60687958	1.18E-07
TMSB15B	2.04717271	0.00023575

BMS1P1	-0.7228918	0.02272897
BMS1P13	-6.1621878	0.07355037
C11orf96	0.74360402	0.08500703
C12orf57	0.7147859	0.00086157
C15orf62	-0.7840001	0.12037566
C1RL-AS1	-0.7107423	0.07378363
C4orf48	0.63259798	3.23E-05
C8G	-2.2361266	0.27916816
CACNB1	-0.6484301	0.00566875
CACTIN-AS1	-1.7140468	0.09162405
CARD14	-1.0477598	0.24795654
CCBE1	1.15560771	2.87E-05
CCDC151	2.20951628	0.15663734
CCDC200	-0.785816	0.2546909
CCDC8	0.93428089	0.29467177
CCL20	1.62181627	0.03079356
CCR7	-6.3819444	0.03239008
CD69	0.73449868	0.06775958
CD79B	1.20465663	0.22250314
CDC42-AS1	-1.7344989	0.2548499
CDK5RAP3	-0.7149364	0.00030322
CEBPD	0.63968325	0.00099446
CEP126	-0.6004416	0.0006119
CFAP69	-0.7160467	0.09864488
CHKB-DT	-0.9963143	0.29714166
CHRNA1	0.68339812	0.29696531
CITED4	0.62035376	0.00313143
CLPTM1L	0.83952723	0.00026753
CLRN3	5.88149641	0.13785406
CNKSR1	-2.0538906	0.28280309
COL18A1-AS1	-0.8980814	0.10246421
COL4A2-AS1	-1.2506407	0.10606076
COPS9	0.67899962	8.11E-06
COX17	0.66349493	0.00044967
COX20	-1.0298655	0.13525905
COX6A1	0.73148657	1.48E-05
COX7C	0.61334677	9.88E-07
CPA3	0.70033942	0.18775357
CPM	-1.9248565	0.00063722
CREG2	-0.758819	0.25504476
CRMP1	-0.6357869	0.01072093

CRYGS	-0.6671392	0.11147151
CSAD	-0.6601328	0.00114008
CSF2	1.63151175	0.13616666
CSF3	0.74426835	0.14287546
CTH	0.78361666	0.03407383
CWC25	-1.989099	0.00585568
CX3CL1	0.75440497	0.0095951
CXCL6	0.87889582	4.95E-08
CYP1A1	-0.6366845	0.00292212
DAW1	0.74183552	0.04796142
DENND6B	-0.8251149	0.08819528
DET1	-1.037076	0.2039007
DHPS	-0.9625993	0.04382797
DHRS4L2	0.63537993	0.01752592
DHRS9	1.5182739	0.16191417
DKK1	0.80545323	0.09002545
DLEU2L	-1.2318645	0.16083044
DNAH1	-0.6139556	0.00320208
DNER	-6.1078333	0.08007443
DNM3OS	-0.7093096	0.03026544
DPF1	-0.846363	0.26503607
DPM3	0.66183945	0.00031229
DPY19L2	-0.7960452	0.19349719
DUSP8	-4.5607823	0.00775526
DYNLRB1	0.72137797	0.01092467
EEF1A2	0.76743123	0.10082141
EEF1D	1.13988081	0.06412967
EFCAB13	-0.6674376	0.08230702
EFHC2	5.52254429	0.28284334
EGLN2	-0.6323284	0.0008266
EIF4A1	-0.7583945	0.00261576
EIF4EBP3	-1.9879956	0.09171768
ELOCP2	0.77681956	0.25002724
EME2	-0.670814	0.00115953
ERFL	-1.9397298	0.29552897
ESR1	-1.3074062	0.22400044
F2RL3	-1.0620007	0.26265111
FAM189A2	-0.6890933	0.0088612
FAM198B-AS1	-0.7582625	0.00237296
FAM24B	0.86748593	0.00361293
FAM72C	1.02107559	0.17123507
FBXO2	1.34127497	0.15710307

FCF1P1	-2.7288924	0.27867885
FOLH1	-1.0548134	0.2902056
FOXP3	-3.0424915	0.27270276
FP565260.6	-0.7282456	0.24898503
FSIP2	-1.1497415	0.10335665
GADD45B	0.65095113	8.98E-06
GAS6-AS1	-0.9742804	0.07633156
GDF15	0.63449892	6.33E-06
GDPD3	-0.719224	0.04322956
GJA4	-0.6263826	0.01234733
GJA5	-0.7594429	0.19861797
GOLGA6L17P	-1.8390766	0.19904229
GOLGA6L4	-1.3037501	0.19377179
GOLGA6L5P	-1.1368646	0.00379005
GOLGA8A	-0.7653194	3.23E-09
GOLGA8J	-5.6707207	0.23746873
GPCPD1	-0.7381817	2.65E-05
GPRACR	-5.7845534	0.16586877
GSN-AS1	-0.8380645	0.0144188
GTF2IP13	-0.7475163	0.18204189
GTF2IP20	-0.7681574	0.00099446
H2BC5	1.4561186	0.24130459
H2BC6	2.18168169	0.29712687
H4C3	5.80008522	0.16409315
HEIH	0.94177082	0.23037789
HENMT1	0.62250116	0.22516936
HERC2P2	-0.6464604	0.11238905
HERC2P3	-0.7721503	0.00863715
HEXD-IT1	-1.7559777	0.19661556
HFM1	-2.2176537	0.09775219
HOPX	0.80815753	0.10082141
HOXA10-AS	-0.9613217	0.15775691
HOXB-AS2	-0.8426843	0.06877646
HOXD4	-0.7109536	0.00024432
HSD3B7	0.81909789	0.27497842
HSPE1	0.75546276	1.05E-05
IDUA	-0.6144867	0.00772333
IFITM1	0.61769308	0.29265259
IGFBPL1	2.30453954	0.20910179
IGSF22	-1.4388455	0.27706617
IGSF23	2.02081336	0.12141682
IL17C	6.04814089	0.08663821

IL31RA	0.62622993	0.29990547
IL6	0.92910815	0.00626459
ILK	-0.8117021	0.24130459
IMPG2	-1.2488517	0.02740651
INE1	-1.0958045	0.01107012
INHBA	0.61771731	9.07E-05
ITCH-AS1	5.6722161	0.21415498
JPH1	-2.1290418	0.1094223
JTB	0.81904779	0.00286981
KCCAT198	2.04668886	0.20678519
KCNH6	5.51152498	0.28593408
KCNMB4	0.65920814	0.19217781
KIF28P	-1.8957516	0.01086005
KIFC2	-0.6030859	0.00314951
KLF1	-5.6283531	0.24692973
LAG3	-0.9813276	0.03708946
LDHB	0.91996912	2.27E-09
LDLRAD2	-0.7630593	0.01348818
LHX4	-0.8561225	0.04480787
LINC00265	-0.8914371	0.08417829
LINC00310	-4.3479364	0.23273952
LINC00342	-0.6818597	8.61E-08
LINC00672	-0.9478597	0.21373719
LINC00680	-0.8216031	0.13529816
LINC00857	1.84588476	0.28323362
LINC00894	-0.6753841	0.21548227
LINC01001	-1.7034348	0.04766566
LINC01089	-0.7048193	0.00024812
LINC01341	-1.4400981	0.09171768
LINC01355	-0.6121653	0.00285182
LINC01560	-0.9034549	0.10335665
LINC02577	0.62318038	0.05485506
LINC02604	-0.6061391	0.09269142
LINC02802	2.19433305	0.01314178
LKAAEAR1	-2.3828225	0.15893395
LPAR2	-0.8788311	0.12037566
LRRC19	3.80557609	0.11891559
LRRC37A3	-0.7291135	0.22400044
LRRFIP1P1	-1.2002479	0.0688805
LSS	-0.855091	2.80E-08
LTB4R	-0.7893056	6.41E-06
LTB4R2	-0.7195445	0.23957336
LY96	0.62935695	0.04050079

MAMDC4	-0.8798639	0.00066858
MARCHF1	-0.9347368	0.00094166
MATN2	-0.9368894	0.09884693
MCF2L	-5.6116977	0.27026459
MED31	0.61223201	0.16093461
MFAP4	-2.6373844	0.05174318
MFSD4A	-0.9347718	0.16724443
MIR1244-2	0.66922335	0.10380451
MIR1244-3	2.44823523	5.91E-06
MIR126	-0.7354165	0.08304703
MIR503HG	-0.6494855	0.00012205
MLLT6	0.89517243	0.24968642
MMP21	-1.0522741	0.27280982
MMP23A	-2.8841995	0.26607011
MMP25-AS1	-0.7762	0.0095951
MRM1	1.54756657	0.24332074
MRPL12	0.7914997	0.00422569
MRPL23	0.69211091	6.41E-06
MS4A2	-1.495068	0.046697
MSANTD1	2.20121269	0.1655939
MST1P2	-0.9863808	0.22400044
MSTO2P	-0.6162201	0.14428636
MT1A	1.47636484	0.00094166
MT1M	1.27966355	0.11238905
MTMR9LP	-0.7495449	3.54E-06
MYEOV	0.63759543	0.23406498
MYH7B	-0.6862226	0.1586825
MYO15B	-0.6036055	0.001157
MZT2B	0.76110184	2.89E-07
NCF1C	5.70747135	0.20584125
NCLP1	-1.24052	0.18214734
NDUFA1	0.67127531	9.49E-06
NDUFC2	0.63215695	0.01220732
NECTIN4	4.3005878	0.16546732
NEDD8	0.65799539	6.41E-06
NEIL1	-0.6883066	3.23E-05
NENF	0.64015028	0.00079737
NFIA-AS2	1.11757346	0.06543558
NIPAL4	-3.962946	0.11499317
NME1	0.63099536	5.74E-05
NNMT	0.64005102	2.14E-07
NOMO3	1.28503515	0.15825801
NOP2	-1.2056243	0.16551708

NPIPA7	-1.1944389	0.27236599
NPIPB4	-0.7298993	0.00664308
NPIPB5	-0.6396935	6.68E-06
NPTN-IT1	-0.697185	0.05790791
NTAN1	1.54260516	0.02562873
NTAN1P2	-1.4170437	0.22286578
NUDT1	0.60365303	0.02273975
NUS1P1	-1.5728738	0.21451092
OCLNP1	-2.4425255	0.0194893
PAQR6	-1.2614178	0.0049624
PAXBP1-AS1	-0.7685423	0.03469902
PCDHA6	-5.5919844	0.27420052
PCDHGA1	-1.9985156	0.25173739
PCDHGA4	-0.9133102	0.21246618
PCDHGA6	-0.7512335	0.19891199
PCDHGB5	-0.7846533	0.0033856
PFN1P2	-0.9780289	0.01168407
PHF1	1.81635983	0.06419253
PHRF1	-0.7797045	0.27647854
PKD1P3	-1.0181484	0.22279655
PKD1P4	-0.6682386	0.06570425
PKD1P6	-0.7425759	0.24047502
PLAC8	0.7486974	0.00551913
PLEKHM1P1	-0.60103	9.60E-05
PLPP7	0.76992356	0.24728184
PLVAP	-0.7062073	0.1121157
PLXNB3	-0.6212541	0.00021981
PNPLA7	-0.7718113	0.2902056
POLE4	0.78330162	0.00073763
POMC	1.40839518	0.03079356
PPIAP91	-2.3711714	0.29537658
PPM1F-AS1	-0.7525709	0.00095411
PRDM6	-3.2092827	0.09166734
PRKAR1B-AS1	1.3882259	0.11147334
PRORP	-0.6721431	0.00084414
PRRT2	-0.6308015	0.25002724
PRSS21	1.53223286	0.124366
PRSS3	0.76774564	0.0736476
PSMA2	-0.7867094	0.24625652
PTDSS2	0.62204448	0.00244714
PTTG1	0.62641178	1.04E-06

PYCARD	0.62790396	0.08319871
QRICH2	-0.8815775	0.00238662
RAB11FIP1P1	-1.0112507	0.05807851
RAB11FIP3	-1.0125317	2.27E-09
RABAC1	0.96585086	9.94E-07
RAMP2-AS1	-0.6633065	0.08331842
RAPSN	-1.6038256	0.2943431
RARB	0.64570491	5.91E-06
RBFOX2	-0.812948	9.58E-05
RCSD1	2.22160984	0.25504476
RFLNA	0.68653991	2.68E-05
RGPD8	-0.610429	0.06805168
RGS11	-0.8123819	0.0128593
RHOV	-2.1572609	0.08315948
RN7SKP287	-4.4156458	0.19619323
RN7SL5P	7.5050552	1.57E-05
RNA5SP483	5.59319958	0.24779276
RNF14P3	-1.9821	0.29345238
RNF152P1	5.80481701	0.1633301
RNU2-28P	2.62101396	0.15800942
RNU7-140P	-5.5009249	0.29794743
ROMO1	0.7678528	2.50E-07
RPA3	0.60446081	0.00333248
RPL12P7	5.52598192	0.2819365
RPL13AP25	0.98422113	0.01845097
RPL21P16	0.76142395	7.47E-05
RPL21P28	1.34658825	2.28E-05
RPL21P75	0.7589733	0.1493013
RPL22L1	0.62467047	1.26E-06
RPL24P8	0.77208114	0.06391046
RPL35A	0.60550632	1.52E-06
RPL36	0.64838449	1.39E-07
RPL37A	0.61630398	1.02E-06
RPL37P2	1.79884011	0.16092765
RPL39	0.72137741	2.27E-09
RPL3P4	0.64154895	4.96E-06
RPL41	0.65598775	1.39E-07
RPS13P2	0.95415033	0.1817827
RPS15P4	0.90349527	0.0001129
RPS20P14	0.70991822	0.19786947
RPS21	0.71753866	2.61E-09
RPS27	0.73692116	1.66E-09

RPS29	0.79541606	2.46E-11
RRAS	0.60076869	5.16E-06
RRN3	-3.3569527	0.18214734
RSPH9	1.3182881	0.13440476
RSPO3	0.80093609	0.00029273
RTEL1-TNFRSF6B	-0.78295	0.03193113
RTL5	-0.6124644	0.24142072
RTP4	5.59546721	0.24728184
RUSC1-AS1	-0.751067	9.12E-05
RYR3	-0.9499613	0.01334605
S100A1	-1.3996931	0.04700179
S100A3	1.6780757	0.16889393
SAMD9L	-0.6098218	5.02E-05
SAMSN1	0.8230177	0.01242146
SCN9A	-0.9001389	0.03944845
SDCCAG8	1.9920222	1.26E-05
SDHAF4	0.70965405	0.00245356
SEC31B	-0.6618144	0.00076087
SELE	0.60106797	0.00076087
SELENOM	0.6592661	1.74E-05
SEPSECS-AS1	1.27909991	0.24525044
SERPINF1	-0.8979867	0.25556055
SETBP1	-0.8285447	0.04887691
SFTPD-AS1	-2.5990579	0.26912669
SGK1	0.61302616	3.24E-06
SH3BP5-AS1	-0.6946733	0.00031105
SH3D21	-0.7857035	0.00239384
SIM1	7.15164027	0.00030322
SLC16A6	-1.5125256	0.11895009
SLC22A20P	-1.5456043	0.27130535
SLC22A4	-0.6453274	0.10836412
SLC25A25-AS1	-0.7356682	0.04603108
SLC25A34	-0.7463672	0.24786394
SLC30A3	-0.6397962	0.24560077
SLC39A1	-1.0463754	0.2639557
SLC5A10	-0.8128294	0.26587612
SMG1P4	1.23264102	0.17045892
SMIM5	-1.4585651	0.08198082
SMN2	-1.8787407	0.01211738
SNHG8	0.66688396	0.00011704

SNRPA1P1	0.61358625	0.20701045
SNRPCP19	-4.4130598	0.1823329
SORCS2	-6.3178718	0.04050079
SPACA6P-AS	-1.5989369	0.25337168
SPNS1	-1.0106349	0.23460892
SPTBN5	-1.0291583	5.01E-16
SRRM2-AS1	-1.4502105	0.12644282
SRSF9P1	-5.8732994	0.12710021
SSPOP	-0.9657946	0.18775688
STAG3L3	-0.6058935	0.08155748
STAG3L5P	-0.6478311	0.08319871
STK31	-3.2896179	0.14738975
STK36	-0.7199633	5.08E-07
STPG3-AS1	-4.2423032	0.28460414
STRADA	-0.6450909	0.0023383
STXBP5-AS1	-0.9482571	0.22450615
SULT4A1	-3.0132742	0.00116536
SUMO2P21	0.82884923	0.16589939
TAC4	-1.2761117	0.24898503
TADA2A	-0.9522733	0.08109843
TAS2R4	-0.9247316	0.23208121
TFEC	0.75231469	0.05386283
TGFB2	0.97917312	2.77E-08
THPO	5.67480141	0.21360342
TMA7	0.60208353	0.00064503
TMED2-DT	-0.9319462	0.01194688
TMEM198B	-0.633867	0.0012851
TMEM256	0.70635828	0.06192929
TMEM258	0.6396963	1.74E-05
TMEM44-AS1	-0.6187487	0.14287546
TMEM9B-AS1	-0.7053129	0.07762015
TNFRSF25	-0.7724756	1.32E-07
TNFSF15	0.62395127	7.54E-07
TNR	-1.4350281	0.13592549
TPM3P7	6.28548032	0.0401713
TRAPPC2B	0.93094807	0.12037566
TRIL	-1.2156948	0.03059045
TSNAXIP1	-1.0320876	0.2668953
TSPAN33	1.32466132	0.1121157

TSPEAR-AS2	-2.2888085	0.18066658
TTC21A	-0.7362668	0.01463915
TUBB3	-1.0556414	0.28731662
U73169.1	-1.1309428	0.09371554
UBE2Q2P1	-0.7219777	0.00392996
UBE2V2P4	5.81157099	0.16191417
UCKL1-AS1	-1.1984319	0.00221292
UNC5B	-0.6089899	0.29009864
UQCR10	0.62490875	0.00661866
UQCRQ	0.63700656	6.68E-06
VKORC1	0.63609856	0.18486799
VSIG2	-0.6947166	0.13212618
WASH5P	-0.7811066	0.26576797
WASH6P	1.56309462	0.00943075
WBP1	-0.617275	0.10450963
WDR73	-0.7560777	0.00307485
WDR97	-1.6007073	0.00998665
WNT9A	-0.6529792	0.04196447
XAF1	-0.8889485	0.00239384
XKRX	-0.8678251	0.19377179
YBX1P1	0.66606134	0.22700338
Z73420.1	-3.9161047	0.14503797
Z83843.1	-0.7868063	0.00034763
Z99289.1	-1.0678378	0.00195486
ZMAT1	-0.8519218	0.00040651
ZNF10	-0.6923517	0.11206851
ZNF117	-0.7229579	8.62E-09
ZNF221	-0.9002029	0.06461566
ZNF224	-0.6861103	0.00078102
ZNF337-AS1	-0.8263745	0.08338303
ZNF577	-0.661072	0.23798976
ZNF585A	-0.6064465	0.27270276
ZNF596	-0.7882218	0.18136575
ZNF682	-0.8083423	0.09707284
ZNF707	-1.8789755	0.17050092
ZNF789	-0.6152763	0.0038805
ZNF808	-0.6216401	0.06615423
ZSWIM5	-0.7346064	0.21209039

Appendix Table 3: KEGG pathways with 3 or more differentially expressed genes in female HUVEC treated with Angiotensin II

Appendix Table 3. KEGG Pathways with 3 or more differentially expressed genes in female HUVEC treated with AngII.

KEGG Pathway	Number of differentially expressed genes	p-value
Metabolic pathways	22	4.73E-05
Ribosome	11	7.75E-06
Pathways of neurodegeneration - multiple diseases	11	7.52E-05
Thermogenesis	10	1.61E-06
Cytokine-cytokine receptor interaction	10	3.73E-05
Alzheimer disease	10	6.86E-05
Oxidative phosphorylation	9	7.75E-06
Prion disease	9	1.28E-05
Huntington disease	9	3.97E-05
Parkinson disease	8	4.96E-05
Amyotrophic lateral sclerosis	8	6.87E-04
Non-alcoholic fatty liver disease	7	9.40E-05
Pathways in cancer	7	5.36E-02
TNF signaling pathway	5	3.68E-04
Cardiac muscle contraction	5	3.80E-04
Viral protein interaction with cytokine and cytokine receptor	5	6.62E-04

MAPK signaling pathway	5	4.01E-03
Chemokine signaling pathway	5	1.01E-02
Rheumatoid arthritis	4	2.53E-03
Hypertrophic cardiomyopathy	4	4.93E-03
Gastric cancer	4	2.03E-02
FoxO signaling pathway	4	2.36E-02
Cellular senescence	4	4.06E-02
Human T-cell leukemia virus 1 infection	4	8.09E-02
Salmonella infection	4	1.62E-01
Malaria	3	3.94E-03
Pertussis	3	5.28E-03
Dilated cardiomyopathy	3	1.60E-02
IL-17 signaling pathway	3	1.69E-02
Oxytocin signaling pathway	3	2.86E-02
Retrograde endocannabinoid signaling	3	3.34E-02
AGE-RAGE signaling pathway in diabetic complications	3	3.49E-02
mTOR signaling pathway	3	5.36E-02
HIF-1 signaling pathway	3	6.29E-02
Melanogenesis	3	6.92E-02
Chagas disease	3	7.32E-02

Cell cycle	3	1.08E-01
Apelin signaling pathway	3	1.17E-01
Phospholipase D signaling pathway	3	1.25E-01
cAMP signaling pathway	3	1.37E-01
Cushing syndrome	3	1.66E-01
Hepatocellular carcinoma	3	2.02E-01
Proteoglycans in cancer	3	2.97E-01
Human cytomegalovirus infection	3	3.11E-01

Appendix Table 4. Hypergeometric analysis of metabolite pathways with differentially expressed metabolites between hpBMEC and hiBMEC

	RxnId	# of DE metabolites	# of total metabolites in pathway	% different metabolites	p-value
0	Amino acids	2	16	0.125	0.277593627
1	Arginine and proline metabolism	1	7	0.142857143	0.401903612
2	Carnitine and fatty acid metabolism	5	11	0.454545455	0.014063523
3	Gamma-glutamyls	1	5	0.2	0.406049675
4	Glycerophospholipid biosynthesis	2	6	0.333333333	0.193223639
5	Glycolysis	1	6	0.166666667	0.409970155
6	Nucleotides	4	26	0.153846154	0.231496974
7	Other sugars	1	4	0.25	0.385582131
8	Phosphates	1	1	1	0.16
9	Serine biosynthesis and one-carbon metabolism	1	4	0.25	0.385582131
10	Sulfur metabolism	3	8	0.375	0.094024494
11	Urea cycle	2	2	1	0.024697987

Appendix Table 5. Normalized metabolite concentrations in APOE ε3 and ε4 hiBMEC treated with serum from sedentary or exercise trained individuals.

	Normalized metabolite concentrations										
	APOE ε3 with Serum								APOE ε3 No Serum		
Metabolite Name	**ε3 Sedentary 1**	**ε3 Sedentary 2**	**ε3 Sedentary 3**	**ε3 Sedentary 4**	**ε3 Trained 1**	**ε3 Trained 2**	**ε3 Trained 3**	**ε3 Trained 4**	**ε3 1**	**ε3 2**	**ε3 3**
D-Glucose	0.8243	-0.5661	0.7502	1.0141	0.6004	0.5823	-0.2777	-0.0296	-2.2254	-1.4201	-2.4671
D-Hexose 6-phosphate	-0.7562	-0.5467	-0.3480	0.1262	-0.7147	-0.4052	-1.2132	-1.9717	1.1955	1.2926	1.2274
D-Fructose 1-6-bisphosphate	-0.5533	-0.8060	-0.6155	-0.6135	-0.1729	-0.2709	-0.5276	-0.5545	1.6629	1.2614	1.4667
D-Glyceraldehyde 3-phosphate	-0.7058	0.3414	-0.3074	-0.5856	-0.0525	-0.2706	-0.7971	-0.4299	1.2014	0.9915	1.3503
3-Phospho-D-glycerate	-0.2325	-0.6732	-0.5893	-0.3260	-0.1380	-0.2912	-0.4348	-0.1434	1.1036	1.2408	1.7525
D-Glycerate	-0.6509	-1.0394	-0.4275	-0.1026	-0.2685	-0.3247	-0.3410	-0.4345	1.6867	2.0037	1.1480
Phosphoenolpyruvate	0.4967	0.3242	1.1036	-0.1353	0.6846	0.4748	-0.8201	0.0969	1.1036	1.1036	-2.1683
Lactate	-0.5440	-0.5992	-0.3364	-0.5687	-0.0515	-0.1307	-0.4177	-0.2171	1.4676	1.5185	1.5259
Pyruvate	-0.4065	-0.9804	-0.2665	-0.5105	-0.1826	-0.0030	-0.3682	-0.2162	1.5167	1.4814	1.5278
Citrate	-0.9315	-0.8736	-0.7627	-0.6553	-0.1673	-0.2924	-0.7743	-0.7883	1.5140	1.5464	1.5744
Succinate	-1.6257	-0.5720	-0.7295	-0.7285	-0.4234	-0.2189	-1.3314	-1.4220	0.3212	1.0849	0.9827
(S)-Malate	-1.8244	-1.0445	-0.3002	-0.1810	-0.3477	0.3127	-1.0716	-1.5753	0.9295	1.1991	0.7964
L-Glutamate	-1.1854	-0.6046	-0.5360	-0.0445	-0.7497	-0.1371	-1.8569	-1.8072	0.8804	0.5288	0.4088
L-Glutamine	-1.1523	-0.7772	-0.5295	-0.0057	0.4598	0.1241	-0.3047	-1.4250	-0.4500	0.3311	-1.2111
2-Oxoglutarate	-1.7079	-0.5202	-0.3632	0.2999	-0.4446	0.2530	-1.3629	-0.9163	1.1691	0.9088	1.2564
Fumarate	-1.4701	-1.3660	0.1603	-0.4430	-0.9503	-0.5908	-1.1653	0.0783	-0.2440	2.3205	0.0833
L-Serine	1.0475	1.3329	1.1131	1.0426	0.0121	0.3061	-1.7244	-0.9380	-1.2281	-1.2982	-1.5461
4-Aminobutanoate	-0.9560	-0.4094	-0.8229	0.1046	-1.2128	0.2404	-1.7200	-2.0315	0.7764	1.0629	0.6725
2-Hydroxyglutarate	-1.2336	-1.8088	0.2829	-0.8396	0.3632	0.1549	1.0249	0.8396	-0.6426	0.4750	0.8419
N-Acetyl-L-aspartate	-0.5249	0.1375	-0.4781	-0.5536	-0.7045	-0.7550	0.8760	0.9408	1.4519	1.2313	0.9466
N-Acetyl-L-glutamate	-1.2538	-1.4314	-0.5839	-1.1794	0.0582	0.0046	0.5310	0.4445	0.8862	0.6582	0.5741
D-Gluconic acid	-0.1003	0.9551	0.5804	1.1683	-0.3099	-0.3646	-0.6607	-0.4841	-1.3216	-1.1927	-1.0587
6-Phospho-D-gluconate	0.3935	-1.6024	-0.0373	1.2213	0.1287	-1.1019	-1.7811	-1.1222	-0.7047	-0.2718	0.6470
D-Ribulose 5-phosphate	-0.9327	-0.3735	-0.3062	-0.8975	0.0433	0.2258	-0.6706	-0.3197	0.8867	1.3497	1.0554
UMP	-0.5626	-0.4113	-0.9169	-0.9560	-0.4272	-0.8972	1.5923	-0.4250	1.3369	0.8109	-0.1505
UDP	0.2414	-0.1943	-0.3284	-0.7611	0.9667	0.9469	1.5417	1.8200	0.4055	0.4333	0.5440
UTP	0.5063	0.1115	-0.4147	-0.6696	0.9558	0.8353	1.8421	1.5488	-0.0465	0.0800	-0.0662
ADP	-0.5546	-0.5686	-0.8597	-0.9645	0.6062	0.5390	0.9835	1.1052	0.6666	0.7343	0.3160
UDP-glucose	-0.6287	-0.4878	-0.7033	-0.8614	0.2775	0.4328	0.3202	0.0435	0.6558	1.4022	0.2044
UDP-N-acetyl-D-glucosamine	-0.0479	-0.4596	-0.3420	-0.7259	0.5435	0.4312	0.9730	1.3801	0.8531	0.9648	0.7522
Octanoic acid	0.2681	0.9129	-1.4403	-1.0348	0.0869	0.3562	0.1923	-1.3172	-0.1574	0.6797	0.7738
Nonanoic acid	0.2706	-0.5141	1.3491	0.8177	-0.7456	-0.2707	0.2072	-0.6022	-1.1484	-2.8515	-0.5113
Decanoic acid	0.4625	0.7682	-0.2982	-0.9162	-1.4702	-0.2061	-1.0188	-0.1375	0.1582	1.1340	1.7820
Dodecanoic acid	-0.9072	-0.5570	-0.9542	-1.0045	-0.4031	-0.6988	-0.3866	-0.4666	1.6515	1.7049	1.4602
Hexadecanoic acid	-1.4623	-0.6671	-0.9792	-1.2915	-0.0510	-0.4623	-0.1176	-0.6497	0.5545	1.2654	1.9828
(9Z)-Hexadecenoic acid	-0.4591	-0.1941	-0.7291	-0.7873	-0.2027	-1.1200	0.5543	0.2332	1.0032	1.6632	1.8614
(9Z)-Octadecenoic acid	-0.3570	-0.2987	-0.8216	-0.7587	-0.6602	-0.5430	-0.2328	-0.4133	1.6771	1.9748	1.8050
Linoleate	0.0452	0.0395	-0.1036	-0.1153	-0.0782	0.0032	0.3579	0.5190	-0.7982	1.3710	-0.0962
(9Z-12Z-15Z)-Octadecatrienoic acid	-0.1893	-0.6272	-0.2971	-0.3032	-0.3634	-0.2045	-0.4297	-0.3461	1.1764	3.5660	-2.0893
(5Z-8Z-11Z-14Z)-Icosatetraenoic acid	0.1578	-0.1665	0.1769	-0.2241	1.9974	1.8986	1.1936	1.2836	-1.3442	-0.4834	-1.3517
(4Z-7Z-10Z-13Z-16Z-19Z)-Docosahexaenoic acid	-0.6305	-0.5422	-0.6298	-0.7361	-0.6159	-0.5493	0.0604	-0.0824	1.6939	1.4476	1.1618
7-10-13-16-Docosatetraenoic acid	-0.8214	-0.6401	-1.4150	-1.7539	0.8737	0.6317	1.8027	1.8770	-0.3400	0.5901	0.3939
(5Z-8Z-11Z-14Z-17Z)-Icosapentaenoic acid	0.6514	0.1842	-0.5197	-0.4397	1.3190	1.2276	0.9378	1.0992	-0.3955	-3.1284	-0.9907
(8Z-11Z-14Z)-Icosatrienoic acid	0.3262	0.6083	-0.8085	-0.7417	-0.5874	-0.6952	1.1441	1.9935	1.0019	0.9803	1.5010
(7Z-10Z-13Z-16Z-19Z)-Docosa-7-10-13-16-19-pentaenoic acid	-0.6640	-0.7551	-1.1142	-1.4756	0.0706	0.3160	1.0249	1.0320	1.4601	1.3130	1.1134
L-Phenylalanine	-2.4143	0.3807	0.3902	0.1470	0.4189	-2.4691	0.4156	0.3830	0.3407	0.3192	0.3503
L-Tryptophan	0.2603	0.0666	0.4393	0.3690	2.8301	-0.3801	0.7005	0.0624	0.5501	-0.5830	-0.1163
L-Tyrosine	-0.5643	-0.9425	0.5416	-0.7151	0.2413	0.4130	0.4883	1.1658	0.0623	-2.7913	0.4491
L-Alanine	-0.5869	-0.8647	-0.2517	-0.7247	0.0722	-0.0153	-0.3885	-0.1565	1.5254	1.4931	1.5870
L-Aspartate	-0.4217	1.8566	0.7585	0.5320	-0.6566	-0.9551	-0.1616	-2.1949	1.0580	-0.3762	0.4845
L-Proline	-0.1596	-1.8686	-0.1865	-0.6429	-0.5193	-1.0162	-0.0779	0.3550	1.0725	0.9236	1.5952
L-Leucine	-0.0627	1.4233	0.4452	0.6699	0.5234	0.1318	0.2989	0.6244	-0.8260	-0.8824	-0.7869
L-Lysine	0.3018	-4.1629	0.6593	-0.0478	0.0580	0.2604	0.9916	-0.0730	0.6885	0.0163	-0.8570
L-Valine	0.0564	1.4421	0.2976	-1.2866	0.1170	-1.0987	-1.9165	-0.4564	0.3964	0.8646	1.0389

	Normalized metabolite concentrations										
	APOE ε4 with Serum								APOE ε4 No Serum		
Metabolite Name	**ε4 Sedentary 1**	**ε4 Sedentary 2**	**ε4 Sedentary 3**	**ε4 Sedentary 4**	**ε4 Trained 1**	**ε4 Trained 2**	**ε4 Trained 3**	**ε4 Trained 4**	**ε4 1**	**ε4 2**	**ε4 3**
D-Glucose	1.0649	0.9713	0.5424	0.3685	0.1695	0.4389	0.6057	0.6325	-0.1386	-0.6120	-0.8284
D-Hexose 6-phosphate	0.1386	-0.1239	-0.6100	-0.4272	-0.4195	-0.7943	-0.3655	0.0659	1.0275	2.1282	1.4943
D-Fructose 1-6-bisphosphate	-0.2737	-0.5561	-0.9937	-0.9247	-0.5915	-0.5614	-0.6580	-0.6911	1.8171	1.6366	1.5196
D-Glyceraldehyde 3-phosphate	-0.1119	-0.2428	-0.6032	-0.8462	-0.9729	-1.3355	-0.9301	-0.8981	1.9114	1.3543	1.9393
3-Phospho-D-glycerate	-0.5324	-0.5003	-0.7938	-0.3719	-0.9503	-0.6687	-1.8023	-0.4597	1.7162	1.7078	1.3869
D-Glycerate	-0.2922	-0.4945	-0.7332	-0.8981	-0.7230	-0.7963	-0.8799	-0.5572	1.5411	2.0037	0.5806
Phosphoenolpyruvate	-1.3692	-0.5864	-2.0481	-0.0396	-0.4557	0.0072	-0.6764	-0.4066	1.1036	1.1036	1.1036
Lactate	-0.5900	-1.0725	-0.7757	-0.7895	-0.4284	-0.4661	-1.0882	-1.1205	1.5810	1.5312	1.5720
Pyruvate	-0.4897	-1.0062	-0.8888	-0.8713	-0.4786	-0.4168	-0.9992	-1.0711	1.5258	1.5155	1.5882
Citrate	-0.3262	-0.5855	-0.3666	-0.6347	-0.4608	-0.7408	-0.3665	-0.6626	1.5556	1.6432	1.5557
Succinate	0.3981	-1.4431	1.5611	0.9012	0.0922	-0.2652	0.1745	0.5744	-0.2476	1.9349	0.9821
(S)-Malate	0.2279	-1.5039	1.5354	0.8650	-0.1730	-0.5180	0.3056	0.3241	-0.2680	1.8674	0.4449
L-Glutamate	0.1551	-1.6347	1.3100	0.9575	0.2268	-0.1803	0.4700	0.9527	0.2510	1.7724	0.8230
L-Glutamine	0.9044	-0.8653	1.6843	1.1600	-0.3021	-0.0845	2.2476	1.6884	-0.5239	-0.7713	-0.1971
2-Oxoglutarate	0.3446	-1.1964	0.8492	-0.2789	0.2143	-1.0048	-0.8732	-0.7982	0.9940	1.6914	1.4858
Fumarate	0.6157	-0.3381	1.5898	0.7665	0.4442	-0.1040	0.0409	0.5940	-1.7108	1.1271	0.5617
L-Serine	0.5880	0.8885	0.5474	0.8979	-1.1226	-0.5444	1.1209	0.7516	-0.2040	-0.3411	-0.7016
4-Aminobutanoate	0.3564	-1.3063	0.9284	0.5590	0.3494	-0.4466	0.6346	0.7141	-0.3375	1.5434	1.3013
2-Hydroxyglutarate	-0.0452	-1.0176	0.1988	-1.0041	-0.1757	-0.5601	-0.7850	-0.8407	2.2379	0.9574	1.5764
N-Acetyl-L-aspartate	-1.3952	-1.6766	-0.6862	-0.3400	0.0472	-0.1625	-0.7575	-1.4310	1.3206	1.1224	1.3905
N-Acetyl-L-glutamate	-1.4700	-2.2248	-0.1678	0.2923	0.7244	0.1625	-0.0237	-0.1597	1.2071	1.5065	1.4450
D-Gluconic acid	1.2954	0.3776	2.2461	1.1312	-0.1934	-0.3881	0.9395	0.5900	-1.1013	-0.7483	-1.3598
6-Phospho-D-gluconate	1.2753	1.2449	1.0380	0.8056	1.0157	0.8261	-0.2524	0.5500	-1.3555	-1.1265	0.2098
D-Ribulose 5-phosphate	0.5758	0.4232	-1.7568	-0.8529	-0.1910	-0.7324	-0.6862	-1.4315	1.4358	1.9700	1.1852
UMP	-0.3484	-0.2448	-0.9178	-0.8357	0.6340	0.4238	-1.1377	-1.1719	1.2772	1.1905	2.1375
UDP	-0.6300	-0.5743	-1.3576	-1.5105	0.4436	0.2655	-1.6958	-1.7337	0.9707	-0.1026	0.3089
UTP	-0.8359	-0.6943	-1.4162	-1.0765	0.3432	0.2662	-1.8950	-1.6164	0.9820	0.3147	0.9453
ADP	-0.8281	-0.0922	-1.8676	-1.0464	0.7541	0.8704	-1.7579	-1.2527	1.2125	1.1203	0.8840
UDP-glucose	0.0170	-0.4185	-1.6497	-0.9095	-0.2287	-0.7410	-0.9288	-1.1458	1.3599	2.0789	1.9109
UDP-N-acetyl-D-glucosamine	-2.0552	-1.4172	-1.0955	-1.1611	0.2848	0.0966	-1.1046	-1.0467	1.2094	0.9537	1.0131
Octanoic acid	-0.6159	-1.3736	0.2006	-0.0393	-0.7737	3.0110	0.5705	-0.9028	0.7050	-0.4648	0.3626
Nonanoic acid	0.0132	-0.2717	-0.0863	-0.4229	-0.0683	0.9331	1.4291	0.3273	0.8511	1.7832	-0.4883
Decanoic acid	-1.6307	-1.2527	1.1786	-0.2807	-0.6990	0.9646	0.5028	1.0805	0.3886	-1.4176	0.9078
Dodecanoic acid	-1.2686	-1.3937	0.8113	-0.4777	-0.1811	-0.1536	-0.4105	0.0073	0.9627	1.4347	1.2306
Hexadecanoic acid	-1.2477	-1.5203	1.3034	-0.0158	0.9609	1.1304	-0.0986	0.0598	-0.0525	0.1359	1.2226
(9Z)-Hexadecenoic acid	-0.7865	-0.8104	-1.3674	-0.4673	-0.6755	-0.6077	-0.6586	-0.5185	1.7792	1.2606	1.0291
(9Z)-Octadecenoic acid	-0.9668	-0.9610	-0.4073	-0.3824	-0.6480	-0.4965	-0.7146	-0.6129	1.3704	1.1519	1.2956
Linoleate	-0.0216	-0.0584	0.0376	-0.0643	0.0740	0.2173	0.0737	0.0524	2.0574	0.1894	-3.7019

(9Z-12Z-15Z)-Octadecatrienoic acid	-0.1530	-0.1410	-0.2946	-0.2252	-0.0871	-0.3565	-0.1954	-0.1774	0.6299	0.7138	0.3939
(5Z-8Z-11Z-14Z)-Icosatetraenoic acid	0.0495	-0.2511	-0.6739	-0.4504	0.9927	1.1011	-0.7871	-0.4309	-1.2467	-0.8022	-0.6390
(4Z-7Z-10Z-13Z-16Z-19Z)-Docosahexaenoic acid	-0.7315	-0.6909	-0.6157	-0.7194	-0.5653	-0.8676	-0.6806	-0.5995	1.9757	1.0106	1.9066
7-10-13-16-Docosatetraenoic acid	-0.9298	-1.2022	-0.4803	-0.2954	0.3269	0.4711	-0.7381	-0.6808	1.3269	0.6670	0.3361
(5Z-8Z-11Z-14Z-17Z)-Icosapentaenoic acid	0.5634	0.0867	-0.7646	-0.2755	0.6376	1.1164	-0.0238	0.0906	-0.9252	0.1019	-0.5526
(8Z-11Z-14Z)-Icosatrienoic acid	-0.8351	-0.4544	-1.3960	-0.7852	-0.6431	-0.6548	-1.3930	-0.8572	1.1575	0.6570	0.4817
(7Z-10Z-13Z-16Z-19Z)-Docosa-7-10-13-16-19-pentaenoic acid	-1.1776	-1.1814	-0.4370	-0.4832	-0.3868	-0.0171	-1.2561	-0.7221	0.9841	1.3431	1.0129
L-Phenylalanine	0.3750	0.5742	0.3109	0.4371	0.5621	0.5298	-2.4601	0.3339	0.2580	0.4370	0.3798
L-Tryptophan	0.7948	-1.4328	0.5932	0.6827	-0.2089	-1.9304	-0.5074	-0.4569	-1.8142	0.4013	-0.3203
L-Tyrosine	-0.1436	-0.6848	0.6778	-0.0441	0.3042	0.1072	1.8990	-1.6378	-0.1102	1.3439	-0.0597
L-Alanine	-0.8577	-0.8513	-0.7531	-0.5266	-0.4236	-0.5087	-1.1340	-1.1322	1.4271	1.5114	1.5594
L-Aspartate	0.6847	-1.8805	0.4115	0.5158	0.0652	1.2290	0.6837	-0.7161	-1.3086	-0.0382	0.4301
L-Proline	0.3804	1.1780	-0.9939	-0.7758	-0.7433	-0.0066	-1.2107	-0.9854	1.6038	0.7161	1.3622
L-Leucine	-0.0152	0.6115	0.2833	-0.0911	-0.9899	-0.1466	0.1753	0.1415	0.8562	1.0864	-3.4705
L-Lysine	0.3566	0.5008	0.3583	0.2062	0.0857	-0.1290	0.1786	0.1662	-0.0988	0.4768	0.0635
L-Valine	-0.6231	1.6544	-0.0936	0.5405	-0.7887	-1.8828	-0.5648	1.0751	0.9028	-0.1120	0.4375

Appendix Table 6. Metabolite contributions to PC1 in APOE ε3 and ε4 hiBMEC with and without serum.

Pathway	Metabolite	PC1 Coefficient	ε3 (Serum)	ε3 (No Serum)	ε4 (Serum)	ε4 (No Serum)
Glycolysis	D-Glucose	-0.17	0.35	0.30	-0.40	0.40
Gluconate metabolism	D-Gluconic acid	-0.17	0.10	-1.19	0.75	-1.07
amino acid	L-Serine	-0.15	0.27	-1.36	0.39	-0.42
Fatty acid metabolism	(5Z-8Z-11Z-14Z-17Z)-Icosapentaenoic acid	-0.10	0.56	-1.50	0.18	-0.46
amino acid	L-Leucine	-0.09	0.51	-0.83	0.00	-0.51
PPP	6-Phospho-D-gluconate	-0.08	-0.49	-0.11	0.81	-0.76
Fatty acid metabolism	(5Z-8Z-11Z-14Z)-Icosatetraenoic acid	-0.08	0.79	-1.06	-0.06	-0.90
amino acid	L-Glutamine	-0.08	-0.45	-0.44	0.80	-0.50
Fatty acid metabolism	Nonanoic acid	-0.07	0.06	-1.50	0.23	0.72
amino acid	L-Tryptophan	-0.03	0.54	-0.05	-0.31	-0.58
Fatty acid metabolism	Linoleate	-0.02	0.08	0.16	0.04	-0.49
amino acid	L-Tyrosine	-0.01	0.08	-0.76	0.06	0.39
amino acid	L-Aspartate	-0.01	-0.16	0.39	0.12	-0.31
amino acid	L-Lysine	0.01	-0.25	-0.05	0.22	0.15
TCA	Fumarate	0.04	-0.72	0.72	0.45	-0.01
Fatty acid metabolism	Octanoic acid	0.05	-0.25	0.43	0.01	0.20
amino acid	L-Valine	0.05	-0.36	0.77	-0.09	0.41
Fatty acid metabolism	Decanoic acid	0.05	-0.35	1.02	-0.02	-0.04
amino acid	L-Phenylalanine	0.05	-0.34	0.34	0.08	0.36
amino acid	L-Glutamate	0.07	-0.87	0.61	0.28	0.95
alanine, aspartate and glutamate metabolism	4-Aminobutanoate	0.08	-0.85	0.84	0.22	0.84
Glycolysis	Phosphoenolpyruvate	0.08	0.28	0.01	-0.70	1.10
TCA	(S)-Malate	0.09	-0.75	0.97	0.13	0.68
TCA	Succinate	0.09	-0.88	0.80	0.25	0.89
Nucleotides	UTP	0.09	0.59	-0.01	-0.87	0.75
Fatty acid metabolism	(9Z-12Z-15Z)-Octadecatrienoic acid	0.10	-0.35	0.88	-0.20	0.58
Nucleotides	UDP	0.10	0.53	0.46	-0.85	0.39

Fatty acid metabolism	7-10-13-16-Docosatetraenoic acid	0.11	0.07	0.21	-0.44	0.78
Fatty acid metabolism	Hexadecanoic acid	0.12	-0.71	1.27	0.07	0.44
TCA	2-Hydroxyglutarate	0.14	-0.15	0.22	-0.53	1.59
Nucleotides	ADP	0.14	0.04	0.57	-0.65	1.07
Fatty acid metabolism	(8Z-11Z-14Z)-Icosatrienoic acid	0.15	0.15	1.16	-0.88	0.77
TCA	2-Oxoglutarate	0.15	-0.60	1.11	-0.34	1.39
PPP	D-Hexose 6-phosphate	0.15	-0.73	1.24	-0.32	1.55
amino acid	L-Proline	0.15	-0.51	1.20	-0.39	1.23
arginine biosynthesis	N-Acetyl-L-glutamate	0.16	-0.43	0.71	-0.36	1.39
aminosugars	UDP-N-acetyl-D-glucosamine	0.16	0.22	0.86	-0.94	1.06
Nucleotides	UMP	0.16	-0.38	0.67	-0.45	1.54
PPP	D-Ribulose 5-phosphate	0.17	-0.40	1.10	-0.58	1.53
aminosugars	UDP-glucose	0.18	-0.20	0.75	-0.75	1.78
Glycolysis	D-Glyceraldehyde 3-phosphate	0.18	-0.35	1.18	-0.74	1.74
Fatty acid metabolism	Dodecanoic acid	0.18	-0.67	1.61	-0.38	1.21
alanine, aspartate and glutamate metabolism	N-Acetyl-L-aspartate	0.18	-0.13	1.21	-0.80	1.28
Fatty acid metabolism	(7Z-10Z-13Z-16Z-19Z)-Docosa-7-10-13-16-19-pentaenoic acid	0.18	-0.20	1.30	-0.71	1.11
PPP	D-Glycerate	0.19	-0.45	1.61	-0.67	1.38
Fatty acid metabolism	(9Z)-Hexadecenoic acid	0.19	-0.34	1.51	-0.74	1.36
Glycolysis	3-Phospho-D-glycerate	0.19	-0.35	1.37	-0.76	1.60
TCA	Citrate	0.19	-0.66	1.54	-0.52	1.58
Glycolysis	D-Fructose 1-6-bisphosphate	0.20	-0.51	1.46	-0.66	1.66
Fatty acid metabolism	(9Z)-Octadecenoic acid	0.20	-0.51	1.82	-0.65	1.27
Fatty acid metabolism	(4Z-7Z-10Z-13Z-16Z-19Z)-Docosahexaenoic acid	0.20	-0.47	1.43	-0.68	1.63

TCA	Pyruvate	0.20	-0.37	1.51	-0.78	1.54
amino acid	L-Alanine	0.20	-0.36	1.54	-0.77	1.50
Glycolysis	Lactate	0.20	-0.36	1.50	-0.79	1.56

References:

[1] “2023 Alzheimer’s disease facts and figures,” *Alzheimer’s & Dementia*, vol. 19, no. 4, pp. 1598–1695, Apr. 2023, doi: 10.1002/alz.13016.

[2] C.-S. Liang *et al.*, “Mortality rates in Alzheimer’s disease and non-Alzheimer’s dementias: a systematic review and meta-analysis,” *Lancet Healthy Longev*, vol. 2, no. 8, pp. e479–e488, Aug. 2021, doi: 10.1016/S2666-7568(21)00140-9.

[3] The Lancet, “Lecanemab for Alzheimer’s disease: tempering hype and hope,” *The Lancet*, vol. 400, no. 10367, p. 1899, Dec. 2022, doi: 10.1016/S0140-6736(22)02480-1.

[4] J. Cummings, G. Lee, K. Zhong, J. Fonseca, and K. Taghva, “Alzheimer’s disease drug development pipeline: 2021,” *Alzheimer’s & Dementia: Translational Research & Clinical Interventions*, vol. 7, no. 1, Jan. 2021, doi: 10.1002/trc2.12179.

[5] T. Hammond and A.-L. Lin, “Glucose Metabolism is a Better Marker for Predicting Clinical Alzheimer’s Disease than Amyloid or Tau,” *J Cell Immunol*, vol. 4, no. 1, Mar. 2022, doi: 10.33696/immunology.4.128.

[6] L. M. Bloudek, D. E. Spackman, M. Blankenburg, and S. D. Sullivan, “Review and Meta-Analysis of Biomarkers and Diagnostic Imaging in Alzheimer’s Disease,” *Journal of Alzheimer’s Disease*, vol. 26, no. 4, pp. 627–645, Oct. 2011, doi: 10.3233/JAD-2011-110458.

[7] L. Mosconi *et al.*, “Multicenter Standardized 18F-FDG PET Diagnosis of Mild Cognitive Impairment, Alzheimer’s Disease, and Other Dementias,” *Journal of Nuclear Medicine*, vol. 49, no. 3, pp. 390–398, Mar. 2008, doi: 10.2967/jnumed.107.045385.

[8] P. Mathew and D. Thoppil, *Hypoglycemia*. Treasure Island (FL): Stat Pearls Publishing, 2024.

[9] S. W. Suh, E. T. Gum, A. M. Hamby, P. H. Chan, and R. A. Swanson, “Hypoglycemic neuronal death is triggered by glucose reperfusion and activation of neuronal NADPH oxidase,” *Journal of Clinical Investigation*, vol. 117, no. 4, pp. 910–918, Apr. 2007, doi: 10.1172/JCI30077.

[10] A. J. Graveling, I. J. Deary, and B. M. Frier, “Acute Hypoglycemia Impairs Executive Cognitive Function in Adults With and Without Type 1 Diabetes,” *Diabetes Care*, vol. 36, no. 10, pp. 3240–3246, Oct. 2013, doi: 10.2337/dc13-0194.

[11] P. Carmeliet and R. K. Jain, “Angiogenesis in cancer and other diseases,” *Nature*, vol. 407, no. 6801, pp. 249–257, Sep. 2000, doi: 10.1038/35025220.

[12] H. Wen, D. D. Watry, M. C. G. Marcondes, and H. S. Fox, “Selective Decrease in Paracellular Conductance of Tight Junctions: Role of the First Extracellular Domain of Claudin-5,” *Mol Cell Biol*, vol. 24, no. 19, pp. 8408–8417, Oct. 2004, doi: 10.1128/MCB.24.19.8408-8417.2004.

[13] S. Ohtsuki, H. Yamaguchi, Y. Katsukura, T. Asashima, and T. Terasaki, “mRNA expression levels of tight junction protein genes in mouse brain capillary endothelial cells highly purified by magnetic cell sorting,” *J Neurochem*, vol. 104, no. 1, pp. 147–154, Oct. 2007, doi: 10.1111/j.1471-4159.2007.05008.x.

[14] M. Furuse *et al.*, “Occludin: a novel integral membrane protein localizing at tight junctions.,” *J Cell Biol*, vol. 123, no. 6, pp. 1777–1788, Dec. 1993, doi: 10.1083/jcb.123.6.1777.

[15] Y. Liu *et al.*, “Human junction adhesion molecule regulates tight junction resealing in epithelia,” *J Cell Sci*, vol. 113, no. 13, pp. 2363–2374, 2000.

[16] W. Jia, T. A. Martin, G. Zhang, and W. G. Jiang, “Junctional adhesion molecules in cerebral endothelial tight junction and brain metastasis,” *Anticancer Res*, vol. 33, no. 6, pp. 2353–2359, 2013.

[17] S. M. Stamatovic, A. M. Johnson, R. F. Keep, and A. V Andjelkovic, “Junctional proteins of the blood-brain barrier: New insights into function and dysfunction,” *Tissue Barriers*, vol. 4, no. 1, p. e1154641, Jan. 2016, doi: 10.1080/21688370.2016.1154641.

[18] C. Zihni, C. Mills, K. Matter, and M. S. Balda, “Tight junctions: From simple barriers to multifunctional molecular gates,” *Nat Rev Mol Cell Biol*, vol. 17, no. 9, pp. 564–580, 2016, doi: 10.1038/nrm.2016.80.

[19] A. Armulik *et al.*, “Pericytes regulate the blood–brain barrier,” *Nature*, vol. 468, no. 7323, pp. 557–561, Nov. 2010, doi: 10.1038/nature09522.

[20] A. N. Stratman and G. E. Davis, “Endothelial Cell-Pericyte Interactions Stimulate Basement Membrane Matrix Assembly: Influence on Vascular Tube Remodeling, Maturation, and Stabilization,” *Microscopy and Microanalysis*, vol. 18, no. 1, pp. 68–80, Feb. 2012, doi: 10.1017/S1431927611012402.

[21] D. Jansson *et al.*, “A role for human brain pericytes in neuroinflammation,” *J Neuroinflammation*, vol. 11, no. 1, p. 104, 2014, doi: 10.1186/1742-2094-11-104.

[22] L. Alarcon-Martinez *et al.*, “Capillary pericytes express α-smooth muscle actin, which requires prevention of filamentous-actin depolymerization for detection,” *Elife*, vol. 7, p. e34861, Mar. 2018, doi: 10.7554/eLife.34861.

[23] C. L. Willis, L. Leach, G. J. Clarke, C. C. Nolan, and D. E. Ray, “Reversible disruption of tight junction complexes in the rat blood-brain barrier, following transitory focal astrocyte loss,” *Glia*, vol. 48, no. 1, pp. 1–13, Oct. 2004, doi: 10.1002/glia.20049.

[24] W. M. Pardridge, P. L. Golden, Y.-S. Kang, and U. Bickel, “Brain Microvascular and Astrocyte Localization of P-Glycoprotein,” *J Neurochem*, vol. 68, no. 3, pp. 1278–1285, Nov. 2002, doi: 10.1046/j.1471-4159.1997.68031278.x.

[25] M. S. McAllister *et al.*, “Mechanisms of glucose transport at the blood–brain barrier: an in vitro study,” *Brain Res*, vol. 904, no. 1, pp. 20–30, Jun. 2001, doi: 10.1016/S0006-8993(01)02418-0.

[26] Z. Zhao, A. R. Nelson, C. Betsholtz, and B. V. Zlokovic, “Establishment and Dysfunction of the Blood-Brain Barrier,” *Cell*, vol. 163, no. 5, pp. 1064–1078, Nov. 2015, doi: 10.1016/j.cell.2015.10.067.

[27] P. Mergenthaler, U. Lindauer, G. A. Dienel, and A. Meisel, “Sugar for the brain: The role of glucose in physiological and pathological brain function,” *Trends in Neurosciences*, vol. 36, no. 10. pp. 587–597, Oct. 2013. doi: 10.1016/j.tins.2013.07.001.

[28] L. F. Barros *et al.*, “Near-critical GLUT1 and Neurodegeneration,” *J Neurosci Res*, vol. 95, no. 11, pp. 2267–2274, Nov. 2017, doi: https://doi.org/10.1002/jnr.23998.

[29] E. A. Winkler *et al.*, “GLUT1 reductions exacerbate Alzheimer’s disease vasculo-neuronal dysfunction and degeneration.,” *Nat Neurosci*, vol. 18, no. 4, pp. 521–530, Apr. 2015, doi: 10.1038/nn.3966.

[30] W. G. Leen *et al.*, “Glucose transporter-1 deficiency syndrome: The expanding clinical and genetic spectrum of a treatable disorder,” *Brain*, vol. 133, no. 3, pp. 655–670, Mar. 2010, doi: 10.1093/brain/awp336.

[31] C. L. Farrell and W. M. Pardridge, “Blood-brain barrier glucose transporter is asymmetrically distributed on brain capillary endothelial lumenal and ablumenal membranes: An electron microscopic immunogold study (cerebral mnicrovasculature),” 1991.

[32] A. J. Al-Ahmad, “Comparative study of expression and activity of glucose transporters between stem cell-derived brain microvascular endothelial cells and hCMEC/D3 cells,” *Am J Physiol Cell Physiol*, vol. 313, no. 4, pp. C421–C429, Oct. 2017, doi: 10.1152/ajpcell.00116.2017.

[33] H. Koepsell and H. De, “Glucose transporters in brain in health and disease,” *Pflügers Archiv-European Journal of Physiology*, vol. 472, pp. 1299–1343, 2020, doi: 10.1007/s00424-020-02441-x/Published.

[34] L. Mosconi, A. Pupi, and M. J. de Leon, “Brain glucose hypometabolism and oxidative stress in preclinical Alzheimer’s disease,” in *Annals of the New York Academy of Sciences*, Blackwell Publishing Inc., 2008, pp. 180–195. doi: 10.1196/annals.1427.007.

[35] M. A. Daulatzai, “Cerebral hypoperfusion and glucose hypometabolism: Key pathophysiological modulators promote neurodegeneration, cognitive impairment, and Alzheimer’s disease,” *J Neurosci Res*, vol. 95, no. 4, pp. 943–972, Apr. 2017, doi: 10.1002/jnr.23777.

[36] M. Tang *et al.*, “An early endothelial cell-specific requirement for Glut1 is revealed in Glut1 deficiency syndrome model mice,” *JCI Insight*, vol. 6, no. 3, Feb. 2021, doi: 10.1172/JCI.INSIGHT.145789.

[37] K. Veys *et al.*, “Role of the GLUT1 Glucose Transporter in Postnatal CNS Angiogenesis and Blood-Brain Barrier Integrity,” *Circ Res*, vol. 127, no. 4, pp. 466–482, Jul. 2020, doi: 10.1161/CIRCRESAHA.119.316463.

[38] I. Pervaiz, F. T. Zahra, C. M. Mikelis, and A. J. Al-Ahmad, “An in vitro model of glucose transporter 1 deficiency syndrome at the blood–brain barrier using induced pluripotent stem cells,” *J Neurochem*, vol. 162, no. 6, pp. 483–500, Sep. 2022, doi: https://doi.org/10.1111/jnc.15684.

[39] I. Pervaiz, Y. Mehta, K. Sherill, D. Patel, and A. J. Al-Ahmad, “Ketone bodies supplementation restores the barrier function, induces a metabolic switch, and elicits beta-hydroxybutyrate diffusion across a monolayer of iPSC-derived brain microvascular endothelial cells,” *Microvasc Res*, vol. 150, p. 104585, 2023, doi: https://doi.org/10.1016/j.mvr.2023.104585.

[40] P. P. Zheng, E. Romme, P. J. Van Der Spek, C. M. F. Dirven, R. Willemsen, and J. M. Kros, “Glut1/SLC2A1 is crucial for the development of the blood-brain barrier in vivo,” *Ann Neurol*, vol. 68, no. 6, pp. 835–844, Dec. 2010, doi: 10.1002/ana.22318.

[41] H. Lee *et al.*, “Endothelium-derived lactate is required for pericyte function and blood–brain barrier maintenance,” *EMBO J*, vol. 41, no. 9, May 2022, doi: 10.15252/embj.2021109890.

[42] O. Yanagida *et al.*, “Human L-type amino acid transporter 1 (LAT1): characterization of function and expression in tumor cell lines,” *Biochimica et Biophysica Acta (BBA) - Biomembranes*, vol. 1514, no. 2, pp. 291–302, Oct. 2001, doi: 10.1016/S0005-2736(01)00384-4.

[43] Y. D. Bhutia and V. Ganapathy, “Glutamine transporters in mammalian cells and their functions in physiology and cancer,” *Biochimica et Biophysica Acta (BBA) - Molecular Cell Research*, vol. 1863, no. 10, pp. 2531–2539, Oct. 2016, doi: 10.1016/j.bbamcr.2015.12.017.

[44] M. van Geldermalsen *et al.*, “ASCT2/SLC1A5 controls glutamine uptake and tumour growth in triple-negative basal-like breast cancer,” *Oncogene*, vol. 35, no. 24, pp. 3201–3208, Jun. 2016, doi: 10.1038/onc.2015.381.

[45] H. Huang *et al.*, “Role of glutamine and interlinked asparagine metabolism in vessel formation,” *EMBO J*, vol. 36, pp. 2334–2352, 2017, doi: 10.15252/embj.201695518.

[46] B. Kim, J. Li, C. Jang, and Z. Arany, “Glutamine fuels proliferation but not migration of endothelial cells,” *EMBO J*, vol. 36, pp. 2321–2333, 2017, doi: 10.15252/embj.201796436.

[47] R. A. Hawkins, “The blood-brain barrier and glutamate,” *Am J Clin Nutr*, vol. 90, no. 3, pp. 867S-874S, Sep. 2009, doi: 10.3945/ajcn.2009.27462BB.

[48] K.-S. Kim, M. T. Jeon, E. S. Kim, C. H. Lee, and D.-G. Kim, “Activation of NMDA receptors in brain endothelial cells increases transcellular permeability,” *Fluids Barriers CNS*, vol. 19, no. 1, p. 70, Sep. 2022, doi: 10.1186/s12987-022-00364-6.

[49] C. D. Sharp *et al.*, “Glutamate causes a loss in human cerebral endothelial barrier integrity through activation of NMDA receptor,” *American Journal of Physiology-Heart and Circulatory Physiology*, vol. 285, no. 6, pp. H2592–H2598, Dec. 2003, doi: 10.1152/ajpheart.00520.2003.

[50] R. S. Beard, J. J. Reynolds, and S. E. Bearden, “Metabotropic glutamate receptor 5 mediates phosphorylation of vascular endothelial cadherin and nuclear localization of β-catenin in response to homocysteine,” *Vascul Pharmacol*, vol. 56, no. 3–4, pp. 159–167, Mar. 2012, doi: 10.1016/j.vph.2012.01.004.

[51] S. Negri *et al.*, “NMDA receptors elicit flux-independent intracellular Ca2+ signals via metabotropic glutamate receptors and flux-dependent nitric oxide release in human brain microvascular endothelial cells,” *Cell Calcium*, vol. 99, p. 102454, Nov. 2021, doi: 10.1016/j.ceca.2021.102454.

[52] M. E. Widlansky and D. D. Gutterman, “Regulation of Endothelial Function by Mitochondrial Reactive Oxygen Species,” *Antioxid Redox Signal*, vol. 15, no. 6, pp. 1517–1530, Sep. 2011, doi: 10.1089/ars.2010.3642.

[53] K. E. Lee and Y. S. Kang, “L-Citrulline restores nitric oxide level and cellular uptake at the brain capillary endothelial cell line (TR-BBB cells) with glutamate cytotoxicity,” *Microvasc Res*, vol. 120, pp. 29–35, Nov. 2018, doi: 10.1016/j.mvr.2018.05.010.

[54] S. Kumari, S. L. Mehta, and P. A. Li, “Glutamate Induces Mitochondrial Dynamic Imbalance and Autophagy Activation: Preventive Effects of Selenium,” *PLoS One*, vol. 7, no. 6, p. 39382, 2012, doi: 10.1371/journal.pone.0039382.

[55] E. Zuccolo *et al.*, “Glutamate triggers intracellular Ca 2+ oscillations and nitric oxide release by inducing NAADP- and InsP 3 -dependent Ca 2+ release in mouse brain endothelial cells,” *J Cell Physiol*, vol. 234, no. 4, pp. 3538–3554, Apr. 2019, doi: 10.1002/jcp.26953.

[56] U. Vazana *et al.*, “Glutamate-mediated blood–brain barrier opening: Implications for neuroprotection and drug delivery,” *Journal of Neuroscience*, vol. 36, no. 29, pp. 7727–7739, Jul. 2016, doi: 10.1523/JNEUROSCI.0587-16.2016.

[57] L. Svennerholm, K. Boström, and B. Jungbjer, “Changes in weight and compositions of major membrane components of human brain during the span of adult human life of Swedes,” *Acta Neuropathol*, vol. 94, no. 4, pp. 345–352, Oct. 1997, doi: 10.1007/s004010050717.

[58] V. Sambra, F. Echeverria, A. Valenzuela, R. Chouinard-Watkins, and R. Valenzuela, “Docosahexaenoic and arachidonic acids as neuroprotective nutrients throughout the life cycle,” *Nutrients*, vol. 13, no. 3. MDPI AG, pp. 1–21, Mar. 01, 2021. doi: 10.3390/nu13030986.

[59] R. W. Mitchell, N. H. On, M. R. Del Bigio, D. W. Miller, and G. M. Hatch, “Fatty acid transport protein expression in human brain and potential role in fatty acid transport across human brain microvessel endothelial cells,” *J Neurochem*, p. no-no, Mar. 2011, doi: 10.1111/j.1471-4159.2011.07245.x.

[60] E. J. Murphy, “The blood–brain barrier and protein-mediated fatty acid uptake: role of the blood–brain barrier as a metabolic barrier,” *J Neurochem*, vol. 141, no. 3, pp. 324–329, May 2017, doi: 10.1111/jnc.14000.

[61] Y. Pan, M. J. Scanlon, Y. Owada, Y. Yamamoto, C. J. H. Porter, and J. A. Nicolazzo, “Fatty Acid-Binding Protein 5 Facilitates the Blood–Brain Barrier Transport of Docosahexaenoic Acid,” *Mol Pharm*, vol. 12, no. 12, pp. 4375–4385, 2015, doi: 10.1021/acs.molpharmaceut.5b00580.

[62] B. Dehouck, L. Fenart, M.-P. Dehouck, A. Pierce, G. Torpier, and R. Cecchelli, “A New Function for the LDL Receptor: Transcytosis of LDL across the Blood–Brain Barrier,” *J Cell Biol*, vol. 138, no. 4, pp. 877–889, Aug. 1997, doi: 10.1083/jcb.138.4.877.

[63] S. Kakava, E. Schlumpf, G. Panteloglou, F. Tellenbach, A. von Eckardstein, and J. Robert, “Brain Endothelial Cells in Contrary to the Aortic Do Not Transport but Degrade Low-Density Lipoproteins via Both LDLR and ALK1,” *Cells*, vol. 11, no. 19, Oct. 2022, doi: 10.3390/cells11193044.

[64] R. J. S. Lacombe, R. Chouinard-Watkins, and R. P. Bazinet, “Brain docosahexaenoic acid uptake and metabolism,” *Mol Aspects Med*, vol. 64, pp. 109–134, Dec. 2018, doi: 10.1016/j.mam.2017.12.004.

[65] A. Ben-Zvi *et al.*, “Mfsd2a is critical for the formation and function of the blood–brain barrier,” *Nature*, vol. 509, no. 7501, pp. 507–511, May 2014, doi: 10.1038/nature13324.

[66] B. J. Andreone *et al.*, “Blood-Brain Barrier Permeability Is Regulated by Lipid Transport-Dependent Suppression of Caveolae-Mediated Transcytosis,” *Neuron*, vol. 94, no. 3, pp. 581-594.e5, May 2017, doi: 10.1016/j.neuron.2017.03.043.

[67] L. N. Nguyen *et al.*, “Mfsd2a is a transporter for the essential omega-3 fatty acid docosahexaenoic acid,” *Nature*, vol. 509, no. 7501, pp. 503–506, May 2014, doi: 10.1038/nature13241.

[68] J. Zhou *et al.*, “Zika virus degrades the ω-3 fatty acid transporter Mfsd2a in brain microvascular endothelial cells and impairs lipid homeostasis,” *Sci Adv*, vol. 5, no. 10, Oct. 2019, doi: 10.1126/sciadv.aax7142.

[69] E. Razmara *et al.*, “Novel neuroclinical findings of autosomal recessive primary microcephaly 15 in a consanguineous Iranian family,” *Eur J Med Genet*, vol. 63, no. 12, p. 104096, Dec. 2020, doi: 10.1016/j.ejmg.2020.104096.

[70] B. H. Wong and D. L. Silver, “Mfsd2a: A Physiologically Important Lysolipid Transporter in the Brain and Eye,” 2020, pp. 223–234. doi: 10.1007/978-981-15-6082-8_14.

[71] V. Alakbarzade *et al.*, “A partially inactivating mutation in the sodium-dependent lysophosphatidylcholine transporter MFSD2A causes a non-lethal microcephaly syndrome,” *Nat Genet*, vol. 47, no. 7, pp. 814–817, Jul. 2015, doi: 10.1038/ng.3313.

[72] N. Rajagopal, F. J. Irudayanathan, and S. Nangia, “Palmitoylation of Claudin-5 Proteins Influences Their Lipid Domain Affinity and Tight Junction Assembly at the Blood-Brain Barrier Interface,” *Journal of Physical Chemistry B*, vol. 123, no. 5, pp. 983–993, Feb. 2019, doi: 10.1021/acs.jpcb.8b09535.

[73] N. Rajagopal, F. J. Irudayanathan, and S. Nangia, “Computational nanoscopy of tight junctions at the blood–brain barrier interface,” *International Journal of Molecular Sciences*, vol. 20, no. 22. MDPI AG, Nov. 02, 2019. doi: 10.3390/ijms20225583.

[74] H. H. Aung *et al.*, “Lipotoxic brain microvascular injury is mediated by activating transcription factor 3-dependent inflammatory and oxidative stress pathways,” *J Lipid Res*, vol. 57, no. 6, pp. 955–968, Jun. 2016, doi: 10.1194/jlr.M061853.

[75] T. Nyunt *et al.*, “Mitochondrial oxidative stress-induced transcript variants of ATF3 mediate lipotoxic brain microvascular injury,” *Free Radic Biol Med*, vol. 143, pp. 25–46, Nov. 2019, doi: 10.1016/j.freeradbiomed.2019.07.024.

[76] R. E. Estes, B. Lin, A. Khera, and M. Y. Davis, “Lipid Metabolism Influence on Neurodegenerative Disease Progression: Is the Vehicle as Important as the Cargo?,” *Front Mol Neurosci*, vol. 14, Dec. 2021, doi: 10.3389/fnmol.2021.788695.

[77] D. J. Vesga-Jiménez, C. Martin, G. E. Barreto, A. F. Aristizábal-Pachón, A. Pinzón, and J. González, “Fatty Acids: An Insight into the Pathogenesis of Neurodegenerative Diseases and Therapeutic Potential,” *Int J Mol Sci*, vol. 23, no. 5, p. 2577, Feb. 2022, doi: 10.3390/ijms23052577.

[78] M. Vandal *et al.*, “Reduction in DHA transport to the brain of mice expressing human APOE4 compared to APOE2,” *J Neurochem*, vol. 129, no. 3, pp. 516–526, May 2014, doi: 10.1111/jnc.12640.

[79] F. Calon, “Omega-3 Polyunsaturated Fatty Acids in Alzheimers Disease: Key Questions and Partial Answers,” *Curr Alzheimer Res*, vol. 8, no. 5, pp. 470–478, Aug. 2011, doi: 10.2174/156720511796391881.

[80] “Estimates of Funding for Various Research, Condition, and Disease Categories (RCDC),” NIH Research Portfolio Online Reporting Tools.

[81] H. A. Cooper, R. Scalia, V. Rizzo, and S. Eguchi, “Angiotensin II- and Alzheimer-Type Cardiovascular Aging ‘Ang’heimer?,” *Circ Res*, vol. 123, no. 6, pp. 651–653, 2018, doi: 10.1161/CIRCRESAHA.118.313477.

[82] Y. Yamazaki, N. Zhao, T. R. Caulfield, C. C. Liu, and G. Bu, “Apolipoprotein E and Alzheimer disease: pathobiology and targeting strategies,” *Nat Rev Neurol*, vol. 15, no. 9, pp. 501–518, 2019, doi: 10.1038/s41582-019-0228-7.

[83] S. Yan *et al.*, “Association between sedentary behavior and the risk of dementia: a systematic review and meta-analysis,” *Transl Psychiatry*, vol. 10, no. 1, 2020, doi: 10.1038/s41398-020-0799-5.

[84] L. E. Hebert, J. Weuve, P. A. Scherr, and D. A. Evans, “Alzheimer disease in the United States (2010-2050) estimated using the 2010 census,” *Neurology*, vol. 80, no. 19, pp. 1778–1783, 2013, doi: 10.1212/WNL.0b013e31828726f5.

[85] L. E. Hebert, P. A. Scherr, J. J. McCann, L. A. Beckett, and D. A. Evans, “Is the Risk of Developing Alzheimer’s Disease Greater for Women than for Men?,” *Am J Epidemiol*, vol. 153, no. 2, pp. 132–136, Jan. 2001, doi: 10.1093/aje/153.2.132.

[86] Y. Yamazaki, N. Zhao, T. R. Caulfield, C.-C. Liu, and G. Bu, “Apolipoprotein E and Alzheimer disease: pathobiology and targeting strategies,” *Nat Rev Neurol*, vol. 15, no. 9, pp. 501–518, Sep. 2019, doi: 10.1038/s41582-019-0228-7.

[87] A. Altmann, L. Tian, V. W. Henderson, and M. D. Greicius, “Sex modifies the APOE-related risk of developing Alzheimer disease,” *Ann Neurol*, vol. 75, no. 4, pp. 563–573, 2014, doi: 10.1002/ana.24135.

[88] D. R. Gustafson, C. Karlsson, I. Skoog, L. Rosengren, L. Lissner, and K. Blennow, “Mid-life adiposity factors relate to blood-brain barrier integrity in late life,” *J Intern Med*, vol. 262, no. 6, pp. 643–650, Nov. 2007, doi: 10.1111/j.1365-2796.2007.01869.x.

[89] C. A. Toro, L. Zhang, J. Cao, and D. Cai, “Sex differences in Alzheimer’s disease: Understanding the molecular impact,” *Brain Res*, vol. 1719, no. January, pp. 194–207, 2019, doi: 10.1016/j.brainres.2019.05.031.

[90] C. M. Weber and A. M. Clyne, “Sex differences in the blood – brain barrier and neurodegenerative diseases,” vol. 011509, no. March, 2021, doi: 10.1063/5.0035610.

[91] R. A. Medina *et al.*, “Estrogen and progesterone up-regulate glucose transporter expression in ZR-75-1 human breast cancer cells,” *Endocrinology*, vol. 144, no. 10, pp. 4527–4535, 2003, doi: 10.1210/en.2003-0294.

[92] Y. Sun *et al.*, “Estradiol promotes pentose phosphate pathway addiction and cell survival via reactivation of Akt in mTORC1 hyperactive cells,” *Cell Death Dis*, vol. 5, no. 5, 2014, doi: 10.1038/cddis.2014.204.

[93] O. Scheyer *et al.*, “Female Sex and Alzheimer’s Risk: The Menopause Connection,” *J Prev Alzheimers Dis*, vol. 5, no. 4, pp. 225–230, 2018, doi: 10.14283/jpad.2018.34.

[94] J. R. Rettberg, J. Yao, and R. D. Brinton, “Estrogen: A master regulator of bioenergetic systems in the brain and body,” *Front Neuroendocrinol*, vol. 35, no. 1, pp. 8–30, Jan. 2014, doi: 10.1016/j.yfrne.2013.08.001.

[95] A. Razmara, S. P. Duckles, D. N. Krause, and V. Procaccio, “Estrogen suppresses brain mitochondrial oxidative stress in female and male rats,” *Brain Res*, vol. 1176, pp. 71–81, Oct. 2007, doi: 10.1016/j.brainres.2007.08.036.

[96] A. Carrano, J. J. M. Hoozemans, S. M. van der Vies, J. van Horssen, H. E. de Vries, and A. J. M. Rozemuller, “Neuroinflammation and Blood-Brain Barrier Changes in Capillary Amyloid Angiopathy,” *Neurodegener Dis*, vol. 10, no. 1–4, pp. 329–331, 2012, doi: 10.1159/000334916.

[97] R. J. G. Hartman *et al.*, “Intrinsic transcriptomic sex differences in human endothelial cells at birth and in adults are associated with coronary artery disease targets,” *Sci Rep*, vol. 10, no. 1, pp. 1–12, 2020, doi: 10.1038/s41598-020-69451-8.

[98] L. Carrel and H. F. Willard, “X-inactivation profile reveals extensive variability in X-linked gene expression in females,” *Nature*, vol. 434, no. 7031, pp. 400–404, 2005, doi: 10.1038/nature03479.

[99] R. Addis *et al.*, “Human umbilical endothelial cells (HUVECs) have a sex: Characterisation of the phenotype of male and female cells,” *Biol Sex Differ*, vol. 5, no. 1, pp. 1–12, 2014, doi: 10.1186/s13293-014-0018-2.

[100] D. Kamm, “The Effects of Diet and Sex Differences on Cortical Tight-Junction Protein Expression in Senescence-Accelerated Mouse-Prone 8 (SAMP8) Mice,” Southern Illinois University, Edwardsville, 2019.

[101] M. Oliva *et al.*, “The impact of sex on gene expression across human tissues,” *Science (1979)*, vol. 369, no. 6509, p. eaba3066, 2020, doi: 10.1126/science.aba3066.

[102] J. W. Lee, M. Profant, and C. Wang, “Metabolic Sex Dimorphism of the Brain at the Gene, Cell, and Tissue Level,” *The Journal of Immunology*, vol. 208, no. 2, pp. 212–220, Jan. 2022, doi: 10.4049/jimmunol.2100853.

[103] P. K. Chandra *et al.*, “Transcriptome analysis reveals sexual disparities in gene expression in rat brain microvessels,” *Journal of Cerebral Blood Flow and Metabolism*, vol. 41, no. 9, pp. 2311–2328, Sep. 2021, doi: 10.1177/0271678X21999553.

[104] M. Lorenz *et al.*, “Sex-specific metabolic and functional differences in human umbilical vein endothelial cells from twin pairs,” *Atherosclerosis*, vol. 291, no. Supplement_1, pp. 99–106, Dec. 2019, doi: 10.1016/j.atherosclerosis.2019.10.007.

[105] A. Trenti *et al.*, “The Glycolytic Enzyme PFKFB3 Is Involved in Estrogen-Mediated Angiogenesis via GPER1,” *Journal of Pharmacology and Experimental Therapeutics*, vol. 361, no. 3, pp. 361–398, 2017, doi: 10.1124/jpet.116.238212.

[106] E. S. Lippmann *et al.*, “Derivation of blood-brain barrier endothelial cells from human pluripotent stem cells,” *Nat Biotechnol*, vol. 30, no. 8, pp. 783–791, 2012, doi: 10.1038/nbt.2247.

[107] S. AbdAlla, A. El Hakim, A. Abdelbaset, Y. Elfaramawy, and U. Quitterer, “Inhibition of ACE retards tau hyperphosphorylation and signs of neuronal degeneration in aged rats subjected to chronic mild stress,” *Biomed Res Int*, vol. 2015, 2015, doi: 10.1155/2015/917156.

[108] F. Y. Noureddine, R. Altara, F. Fan, A. Yabluchanskiy, G. W. Booz, and F. A. Zouein, “Impact of the renin–angiotensin system on the endothelium in vascular dementia: Unresolved issues and future perspectives,” *Int J Mol Sci*, vol. 21, no. 12, pp. 1–14, 2020, doi: 10.3390/ijms21124268.

[109] P. G. Kehoe, S. Miners, and S. Love, “Angiotensins in Alzheimer’s disease - friend or foe?,” *Trends Neurosci*, vol. 32, no. 12, pp. 619–628, 2009, doi: 10.1016/j.tins.2009.07.006.

[110] V. J. Dzau and H. C. Herrmann, “Hormonal control of angiotensinogen production,” *Life Sci*, vol. 30, no. 7–8, pp. 577–584, Feb. 1982, doi: 10.1016/0024-3205(82)90272-7.

[111] G. Yang, Z.-X. Xi, Y. Wan, H. Wang, and G. Bi, “Changes in Circulating and Tissue Angiotensin II during Acute and Chronic Stress,” *Neurosignals*, vol. 2, no. 3, pp. 166–172, 1993, doi: 10.1159/000109488.

[112] N. J. Justice, “The relationship between stress and Alzheimer’s disease,” *Neurobiol Stress*, vol. 8, no. January, pp. 127–133, 2018, doi: 10.1016/j.ynstr.2018.04.002.

[113] V. C. Biancardi, S. J. Son, S. Ahmadi, J. A. Filosa, and J. E. Stern, “Circulating angiotensin II gains access to the hypothalamus and brain stem during hypertension via breakdown of the blood-brain barrier,” *Hypertension*, vol. 63, no. 3, pp. 572–579, 2014, doi: 10.1161/HYPERTENSIONAHA.113.01743.

[114] K. Wakayama *et al.*, “Angiotensin II Peptide Vaccine Protects Ischemic Brain Through Reducing Oxidative Stress,” *Stroke*, vol. 48, no. 5, pp. 1362–1368, 2017, doi: 10.1161/STROKEAHA.116.016269.

[115] T. V. Lanz *et al.*, “Angiotensin II sustains brain inflammation in mice via TGF-β,” *Journal of Clinical Investigation*, vol. 120, no. 8, pp. 2782–2794, 2010, doi: 10.1172/JCI41709.

[116] T. Ito, H. Yamakawa, C. Bregonzio, J. A. Terrón, A. Falcón-Neri, and J. M. Saavedra, “Protection against ischemia and improvement of cerebral blood flow in genetically hypertensive rats by chronic pretreatment with an angiotensin II AT1 antagonist,” *Stroke*, vol. 33, no. 9, pp. 2297–2303, 2002, doi: 10.1161/01.STR.0000027274.03779.F3.

[117] D. A. Nation *et al.*, “Blood–brain barrier breakdown is an early biomarker of human cognitive dysfunction,” *Nat Med*, vol. 25, no. 2, pp. 270–276, 2019, doi: 10.1038/s41591-018-0297-y.

[118] E. Giraldo, A. Lloret, T. Fuchsberger, and J. Viña, “Aβ and tau toxicities in Alzheimer’s are linked via oxidative stress-induced p38 activation: Protective role of vitamin E,” *Redox Biol*, vol. 2, no. 1, pp. 873–877, 2014, doi: 10.1016/j.redox.2014.03.002.

[119] B. Zhang *et al.*, “Integrated systems approach identifies genetic nodes and networks in late-onset Alzheimer’s disease,” *Cell*, vol. 153, no. 3, pp. 707–720, 2013, doi: 10.1016/j.cell.2013.03.030.

[120] A. Roher *et al.*, “Cerebral blood flow in Alzheimer’s disease,” *Vasc Health Risk Manag*, vol. 336, no. 8712, p. 599, Oct. 2012, doi: 10.2147/VHRM.S34874.

[121] A. K. Doughan, D. G. Harrison, and S. I. Dikalov, “Molecular mechanisms of angiotensin II-mediated mitochondrial dysfunction: Linking mitochondrial oxidative damage and vascular endothelial dysfunction,” *Circ Res*, vol. 102, no. 4, pp. 488–496, 2008, doi: 10.1161/CIRCRESAHA.107.162800.

[122] I. Montorfano *et al.*, “Oxidative stress mediates the conversion of endothelial cells into myofibroblasts via a TGF-b1 and TGF-b2-dependent pathway,” *Laboratory Investigation*, vol. 94, no. 10, pp. 1068–1082, 2014, doi: 10.1038/labinvest.2014.100.

[123] C. Derada Troletti *et al.*, “Inflammation-induced endothelial to mesenchymal transition promotes brain endothelial cell dysfunction and occurs during multiple sclerosis pathophysiology,” *Cell Death Dis*, vol. 10, no. 2, 2019, doi: 10.1038/s41419-018-1294-2.

[124] T. A. Libermann and D. Baltimore, “Activation of interleukin-6 gene expression through the NF-kappa B transcription factor,” *Mol Cell Biol*, vol. 10, no. 5, pp. 2327–2334, 1990, doi: 10.1128/mcb.10.5.2327-2334.1990.

[125] T. M. De Silva, B. Biomed, B. R. S. Broughton, G. R. Drummond, C. G. Sobey, and A. A. Miller, “Gender influences cerebral vascular responses to angiotensin II through Nox2-derived reactive oxygen species,” *Stroke*, vol. 40, no. 4, pp. 1091–1097, 2009, doi: 10.1161/STROKEAHA.108.531707.

[126] Y. Zhang *et al.*, “Genes that escape X-inactivation in humans have high intraspecific variability in expression, are associated with mental impairment but are not slow evolving,” *Mol Biol Evol*, vol. 30, no. 12, pp. 2588–2601, 2013, doi: 10.1093/molbev/mst148.

[127] D. T. A. Eisenberg, C. W. Kuzawa, and M. G. Hayes, “Worldwide allele frequencies of the human apolipoprotein E gene: Climate, local adaptations, and evolutionary history,” *Am J Phys Anthropol*, vol. 143, no. 1, pp. 100–111, 2010, doi: 10.1002/ajpa.21298.

[128] L. Wu, X. Zhang, and L. Zhao, “Human apoe isoforms differentially modulate brain glucose and ketone body metabolism: Implications for Alzheimer’s disease risk reduction and early intervention,” *Journal of Neuroscience*, vol. 38, no. 30, pp. 6665–6681, 2018, doi: 10.1523/JNEUROSCI.2262-17.2018.

[129] W. Alata, Y. Ye, I. St-Amour, M. Vandal, and F. Calon, “Human apolipoprotein E ε4 expression impairs cerebral vascularization and blood-brain barrier function in mice,” *Journal of Cerebral Blood Flow and Metabolism*, vol. 35, no. 1, pp. 86–94, 2015, doi: 10.1038/jcbfm.2014.172.

[130] F. M. Marottoli *et al.*, “Autocrine Effects of Brain Endothelial Cell-Produced Human Apolipoprotein E on Metabolism and Inflammation in vitro,” *Front Cell Dev Biol*, vol. 9, Jun. 2021, doi: 10.3389/fcell.2021.668296.

[131] F. Liao, H. Yoon, and J. Kim, “Apolipoprotein e metabolism and functions in brain and its role in Alzheimer’s disease,” *Curr Opin Lipidol*, vol. 28, no. 1, pp. 60–67, 2017, doi: 10.1097/MOL.0000000000000383.

[132] J. Ruiz *et al.*, “The apoE isoform binding properties of the VLDL receptor reveal marked differences from LRP and the LDL receptor,” *J Lipid Res*, vol. 46, no. 8, pp. 1721–1731, 2005, doi: 10.1194/jlr.M500114-JLR200.

[133] N. Zhao *et al.*, “Apolipoprotein E4 Impairs Neuronal Insulin Signaling by Trapping Insulin Receptor in the Endosomes,” *Neuron*, vol. 96, no. 1, pp. 115-129.e5, Sep. 2017, doi: 10.1016/j.neuron.2017.09.003.

[134] M. Kim and I. Bezprozvanny, “Differences in recycling of apolipoprotein e3 and e4—ldl receptor complexes—a mechanistic hypothesis,” *Int J Mol Sci*, vol. 22, no. 9, 2021, doi: 10.3390/ijms22095030.

[135] A. Riskin, V. H. Nannegari, and Y. Mond, “Acute effectors of GLUT1 glucose transporter subcellular targeting in CIT3 mouse mammary epithelial cells,” *Pediatr Res*, vol. 63, no. 1, pp. 56–61, 2008, doi: 10.1203/PDR.0b013e31815b440b.

[136] E. Świderska, J. Strycharz, A. Wróblewski, J. Szemraj, J. Drzewoski, and A. Śliwińska, “Role of PI3K/AKT Pathway in Insulin-Mediated Glucose Uptake,” in *Blood Glucose Levels*, IntechOpen, 2020. doi: 10.5772/intechopen.80402.

[137] G. Sienski *et al.*, “APOE4 disrupts intracellular lipid homeostasis in human iPSC-derived glia,” *Sci Transl Med*, vol. 13, no. 583, pp. 1–12, 2021, doi: 10.1126/scitranslmed.aaz4564.

[138] V. Theendakara, C. A. Peters-Libeu, P. Spilman, K. S. Poksay, D. E. Bredesen, and R. V Rao, “Direct transcriptional effects of apolipoprotein E,” *Journal of Neuroscience*, vol. 36, no. 3, pp. 685–700, 2016, doi: 10.1523/JNEUROSCI.3562-15.2016.

[139] D. Kim *et al.*, “SIRT1 deacetylase protects against neurodegeneration in models for Alzheimer’s disease and amyotrophic lateral sclerosis,” *EMBO Journal*, vol. 26, no. 13, pp. 3169–3179, Jul. 2007, doi: 10.1038/SJ.EMBOJ.7601758.

[140] T. Chen *et al.*, “Sirt1-Sirt3 axis regulates human blood-brain barrier permeability in response to ischemia,” *Redox Biol*, vol. 14, pp. 229–236, 2017, doi: 10.1016/j.redox.2017.09.016.

[141] Y. Chen *et al.*, “SIRT1 regulated hexokinase-2 promoting glycolysis is involved in hydroquinone-enhanced malignant progression in human lymphoblastoid TK6 cells,” *Ecotoxicol Environ Saf*, vol. 241, Aug. 2022, doi: 10.1016/j.ecoenv.2022.113757.

[142] F.-L. Li *et al.*, “Acetylation accumulates PFKFB3 in cytoplasm to promote glycolysis and protects cells from cisplatin-induced apoptosis”, doi: 10.1038/s41467-018-02950-5.

[143] R. X. Jia, J. H. Liang, Y. Xu, and Y. Q. Wang, “Effects of physical activity and exercise on the cognitive function of patients with Alzheimer disease: A meta-analysis,” *BMC Geriatr*, vol. 19, no. 1, pp. 1–14, 2019, doi: 10.1186/s12877-019-1175-2.

[144] J. T. Yu *et al.*, “Evidence-based prevention of Alzheimer’s disease: Systematic review and meta-analysis of 243 observational prospective studies and 153 randomised controlled trials,” *J Neurol Neurosurg Psychiatry*, vol. 91, no. 11, pp. 1201–1209, 2020, doi: 10.1136/jnnp-2019-321913.

[145] S. Norton, F. E. Matthews, D. E. Barnes, K. Yaffe, and C. Brayne, “Potential for primary prevention of Alzheimer’s disease: An analysis of population-based data,” *Lancet Neurol*, vol. 13, no. 8, pp. 788–794, 2014, doi: 10.1016/S1474-4422(14)70136-X.

[146] M. Hamer and Y. Chida, “Physical activity and risk of neurodegenerative disease: A systematic review of prospective evidence,” *Psychol Med*, vol. 39, no. 1, pp. 3–11, 2008, doi: 10.1017/S0033291708003681.

[147] J. Won *et al.*, “Hippocampal functional connectivity and memory performance after exercise intervention in older adults with mild cognitive impairment,” *Journal of Alzheimer’s Disease*, vol. 82, no. 3, pp. 1015–1031, 2021, doi: 10.3233/JAD-210051.

[148] K. Reiter, K. A. Nielson, T. J. Smith, L. R. Weiss, J. Alfonso, and J. C. Smith, “Improved Cardiorespiratory Fitness is Associated with Increased,” vol. 21, no. 10, pp. 757–767, 2016, doi: 10.1017/S135561771500079X.Improved.

[149] E. G. A. (Esther) Karssemeijer, J. A. (Justine) Aaronson, W. J. (Willem) Bossers, T. (Tara) Smits, M. G. M. (Marcel) Olde Rikkert, and R. P. C. (Roy) Kessels, “Positive effects of combined cognitive and physical exercise training on cognitive function in older adults with mild cognitive impairment or dementia: A meta-analysis,” *Ageing Res Rev*, vol. 40, no. September, pp. 75–83, 2017, doi: 10.1016/j.arr.2017.09.003.

[150] J. C. Smith *et al.*, “Physical activity reduces hippocampal atrophy in elders at genetic risk for Alzheimer’s disease,” *Front Aging Neurosci*, vol. 6, no. APR, Apr. 2014, doi: 10.3389/fnagi.2014.00061.

[151] H. Kinni *et al.*, “Cerebral metabolism after forced or voluntary physical exercise,” *Brain Res*, vol. 1388, pp. 48–55, 2011, doi: 10.1016/j.brainres.2011.02.076.

[152] R. J. G. Hartman *et al.*, “Intrinsic transcriptomic sex differences in human endothelial cells at birth and in adults are associated with coronary artery disease targets,” *Sci Rep*, vol. 10, no. 1, pp. 1–12, 2020, doi: 10.1038/s41598-020-69451-8.

[153] L. Carrel and H. F. Willard, “X-inactivation profile reveals extensive variability in X-linked gene expression in females,” *Nature*, vol. 434, no. 7031, pp. 400–404, 2005, doi: 10.1038/nature03479.

[154] Y. Zhang *et al.*, “Genes that escape X-inactivation in humans have high intraspecific variability in expression, are associated with mental impairment but are not slow evolving,” *Mol Biol Evol*, vol. 30, no. 12, pp. 2588–2601, 2013, doi: 10.1093/molbev/mst148.

[155] M. Lorenz *et al.*, “Does cellular sex matter? Dimorphic transcriptional differences between female and male endothelial cells,” *Atherosclerosis*, vol. 240, no. 1, pp. 61–72, 2015, doi: 10.1016/j.atherosclerosis.2015.02.018.

[156] M. Lorenz *et al.*, “Sex-specific metabolic and functional differences in human umbilical vein endothelial cells from twin pairs,” *Atherosclerosis*, vol. 291, no. Supplement_1, pp. 99–106, Dec. 2019, doi: 10.1016/j.atherosclerosis.2019.10.007.

[157] R. Addis *et al.*, “Human umbilical endothelial cells (HUVECs) have a sex: Characterisation of the phenotype of male and female cells,” *Biol Sex Differ*, vol. 5, no. 1, pp. 1–12, 2014, doi: 10.1186/s13293-014-0018-2.

[158] B. D. James and J. B. Allen, “Sex-Specific Response to Combinations of Shear Stress and Substrate Stiffness by Endothelial Cells In Vitro,” *Adv Healthc Mater*, vol. 10, no. 18, Sep. 2021, doi: 10.1002/ADHM.202100735.

[159] S. AbdAlla, A. El Hakim, A. Abdelbaset, Y. Elfaramawy, and U. Quitterer, “Inhibition of ACE retards tau hyperphosphorylation and signs of neuronal degeneration in aged rats subjected to chronic mild stress,” *Biomed Res Int*, vol. 2015, 2015, doi: 10.1155/2015/917156.

[160] P. G. Kehoe, E. Hibbs, L. E. Palmer, and J. S. Miners, “Angiotensin-III is Increased in Alzheimer’s Disease in Association with Amyloid-β and Tau Pathology,” *Journal of Alzheimer’s Disease*, vol. 58, no. 1, pp. 203–214, May 2017, doi: 10.3233/JAD-161265.

[161] H. Choi, T. L. Leto, L. Hunyady, K. J. Catt, S. B. Yun, and G. R. Sue, “Mechanism of angiotensin II-induced superoxide production in cells reconstituted with angiotensin type 1 receptor and the components of NADPH oxidase,” *Journal of Biological Chemistry*, vol. 283, no. 1, pp. 255–267, 2008, doi: 10.1074/jbc.M708000200.

[162] S. Heeneman, J. F. M. Smits, P. J. A. Leenders, P. M. H. Schiffers, and M. J. A. P. Daemen, “Effects of angiotensin II on cardiac function and peripheral vascular structure during compensated heart failure in the rat,” *Arterioscler Thromb Vasc Biol*, vol. 17, no. 10, pp. 1985–1994, 1997, doi: 10.1161/01.ATV.17.10.1985/FORMAT/EPUB.

[163] U. Landmesser *et al.*, “Role of p47phox in vascular oxidative stress and hypertension caused by angiotensin II,” *Hypertension*, vol. 40, no. 4, pp. 511–515, Oct. 2002, doi: 10.1161/01.HYP.0000032100.23772.98/FORMAT/EPUB.

[164] M. S. Madhur *et al.*, “Role of interleukin 17 in inflammation, atherosclerosis, and vascular function in apolipoprotein e-deficient mice,” *Arterioscler Thromb Vasc Biol*, vol. 31, no. 7, pp. 1565–1572, Jul. 2011, doi: 10.1161/ATVBAHA.111.227629/FORMAT/EPUB.

[165] W. J. Li *et al.*, “‘angiotensin II memory’ contributes to the development of hypertension and vascular injury via activation of NADPH oxidase,” *Life Sci*, vol. 149, pp. 18–24, Mar. 2016, doi: 10.1016/J.LFS.2016.02.037.

[166] M. J. Ryan, S. P. Didion, S. Mathur, F. M. Faraci, and C. D. Sigmund, “Angiotensin II-Induced Vascular Dysfunction is Mediated by the AT 1A Receptor in Mice,” *Hypertension*, vol. 43, no. 5, pp. 1074–1079, May 2004, doi: 10.1161/01.HYP.0000123074.89717.3D/FORMAT/EPUB.

[167] C. M. Weber *et al.*, “Angiotensin II Increases Oxidative Stress and Inflammation in Female, But Not Male, Endothelial Cells,” *Cell Mol Bioeng*, vol. 16, no. 2, pp. 127–141, Apr. 2023, doi: 10.1007/s12195-023-00762-2.

[168] D. C. Rio, M. Ares, G. J. Hannon, and T. W. Nilsen, “Purification of RNA using TRIzol (TRI Reagent),” *Cold Spring Harb Protoc*, vol. 5, no. 6, Jun. 2010, doi: 10.1101/pdb.prot5439.

[169] A. L. Tarca *et al.*, “A novel signaling pathway impact analysis,” *BIOINFORMATICS ORIGINAL PAPER*, vol. 25, no. 1, pp. 75–82, 2009, doi: 10.1093/bioinformatics/btn577.

[170] S. Ahsan and S. Drăghici, “Identifying significantly impacted pathways and putative mechanisms with iPathwayGuide,” *Curr Protoc Bioinformatics*, vol. 2017, pp. 7.15.1-7.15.30, Mar. 2017, doi: 10.1002/CPBI.24.

[171] M. Maleszewska, J. R. A. J. Moonen, N. Huijkman, B. van de Sluis, G. Krenning, and M. C. Harmsen, “IL-1β and TGFβ2 synergistically induce endothelial to mesenchymal transition in an NFκB-dependent manner,” *Immunobiology*, vol. 218, no. 4, pp. 443–454, Apr. 2013, doi: 10.1016/J.IMBIO.2012.05.026.

[172] D. Vacondio *et al.*, “Liver X receptor alpha ensures blood-brain barrier function by suppressing SNAI2,” *Cell Death Dis*, vol. 14, no. 11, Nov. 2023, doi: 10.1038/s41419-023-06316-8.

[173] M. Birk *et al.*, “Angiotensin II Induces Oxidative Stress and Endothelial Dysfunction in Mouse Ophthalmic Arteries via Involvement of AT1 Receptors and NOX2,” *Antioxidants*, vol. 10, no. 8, p. 1238, Aug. 2021, doi: 10.3390/antiox10081238.

[174] P. G. Kehoe, S. Miners, and S. Love, “Angiotensins in Alzheimer’s disease - friend or foe?,” *Trends Neurosci*, vol. 32, no. 12, pp. 619–628, 2009, doi: 10.1016/j.tins.2009.07.006.

[175] Alzheimer’s Association, “2022 Alzheimer’s Disease Facts and Figures,” *Alzheimer’s and Dementia*, 2022.

[176] E. A. Khramtsova, L. K. Davis, and B. E. Stranger, “The role of sex in the genomics of human complex traits,” *Nature Reviews Genetics*, vol. 20, no. 3. Nature Publishing Group, pp. 173–190, Mar. 01, 2019. doi: 10.1038/s41576-018-0083-1.

[177] L. Xiao *et al.*, “Tumor endothelial cells with distinct patterns of TGFβ-driven endothelial-to-mesenchymal transition HHS Public Access,” *Cancer Res*, vol. 75, no. 7, pp. 1244–1254, 2015, doi: 10.1158/0008-5472.CAN-14-1616.

[178] I. B. Robertson and D. B. Rifkin, “Regulation of the Bioavailability of TGF-β and TGF-β-Related Proteins,” *Cold Spring Harb Perspect Biol*, vol. 8, no. 6, p. a021907, Jun. 2016, doi: 10.1101/cshperspect.a021907.

[179] K. L. Walton *et al.*, “Two Distinct Regions of Latency-associated Peptide Coordinate Stability of the Latent Transforming Growth Factor-Î²1 Complex*,” *Journal of Biological Chemistry*, vol. 285, pp. 17029–17037, 2010, doi: 10.1074/jbc.M110.110288.

[180] K. Miyazono, A. Olofsson, P. Colosetti, and C. H. Heldin, “A role of the latent TGF-β1-binding protein in the assembly and secretion of TGF-β1,” *EMBO Journal*, vol. 10, no. 5, pp. 1091–1101, 1991, doi: 10.1002/J.1460-2075.1991.TB08049.X.

[181] Y. Yoshimatsu *et al.*, “TNF-α enhances TGF-β-induced endothelial-to-mesenchymal transition via TGF-β signal augmentation,” *Cancer Sci*, vol. 111, no. 7, pp. 2385–2399, Jul. 2020, doi: 10.1111/CAS.14455.

[182] S. M. Evrard *et al.*, “Endothelial to mesenchymal transition is common in atherosclerotic lesions and is associated with plaque instability,” *Nat Commun*, vol. 7, no. May, 2016, doi: 10.1038/ncomms11853.

[183] B. A. Aguado *et al.*, “Genes That Escape X Chromosome Inactivation Modulate Sex Differences in Valve Myofibroblasts,” *Circulation*, vol. 145, no. 7, pp. 513–530, Feb. 2022, doi: 10.1161/CIRCULATIONAHA.121.054108/FORMAT/EPUB.

[184] J. Ma *et al.*, “TGF-β-Induced Endothelial to Mesenchymal Transition Is Determined by a Balance Between SNAIL and ID Factors,” *Front Cell Dev Biol*, vol. 9, p. 182, Feb. 2021, doi: 10.3389/FCELL.2021.616610/BIBTEX.

[185] S. Paschoud, A. M. Dogar, C. Kuntz, B. Grisoni-Neupert, L. Richman, and L. C. Kühn, “Destabilization of Interleukin-6 mRNA Requires a Putative RNA Stem-Loop Structure, an AU-Rich Element, and the RNA-Binding Protein AUF1,” *Mol Cell Biol*, vol. 26, no. 22, pp. 8228–8241, 2006, doi: 10.1128/MCB.01155-06.

[186] K. Masuda *et al.*, “Arid5a controls IL-6 mRNA stability, which contributes to elevation of IL-6 level in vivo,” *Proc Natl Acad Sci U S A*, vol. 110, no. 23, pp. 9409–9414, Jun. 2013, doi: 10.1073/pnas.1307419110.

[187] K. Matsushita *et al.*, “Zc3h12a is an RNase essential for controlling immune responses by regulating mRNA decay,” *Nature*, vol. 458, no. 7242, pp. 1185–1190, Apr. 2009, doi: 10.1038/nature07924.

[188] J. A. Elias and V. Lentz, “IL-1 and tumor necrosis factor synergistically stimulate fibroblast IL-6 production and stabilize IL-6 messenger RNA,” *The Journal of Immunology*, vol. 145, no. 1, pp. 161–166, 1990, Accessed: Sep. 12, 2022. [Online]. Available: http://www.jimmunol.org/

[189] G. Simonneau *et al.*, “Haemodynamic definitions and updated clinical classification of pulmonary hypertension,” *European Respiratory Journal*, vol. 53, no. 1, p. 1801913, Jan. 2019, doi: 10.1183/13993003.01913-2018.

[190] M. D. McGoon *et al.*, “Pulmonary arterial hypertension: Epidemiology and registries,” *J Am Coll Cardiol*, vol. 62, no. 25 SUPPL., Dec. 2013, doi: 10.1016/J.JACC.2013.10.023.

[191] D. S. Kostyunina and P. McLoughlin, “Sex dimorphism in pulmonary hypertension: The role of the sex chromosomes,” *Antioxidants*, vol. 10, no. 5. MDPI, May 01, 2021. doi: 10.3390/antiox10050779.

[192] K. J. Catt, M. C. Cain, and J. P. Coghlan, “MEASUREMENT OF ANGIOTENSIN II IN BLOOD,” *The Lancet*, vol. 290, no. 7524, pp. 1005–1007, Nov. 1967, doi: 10.1016/S0140-6736(67)90285-1.

[193] P. J. Admiraal, A. H. Danser, M. S. Jong, H. Pieterman, F. H. Derkx, and M. A. Schalekamp, “Regional angiotensin II production in essential hypertension and renal artery stenosis.,” *Hypertension*, vol. 21, no. 2, pp. 173–184, Feb. 1993, doi: 10.1161/01.HYP.21.2.173.

[194] P. Mergenthaler, U. Lindauer, G. A. Dienel, and A. Meisel, “Sugar for the brain: the role of glucose in physiological and pathological brain function,” *Trends Neurosci*, vol. 36, no. 10, pp. 587–597, Oct. 2013, doi: 10.1016/j.tins.2013.07.001.

[195] M. S. Goyal and M. E. Raichle, “Glucose Requirements of the Developing Human Brain,” *J Pediatr Gastroenterol Nutr*, vol. 66, no. 3, pp. S46–S49, Jun. 2018, doi: 10.1097/MPG.0000000000001875.

[196] L. Mosconi, A. Pupi, and M. J. De Leon, “Brain Glucose Hypometabolism and Oxidative Stress in Preclinical Alzheimer’s Disease,” *Ann N Y Acad Sci*, vol. 1147, no. 1, pp. 180–195, Dec. 2008, doi: 10.1196/annals.1427.007.

[197] Y. Liu, F. Liu, K. Iqbal, I. Grundke-Iqbal, and C.-X. Gong, “Decreased glucose transporters correlate to abnormal hyperphosphorylation of tau in Alzheimer disease,” *FEBS Lett*, vol. 582, no. 2, pp. 359–364, Jan. 2008, doi: 10.1016/j.febslet.2007.12.035.

[198] V. Baghel *et al.*, “In Vivo Assessment of Tau Deposition in Alzheimer Disease and Assessing Its Relationship to Regional Brain Glucose Metabolism and Cognition,” *Clin Nucl Med*, vol. 44, no. 11, pp. e597–e601, Nov. 2019, doi: 10.1097/RLU.0000000000002791.

[199] Z. Chen and C. Zhong, “Decoding Alzheimer’s disease from perturbed cerebral glucose metabolism: Implications for diagnostic and therapeutic strategies,” *Prog Neurobiol*, vol. 108, pp. 21–43, Sep. 2013, doi: 10.1016/j.pneurobio.2013.06.004.

[200] M. A. Daulatzai, “Cerebral hypoperfusion and glucose hypometabolism: Key pathophysiological modulators promote neurodegeneration, cognitive impairment, and Alzheimer’s disease,” *J Neurosci Res*, vol. 95, no. 4, pp. 943–972, Apr. 2017, doi: 10.1002/jnr.23777.

[201] P. Vogelsang *et al.*, “Reduced glucose transporter-1 in brain derived circulating endothelial cells in mild Alzheimer’s disease patients,” *Brain Res*, vol. 1678, pp. 304–309, Jan. 2018, doi: 10.1016/j.brainres.2017.10.035.

[202] H. Fischer, R. Gottschlich, and A. Seelig, “Blood-Brain Barrier Permeation: Molecular Parameters Governing Passive Diffusion”.

[203] W. M. Pardridge, *Brain Drug Targeting*. Cambridge University Press, 2001. doi: 10.1017/CBO9780511549571.

[204] K. De Bock *et al.*, “Role of PFKFB3-driven glycolysis in vessel sprouting,” *Cell*, vol. 154, no. 3, Aug. 2013, doi: 10.1016/J.CELL.2013.06.037.

[205] A. Krützfeldt, R. Spahr, S. Mertens, B. Siegmund, and H. M. Piper, “Metabolism of exogenous substrates by coronary endothelial cells in culture,” *J Mol Cell Cardiol*, vol. 22, no. 12, pp. 1393–1404, 1990, doi: 10.1016/0022-2828(90)90984-A.

[206] L. N. Groschner, M. Waldeck-Weiermair, R. Malli, and W. F. Graier, “Endothelial mitochondria-less respiration, more integration”, doi: 10.1007/s00424-012-1085-z.

[207] R. A. Gatenby and R. J. Gillies, “Why do cancers have high aerobic glycolysis?,” *Nature Reviews Cancer*, vol. 4, no. 11. pp. 891–899, Nov. 2004. doi: 10.1038/nrc1478.

[208] G. Eelen, P. de Zeeuw, L. Treps, U. Harjes, B. W. Wong, and P. Carmeliet, “Endothelial cell metabolism,” *Physiol Rev*, vol. 98, no. 1, pp. 3–58, Jan. 2018, doi: 10.1152/PHYSREV.00001.2017.

[209] T. K. Hunt *et al.*, “Aerobically derived lactate stimulates revascularization and tissue repair via redox mechanisms,” *Antioxid Redox Signal*, vol. 9, no. 8, pp. 1115–1124, Aug. 2007, doi: 10.1089/ARS.2007.1674.

[210] W. M. Lawrence, N. A. Marinelli, and E. S. Lippmann, “Investigating the Metabolic Characteristics of Brain Microvascular Endothelial Cells,” *Young Scientist*, Dec. 2020.

[211] W. H. Oldendorf, M. E. Cornford, and W. J. Brown, “The large apparent work capability of the blood-brain barrier: A study of the mitochondrial content of capillary endothelial cells in brain and other tissues of the rat,” *Ann Neurol*, vol. 1, no. 5, pp. 409–417, May 1977, doi: 10.1002/ana.410010502.

[212] S. B. Hinca *et al.*, “Brain endothelial cells metabolize glutamate via glutamate dehydrogenase to replenish TCA-intermediates and produce ATP under hypoglycemic conditions,” *J Neurochem*, vol. 157, no. 6, pp. 1861–1875, Jun. 2021, doi: 10.1111/jnc.15207.

[213] E. K. Hollmann, A. K. Bailey, A. V. Potharazu, M. D. Neely, A. B. Bowman, and E. S. Lippmann, “Accelerated differentiation of human induced pluripotent stem cells to blood-brain barrier endothelial cells,” *Fluids Barriers CNS*, vol. 14, no. 1, p. 9, 2017, doi: 10.1186/s12987-017-0059-0.

[214] Y. He, Y. Yao, S. E. Tsirka, and Y. Cao, “Cell-Culture Models of the Blood–Brain Barrier,” *Stroke*, vol. 45, no. 8, pp. 2514–2526, Aug. 2014, doi: 10.1161/STROKEAHA.114.005427.

[215] C. J. McDonald, Z. J. Blankenheim, and L. R. Drewes, “Brain Endothelial Cells: Metabolic Flux and Energy Metabolism,” *Handb Exp Pharmacol*, vol. 273, pp. 59–79, 2022, doi: 10.1007/164_2021_494.

[216] E. H. Neal *et al.*, “A Simplified, Fully Defined Differentiation Scheme for Producing Blood-Brain Barrier Endothelial Cells from Human iPSCs,” *Stem Cell Reports*, vol. 12, no. 6, pp. 1380–1388, Jun. 2019, doi: 10.1016/j.stemcr.2019.05.008.

[217] T. M. Lu *et al.*, “Pluripotent stem cell-derived epithelium misidentified as brain microvascular endothelium requires ETS factors to acquire vascular fate,” *Proc Natl Acad Sci U S A*, vol. 118, no. 8, 2021, doi: 10.1073/pnas.2016950118.

[218] E. S. Lippmann, S. M. Azarin, S. P. Palecek, and E. V. Shusta, “Commentary on human pluripotent stem cell-based blood–brain barrier models,” *Fluids Barriers CNS*, vol. 17, no. 1, p. 64, Dec. 2020, doi: 10.1186/s12987-020-00222-3.

[219] C. M. Weber, B. Moiz, S. M. Zic, V. Alpízar Vargas, A. Li, and A. M. Clyne, “Induced pluripotent stem cell-derived cells model brain microvascular endothelial cell glucose metabolism,” *Fluids Barriers CNS*, vol. 19, no. 1, p. 98, Dec. 2022, doi: 10.1186/s12987-022-00395-z.

[220] J. Yu *et al.*, “Induced pluripotent stem cell lines derived from human somatic cells,” *Science (1979)*, vol. 318, no. 5858, pp. 1917–1920, Dec. 2007, doi: 10.1126/SCIENCE.1151526.

[221] K. P. Chennazhy and L. K. Krishnan, “Effect of passage number and matrix characteristics on differentiation of endothelial cells cultured for tissue engineering,” *Biomaterials*, vol. 26, no. 28, pp. 5658–5667, Oct. 2005, doi: 10.1016/J.BIOMATERIALS.2005.02.024.

[222] J. Kalucka *et al.*, “Quiescent Endothelial Cells Upregulate Fatty Acid β-Oxidation for Vasculoprotection via Redox Homeostasis,” *Cell Metab*, vol. 28, no. 6, pp. 881-894.e13, Dec. 2018, doi: 10.1016/J.CMET.2018.07.016.

[223] D. C. Rio, M. Ares, G. J. Hannon, and T. W. Nilsen, “Purification of RNA using TRIzol (TRI Reagent),” *Cold Spring Harb Protoc*, vol. 5, no. 6, 2010, doi: 10.1101/pdb.prot5439.

[224] B. Tasic *et al.*, “Shared and distinct transcriptomic cell types across neocortical areas,” *Nature*, vol. 563, no. 7729, pp. 72–78, Nov. 2018, doi: 10.1038/s41586-018-0654-5.

[225] R. D. Hodge *et al.*, “Conserved cell types with divergent features in human versus mouse cortex,” *Nature*, vol. 573, no. 7772, pp. 61–68, Sep. 2019, doi: 10.1038/s41586-019-1506-7.

[226] T. Nemkov, K. C. Hansen, and A. D’Alessandro, “A three-minute method for high-throughput quantitative metabolomics and quantitative tracing experiments of central carbon and nitrogen pathways,” *Rapid Communications in Mass Spectrometry*, vol. 31, no. 8, pp. 663–673, Apr. 2017, doi: 10.1002/rcm.7834.

[227] T. Nemkov, J. A. Reisz, S. Gehrke, K. C. Hansen, and A. D’Alessandro, “High-Throughput Metabolomics: Isocratic and Gradient Mass Spectrometry-Based Methods,” 2019, pp. 13–26. doi: 10.1007/978-1-4939-9236-2_2.

[228] T. Nemkov, A. D’Alessandro, and K. C. Hansen, “Three-minute method for amino acid analysis by UHPLC and high-resolution quadrupole orbitrap mass spectrometry,” *Amino Acids*, vol. 47, no. 11, pp. 2345–2357, Nov. 2015, doi: 10.1007/s00726-015-2019-9.

[229] P. Millard, B. Delépine, M. Guionnet, M. Heuillet, F. Bellvert, and F. Létisse, “IsoCor: isotope correction for high-resolution MS labeling experiments,” *Bioinformatics*, vol. 35, no. 21, pp. 4484–4487, Nov. 2019, doi: 10.1093/bioinformatics/btz209.

[230] Z. Pang *et al.*, “Using MetaboAnalyst 5.0 for LC–HRMS spectra processing, multi-omics integration and covariate adjustment of global metabolomics data,” *Nat Protoc*, vol. 17, no. 8, pp. 1735–1761, Aug. 2022, doi: 10.1038/s41596-022-00710-w.

[231] C. A. A. Lee, H. S. Seo, A. G. Armien, F. S. Bates, J. Tolar, and S. M. Azarin, “Modeling and rescue of defective blood–brain barrier function of induced brain microvascular endothelial cells from

childhood cerebral adrenoleukodystrophy patients," *Fluids Barriers CNS*, vol. 15, no. 1, p. 9, Dec. 2018, doi: 10.1186/s12987-018-0094-5.

[232] T. Kurosawa *et al.*, "Expression and Functional Characterization of Drug Transporters in Brain Microvascular Endothelial Cells Derived from Human Induced Pluripotent Stem Cells," *Mol Pharm*, vol. 15, no. 12, pp. 5546–5555, Dec. 2018, doi: 10.1021/acs.molpharmaceut.8b00697.

[233] A. Paradis, D. Leblanc, and N. Dumais, "Optimization of an in vitro human blood-brain barrier model: Application to blood monocyte transmigration assays," *MethodsX*, vol. 3, pp. 25–34, 2016, doi: 10.1016/j.mex.2015.11.009.

[234] T. Qian *et al.*, "Directed differentiation of human pluripotent stem cells to blood-brain barrier endothelial cells," *Sci Adv*, vol. 3, no. 11, p. e1701679, Nov. 2017, doi: 10.1126/sciadv.1701679.

[235] G. N. Grifno *et al.*, "Tissue-engineered blood-brain barrier models via directed differentiation of human induced pluripotent stem cells," *Sci Rep*, vol. 9, no. 1, p. 13957, Dec. 2019, doi: 10.1038/s41598-019-50193-1.

[236] D. Nowis *et al.*, "Statins impair glucose uptake in human cells", doi: 10.1136/bmjdrc-2014-000017.

[237] E. M. Reiman *et al.*, "Preclinical Evidence of Alzheimer's Disease in Persons Homozygous for the ε4 Allele for Apolipoprotein E," *New England Journal of Medicine*, vol. 334, no. 12, pp. 752–758, 1996, doi: 10.1056/nejm199603213341202.

[238] L. Dunn *et al.*, "Dysregulation of glucose metabolism is an early event in sporadic Parkinson's disease," *Neurobiol Aging*, vol. 35, no. 5, pp. 1111–1115, May 2014, doi: 10.1016/j.neurobiolaging.2013.11.001.

[239] H. Endo, K. Sekiguchi, T. Ueda, H. Kowa, F. Kanda, and T. Toda, "Regional glucose hypometabolic spread within the primary motor cortex is associated with amyotrophic lateral sclerosis disease progression: A fluoro-deoxyglucose positron emission tomography study," *eNeurologicalSci*, vol. 6, pp. 74–79, Mar. 2017, doi: 10.1016/j.ensci.2017.01.001.

[240] C. D. L. Folmes and A. Terzic, "Energy metabolism in the acquisition and maintenance of stemness," *Seminars in Cell and Developmental Biology*, vol. 52. Academic Press, pp. 68–75, Apr. 01, 2016. doi: 10.1016/j.semcdb.2016.02.010.

[241] L. M. Williams *et al.*, "Prolonged culturing of iPSC-derived brain endothelial-like cells is associated with quiescence, downregulation of glycolysis, and resistance to disruption by an Alzheimer's brain milieu", doi: 10.1186/s12987-022-00307-1.

[242] H. Legros *et al.*, "Newborn- and adult-derived brain microvascular endothelial cells show age-related differences in phenotype and glutamate-evoked protease release," *Journal of Cerebral Blood Flow and Metabolism*, vol. 29, no. 6, pp. 1146–1158, Jun. 2009, doi: 10.1038/JCBFM.2009.39/FORMAT/EPUB.

[243] E. H. Neal *et al.*, "A Simplified, Fully Defined Differentiation Scheme for Producing Blood-Brain Barrier Endothelial Cells from Human iPSCs," *Stem Cell Reports*, vol. 12, no. 6, pp. 1380–1388, Jun. 2019, doi: 10.1016/j.stemcr.2019.05.008.

[244] S. Schoors *et al.*, “Partial and transient reduction of glycolysis by PFKFB3 blockade reduces pathological angiogenesis,” *Cell Metab*, vol. 19, no. 1, pp. 37–48, Jan. 2014, doi: 10.1016/J.CMET.2013.11.008.

[245] M. Dambrova *et al.*, “Acylcarnitines: Nomenclature, Biomarkers, Therapeutic Potential, Drug Targets, and Clinical Trials,” *Pharmacol Rev*, vol. 74, no. 3, pp. 506–551, Jul. 2022, doi: 10.1124/pharmrev.121.000408.

[246] O. Yanes *et al.*, “Metabolic oxidation regulates embryonic stem cell differentiation,” *Nat Chem Biol*, vol. 6, no. 6, pp. 411–417, Jun. 2010, doi: 10.1038/nchembio.364.

[247] E. Fathi, R. Farahzadi, and H. N. Charoudeh, “L-carnitine contributes to enhancement of neurogenesis from mesenchymal stem cells through Wnt/β-catenin and PKA pathway,” *Exp Biol Med*, vol. 242, no. 5, pp. 482–486, Mar. 2017, doi: 10.1177/1535370216685432.

[248] L. Grossbard and R. T. Schimke, “Multiple Hexokinases of Rat Tissues PURIFICATION AND COMPARISON OF SOLUBLE FORMS,” *J Biol Chem*, vol. 241, no. 15, pp. 3546–3560, 1966, doi: 10.1016/S0021-9258(18)99866-2.

[249] S. Varum *et al.*, “Energy Metabolism in Human Pluripotent Stem Cells and Their Differentiated Counterparts”, doi: 10.1371/journal.pone.0020914.

[250] J. H. Jang *et al.*, “Tristetraprolin posttranscriptionally downregulates PFKFB3 in cancer cells,” *Biochem Biophys Res Commun*, vol. 521, no. 2, pp. 389–394, Jan. 2020, doi: 10.1016/J.BBRC.2019.10.128.

[251] K. Maxwell, J. A. Berliner, and P. A. Cancilla, “Stimulation of glucose analogue uptake by cerebral microvessel endothelial cells by a product released by astrocytes,” *J Neuropathol Exp Neurol*, vol. 48, no. 1, 1989, doi: 10.1097/00005072-198901000-00006.

[252] G. J. Prud’homme, “Pathobiology of transforming growth factor β in cancer, fibrosis and immunologic disease, and therapeutic considerations,” *Laboratory Investigation*, vol. 87, no. 11. 2007. doi: 10.1038/labinvest.3700669.

[253] J. Soukupova *et al.*, “Role of the Transforming Growth Factor-β in regulating hepatocellular carcinoma oxidative metabolism,” *Sci Rep*, vol. 7, no. 1, 2017, doi: 10.1038/s41598-017-12837-y.

[254] E. Alpert *et al.*, “Delayed autoregulation of glucose transport in vascular endothelial cells,” *Diabetologia*, vol. 48, pp. 752–755, 2005, doi: 10.1007/s00125-005-1681-y.

[255] Agnieszka Koziel, Andrzej Woyda-Ploszczyca, Anna Kicinska, and Wieslawa Jarmuszkiewicz, “The influence of high glucose on the aerobic metabolism of endothelial EA.hy926 cells,” *Signaling and Cell Physiology*, vol. 464, pp. 657–669, 2012, doi: 10.1007/s00424-012-1156-1.

[256] W. Li, R. E. Maloney, and Y. Aw, “High glucose, glucose fluctuation and carbonyl stress enhance brain microvascular endothelial barrier dysfunction: Implications for dia-betic cerebral microvasculature,” *Redox Biol*, vol. 5, pp. 80–90, 2015, doi: 10.1016/j.redox.2015.03.005.

[257] B. Shao and U. Bayraktutan, “Hyperglycaemia promotes human brain microvascular endothelial cell apoptosis via induction of protein kinase C-βI and prooxidant enzyme NADPH oxidase,” *Redox Biol*, vol. 2, no. 1, pp. 694–701, 2014, doi: 10.1016/J.REDOX.2014.05.005.

[258] J. E. Vance, “Dysregulation of cholesterol balance in the brain: contribution to neurodegenerative diseases,” *Dis Model Mech*, vol. 5, no. 6, pp. 746–755, 2012, doi: 10.1242/dmm.010124.

[259] S. Mäkinen, N. Datta, Y. H. Nguyen, P. Kyrylenko, M. Laakso, and H. A. Koistinen, “Simvastatin profoundly impairs energy metabolism in primary human muscle cells,” 2020, doi: 10.1530/EC-20-0444.

[260] S. Man, E. E. Ubogu, K. A. Williams, B. Tucky, M. K. Callahan, and R. M. Ransohoff, “Human Brain Microvascular Endothelial Cells and Umbilical Vein Endothelial Cells Differentially Facilitate Leukocyte Recruitment and Utilize Chemokines for T Cell Migration,” *Clin Dev Immunol*, vol. 2008, pp. 1–8, 2008, doi: 10.1155/2008/384982.

[261] H. Kilpinen *et al.*, “Common genetic variation drives molecular heterogeneity in human iPSCs,” *Nature*, vol. 546, no. 7658, pp. 370–375, 2017, doi: 10.1038/nature22403.

[262] X. Sun and M. W. Feinberg, “Regulation of Endothelial Cell Metabolism,” *Arterioscler Thromb Vasc Biol*, vol. 35, no. 1, pp. 13–15, Jan. 2015, doi: 10.1161/ATVBAHA.114.304869.

[263] S.-G. Hong *et al.*, “Flow pattern–dependent mitochondrial dynamics regulates the metabolic profile and inflammatory state of endothelial cells,” *JCI Insight*, vol. 7, no. 18, Sep. 2022, doi: 10.1172/jci.insight.159286.

[264] H. Ge, M. Tian, Q. Pei, F. Tan, and H. Pei, “Extracellular Matrix Stiffness: New Areas Affecting Cell Metabolism,” *Front Oncol*, vol. 11, Feb. 2021, doi: 10.3389/fonc.2021.631991.

[265] S. Bellosta, R. Paoletti, and A. Corsini, “Safety of statins: Focus on clinical pharmacokinetics and drug interactions,” *Circulation*, vol. 109, no. 23 SUPPL., Jun. 2004, doi: 10.1161/01.CIR.0000131519.15067.1F/FORMAT/EPUB.

[266] I. Ifergan *et al.*, “Statins reduce human blood-brain barrier permeability and restrict leukocyte migration: Relevance to multiple sclerosis,” *Ann Neurol*, vol. 60, no. 1, pp. 45–55, Jul. 2006, doi: 10.1002/ANA.20875.

[267] C. Wilson, M. D. Lee, C. Buckley, X. Zhang, and J. G. Mccarron, “Mitochondrial ATP Production is Required for Endothelial Cell Control of Vascular Tone,” *FUNCTION*, vol. 4, no. 2, 2022, doi: 10.1093/function/zqac063.

[268] S.-G. Hong, X. Yang, and J.-Y. Park, “Flow pattern-dependent mitochondrial dynamics regulates the metabolic profile and inflammatory state of endothelial cells Graphical abstract,” 2022, doi: 10.1172/jci.insight.159286.

[269] S. B. Hinca *et al.*, “Brain endothelial cells metabolize glutamate via glutamate dehydrogenase to replenish TCA-intermediates and produce ATP under hypoglycemic conditions,” *J Neurochem*, vol. 157, no. 6, pp. 1861–1875, Jun. 2021, doi: 10.1111/JNC.15207.

[270] G. Wu, T. E. Haynes, H. Li, and C. J. Meininger, “Glutamine metabolism in endothelial cells: ornithine synthesis from glutamine via pyrroline-5-carboxylate synthase,” *Comparative Biochemistry and Physiology Part A*, vol. 126, pp. 115–123, 2000, Accessed: Jan. 11, 2024. [Online]. Available: www.elsevier.com/locate/cbpa

[271] G. Wu, A. G. Borbolla, and D. A. Knabe, “The uptake of glutamine and release of arginine, citrulline and proline by the small intestine of developing pigs,” *J Nutr*, vol. 124, no. 12, pp. 2437–2444, Dec. 1994.

[272] M. Watford, “Hepatic glutaminase expression: relationship to kidney-type glutaminase and to the urea cycle,” *The FASEB Journal*, vol. 7, no. 15, pp. 1468–1474, Dec. 1993, doi: 10.1096/FASEBJ.7.15.8262331.

[273] P. Newsholme, S. Gordont, and E. A. Newsholme, “Rates of utilization and fates of glucose, glutamine, pyruvate, fatty acids and ketone bodies by mouse macrophages,” *Biochem. J*, vol. 242, pp. 631–636, 1987.

[274] D.-F. Dai, M. E. Danoviz, B. Wiczer, M. A. Laflamme, and R. Tian, “Mitochondrial Maturation in Human Pluripotent Stem Cell Derived Cardiomyocytes,” *Stem Cells Int*, vol. 2017, 2017, doi: 10.1155/2017/5153625.

[275] N. G. Lee *et al.*, “TGF-β and SHH Regulate Pluripotent Stem Cell Differentiation into Brain Microvascular Endothelial Cells in Generating an In Vitro Blood–Brain Barrier Model,” *Bioengineering*, vol. 10, no. 10, Oct. 2023, doi: 10.3390/bioengineering10101132.

[276] A. Rohani, J. A. Kashatus, D. T. Sessions, S. Sharmin, and D. F. Kashatus, “Mito Hacker: a set of tools to enable high-throughput analysis of mitochondrial network morphology,” *Sci Rep*, vol. 10, no. 1, Dec. 2020, doi: 10.1038/s41598-020-75899-5.

[277] B. Moiz *et al.*, “13 C Metabolic Flux Analysis Indicates Endothelial Cells Attenuate Metabolic Perturbations By Modulating Tca Activity,” *Metabolites*, vol. 11, no. 4, 2021, doi: 10.3390/metabo11040226.

[278] S. N. Vallerie and K. E. Bornfeldt, “Metabolic Flexibility and Dysfunction in Cardiovascular Cells”, doi: 10.1161/ATVBAHA.115.306226.

[279] H. Song, J. Zhu, P. Li, F. Han, L. Fang, and P. Yu, “Metabolic flexibility maintains proliferation and migration of FGFR signaling-deficient lymphatic endothelial cells,” *Journal of Biological Chemistry*, vol. 297, p. 101149, 2021, doi: 10.1016/j.jbc.2021.101149.

[280] A. Prigione, B. Fauler, R. Lurz, H. Lehrach, and J. Adjaye, “The senescence-related mitochondrial/oxidative stress pathway is repressed in human induced pluripotent stem cells,” *Stem Cells*, vol. 28, no. 4, pp. 721–733, Apr. 2010, doi: 10.1002/STEM.404.

[281] S. Varum *et al.*, “Energy Metabolism in Human Pluripotent Stem Cells and Their Differentiated Counterparts,” *PLoS One*, vol. 6, no. 6, p. e20914, 2011, doi: 10.1371/journal.pone.0020914.

[282] S. M. Sears and S. J. Hewett, “Minireview Influence of glutamate and GABA transport on brain excitatory/ inhibitory balance,” *Exp Biol Med*, vol. 246, pp. 1069–1083, 2021, doi: 10.1177/1535370221989263.

[283] T. Fraser, H. Tayler, and S. Love, “Fatty acid composition of frontal, temporal and parietal neocortex in the normal human brain and in Alzheimer’s disease,” *Neurochem Res*, vol. 35, no. 3, pp. 503–513, Mar. 2010, doi: 10.1007/s11064-009-0087-5.

[284] Z. J. Wang, G. M. Li, W. L. Tang, and M. Yin, “Neuroprotective effects of stearic acid against toxicity of oxygen/glucose deprivation or glutamate on rat cortical or hippocampal slices,” *Acta Pharmacol Sin*, vol. 27, no. 2, pp. 145–150, Feb. 2006, doi: 10.1111/j.1745-7254.2006.00259.x.

[285] Q. Shang *et al.*, “Myristic acid alleviates hippocampal aging correlated with GABAergic signaling,” *Front Nutr*, vol. 9, 2022, [Online]. Available: https://www.

[286] E. K. Ruzzo *et al.*, “Deficiency of Asparagine Synthetase Causes Congenital Microcephaly and a Progressive Form of Encephalopathy,” *Neuron*, vol. 80, pp. 429–441, 2013, doi: 10.1016/j.neuron.2013.08.013.

[287] B. Dannenmann *et al.*, “High Glutathione and Glutathione Peroxidase-2 Levels Mediate Cell-Type-Specific DNA Damage Protection in Human Induced Pluripotent Stem Cells,” *Stem Cell Reports*, vol. 4, pp. 886–898, 2015, doi: 10.1016/j.stemcr.2015.04.004.

[288] J. J. Chen *et al.*, “Altered central and blood glutathione in Alzheimer’s disease and mild cognitive impairment: a meta-analysis,” *Alzheimers Res Ther*, vol. 14, no. 1, Dec. 2022, doi: 10.1186/s13195-022-00961-5.

[289] I.-Y. Choi *et al.*, “In vivo evidence of oxidative stress in brains of patients with progressive multiple sclerosis,” *Multiple Sclerosis*, vol. 24, no. 8, pp. 1029–1038, 2018, doi: 10.1177/1352458517711568.

[290] D. Shukla *et al.*, “Glutathione Depletion and Concomitant Elevation of Susceptibility in Patients with Parkinson’s Disease: State-of-the-Art MR Spectroscopy and Neuropsychological Study,” *ACS Chem Neurosci*, vol. 14, pp. 4383–4394, Dec. 2023, doi: 10.1021/ACSCHEMNEURO.3C00717.

[291] X. Wang *et al.*, “α-Ketoglutarate-Activated NF-κB Signaling Promotes Compensatory Glucose Uptake and Brain Tumor Development,” *Mol Cell*, vol. 76, no. 1, pp. 148-162.e7, Oct. 2019, doi: 10.1016/j.molcel.2019.07.007.

[292] S. E. Basehore *et al.*, “Laminar Flow on Endothelial Cells Suppresses eNOS O-GlcNAcylation to Promote eNOS Activity,” *Circ Res*, vol. 129, no. 11, pp. 1054–1066, Nov. 2021, doi: 10.1161/CIRCRESAHA.121.318982/FORMAT/EPUB.

[293] A. Doddaballapur *et al.*, “Laminar shear stress inhibits endothelial cell metabolism via KLF2-mediated repression of PFKFB3,” *Arterioscler Thromb Vasc Biol*, vol. 35, no. 1, pp. 137–145, Jan. 2015, doi: 10.1161/ATVBAHA.114.304277/FORMAT/EPUB.

[294] Y. Wang *et al.*, “Slow flow induces endothelial dysfunction by regulating thioredoxin-interacting protein-mediated oxidative metabolism and vascular inflammation,” *Front Cardiovasc Med*, vol. 9, Nov. 2022, doi: 10.3389/fcvm.2022.1064375.

[295] L. H. Wu, H. C. Chang, P. C. Ting, and D. L. Wang, “Laminar shear stress promotes mitochondrial homeostasis in endothelial cells,” *J Cell Physiol*, vol. 233, no. 6, pp. 5058–5069, Jun. 2018, doi: 10.1002/JCP.26375.

[296] T. Bertero *et al.*, “Vascular stiffness mechanoactivates YAP/TAZ-dependent glutaminolysis to drive pulmonary hypertension,” *Journal of Clinical Investigation*, vol. 126, no. 9, pp. 3313–3335, Sep. 2016, doi: 10.1172/JCI86387.

[297] A. J. C. Slooter *et al.*, “Risk Estimates of Dementia by Apolipoprotein E Genotypes From a Population-Based Incidence Study: The Rotterdam Study,” *Arch Neurol*, vol. 55, no. 7, p. 964, Jul. 1998, doi: 10.1001/archneur.55.7.964.

[298] G. W. Small *et al.*, “Cerebral metabolic and cognitive decline in persons at genetic risk for Alzheimer’s disease,” *Proceedings of the National Academy of Sciences*, vol. 97, no. 11, pp. 6037–6042, May 2000, doi: 10.1073/pnas.090106797.

[299] A. Montagne *et al.*, “APOE4 leads to blood–brain barrier dysfunction predicting cognitive decline,” *Nature*, vol. 581, no. 7806, pp. 71–76, 2020, doi: 10.1038/s41586-020-2247-3.

[300] M. S. Baek, H. Cho, H. S. Lee, J. H. Lee, Y. H. Ryu, and C. H. Lyoo, “Effect of APOE ε4 genotype on amyloid-β and tau accumulation in Alzheimer’s disease,” *Alzheimers Res Ther*, vol. 12, no. 1, p. 140, Dec. 2020, doi: 10.1186/s13195-020-00710-6.

[301] K. Nishitsuji, T. Hosono, T. Nakamura, G. Bu, and M. Michikawa, “Apolipoprotein E Regulates the Integrity of Tight Junctions in an Isoform-dependent Manner in an in Vitro Blood-Brain Barrier Model,” *Journal of Biological Chemistry*, vol. 286, no. 20, pp. 17536–17542, May 2011, doi: 10.1074/jbc.M111.225532.

[302] A. Montagne *et al.*, “APOE4 accelerates advanced-stage vascular and neurodegenerative disorder in old Alzheimer’s mice via cyclophilin A independently of amyloid-β,” *Nat Aging*, vol. 1, no. 6, pp. 506–520, Jun. 2021, doi: 10.1038/s43587-021-00073-z.

[303] H. C. Williams *et al.*, “APOE alters glucose flux through central carbon pathways in astrocytes,” *Neurobiol Dis*, vol. 136, no. January, p. 104742, 2020, doi: 10.1016/j.nbd.2020.104742.

[304] N. Zhao *et al.*, “Apolipoprotein E4 Impairs Neuronal Insulin Signaling by Trapping Insulin Receptor in the Endosomes,” *Neuron*, vol. 96, no. 1, pp. 115-129.e5, 2017, doi: 10.1016/j.neuron.2017.09.003.

[305] A. Riskin, V. H. Nannegari, and Y. Mond, “Acute effectors of GLUT1 glucose transporter subcellular targeting in CIT3 mouse mammary epithelial cells,” *Pediatr Res*, vol. 63, no. 1, pp. 56–61, 2008, doi: 10.1203/PDR.0b013e31815b440b.

[306] S. Egert, N. Nguyen, and M. Schwaiger, “Myocardial Glucose Transporter GLUT1: Translocation Induced by Insulin and Ischemia,” *J Mol Cell Cardiol*, vol. 31, no. 7, pp. 1337–1344, Jul. 1999, doi: 10.1006/jmcc.1999.0965.

[307] V. Theendakara *et al.*, “Neuroprotective Sirtuin ratio reversed by ApoE4,” *Proc Natl Acad Sci U S A*, vol. 110, no. 45, pp. 18303–18308, Nov. 2013, doi: 10.1073/pnas.1314145110.

[308] J. Chen, L. Cao, Z. Li, and Y. Li, “SIRT1 promotes GLUT1 expression and bladder cancer progression via regulation of glucose uptake,” *Hum Cell*, vol. 32, no. 2, pp. 193–201, Apr. 2019, doi: 10.1007/s13577-019-00237-5.

[309] C. Fu *et al.*, “Activation of SIRT1 ameliorates LPS-induced lung injury in mice via decreasing endothelial tight junction permeability,” *Acta Pharmacol Sin*, vol. 40, no. 5, pp. 630–641, May 2019, doi: 10.1038/s41401-018-0045-3.

[310] Y. Zhang, G. Cui, Y. Wang, Y. Gong, and Y. Wang, “SIRT1 activation alleviates brain microvascular endothelial dysfunction in peroxisomal disorders,” *Int J Mol Med*, Jun. 2019, doi: 10.3892/ijmm.2019.4250.

[311] E. H. Neal, K. A. Katdare, Y. Shi, N. A. Marinelli, K. A. Hagerla, and E. S. Lippmann, “Influence of basal media composition on barrier fidelity within human pluripotent stem cell-derived blood-brain barrier models,” *J Neurochem*, vol. 159, no. 6, pp. 980–991, Dec. 2021, doi: 10.1111/jnc.15532.

[312] S. Schaffer, V. Y. M. Lam, I. M. A. Ernst, P. Huebbe, G. Rimbach, and B. Halliwell, “Variability in APOE genotype status in human-derived cell lines: a cause for concern in cell culture studies?,” *Genes Nutr*, vol. 9, no. 1, p. 364, Jan. 2014, doi: 10.1007/s12263-013-0364-4.

[313] B. Schmid *et al.*, “Generation of a set of isogenic, gene-edited iPSC lines homozygous for all main APOE variants and an APOE knock-out line,” *Stem Cell Res*, vol. 34, no. June 2017, p. 101349, 2019, doi: 10.1016/j.scr.2018.11.010.

[314] K. M. Gray, J. W. Jung, C. T. Inglut, H. C. Huang, and K. M. Stroka, “Quantitatively relating brain endothelial cell-cell junction phenotype to global and local barrier properties under varied culture conditions via the Junction Analyzer Program,” *Fluids Barriers CNS*, vol. 17, no. 1, pp. 1–20, 2020, doi: 10.1186/s12987-020-0177-y.

[315] A. Montagne *et al.*, “APOE4 leads to blood–brain barrier dysfunction predicting cognitive decline,” *Nature*, vol. 581, no. 7806, pp. 71–76, May 2020, doi: 10.1038/s41586-020-2247-3.

[316] K. B. Koronowski *et al.*, “Neuronal SIRT1 (silent information regulator 2 homologue 1) regulates glycolysis and mediates resveratrol-induced ischemic tolerance,” *Stroke*, vol. 48, no. 11, pp. 3117–3125, Nov. 2017, doi: 10.1161/STROKEAHA.117.018562.

[317] S. M. Stamatovic, G. Martinez-Revollar, A. Hu, J. Choi, R. F. Keep, and A. V. Andjelkovic, “Decline in Sirtuin-1 expression and activity plays a critical role in blood-brain barrier permeability in aging,” *Neurobiol Dis*, vol. 126, pp. 105–116, Jun. 2019, doi: 10.1016/j.nbd.2018.09.006.

[318] X. Zhang, J. Chen, L. Sun, and Y. Xu, “SIRT1 deacetylates KLF4 to activate Claudin-5 transcription in ovarian cancer cells,” *J Cell Biochem*, vol. 119, no. 2, pp. 2418–2426, Feb. 2018, doi: 10.1002/jcb.26404.

[319] J. Ma, P. Wang, Y. Liu, L. Zhao, Z. Li, and Y. Xue, “Krüppel-Like Factor 4 Regulates Blood-Tumor Barrier Permeability via ZO-1, Occludin and Claudin-5,” *J Cell Physiol*, vol. 229, no. 7, pp. 916–926, Jul. 2014, doi: 10.1002/jcp.24523.

[320] E. McNeil, C. T. Capaldo, and I. G. Macara, “Zonula Occludens-1 Function in the Assembly of Tight Junctions in Madin-Darby Canine Kidney Epithelial Cells,” *Mol Biol Cell*, vol. 17, no. 4, pp. 1922–1932, Apr. 2006, doi: 10.1091/mbc.e05-07-0650.

[321] O. Tornavaca *et al.*, “ZO-1 controls endothelial adherens junctions, cell–cell tension, angiogenesis, and barrier formation,” *Journal of Cell Biology*, vol. 208, no. 6, pp. 821–838, Mar. 2015, doi: 10.1083/jcb.201404140.

[322] X. Zhang, L. Wu, R. H. Swerdlow, and L. Zhao, “Opposing Effects of ApoE2 and ApoE4 on Glycolytic Metabolism in Neuronal Aging Supports a Warburg Neuroprotective Cascade against Alzheimer’s Disease,” *Cells*, vol. 12, no. 3, p. 410, Jan. 2023, doi: 10.3390/cells12030410.

[323] S. Nagamatsu, J. M. Kornhauser, C. F. Burant, S. Seino, K. E. Mayo, and G. I. Bell, “Glucose transporter expression in brain. cDNA sequence of mouse GLUT3, the brain facilitative glucose transporter isoform, and identification of sites of expression by in situ hybridization.,” *Journal of Biological Chemistry*, vol. 267, no. 1, pp. 467–472, Jan. 1992, doi: 10.1016/S0021-9258(18)48518-3.

[324] J. E. Pessin and G. I. Bell, “Mammalian Facilitative Glucose Transporter Family: Structure and Molecular Regulation,” *Annu Rev Physiol*, vol. 54, no. 1, pp. 911–930, Oct. 1992, doi: 10.1146/annurev.ph.54.030192.004403.

[325] M. Mueckler, “Facilitative glucose transporters,” *Eur J Biochem*, vol. 219, no. 3, pp. 713–725, Feb. 1994, doi: 10.1111/j.1432-1033.1994.tb18550.x.

[326] K. Suzuki and T. Kono, “Evidence that insulin causes translocation of glucose transport activity to the plasma membrane from an intracellular storage site.,” *Proceedings of the National Academy of Sciences*, vol. 77, no. 5, pp. 2542–2545, May 1980, doi: 10.1073/pnas.77.5.2542.

[327] M. F. Hirshman, L. J. Goodyear, L. J. Wardzala, E. D. Horton, and E. S. Horton, “Identification of an intracellular pool of glucose transporters from basal and insulin-stimulated rat skeletal muscle.,” *J Biol Chem*, vol. 265, no. 2, pp. 987–91, Jan. 1990.

[328] W. I. Sivitz, S. L. DeSautel, T. Kayano, G. I. Bell, and J. E. Pessin, “Regulation of glucose transporter messenger RNA in insulin-deficient states,” *Nature*, vol. 340, no. 6228, pp. 72–74, Jul. 1989, doi: 10.1038/340072a0.

[329] C. Taha, Y. Mitsumoto, Z. Liu, E. Y. Skolnik, and A. Klip, “The Insulin-dependent Biosynthesis of GLUT1 and GLUT3 Glucose Transporters in L6 Muscle Cells Is Mediated by Distinct Pathways,” *Journal of Biological Chemistry*, vol. 270, no. 42, pp. 24678–24681, Oct. 1995, doi: 10.1074/jbc.270.42.24678.

[330] H. N. Frazier *et al.*, “Elevating Insulin Signaling Using a Constitutively Active Insulin Receptor Increases Glucose Metabolism and Expression of GLUT3 in Hippocampal Neurons,” *Front Neurosci*, vol. 14, Jul. 2020, doi: 10.3389/fnins.2020.00668.

[331] L. Wu, X. Zhang, and L. Zhao, “Human apoe isoforms differentially modulate brain glucose and ketone body metabolism: Implications for Alzheimer’s disease risk reduction and early intervention,” *Journal of Neuroscience*, vol. 38, no. 30, pp. 6665–6681, Jul. 2018, doi: 10.1523/JNEUROSCI.2262-17.2018.

[332] A. Doddaballapur *et al.*, “Laminar Shear Stress Inhibits Endothelial Cell Metabolism via KLF2-Mediated Repression of PFKFB3,” *Arterioscler Thromb Vasc Biol*, vol. 35, no. 1, pp. 137–145, Jan. 2015, doi: 10.1161/ATVBAHA.114.304277.

[333] M. Obach *et al.*, “6-Phosphofructo-2-kinase (pfkfb3) Gene Promoter Contains Hypoxia-inducible Factor-1 Binding Sites Necessary for Transactivation in Response to Hypoxia,” *Journal of Biological Chemistry*, vol. 279, no. 51, pp. 53562–53570, Dec. 2004, doi: 10.1074/jbc.M406096200.

[334] S. M. Casillo *et al.*, “An ERK5-PFKFB3 axis regulates glycolysis and represents a therapeutic vulnerability in pediatric diffuse midline glioma,” *Cell Rep*, vol. 43, no. 1, p. 113557, Jan. 2024, doi: 10.1016/j.celrep.2023.113557.

[335] S. Krasemann *et al.*, “The TREM2-APOE Pathway Drives the Transcriptional Phenotype of Dysfunctional Microglia in Neurodegenerative Diseases,” *Immunity*, vol. 47, no. 3, pp. 566-581.e9, Sep. 2017, doi: 10.1016/j.immuni.2017.08.008.

[336] S. Ritter, “Monitoring and Maintenance of Brain Glucose Supply,” in *Appetite and Food Intake*, Second edition. | Boca Raton : CRC Press, 2017. | Previous edition: CRC Press, 2017, pp. 177–204. doi: 10.1201/9781315120171-9.

[337] B. E. Lee, P.-G. Suh, and J.-I. Kim, “O-GlcNAcylation in health and neurodegenerative diseases,” *Exp Mol Med*, vol. 53, no. 11, pp. 1674–1682, Nov. 2021, doi: 10.1038/s12276-021-00709-5.

[338] J. Park *et al.*, “O-GlcNAcylation ameliorates the pathological manifestations of Alzheimer’s disease by inhibiting necroptosis,” *Sci Adv*, vol. 7, no. 3, Jan. 2021, doi: 10.1126/sciadv.abd3207.

[339] C. Kim *et al.*, “O-linked β-N-acetylglucosaminidase inhibitor attenuates β-amyloid plaque and rescues memory impairment,” *Neurobiol Aging*, vol. 34, no. 1, pp. 275–285, Jan. 2013, doi: 10.1016/j.neurobiolaging.2012.03.001.

[340] F. Liu *et al.*, “Reduced O-GlcNAcylation links lower brain glucose metabolism and tau pathology in Alzheimer’s disease,” *Brain*, vol. 132, no. 7, pp. 1820–1832, Jul. 2009, doi: 10.1093/brain/awp099.

[341] S. Thomas and D. A. Fell, “A control analysis exploration of the role of ATP utilisation in glycolytic-flux control and glycolytic-metabolite-concentration regulation,” *Eur J Biochem*, vol. 258, no. 3, pp. 956–967, Dec. 1998, doi: 10.1046/j.1432-1327.1998.2580956.x.

[342] G. Paglia *et al.*, “Unbiased Metabolomic Investigation of Alzheimer’s Disease Brain Points to Dysregulation of Mitochondrial Aspartate Metabolism,” *J Proteome Res*, vol. 15, no. 2, pp. 608–618, Feb. 2016, doi: 10.1021/acs.jproteome.5b01020.

[343] E. Staurenghi *et al.*, “ApoE3 vs. ApoE4 Astrocytes: A Detailed Analysis Provides New Insights into Differences in Cholesterol Homeostasis,” *Antioxidants*, vol. 11, no. 11, p. 2168, Nov. 2022, doi: 10.3390/antiox11112168.

[344] M. F. Lanfranco, J. Sepulveda, G. Kopetsky, and G. W. Rebeck, “Expression and secretion of apoE isoforms in astrocytes and microglia during inflammation,” *Glia*, vol. 69, no. 6, pp. 1478–1493, Jun. 2021, doi: 10.1002/glia.23974.

[345] A. Sen, T. J. Nelson, and D. L. Alkon, “ApoE4 and Aβ Oligomers Reduce BDNF Expression via HDAC Nuclear Translocation,” *The Journal of Neuroscience*, vol. 35, no. 19, pp. 7538–7551, May 2015, doi: 10.1523/JNEUROSCI.0260-15.2015.

[346] M. Hamer and Y. Chida, “Physical activity and risk of neurodegenerative disease: A systematic review of prospective evidence,” *Psychol Med*, vol. 39, no. 1, pp. 3–11, 2008, doi: 10.1017/S0033291708003681.

[347] J. Liu *et al.*, “The effect of exercise on cerebral blood flow and executive function among young adults: a double-blinded randomized controlled trial,” *Sci Rep*, vol. 13, no. 1, p. 8269, May 2023, doi: 10.1038/s41598-023-33063-9.

[348] J. C. Smith *et al.*, “Physical activity reduces hippocampal atrophy in elders at genetic risk for Alzheimer’s disease,” *Front Aging Neurosci*, vol. 6, no. APR, Apr. 2014, doi: 10.3389/fnagi.2014.00061.

[349] R. J. Dougherty *et al.*, “Moderate Physical Activity is Associated with Cerebral Glucose Metabolism in Adults at Risk for Alzheimer’s Disease,” *Journal of Alzheimer’s Disease*, vol. 58, no. 4, pp. 1089–1097, Jun. 2017, doi: 10.3233/JAD-161067.

[350] X. He *et al.*, “Voluntary Exercise Promotes Glymphatic Clearance of Amyloid Beta and Reduces the Activation of Astrocytes and Microglia in Aged Mice,” *Front Mol Neurosci*, vol. 10, May 2017, doi: 10.3389/fnmol.2017.00144.

[351] L. D. Baker *et al.*, “Effects of Aerobic Exercise on Mild Cognitive Impairment,” *Arch Neurol*, vol. 67, no. 1, Jan. 2010, doi: 10.1001/archneurol.2009.307.

[352] K. Nay *et al.*, “Molecular Mechanisms Underlying the Beneficial Effects of Exercise on Brain Function and Neurological Disorders,” *Int J Mol Sci*, vol. 22, no. 8, p. 4052, Apr. 2021, doi: 10.3390/ijms22084052.

[353] M. V. Lourenco *et al.*, “Exercise-linked FNDC5/irisin rescues synaptic plasticity and memory defects in Alzheimer’s models,” *Nat Med*, vol. 25, no. 1, pp. 165–175, Jan. 2019, doi: 10.1038/s41591-018-0275-4.

[354] L. El Hayek *et al.*, “Lactate mediates the effects of exercise on learning and memory through SIRT1-dependent activation of hippocampal brain-derived neurotrophic factor (BDNF),” *The Journal of Neuroscience*, pp. 1661–18, Jan. 2019, doi: 10.1523/JNEUROSCI.1661-18.2019.

[355] H. Y. Moon *et al.*, “Running-Induced Systemic Cathepsin B Secretion Is Associated with Memory Function,” *Cell Metab*, vol. 24, no. 2, pp. 332–340, Aug. 2016, doi: 10.1016/j.cmet.2016.05.025.

[356] S. Vaynman, Z. Ying, and F. Gomez-Pinilla, “Hippocampal BDNF mediates the efficacy of exercise on synaptic plasticity and cognition,” *European Journal of Neuroscience*, vol. 20, no. 10, pp. 2580–2590, Nov. 2004, doi: 10.1111/j.1460-9568.2004.03720.x.

[357] K. L. Szuhany, M. Bugatti, and M. W. Otto, “A meta-analytic review of the effects of exercise on brain-derived neurotrophic factor,” *J Psychiatr Res*, vol. 60, pp. 56–64, Jan. 2015, doi: 10.1016/j.jpsychires.2014.10.003.

[358] F. Gomez-Pinilla and Z. Ying, “Differential effects of exercise and dietary docosahexaenoic acid on molecular systems associated with control of allostasis in the hypothalamus and hippocampus,” *Neuroscience*, vol. 168, no. 1, pp. 130–137, Jun. 2010, doi: 10.1016/j.neuroscience.2010.02.070.

[359] C.-K. Cheng *et al.*, “Activation of AMPK/miR-181b Axis Alleviates Endothelial Dysfunction and Vascular Inflammation in Diabetic Mice,” *Antioxidants*, vol. 11, no. 6, p. 1137, Jun. 2022, doi: 10.3390/antiox11061137.

[360] C. Cantó *et al.*, “AMPK regulates energy expenditure by modulating NAD+ metabolism and SIRT1 activity,” *Nature*, vol. 458, no. 7241, pp. 1056–1060, Apr. 2009, doi: 10.1038/nature07813.

[361] M. J. Stebbins, H. K. Wilson, S. G. Canfield, T. Qian, S. P. Palecek, and E. V. Shusta, “Differentiation and characterization of human pluripotent stem cell-derived brain microvascular endothelial cells,” *Methods*, vol. 101, pp. 93–102, May 2016, doi: 10.1016/j.ymeth.2015.10.016.

[362] J. M. Gaitán *et al.*, “Brain Glucose Metabolism, Cognition, and Cardiorespiratory Fitness Following Exercise Training in Adults at Risk for Alzheimer’s Disease,” *Brain Plasticity*, vol. 5, no. 1, pp. 83–95, Dec. 2019, doi: 10.3233/BPL-190093.

[363] J.-P. Hu, Y.-H. Guo, F. Wang, X.-P. Zhao, Q.-H. Zhang, and Q.-H. Song, “Exercise improves cognitive function in aging patients.,” *Int J Clin Exp Med*, vol. 7, no. 10, pp. 3144–9, 2014.

[364] G. Huang, C. A. Gibson, Z. V. Tran, and W. H. Osness, “Controlled Endurance Exercise Training and VO_{2max} Changes in Older Adults: A Meta-Analysis,” *Prev Cardiol*, vol. 8, no. 4, pp. 217–225, Sep. 2005, doi: 10.1111/j.0197-3118.2005.04324.x.

[365] C. G. Juan, K. B. Matchett, and G. W. Davison, “A systematic review and meta-analysis of the SIRT1 response to exercise,” *Sci Rep*, vol. 13, no. 1, p. 14752, Sep. 2023, doi: 10.1038/s41598-023-38843-x.

[366] L. El Hayek *et al.*, “Lactate mediates the effects of exercise on learning and memory through SIRT1-dependent activation of hippocampal brain-derived neurotrophic factor (BDNF),” *The Journal of Neuroscience*, pp. 1661–18, Jan. 2019, doi: 10.1523/JNEUROSCI.1661-18.2019.

[367] H. Y. Cohen *et al.*, “Calorie Restriction Promotes Mammalian Cell Survival by Inducing the SIRT1 Deacetylase,” *Science (1979)*, vol. 305, no. 5682, pp. 390–392, Jul. 2004, doi: 10.1126/science.1099196.

[368] J.-Y. Luo *et al.*, “Induction of KLF2 by Exercise Activates eNOS to Improve Vasodilatation in Diabetic Mice,” *Diabetes*, vol. 72, no. 9, pp. 1330–1342, Sep. 2023, doi: 10.2337/db23-0070.

[369] N. K. Bennett *et al.*, “Defining the ATPome reveals cross-optimization of metabolic pathways,” *Nat Commun*, vol. 11, no. 1, p. 4319, Aug. 2020, doi: 10.1038/s41467-020-18084-6.

[370] V. E. Mulgrave *et al.*, “Exercise modulates APOE expression in brain cortex of female APOE3 and APOE4 targeted replacement mice,” *Neuropeptides*, vol. 97, p. 102307, Feb. 2023, doi: 10.1016/j.npep.2022.102307.

[371] J. P. D. Kleinloog, R. P. Mensink, D. Ivanov, J. J. Adam, K. Uludağ, and P. J. Joris, “Aerobic Exercise Training Improves Cerebral Blood Flow and Executive Function: A Randomized, Controlled Cross-Over Trial in Sedentary Older Men,” *Front Aging Neurosci*, vol. 11, Dec. 2019, doi: 10.3389/fnagi.2019.00333.

[372] L. Cucullo, M. Hossain, V. Puvenna, N. Marchi, and D. Janigro, “The role of shear stress in Blood-Brain Barrier endothelial physiology,” *BMC Neurosci*, vol. 12, May 2011, doi: 10.1186/1471-2202-12-40.

[373] D. Ranadewa, J. Wu, V. A. Subramanianbalachandar, and R. L. Steward, “Variable fluid flow regimes alter human brain microvascular endothelial cell–cell junctions and cytoskeletal structure,” *Cytoskeleton*, vol. 78, no. 6, pp. 323–334, Jun. 2021, doi: 10.1002/cm.21687.

[374] J. A. Timmons *et al.*, “Modulation of extracellular matrix genes reflects the magnitude of physiological adaptation to aerobic exercise training in humans,” *BMC Biol*, vol. 3, no. 1, p. 19, Dec. 2005, doi: 10.1186/1741-7007-3-19.

[375] B. J. Nicklas and T. E. Brinkley, “Exercise Training as a Treatment for Chronic Inflammation in the Elderly,” *Exerc Sport Sci Rev*, vol. 37, no. 4, pp. 165–170, Oct. 2009, doi: 10.1097/JES.0b013e3181b7b3d9.

[376] J. G. DeStefano, Z. S. Xu, A. J. Williams, N. Yimam, and P. C. Searson, “Effect of shear stress on iPSC-derived human brain microvascular endothelial cells (dhBMECs),” *Fluids Barriers CNS*, vol. 14, no. 1, pp. 1–15, 2017, doi: 10.1186/s12987-017-0068-z.

[377] H. Nishihara *et al.*, “Advancing human induced pluripotent stem cell-derived blood-brain barrier models for studying immune cell interactions,” *The FASEB Journal*, vol. 34, no. 12, pp. 16693–16715, Dec. 2020, doi: 10.1096/fj.202001507RR.

[378] D. A. M. Feyen *et al.*, “Metabolic Maturation Media Improve Physiological Function of Human iPSC-Derived Cardiomyocytes,” *Cell Rep*, vol. 32, no. 3, p. 107925, Jul. 2020, doi: 10.1016/j.celrep.2020.107925.

[379] N. R. Wevers *et al.*, “A perfused human blood–brain barrier on-a-chip for high-throughput assessment of barrier function and antibody transport,” *Fluids Barriers CNS*, vol. 15, no. 1, p. 23, Dec. 2018, doi: 10.1186/s12987-018-0108-3.

[380] T.-E. Park *et al.*, “Hypoxia-enhanced Blood-Brain Barrier Chip recapitulates human barrier function and shuttling of drugs and antibodies,” *Nat Commun*, vol. 10, no. 1, p. 2621, Dec. 2019, doi: 10.1038/s41467-019-10588-0.

[381] S. Seo, S. Nah, K. Lee, N. Choi, and H. N. Kim, “Triculture Model of In Vitro BBB and its Application to Study BBB-Associated Chemosensitivity and Drug Delivery in Glioblastoma,” *Adv Funct Mater*, vol. 32, no. 10, Mar. 2022, doi: 10.1002/adfm.202106860.

[382] S. Bang *et al.*, “A Low Permeability Microfluidic Blood-Brain Barrier Platform with Direct Contact between Perfusable Vascular Network and Astrocytes,” *Sci Rep*, vol. 7, no. 1, p. 8083, Aug. 2017, doi: 10.1038/s41598-017-07416-0.

[383] S. I. Ahn *et al.*, “Microengineered human blood–brain barrier platform for understanding nanoparticle transport mechanisms,” *Nat Commun*, vol. 11, no. 1, p. 175, Jan. 2020, doi: 10.1038/s41467-019-13896-7.

[384] R. Booth and H. Kim, “Characterization of a microfluidic in vitro model of the blood-brain barrier (μBBB),” *Lab Chip*, vol. 12, no. 10, p. 1784, 2012, doi: 10.1039/c2lc40094d.

[385] J. H. Yeon, D. Na, K. Choi, S.-W. Ryu, C. Choi, and J.-K. Park, “Reliable permeability assay system in a microfluidic device mimicking cerebral vasculatures,” *Biomed Microdevices*, vol. 14, no. 6, pp. 1141–1148, Dec. 2012, doi: 10.1007/s10544-012-9680-5.

[386] A. K. H. Achyuta *et al.*, “A modular approach to create a neurovascular unit-on-a-chip,” *Lab Chip*, vol. 13, no. 4, pp. 542–553, 2013, doi: 10.1039/C2LC41033H.

[387] L. M. Griep *et al.*, “BBB ON CHIP: microfluidic platform to mechanically and biochemically modulate blood-brain barrier function,” *Biomed Microdevices*, vol. 15, no. 1, pp. 145–150, Feb. 2013, doi: 10.1007/s10544-012-9699-7.

[388] B. Prabhakarpandian *et al.*, “SyM-BBB: a microfluidic blood brain barrier model,” *Lab Chip*, vol. 13, no. 6, p. 1093, 2013, doi: 10.1039/c2lc41208j.

[389] J. A. Brown *et al.*, “Recreating blood-brain barrier physiology and structure on chip: A novel neurovascular microfluidic bioreactor,” *Biomicrofluidics*, vol. 9, no. 5, Sep. 2015, doi: 10.1063/1.4934713.

[390] H. Cho *et al.*, “Three-Dimensional Blood-Brain Barrier Model for in vitro Studies of Neurovascular Pathology,” *Sci Rep*, vol. 5, no. 1, p. 15222, Oct. 2015, doi: 10.1038/srep15222.

[391] S. P. Deosarkar, B. Prabhakarpandian, B. Wang, J. B. Sheffield, B. Krynska, and M. F. Kiani, “A Novel Dynamic Neonatal Blood-Brain Barrier on a Chip,” *PLoS One*, vol. 10, no. 11, p. e0142725, Nov. 2015, doi: 10.1371/journal.pone.0142725.

[392] S. Kim *et al.*, “Human bone marrow-derived mesenchymal stem cells play a role as a vascular pericyte in the reconstruction of human BBB on the angiogenesis microfluidic chip,” *Biomaterials*, vol. 279, p. 121210, Dec. 2021, doi: 10.1016/j.biomaterials.2021.121210.

[393] F. R. Walter *et al.*, “A versatile lab-on-a-chip tool for modeling biological barriers,” *Sens Actuators B Chem*, vol. 222, pp. 1209–1219, Jan. 2016, doi: 10.1016/j.snb.2015.07.110.

[394] K. L. Sellgren, B. T. Hawkins, and S. Grego, “An optically transparent membrane supports shear stress studies in a three-dimensional microfluidic neurovascular unit model,” *Biomicrofluidics*, vol. 9, no. 6, Nov. 2015, doi: 10.1063/1.4935594.

[395] Y. I. Wang, H. E. Abaci, and M. L. Shuler, “Microfluidic blood–brain barrier model provides in vivo-like barrier properties for drug permeability screening,” *Biotechnol Bioeng*, vol. 114, no. 1, pp. 184–194, Jan. 2017, doi: 10.1002/bit.26045.

[396] H. Xu *et al.*, “A dynamic in vivo-like organotypic blood-brain barrier model to probe metastatic brain tumors,” *Sci Rep*, vol. 6, no. 1, p. 36670, Nov. 2016, doi: 10.1038/srep36670.

[397] G. Adriani, D. Ma, A. Pavesi, R. D. Kamm, and E. L. K. Goh, “A 3D neurovascular microfluidic model consisting of neurons, astrocytes and cerebral endothelial cells as a blood–brain barrier,” *Lab Chip*, vol. 17, no. 3, pp. 448–459, 2017, doi: 10.1039/C6LC00638H.